**UNIVERSITA' DEGLI STUDI "G. d'Annunzio"**

**Chieti-Pescara**

**SCUOLA SUPERIORE "G. d'Annunzio"**

*DOTTORATO DI RICERCA IN*

**ENGINEERING SCIENCES**

*CICLO*

**XXXVIII**

# "Recurrent fault surface ruptures and Probabilistic Fault Displacement Hazard Assessment: case studies from Taiwan and northern Calabria, Italy"

**Dipartimento di Ingegneria e Geologia**

**Settore Scientifico Disciplinare** GEOS-04/A

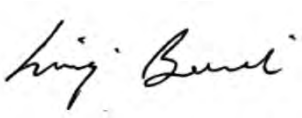

Dottorando

Dott. Hugo Fernandez



Coordinatore

Prof. Luigi Berardi



Tutor

Prof. Bruno Pace



Dott.ssa Laura Peruzza




Anni Accademici 2023/2024 – 2025/2026

# Abstract

The aim of this work is to investigate the fault surface rupture phenomenon and its hazard assessment through Probabilistic Fault Displacement Hazard Analysis (PFDHA). Surface rupture is a natural phenomenon occurring during an earthquake, representing an important hazard for critical infrastructures, that must be addressed in our society. PFDHA is the main methodology used in the literature to estimate this hazard but, despite many efforts to collect new data and develop new models, fault displacement hazard remains poorly integrated in the national and international safety guidelines. This approach is based on observed past surface rupture and on the assumption that future ruptures will be similar to past ones.

This assumption is examined through the Longitudinal Valley Fault system in Taiwan, where surface ruptures have been documented multiple times on the same faults in the last decades (1951–present). Comparison of two surface-rupturing earthquake sequences shows that fault surface expressions were broadly similar, with observed differences largely attributable to the aleatory uncertainty of earthquake nucleation (epicentral location, magnitude).

A PFDHA study is then conducted for the northern Calabria region in Italy, one of Europe's most seismically active regions, using a range of existing empirical models. This study provides a comprehensive hazard assessment through a new approach, at the regional-scale instead of the common site-specific approach. The hazard is mostly concentrated on and around the main tectonic structures in the area: the Crati and the Laghi-Cecita faults where significant surface displacement (> 10 cm) can be expected with return periods of 10-100 ka.

This new approach is beneficial to explore various fault configuration, to highlight the spatial distribution of the hazard around the main fault traces and could be used as a first-order tool for decision-making authorities or for land-use planning.

# Acknowledgements

I would like to express my sincere gratitude to my two PhD supervisors for their continuous guidance, encouragement, and support throughout my PhD journey, in particular at my arrival in Italy and during the writing of this thesis. Their trust, patience, availability and advice have been invaluable not only for this work, but also for my personal and scientific development.

I would also like to thank my colleagues and friends at OGS and at the University of Chieti-Pescara, who made my everyday life there so enjoyable. Their kindness, hospitality, the lunches together, and the more or less “short” walks around OGS brought so much joy and balance to these years. I am deeply grateful for all the moments we shared together.

A special thank you to Professor Kuo at National Central University for welcoming me into his research group in Taiwan for more than seven months, and for his guidance, support, and kindness during my stay. He gave me with the opportunity to discover a research environment and cultural context significantly different from my own. My time in Taiwan was an enriching personal and scientific experience that I will never forget. I would also like to thank all the students and members of his lab for making this research stay even more enjoyable and memorable (let's go T1!).

To all the people I met during summer schools, conferences, and scientific meetings: thank you for the enriching discussions, the friendships, and the unforgettable experiences. Meeting and exchanging ideas with you, coming from all the parts of the world, has been a true privilege, and I sincerely hope our paths will cross again in the future. I will always enjoy the memories we created together, both professionally and personally, from fieldworks in Pompeii, the Vesuvius, or an abandoned village in Sicily, to a typhoon during a conference in Yilan, with so many other adventures in between.

A few lighter acknowledgements: thank you to Oda, Faker and to my cat, Kachou, le p'tit con, that all helped me disconnect from research from time to time.

Enfin, un petit mot en français pour terminer. Un immense merci à tous mes proches en France, mes amis, ma famille. Je sais que vous ne comprenez pas trop ce que je fais en Italie, mais malgré tout vous m'avez toujours apporté votre soutien et permis de me changer les idées. Chaque retour en France était une vraie bouffée d'oxygène qui me permettait de me ressourcer

à vos côtés, et cela a grandement contribué au fait que je puisse aller au bout de cette aventure. Mention spéciale à Paul qui est quand même venu me voir jusqu'à Taiwan !

Le mot de la fin sera évidemment pour ma famille : un grand merci à ma sœur et les trois vilains petits canards à l'insouciance et l'énergie débordantes, et évidemment à mes parents sans qui tout cela n'aurait pas été possible.

# Table of Content

Abstract ..... 2

Acknowledgements ..... 3

Table of Content ..... 5

List of Figures ..... 7

List of Tables ..... 11

1. Introduction to fault surface rupture and Probabilistic Fault Displacement Hazard Assessment (PFDHA) ..... 12

1.1. Surface ruptures around the world ..... 12

1.2. Fault Displacement Hazard Assessment (FDHA) ..... 14

1.2.1. A pioneer model: Youngs et al. (2003) ..... 15

1.2.2. New PFDHA models ..... 25

1.3. Regulations and published PFDHA application cases ..... 33

1.3.1. Regulatory framework ..... 33

1.3.2. Published PFDHA application cases ..... 34

1.4. Summary and research gap: main questions ..... 35

2. A particular case of recent repeated fault surface rupture: the Longitudinal Valley in Taiwan ..... 38

2.1. Introduction ..... 38

2.2. LVF earthquakes sequences in 1951 and 2018-2022 ..... 40

2.3. Methods and surface rupture data collection ..... 41

2.4. Hualien earthquakes ..... 46

2.4.1. Rupture trace and along-fault displacement comparisons ..... 47

2.4.2. Surface rupture length comparisons ..... 49

2.4.3. 1951 Mw 7.3 event displacement amplitude comparison ..... 50

2.4.4. 2018 Mw 6.42 event displacement amplitude comparison ..... 53
2.4.5 Brief summary and conclusions of the Hualien successive surface ruptures comparisons ..... 60
2.5. Southern LVF Taitung and Chihshang earthquakes ..... 62
2.5.1. Rupture location comparisons ..... 63
2.5.2. 1951 Mw 6.2 and Mw 7.0 Taitung event displacement amplitude comparison ..... 67
2.5.3. 2022 Mw 7.0 Chihshang event displacement amplitude comparison ..... 69
2.5.4. Brief summary and conclusions of the south LV successive rupture analysis ..... 75
2.6. Conclusions ..... 75
3. PFDHA application to the northern Calabria region, Italy ..... 77
3.1. Introduction ..... 77
3.2. Local earthquake relocation ..... 79
3.3. Refining the seismotectonic model in northern Calabria ..... 84
3.3.1. Seismogenic sources review ..... 85
3.3.2. Seismogenic sources parametrisation ..... 100
3.3.3. Rupture scenarios ..... 111
3.4. MFD characterisation ..... 113
3.5. PSHA calculations in northern Calabria ..... 115
3.6. PFDHA calculations in northern Calabria ..... 118
3.6.1. Model selection and parametrisation ..... 118
3.6.2. Regional-scale mapping ..... 121
3.6.3. Results and discussions ..... 124
3.7. Conclusions ..... 129
4. General conclusions and perspectives ..... 131
References ..... 135

# List of Figures

*Figure 1-1: Collection of surface rupture photographs around the world* ..... 13
*Figure 1-2: Simplified scheme illustrating the PFDHA earthquake approach* ..... 17
*Figure 1-3: Conditional probability of occurrence of principal surface rupture* ..... 19
*Figure 1-4: Normalised displacement distributions along the principal fault* ..... 21
*Figure 1-5: Conditional probability of exceedance for principal faulting* ..... 22
*Figure 1-6: Conditional probability of occurrence of distributed rupture* ..... 24
*Figure 1-7: Distributions of the $D_{distributed}$/MD ratio with distance from the main fault* ..... 25
*Figure 1-8: Overview of the key PFDHA models published in the literature up to 2025* ..... 26
*Figure 1-9: Probability of principal surface rupture for various faulting styles and multiple datasets* ..... 28
*Figure 1-10: Location and style of faulting of the FDHI database earthquakes* ..... 29
*Figure 1-11: Earthquake magnitude and epicentral depth distributions using data from the SURE 2.0 and FDHI databases* ..... 30
*Figure 1-12: Fault displacement metrics and definitions proposed in literature* ..... 31
*Figure 1-13: Slip components in FDHA* ..... 33
*Figure 2-1: Map of the Longitudinal Valley fault (LVF) system* ..... 39
*Figure 2-2: Geometry of the southern part of Longitudinal Valley fault system* ..... 40
*Figure 2-3: Process followed to relocate one surface rupture photograph from the 1951 Taitung earthquake* ..... 43
*Figure 2-4: Rupture traces and surface displacement data of the 1951 and 2018 Hualien earthquakes.* ..... 47
*Figure 2-5: Comparison of the average fault displacement observed along the Milun fault during the 1951 and 2018 Hualien earthquakes.* ..... 49
*Figure 2-6: Comparison of the principal horizontal displacement observed along the Milun fault during the 1951 Hualien earthquake with the PEA11 models.* ..... 51
*Figure 2-7: Comparison of the principal vertical displacement observed along the Milun fault during the 1951 Hualien earthquake with AD and MD estimated from MEA24.* ..... 51
*Figure 2-8: Comparison of the distributed horizontal displacement observed during the 1951 Hualien earthquake with PEA11 model* ..... 52

*Figure 2-9: Comparison of the distributed vertical displacement observed during the 1951 Hualien earthquake with empirical regressions ..... 53*
*Figure 2-10: Comparison of the principal horizontal displacement observed along the Milun fault during the 2018 Hualien earthquake with the PEA11 models. ..... 57*
*Figure 2-11: Comparison of the principal vertical displacement observed along the Milun fault during the 2018 Hualien earthquake with AD and MD estimated from MEA24. .... 58*
*Figure 2-12: Comparison of the distributed horizontal displacement observed during the 2018 Hualien earthquake with PEA11 model ..... 59*
*Figure 2-13: Comparison of the distributed vertical surface displacement observed during the 2018 Hualien earthquake with empirical regressions ..... 60*
*Figure 2-14: Location of the surface rupture data collected for the 1951 and 2022 earthquakes in the southern part of the LVF ..... 62*
*Figure 2-15: Spatial slip component comparison of the surface ruptures observed during the 1951 and 2022 earthquakes ..... 64*
*Figure 2-16: Direct spatial comparison of the observed surface ruptures along the LV during the 1951 and 2022 events..... 65*
*Figure 2-17: Comparison of the 2022 Chihshang earthquake surface ruptures with a proposed finite fault model..... 66*
*Figure 2-18: Comparison of the principal horizontal displacement observed along the LV during Taitung 1951 1st shock and 2nd shock with the PEA11 models. ..... 68*
*Figure 2-19: Comparison of the principal vertical displacement observed during the 1951 Taitung earthquakes with the AD and MD estimated with MEA24. ..... 69*
*Figure 2-20: Comparison of the principal horizontal displacement observed along the Yuli and Chihshang faults during the 2022 earthquake with the PEA11 models. ..... 71*
*Figure 2-21: Comparison of the principal vertical displacement observed along the Yuli and Chihshang faults during the 2022 earthquake with the AD and MD estimated with MEA24..... 72*
*Figure 2-22: Comparison of the distributed horizontal displacement observed during the 2022 Chihshang earthquake with PEA11 model..... 73*
*Figure 2-23: Comparison of the distributed vertical displacement observed during the 2022 Chihshang earthquake with empirical regressions..... 74*
*Figure 3-1: Seismicity map of the study area, in Calabria region, Italy..... 78*

*Figure 3-2: Magnitude of completeness of the ISIDe catalogue* ..... *80*
*Figure 3-3: Seismic network around the Farneto dam in 2023, in northern Calabria.* ..... *81*
*Figure 3-4: Earthquake data collection around the Farneto dam* ..... *82*
*Figure 3-5: Relocated dataset using Hypo71 software.* ..... *83*
*Figure 3-6: Gutenberg-Richter law computed from the 42 events of the relocated events dataset.* ..... *84*
*Figure 3-7: Seismogenic sources and capable faults in northern Calabria* ..... *86*
*Figure 3-8: Faults in the Pollino chain* ..... *88*
*Figure 3-9: Castrovillari fault system* ..... *89*
*Figure 3-10: Sibari Fault Zone* ..... *90*
*Figure 3-11: Tectonic map of the Amendolara ridge, in the Gulf of Taranto* ..... *91*
*Figure 3-12: Fault segments located in the northern part of the Crati Valley* ..... *92*
*Figure 3-13: Interpretation of a seismic line in the northern part of the Crati valley* ..... *92*
*Figure 3-14: Geological map of the Crati Valley* ..... *94*
*Figure 3-15: Interpretation of a seismic line across the central part of the Crati Valley* ..... *95*
*Figure 3-16: Rossano fault system* ..... *98*
*Figure 3-17: Potential active faults in the Sila Massif* ..... *99*
*Figure 3-18: Refined active and capable faults in Northern Calabria* ..... *101*
*Figure 3-19: Focal mechanism of the Mw 2.8 November 2023 earthquake in the central Crati Valley area* ..... *104*
*Figure 3-20: Details regarding the construction of the final fault sources in the Crati Valley* .. *106*
*Figure 3-21: Hypocentral depth distribution in northern Calabria* ..... *108*
*Figure 3-22: Map of the focal mechanisms collected in northern Calabria* ..... *109*
*Figure 3-23: Maximum strain field obtained from GNSS data in northern Calabria* ..... *111*
*Figure 3-24: Geometric sketch of the four scenarios used in our study* ..... *113*
*Figure 3-25: MFD characterisation for the West Crati source* ..... *114*
*Figure 3-26: Northern Calabria hazard map representing the PGA having 10% chance to be exceeded in the next 50 years* ..... *116*
*Figure 3-27: Seismic hazard maps derived from our fault model for northern Calabria* ..... *117*
*Figure 3-28: Probability of exceedance in 50 years comparison for two sites in northern Calabria* ..... *118*
*Figure 3-29: Logic flow used for fault displacement hazard map calculations* ..... *119*

*Figure 3-30: Fault Displacement Hazard maps comparison between YEA03 and VEA25 for scenario 3 and a return period of 100 ka* ..... *122*
*Figure 3-31: 4 scenario hazard maps using YEA03 and VEA25 models equally weighted* ..... *123*
*Figure 3-32: Differences map between scenario 2 and scenario 3* ..... *124*
*Figure 3-33: Fault displacement hazard models variability* ..... *127*
*Figure 3-34: Sigma truncation exploration at the Rovito site* ..... *129*

# List of Tables

*Table 1-1: General overview of the existing PFDHA. ..... 27*

*Table 2-1: Earthquakes data of the 1951 and 2018 sequences in the Longitudinal Valley. ..... 41*

*Table 2-2: Compiled surface rupture data for the 1951 Hualien and Taitung earthquakes ..... 42*

*Table 2-3: Compiled surface rupture dataset for the 2022 Chihshang earthquake. ..... 46*

*Table 2-4: Hualien earthquakes surface rupture lengths comparison ..... 49*

*Table 2-5: Summary of the 1951 Hualien earthquake observed surface rupture data ..... 50*

*Table 2-6: Data statistics of the 2018 Hualien earthquake surface rupture. ..... 54*

*Table 2-7: Final surface rupture dataset compiled for the 2018 Hualien earthquake ..... 56*

*Table 2-8: Detailed surface rupture data for the 1951 Taitung events. ..... 63*

*Table 2-9: Compiled dataset of surface rupture of the 2022 Chihshang earthquake ..... 71*

*Table 2-10: Vertical distributed surface rupture data of the 2022 Chihshang earthquake ..... 74*

*Table 3-1: Detailed source parameters used to build the final seismotectonic model in northern Calabria ..... 100*

*Table 3-2: Collection of the focal mechanism solutions in northern Calabria ..... 110*

*Table 3-3: Final parametrised source model for northern Calabria. ..... 115*

*Table 3-4: Summary of the fault displacement hazard models used in our calculations. ..... 119*

# 1. Introduction to fault surface rupture and Probabilistic Fault Displacement Hazard Assessment (PFDHA)

## 1.1. Surface ruptures around the world

Surface rupture, or surface faulting, here refers exclusively to the permanent tectonic ruptures, i.e. the coseismic effect directly caused by the movement of the fault plane during an earthquake. Fault creep and non-tectonic deformations, such as liquefaction, gravitational slip or any other aseismic deformations, are excluded from this definition. Surface rupture is produced when an earthquake rupture initiates at the level of the seismogenic source (nucleation at depth) and propagates vertically and laterally along the fault plane(s) until it reaches the Earth's surface, where it is expressed along active and capable faults. The resulting surface rupture is a complex phenomenon influenced by a combination of factors controlling both rupture nucleation and propagation. It has been observed and documented in various places and kinematic contexts worldwide (Figure 1-1).

Remarkable cases are illustrated in Figure 1-1, including the famous pictures of the surface offsets along the Chelungpu fault after the 1999 Mw 7.7 Chi-Chi earthquake in Taiwan. During this reverse faulting event, a 6 metres high waterfall was formed in the Tachia river, and a vertical offset of approximately 9 m was measured on the Shigang dam. Another notable case of surface rupture, this time for engineering applications, is the 2002 Mw 7.9 Denali earthquake in Alaska (Figure 1-1). Indeed, this event produced important horizontal surface displacements, especially where the fault intersects the Trans-Alaska oil pipeline (6 m, Honegger et al., 2004). Remarkably, these displacements caused no major damage on the pipeline, as it has been designed in a way to accommodate such horizontal displacement at the estimated intersection with the fault, with a system of ground-mounted cross beams and sliding shoes capable of tolerating several metres of both horizontal and vertical movement. This makes it one of the few successful engineering examples of fault displacement mitigation.

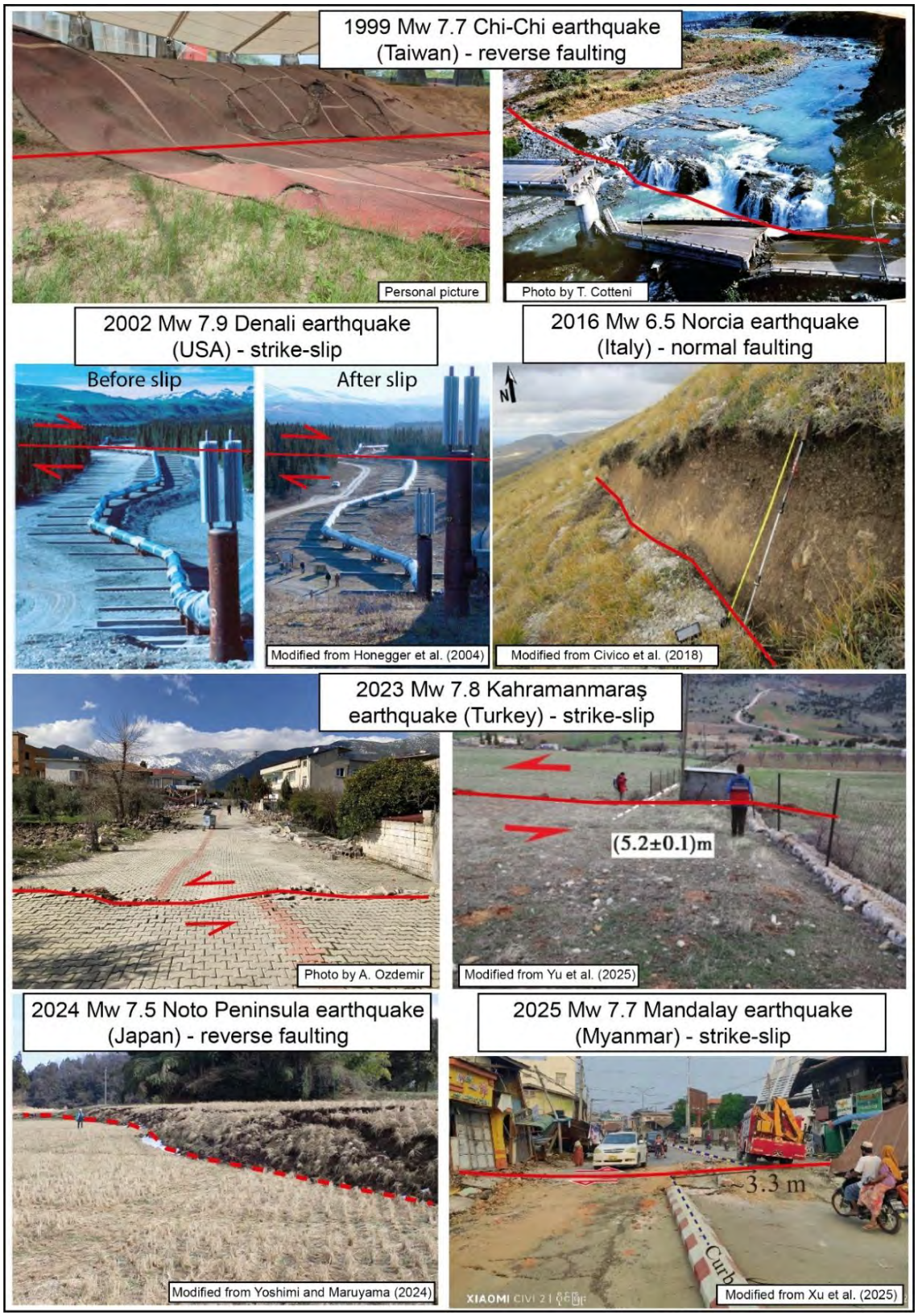



*Figure 1-1: Collection of surface rupture photographs around the world, taken in various places and kinematic contexts.*

Surface faulting can be and have been observed worldwide and in very different kinematic contexts, leading to horizontal, vertical or combined surface offsets. When affecting strategic infrastructures such as nuclear or any energy-related sites, these surface displacements have the potential to create an additional layer of earthquake-related consequences, beyond the classic ground-motion. Like other natural phenomena, this hazard must be assessed in advance to avoid catastrophic consequences in the future, and this forecasting relies fundamentally on the collection and analysis of past observations, which form the empirical basis upon which predictive models are built.

Driven by growing scientific and engineering interest and also advances in observation and measurement technologies, surface ruptures observations are now more numerous and accurately measured, with increased attention given to this phenomenon after an earthquake. Dedicated field campaigns, focused only on collecting surface rupture data, are now organised as soon as possible after a major earthquake (for example in Taiwan after the 2018 Hualien earthquake led by the Central Geological Survey of Taiwan, CGS, 2018; or in Turkey after the 2023 earthquake, led by the China Earthquake Administration, CEA, 2024).

In this context, a particularly remarkable observation was made during the 2016 $M_w$ 6.6 Vettore earthquake in Central Italy, during which the temporal evolution of surface slip was recorded using a simple GNSS network installed along the fault (Wilkinson et al., 2017). Similarly, during the 2025 Mandalay earthquake in Myanmar, the moment the surface ruptured, and the ground was offset was captured by a CCTV camera. Such observations are exceptionally valuable, as they provide a direct and precise visualisation of a phenomenon that is extremely brief and of which only the consequences are usually observed. Such recordings also provide information on the nature of the seismic rupture and the slip type, as well as earthquake source properties (Wilkinson et al., 2017; Latour et al., 2025). The systematic installation and deployment of such monitoring systems (CCTV cameras, simple and low-cost GNSS station networks) along major active fault traces worldwide could provide direct recordings of fault surface rupture events, representing a valuable source of data for improving our understanding of slip behaviour and the processes governing surface rupture .

## 1.2. Fault Displacement Hazard Assessment (FDHA)

Surface rupture forecasting was first introduced by Youngs et al. (2003) for the Yucca Mountain nuclear waste repository in Nevada, USA. This study developed a new methodology based on the standard seismic shaking hazard (Probabilistic Seismic Hazard Assessment,

PSHA) developed in the 60's by Cornell, (1968), to assess the fault displacement hazard in a probabilistic way: PFDHA.

In any Fault Displacement Hazard analysis, the concepts of active and capable faults are fundamental. An *active fault* is a fault that has shown evidence of activity during late Pleistocene, generally up to the last 100-125 ka (Boschi et al., 1996). However, this threshold can vary across frameworks and tectonic settings, ranging from 10 ka to 2 Ma (Slemmons and McKinney, 1977; WSSPC, 1997; NRC, 1997; Machette, 2000; IAEA SSG-9, 2010). A *capable fault* is defined as an active fault that has already produced fault displacement at the surface in the past and is likely to do so again in the future (IAEA SSG-9 (Rev. 1), 2019).

The nuclear industry, led by the IAEA, provides a rare and valuable guidance regarding the FDHA for nuclear sites and is therefore usually taken as a reference, even for non-nuclear related sites. Within this framework, the deterministic approach (DFDHA) estimates the fault displacement hazard at a site assuming a single rupture size scenario, similar to a worst-case scenario, without considering the frequency for which that earthquake might occur (IAEA TECDOC-1987, 2021). In practice, this approach outputs a single maximum surface displacement value and is usually used as a primary tool to determine if a fault can be considered as capable or not. If the deterministic assessment, combined with all available geological data, provides a sufficient basis to demonstrate the non-capability of the fault, no further analysis is required (IAEA TECDOC-1987, 2021).

However, if the deterministic approach fails to exclude the capability of the fault, the probabilistic approach (PFDHA) must be applied (IAEA TECDOC-1987, 2021). This methodology estimates the fault displacement probability while accounting for the source geometry and the earthquake occurrence uncertainties. This output is shaped as a hazard curve expressing the annual frequency of exceedance (AFOE) for a given surface displacement value. Two approaches are commonly used in state-of-the-practice applications: the *earthquake* and *displacement* approaches from Youngs et al. (2003), which are explained in the following section 1.2.1.

### 1.2.1. A pioneer model: Youngs et al. (2003)

PFDHA has been first introduced by Youngs et al. (2003) in a normal faulting context, for the Yucca Mountain nuclear waste repository in Nevada, USA. Youngs et al. (2003) introduced two different approaches to estimate the fault displacement at or near the surface. The *earthquake approach* relates the probability of exceeding a given displacement value *d* at

the site of interest with the probability of having a surface rupturing earthquake. This approach is directly taken from the PSHA methodology but differs in that it replaces the standard ground-motion attenuation function (or ground-motion prediction equations) by a fault displacement attenuation function (Fault Displacement Model, FDM). The *displacement approach*, conversely, estimates the rate of displacement events and the probability distribution for the amount *d* of fault displacement at the specific site. This second method is only used when surface rupture has already been observed on the fault at or near the site of interest and that sufficient data are available, which is a quite rare situation.

#### *1.2.1.1. Earthquake approach*

The earthquake-based approach follows the same methodology as the standard PSHA (Figure 1-2). The first step is to identify and parametrise all the seismogenic sources in the study area, by collecting various information on the sources: geometry, slip-rates, dip angle, kinematic. The second step is to characterise earthquake occurrence on these sources, in terms of maximum magnitude ($M_{max}$) and activity rates. A key difference from PSHA lies in the third step: instead of modelling ground-motion attenuation, PFDHA requires the characterisation of displacement distributions (Figure 1-2), both along strike for principal fault rupture and as a function of distance from the fault trace for distributed faulting (see section 1.2.2.2. for an in-depth analysis of the terminology). Finally, hazard curves are constructed to express the annual frequency of exceedance of a given displacement value at a site k.

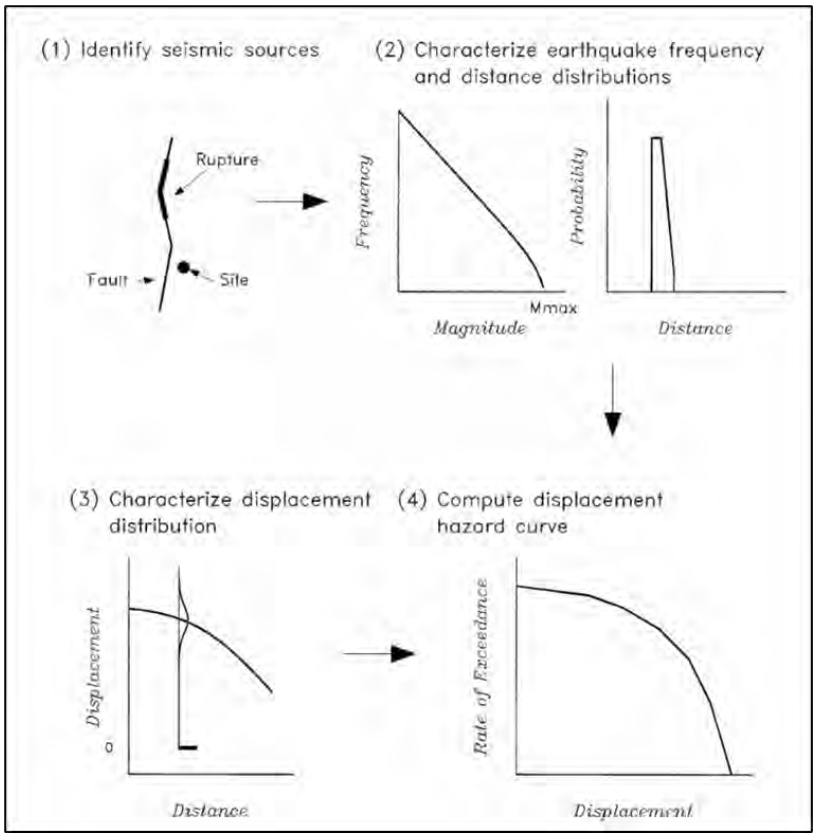



*Figure 1-2: Simplified scheme illustrating the PFDHA earthquake approach steps (from Youngs et al., 2003; Figure 2)*

In PFDHA, for a given location *k*, the annual rate of exceedance of displacement *d* is computed as:

$$\nu_D(d|k) = \sum_{n=1}^{N_f} \int_{M_{min}}^{M_{max}} \alpha_n(M) P(D \geq d|M, r_n(x), \theta) dM \tag{1}$$

where $N_f$ is the number of faults, $\alpha_n(M)$ is the annual occurrence rate of magnitude $M$ earthquakes on fault $n$, $r_n(k)$ is the distance from location $k$ to fault $n$, $\theta$ represents model parameters, and $P(D \geq d \mid M, r, \theta)$ is the conditional exceedance probability. The annual probability of exceedance in a time window T assuming a Poissonian occurrence model is then:

$$P(D \geq d|k, T) = 1 - exp[-\nu_d(d|k)T] \tag{2}$$

The general equation proposed by Youngs to obtain the rate of exceeding a given displacement value at a site *k* is:

$$\nu_k(d) = \sum_n \alpha_n(m^0) \int_{m^0}^{m^u} f_n(m) \left[ \int_0^{\infty} f_{kn}(r|m) \cdot P^*_{kn}(D > d|m, r) \cdot dr \right] \cdot dm \tag{3}$$

where $\upsilon_k(d)$ is the annual exceedance rate of a given displacement $d$, $\alpha_n(m^0)$ is the occurrence rate of earthquakes greater than magnitude $m^0$ on a seismogenic source $n$; $f_n(m)$ is the probability density function for the k-th source of earthquakes having magnitude between $m^0$ and $m^u$, $f_{kn}(r|m)$ is the conditional probability function of having at the source $n$ an earthquake of magnitude $m$ at distance $r$ from the site $k$; and $P_{kn}(D>d|m,r)$ can be considered an attenuation function of the displacement, defined by two terms:

$$P_{kn}^{*}\left(D > d|m, r\right) = P_{kn}\left(Slip|m, r\right) \cdot P_{kn}\left(D > d|m, r, Slip\right) \tag{4}$$

where $P_{kn}(Slip|m,r)$ is the conditional probability that some amount of displacement occurs at site $k$ as a result of an earthquake of magnitude $m$ at the n-th source, at distance $r$ from the site $k$; $P_{kn}(D>d|m, r, Slip)$ is the conditional distribution of the displacement. Note that differently from the assumptions used by ground motion attenuation relationships, there is a finite probability that no slip occurs.

Equation (3) can be simplified in Eq. (5) and Eq. (6) in the case of on-fault (principal, i.e., distance r = 0) rupture and off-fault (distributed, i.e., distance r ≠ 0) rupture, respectively:

$$\nu_k\left(d\right) = \alpha \cdot P(surf.rupture)_{princ.} \cdot P(D > d)_{princ.} \tag{5}$$

$$\nu_k\left(d\right) = \alpha \cdot P(surf.rupture)_{princ.} \cdot P(surf.rupture)_{dist.} \cdot P(D > d)_{dist.} \tag{6}$$

These contributions must be summed to obtain the total annual rate of exceedance at the study site $k$.

### *1.2.1.2. Principal faulting*

**Probability of occurrence P (surf. rupture):**

The first term of Eq. (4) represents the conditional probability that an earthquake produces surface faulting, or in other words, that the rupture reaches the surface. This term is not present in the standard PSHA methodology, and depends on the magnitude and the kinematic context as observed in different databases (Wells & Coppersmith, 1993; De Polo, 1994; Pezzopane & Dawson, 1996). Indeed, small earthquakes never produce surface ruptures, and surface ruptures are less common in reverse faulting context compared with normal or strike-slip faulting (Figure 1-9 – section 1.2.2.). The rate at which an earthquake produces surface rupture is expressed using a logistic regression from Wells & Coppersmith (1993). The outcome is binary, either positive or negative, and the probability of having a surface rupture

on the principal fault is given by:

$$P = \frac{e^{a+b*m}}{1+e^{a+b*m}} \tag{7}$$

where $a$ and $b$ are coefficients estimated from data and $m$ is the moment magnitude of the earthquake. Coefficients $a$ and $b$ were initially calculated from 3 normal faults datasets from Pezzopane & Dawson (1996) and from another one containing all styles of faulting (Wells & Coppersmith, 1993). Figure 1-3 represents the probability of occurrence of principal surface rupture against magnitude, for the various databases used initially. It is clear that the probability is significantly rising for earthquakes above Mw 5 - Mw 5.5 and reaches almost 100% for Mw > 7.5 – 8.

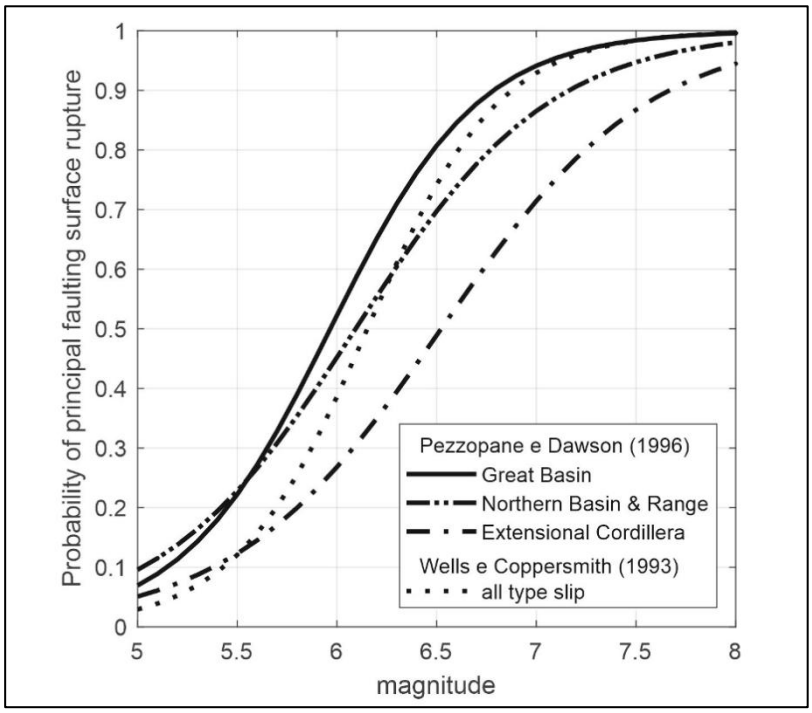



*Figure 1-3: Conditional probability of occurrence of principal surface rupture obtained from the logistic regression and the various databases indicated (taken from Youngs et al., 2003; Figure 4).*

**Probability of exceedance P (D>d):**

The second term of Eq. (4) provides the conditional probability that the surface displacement $D$ exceeds a given displacement value $d$, given an earthquake with magnitude $m$ at distance $r$ from the site of interest produces a surface rupture (probability of occurrence term). This probability is calculated from a surface displacement database from McCalpin & Slemmons (1998), containing 11 normal faulting events, and is related to the location along the fault. These

data, when plotted as the ratio D/MD (displacement over maximum displacement, $0 < D/MD \leq 1$) versus x/L (the position of the site along the principal fault, with x the shortest distance between the site and the end of the rupture, and L the rupture length), tend to follow a beta distribution of the form:

$$F(y) = \frac{\Gamma(a+b)}{\Gamma(a)\Gamma(b)} \int_0^y z^{a-1}(1-z)^{b-1} dz \tag{8}$$

with *F(y)* the cumulative probability that a variable *Y* is lower or equal to a given value *y*, *Γ* is the gamma function and *a* and *b* are coefficients calculated from the data. The ratio D/MD is taken as the variable *y* (comprised between 0 and 1) and is then defined as a function of x/L. This along-fault ratio is supposed to be symmetrical and varies between 0 and 0.5, assuming a maximum displacement for x/L = 0.5, at the centre of the rupture.

Youngs et al. (2003) also propose an alternative method to estimate this probability of exceedance, which is by normalising the displacement *D* with the average displacement AD instead of MD. Similarly, the ratio D/AD follows this time a gamma distribution of the form:

$$F(y) = \frac{1}{\Gamma(a)} \int_0^{y/b} e^{-t} t^{a-1} dt \tag{9}$$

where *F(y)* the cumulative probability that a variable *Y* is lower or equal to a given value *y* (there D/AD), *Γ* is the gamma function and *a* and *b* are coefficients calculated from the data. The two variables AD and MD depend on the magnitude, following a log-normal distribution, and can be obtained using empirical relationships such as the ones from Wells & Coppersmith (1994). The two normalised displacement distributions along the fault are shown in Figure 1-4.

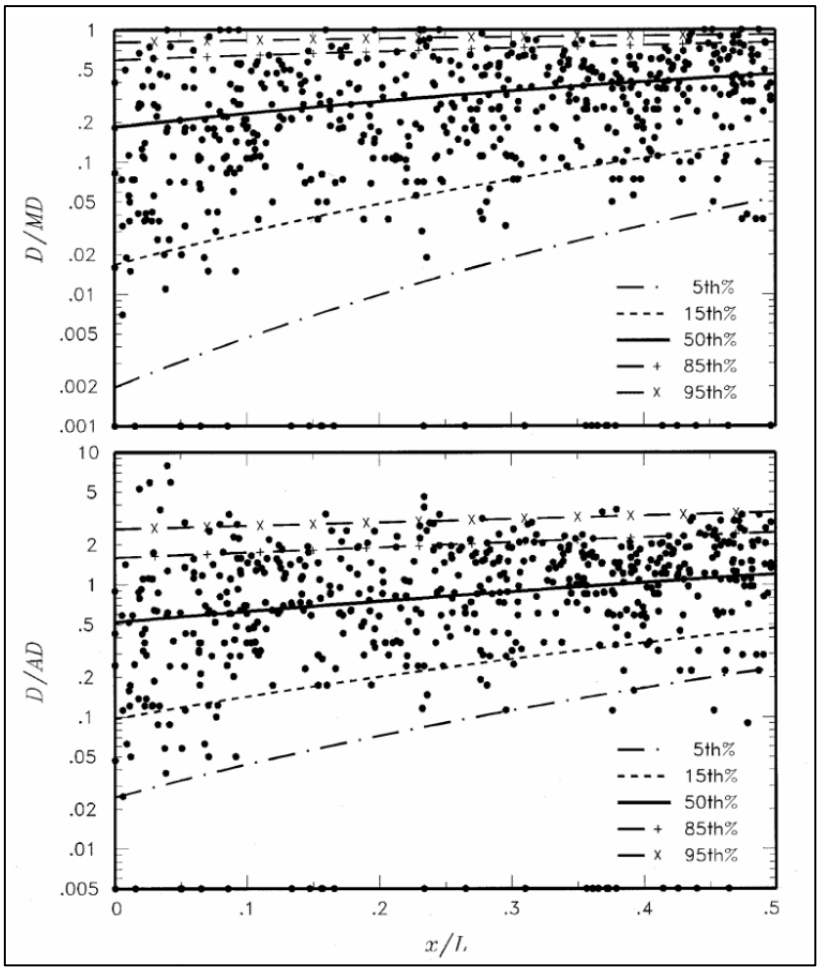



*Figure 1-4: Normalised displacement distributions along the principal fault using data from McCalpin and Slemmons (1998). Top: D/MD using a beta distribution. Bottom: D/AD distribution using a gamma distribution (taken from Youngs et al., 2003; Figure 7)*

Finally, the conditional probability of exceedance is obtained by convolving the log-normal distributions of the normalised displacement with the beta or the gamma distribution (for D/MD and D/AD, respectively). Some examples of conditional probability of exceedance curves are provided in Figure 1-5, representing different earthquake and along-fault location scenarios.

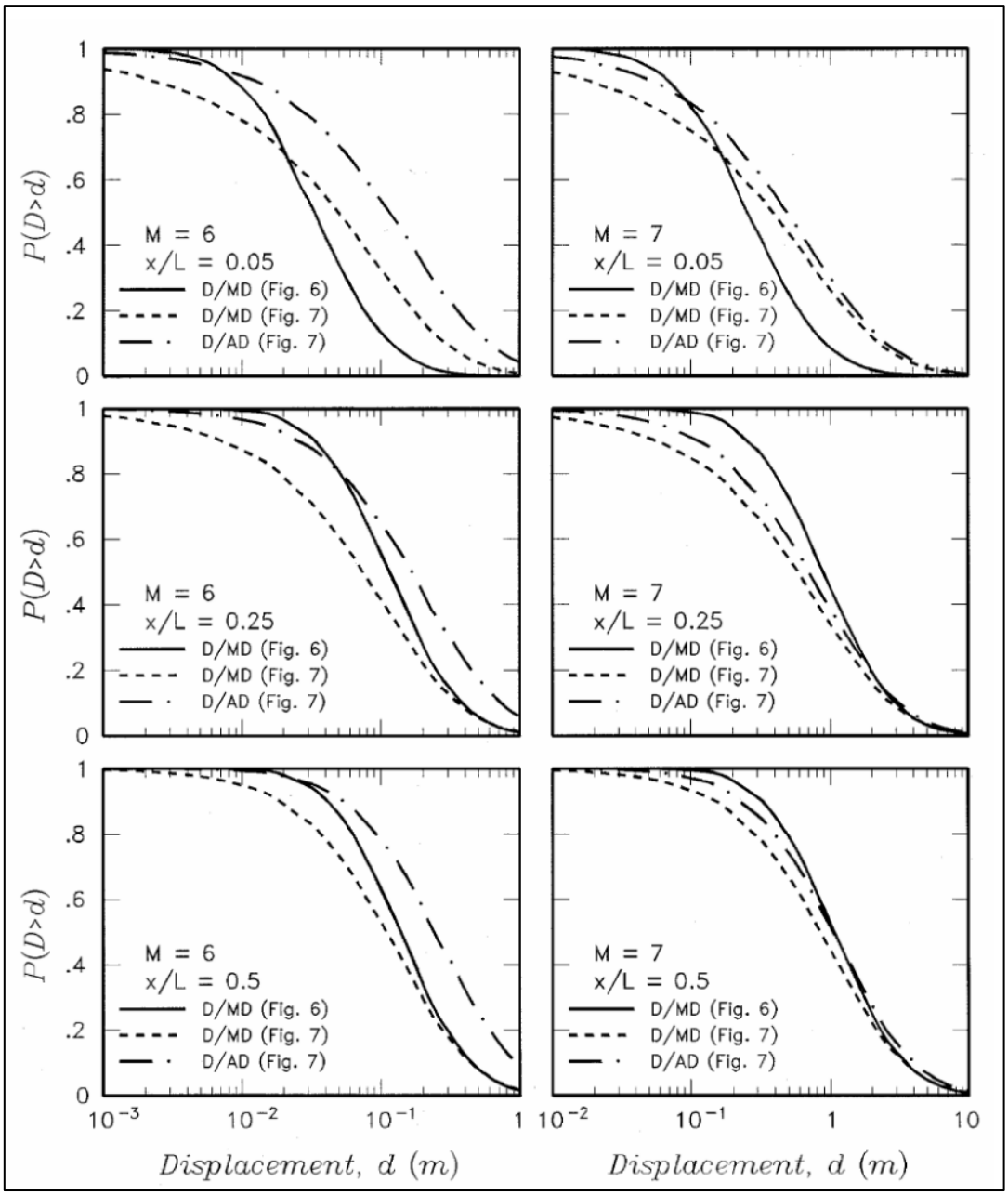



*Figure 1-5: Conditional probability of exceedance for principal faulting, for various earthquake magnitude and x/L values (taken from Youngs et al., 2003; Figure 8).*

### *1.2.1.3. Distributed faulting*

The determination of distributed faulting follows the same logic as that applied to principal faulting, with the additional starting condition that surface rupture is produced on a nearby principal fault.

**Probability of occurrence P (surf. rupture):**

The first term in Eq. (4) represents the probability that an earthquake produces surface rupture at a site *k*, located away from the principal fault. This probability is defined by Youngs et al. (2003) based on a database of distributed surface ruptures in the Basin and Range area (USA), originally compiled by Pezzopane & Dawson (1996). The data are organised using a grid with 500 m × 500 m pixels. For a single earthquake, the occurrence rate is calculated as the ratio between the number of pixels containing distributed faulting and the total number of pixels within the study area. These data show that the conditional probability $P_D$ of distributed faulting is correlated with the magnitude and anti-correlated with the distance to the principal fault, and can be calculated using :

$$P_D = \frac{e^{f(x)}}{1+e^{f(x)}} \tag{10}$$

with :

$$f(x) = C_1 + (C_2 + C_3 \cdot m + C_4 \cdot h) \cdot \ln(r + C_5) \tag{11}$$

where *m* is the magnitude, *r* is the distance to the principal fault (km), *h* is a parameter equals to 0 or 1 depending on the site location relative to the principal fault (1 for the hanging wall and 0 for the footwall). Coefficients $C_1$ to $C_5$ are estimated from the initial data used by Youngs et al. (2003).

Youngs et al. (2003) also introduce another way to express this probability, accounting for the high variability in the initial Pezzopane & Dawson (1996) dataset. Using a random variable approach (Brillinger and Preisler, 1983), it can be calculated as:

$$f(x) = C_1 + (C_2 + C_3 \cdot m + C_4 \cdot h) \cdot \ln(r + C_5) + \tau\, z_i \tag{12}$$

where $\boldsymbol{\tau}$ is the measure of variability from event to event and $z_i$ is a normal variate with mean 0 and unit variance representing the random effect for the i-th event.

The data and the curves of the conditional probability of occurrence using both equations are shown in Figure 1-6, in function of the magnitude and the distance from the principal rupture. The hanging wall exhibits more surface ruptures compared with the foot wall, the probability there is thus higher. Similarly, Eq. (12) shows a higher probability of occurrence than Eq. (11).

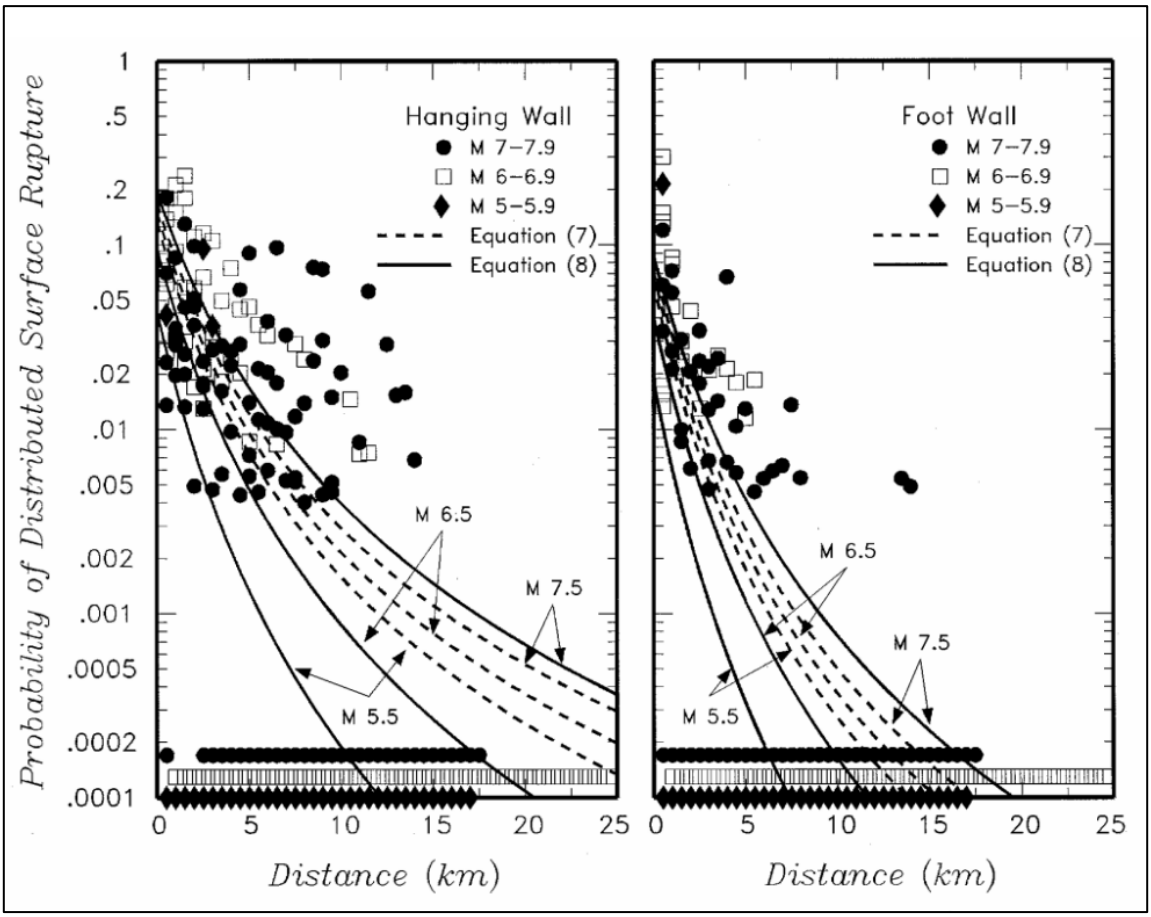



*Figure 1-6: Conditional probability of occurrence of distributed rupture (taken from Youngs et al., 2003, Figure 9).*

**Probability of exceedance P (D>d):**

The method to compute the probability of exceedance for distributed faulting, representing the conditional probability of exceeding a given displacement value, is similar to the one used for principal faulting. The main difference lies in the availability of data to set the model. Youngs et al. (2003) rely on the database of 5 events from De Polo (1994) and model the distribution of the ratio of distributed rupture ($D_{distributed}$) over MD on the main fault. This distribution is expressed as a function of the position with respect to the main fault (hanging wall / foot wall) and the orthogonal distance from it, and is determined by a gamma distribution with a shape parameter $\alpha = 2.5$. Youngs et al. (2003) use a high percentile of this distribution (typically the 85th or 95th) to anchor the model to the upper-bound displacement ratios.

Finally, the probability of exceeding a given displacement value at a given site is obtained by convolving this gamma distribution with the lognormal distribution of MD, as for the principal faulting described before. Figure 1-7 represents the distributions of $D_{distributed}/MD_{principal}$ for both a hanging wall and a foot wall position.

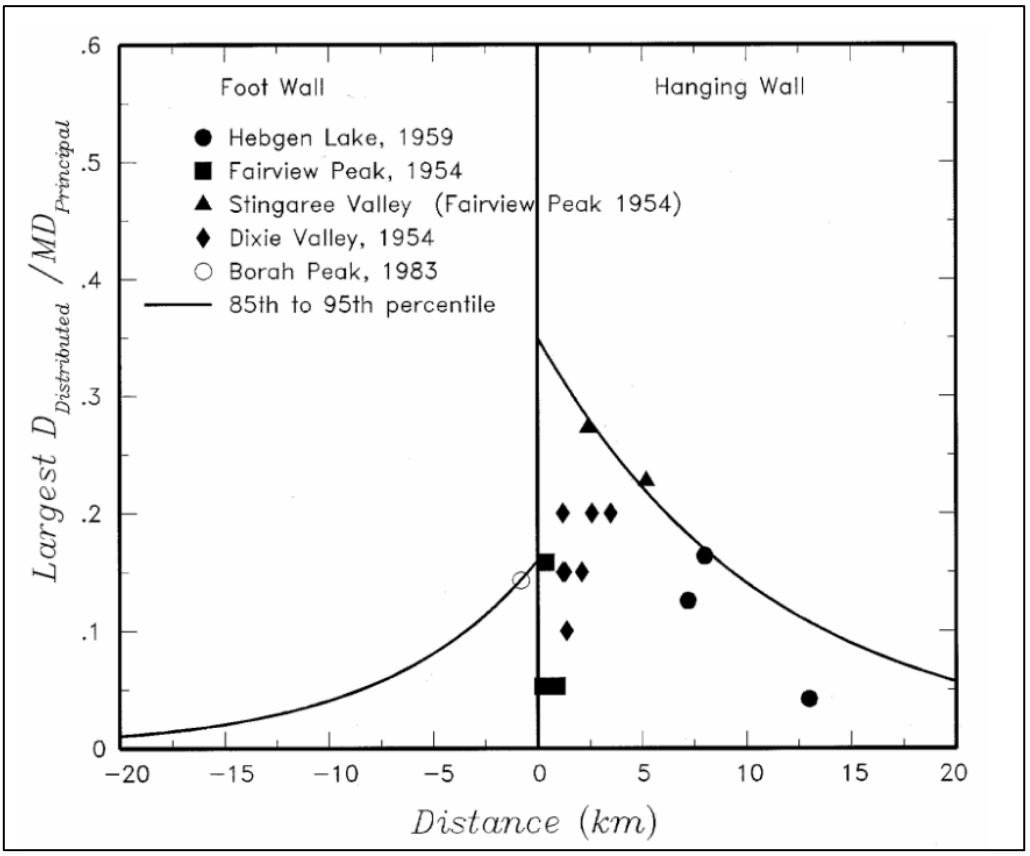



*Figure 1-7: Distributions of the $D_{distributed}$/MD ratio with distance from the main fault, for the foot wall (left) and the hanging wall (righ)t. Data from De Polo (1994) used to calculate them are also plotted. (taken from Youngs et al., 2003, Figure 11).*

### 1.2.2. New PFDHA models

After Youngs et al. (2003) model, several working groups have adapted their *earthquake approach* for other kinematic contexts, such as Moss & Ross (2011) for reverse faulting and Petersen et al. (2011) for strike-slip faulting. Similarly, Takao et al. (2013; 2014; 2016) developed specific models for reverse and strike-slip faults in Japan. A general overview of all the PFDHA published models is shown in Figure 1-8, from Valentini et al. (2025).

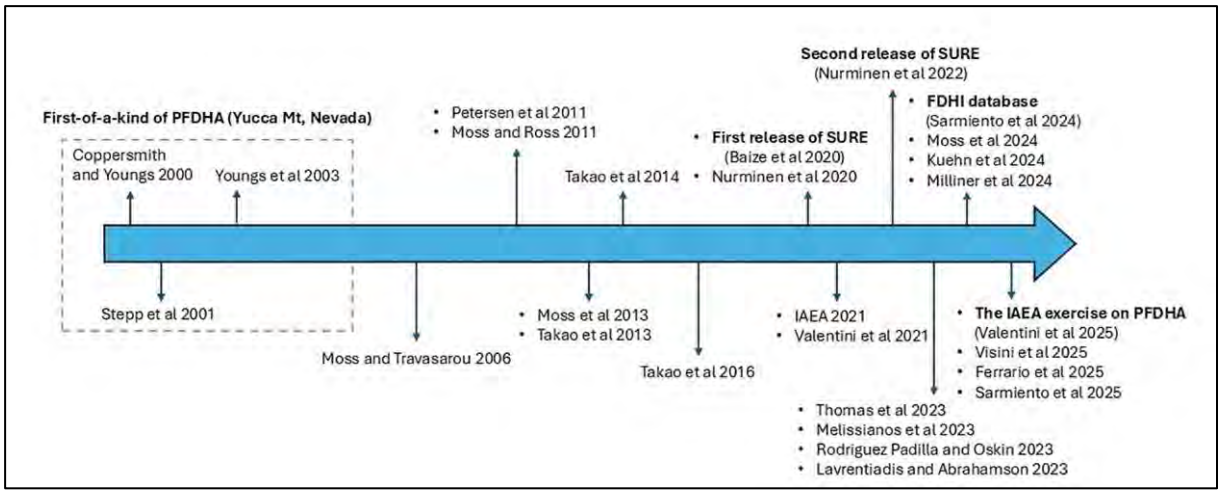



*Figure 1-8: Overview of the key PFDHA models published in the literature up to 2025 (taken from Valentini et al. (2025), Figure 1).*

Beyond the development of models for specific faulting styles, new works have been published especially during the last decade and have focused on updating the empirical parameters of the initial models using expanded and more robust datasets. Ferrario & Livio (2021) updated the conditional probability of occurrence of distributed faulting originally estimated by Youngs et al. (2003), using a substantially larger database. Similarly, more recently, Pizza et al. (2023) updated the *probability of occurrence* term for principal faulting, again using a larger dataset than that available to Youngs et al. (2003).

In parallel, international initiatives to improve the datasets from which the models are built were organised. Two international efforts are notable: the Fault Displacement Hazard Initiative (FDHI, coordinated by the University of California, Los Angeles, from 2018, Sarmiento et al., 2021) and the SUrface Ruptures due to Earthquake (SURE) data collection efforts (SURE 1.0: Baize et al., 2019; Nurminen et al., 2020; SURE 2.0: Nurminen et al., 2022). These two recent international initiatives were mostly focused on the surface rupture data collection and homogenisation; and they are described in more details in the following section 1.2.2.1.

A general overview of the existing PFDHA models and their main characteristics is presented in Table 1-1.

| | | | | | Surface Rupture Models | | Fault Displacement Models | | |
|---|---|---|---|---|---|---|---|---|---|
| **Model** | **Faulting style** | **Mw range** | **Component** | **Displacement type** | **PF** | **DR** | **PF** | **DR** | **Notes** |
| Wells & Coppersmith (1993) | All | | | | ✓ | | | | |
| Youngs et al. (2003) | N | | vertical | Single principal and single distributed | ✓ | ✓ | ✓ | ✓ | |
| Petersen et al. (2011) | SS | 6.0-8.0 | horizontal | Single principal and single distributed | | ✓ | ✓ | ✓ | |
| Moss & Ross (2011) | R | 5.5-8.0 | vertical | Single principal and single distributed | ✓ | | ✓ | | |
| Moss & Ross (2013) | R/SS | 4.2-8.7 | | | ✓ | | | | For stiff and soft soils |
| Takao et al. (2013; 2014; 2016) | R/SS | | | | ✓ | ✓ | ✓ | ✓ | Only applicable in Japan |
| Ferrario & Livio (2021) | N | 6.0-7.5 | | Single distributed | | ✓ | | | Update of the distributed surface faulting regression model from Youngs |
| Yang et al. (2021) | R | 4.7-6.6 | | | ✓ | | | | Focused on Australia intraplate reverse faults |
| Rodriguez Padilla et al. (2023) | SS | | | | | ✓ | | | DR model from 5 eq. in southern California and Mexico (from FDHI database) |
| Pizza et al. (2023) | All | 5.5-7.9 | | Single principal | ✓ | | | | |
| Kuehn et al. (2024) | N | 6.0-8.0 | net | Aggregate displacement (principal + distributed) | | | ✓ | | Using FDHI database |
| | SS | 6.0-8.0 | | | | | | | |
| | R | 5.0-8.0 | | | | | | | |
| Lavrentiadis et al. (2023) | N | 5.0-8.5 | net | Sum of principal & Aggregate displacement | | | ✓ | | Using FDHI database |
| | SS | 5.0-8.5 | | | | | | | |
| | R | 5.0-8.5 | | | | | | | |
| Moss et al. (2024) | R | 4.7-8.0 | vertical | Single principal | | | | | Update of Moss et al., 2011, using FDHI database |
| Chiou et al. (2025) | SS | 6.0-8.3 | net | Sum of principal | | | ✓ | | Using FDHI database |
| Gómez-Novell et al. (2025) | All | | | | ✓ | | | | Compute the coseismic surface rupture probability using earthquake cycle simulator, based on fault geometry |
| Mammarella et al. (2025) | All | 5.0-8.0 | | | | | | | Numerical model: compute the conditional probability of surface rupture by convolving probability distributions for hypocentral depth, rupture width, and hypocentral depth ratio |
| Visini et al. (2025) | N | 5.6-7.5 | vertical | Single principal & new ranks for distributed | | ✓ | | ✓ | Focused on DR models: 3 different distributed rupture classes: pre-existing fault triggered (3), simple DR (2) and rupture on splays connected to the PF (1.5). Using the SURE 2.0 database |
| | R | 4.9-7.9 | | | | | | | |

*Table 1-1: General overview of the existing PFDHA models and their main characteristics.*

All these models, developed more or less recently, present various characteristics, displacement components, displacement metrics and present a large offer for PFDHA application in a wide variety of contexts. Naturally, for a given context, these models can provide significantly different estimates, as illustrated for example by the variability in probability of occurrence of principal surface rupture shown in Figure 1-9.

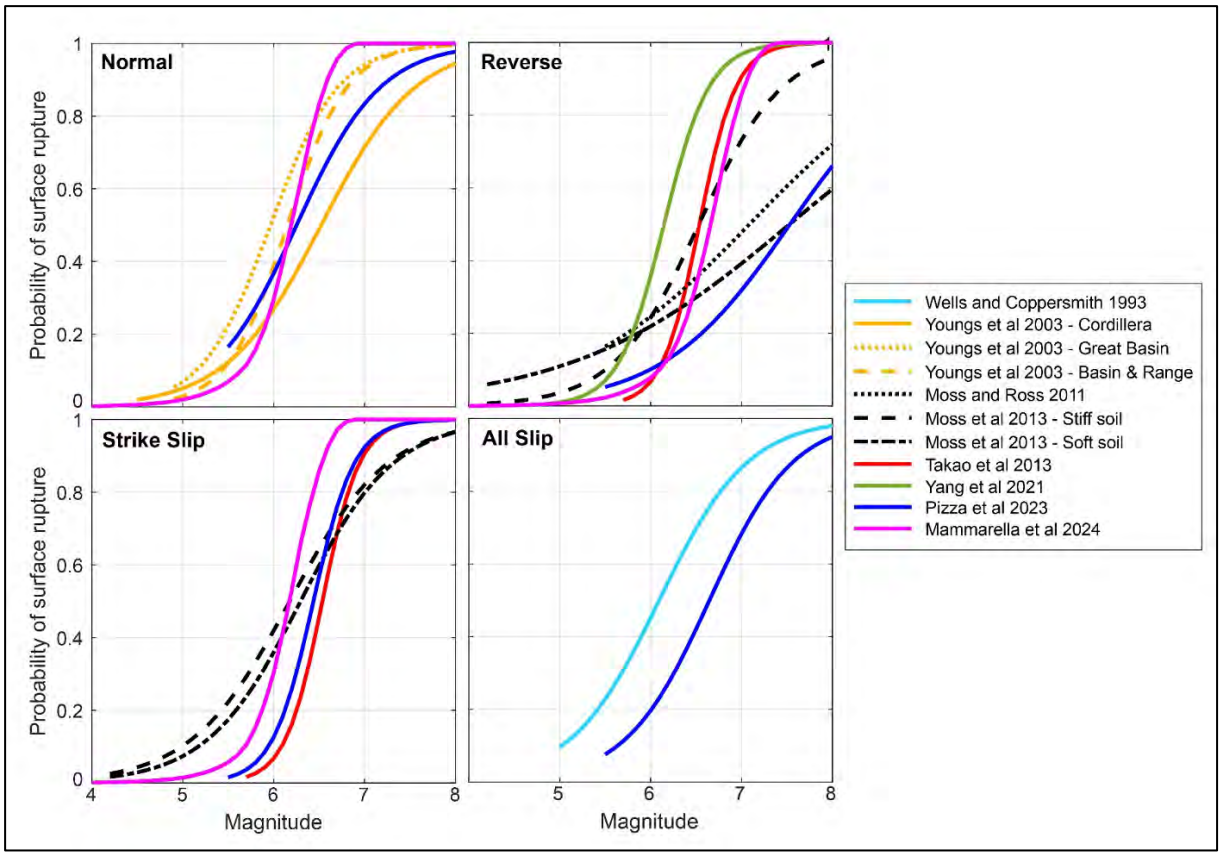



*Figure 1-9: Probability of principal surface rupture for various faulting styles and multiple datasets (taken from Valentini et al., 2025; Figure 10).*

This *probability of occurrence* for principal faulting is particularly critical in PFDHA, as it directly controls the plateau of the hazard curve, as demonstrated by Moss et al. (2011). Therefore, for any PFDHA application, careful model selection is essential, ensuring it is appropriate for the study tectonic context (normal, strike-slip or reverse faulting) and consistent with the desired output (correct displacement component for example).

### *1.2.2.1. Fault surface rupture databases*

As mentioned previously, fault surface rupture databases are crucial for developing empirical models predicting fault displacement. Apart from the regional data used in the initial Youngs et al. (2003) model, such as Wells & Coppersmith (1993); De Polo (1994) or Pezzopane & Dawson (1996), more recent efforts have compiled larger and worldwide data, such as the SURE 1.0 and 2.0 databases (Baize et al., 2019; Nurminen et al., 2020; Nurminen et al., 2022), or the FDHI database (Sarmiento et al., 2021). These new databases were motivated by the lack of homogeneity in data collection (displacement components and metrics, uncertainty consideration, measurement conventions) both within and across previous works.

The SURE databases were compiled by an international team of researchers. The latest version, SURE 2.0, contains more than 19 000 rupture measurements from 50 surface rupturing earthquakes around the world, including normal, reverse and strike-slip faulting events. A key novelty of this database is the introduction of a new fault ranking scheme: principal faulting (rank 1) and distributed faulting (rank 2) but with distributed ruptures classified in different categories related to their geologic and structural setting. More details on these rankings are provided in the next section (1.2.2.2.). This database and its ranking definitions formed the basis for the new model developed by Visini et al. (2025) (Table 1-1).

The FDHI database includes surface ruptures data from 75 earthquakes worldwide from 1872 to 2018 and with Mw ranging from 4.9 to 8.0 (approximately 45% strike-slip, 35% reverse, and 20% normal faulting events) (Figure 1-10). In total, more than 40 000 accurately measured and located rupture data were collected in various geologic contexts. Several PFDHA empirical models have been developed based on this database, such as the Lavrentiadis et al. (2023), Rodriguez Padilla et al. (2023) or the Kuehn et al. (2024) (Table 1-1).

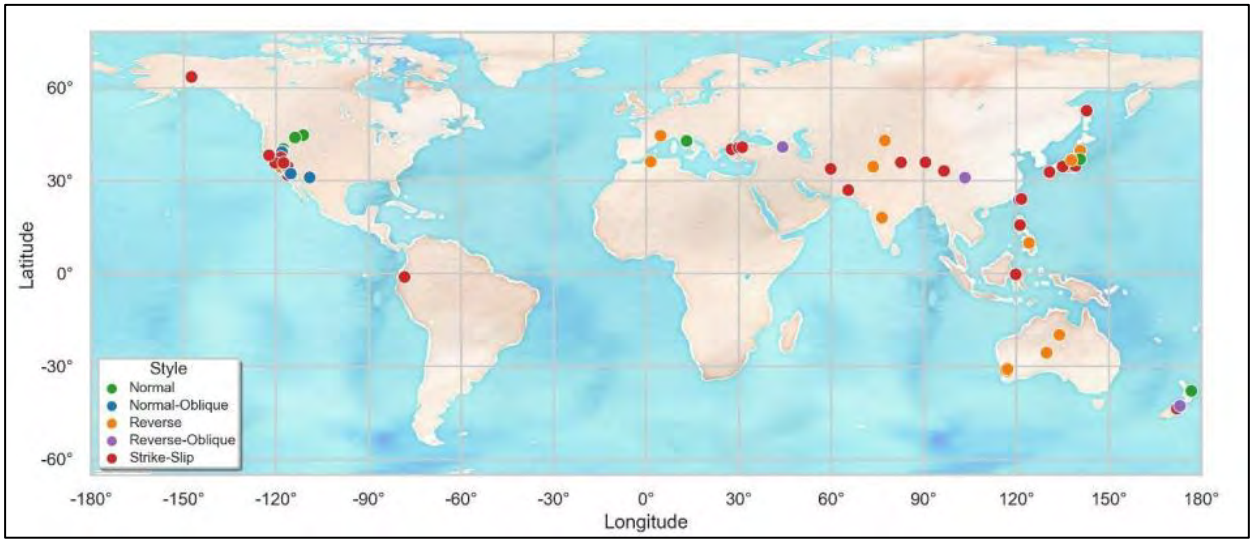



*Figure 1-10: Location and style of faulting of the FDHI database earthquakes (from Sarmiento et al., 2021; Figure 1.1).*

Figure 1-11 represents the earthquake data from these two databases. A strong relationship is revealed between the observed surface ruptures, the earthquake magnitude and the hypocentral depth. Indeed, surface ruptures are mainly associated with moderate to strong earthquakes (Mw > 5.5), with the number of documented cases increasing for higher magnitudes. However, this increase is not linear (lower panels of Figure 1-11) because strong earthquakes, Mw ~8.0, are rarer than those with Mw 6.0-7.0.

Another notable observation is that surface ruptures have also been observed for lower magnitude (Mw 4.9-5.5), but only in cases of very shallow earthquakes, such as 2019 Mw 4.9 Le Teil earthquake in France. Finally, the three main faulting styles are represented for the full magnitude range. However, strike-slip faulting events seem to be overrepresented compared to normal and reverse faulting ones. This may reflect an observational bias, as horizontal displacements are usually easier to observe and identify at the surface rather than vertical ones (normal and reverse faulting).

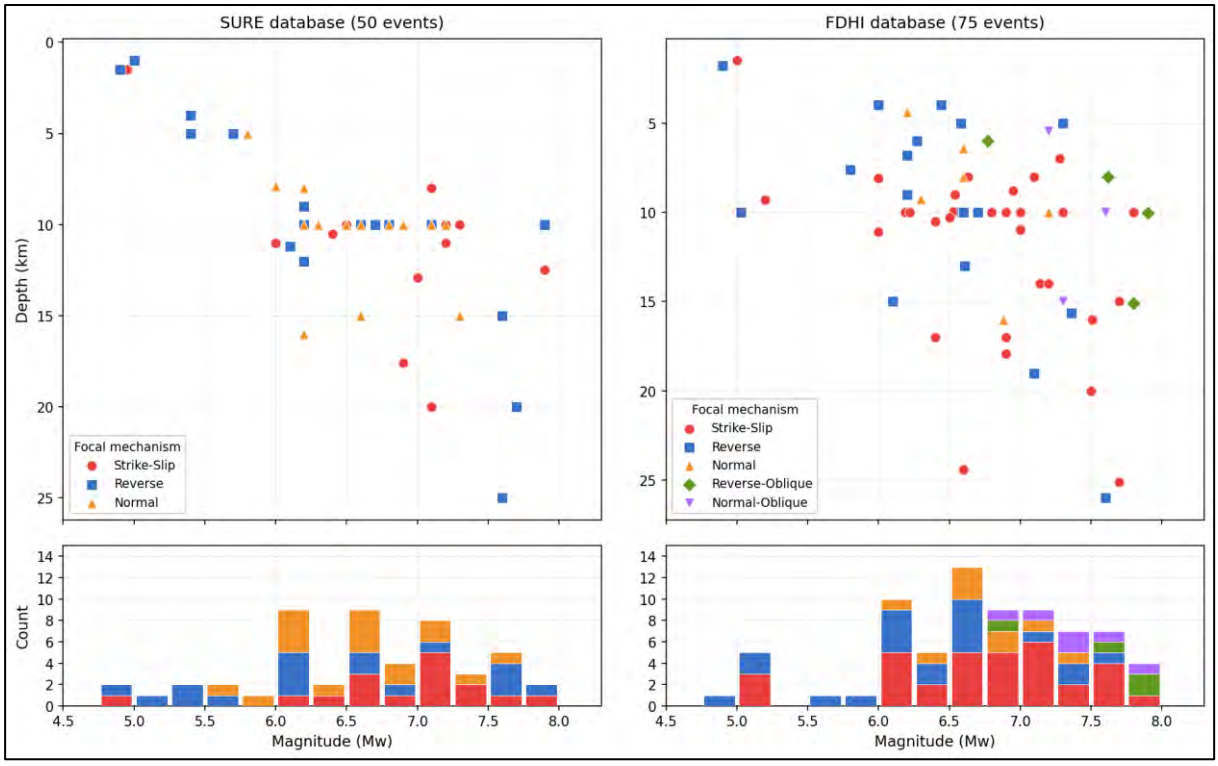



*Figure 1-11: Earthquake magnitude and epicentral depth distributions using data from the SURE 2.0 and FDHI databases. Events with no reported epicentral depth are excluded.*

### *1.2.2.2. Fault displacement metrics*

About the terminology, Youngs et al. (2003) used 'on-fault' and 'off-fault' displacements, respectively referring to principal (also called 'primary') faulting and distributed (also called 'secondary') faulting. The parameter influencing the displacement is the location relative to the main fault, where the earthquake nucleates. This location can be along the fault trace ('on-fault'), in which case the l/L (or often named X/L) ratio is considered (Figure 1-12a); or around the main fault trace ('off-fault'), where the distance between this secondary surface displacement and the main fault is crucial. This definition is rather simplified and often does not reflect reality since the surface rupture is rarely a straight and continuous line.

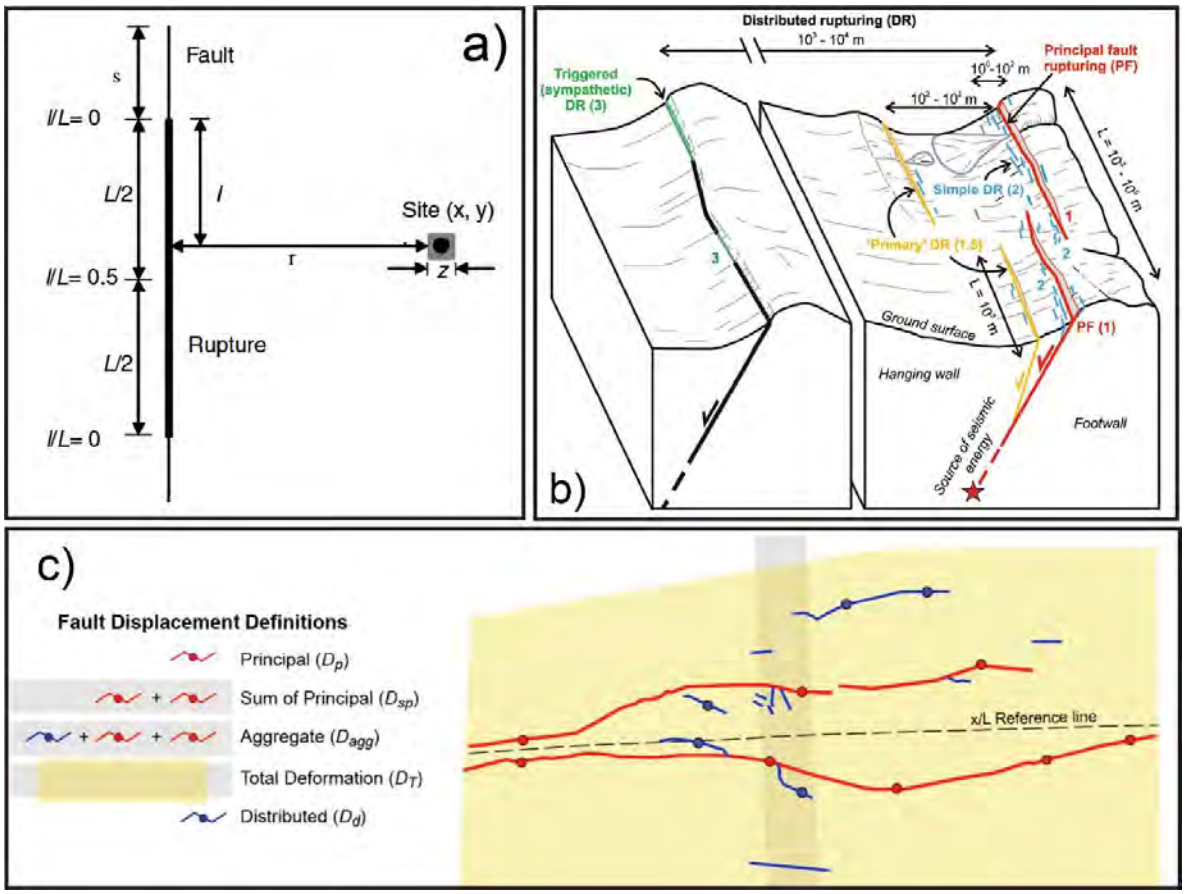



*Figure 1-12: Fault displacement metrics and definitions proposed in literature. a) Distance variables definition (taken from Petersen et al., 2011; Figure 1); b) New terminology with variable fault ranking in a normal faulting case (taken from Nurminen et al., 2022; Figure 1a); c) Definitions used for more complex fault geometries at the surface (taken from Thompson, 2024): "Sum of principal" accounts for sub-parallel principal faulting: "Aggregate" displacement is the sum of the principal and the distributed faulting, as used by Youngs, within an orthogonal area relative to the main fault.*

Nurminen et al. (2022) proposed a more specific displacement classification (Figure 1-12b) incorporating new distributed rupture sub-categories. Rank 1, shown in red in Figure 1-12b, refer to the classical principal rupture, representing the surface expression of the earthquake fault source. Rank 2, shown in blue in Figure 1-12b, represents the simple distributed rupture in surface around the main rupture (rank 1). In addition, new distributed rupture ranks are introduced, accounting, for example, for distributed surface displacement occurring on a pre-existing fault connected to the principal fault, or for displacement on a remotely triggered fault (ranks 1.5 and 3 in yellow and in green, respectively, in Figure 1-12b). Additional rupture ranks related to compressional tectonic processes in reverse faulting contexts are also included, such as bending-moment faulting (rank 21) and flexural-slip faulting (rank 22). Visini et al. (2025) use these new ruptures classification in their distributed faulting model, introducing different combinations that account for various distributed ruptures (DR) calculations relative to principal faulting (PF, rank 1). Combination A considers the DR (rank 2) relative to rank 1,

representing the classic case used in Youngs et al. (2003) and other 'first generation' models (e.g. Petersen et al., 2011). Combination B considers the rank 2 DR relative to rank 1.5 traces as PF. Finally, Combination C considers all types of DR, including rank 1.5, relative to rank 1 PF traces.

Additionally, new displacement metrics accounting for the complexity of the surface rupture geometry, such as the *sum of principal* or the *aggregate displacement* (Figure 1-12c), have been introduced in some FDHI empirical models: Lavrentiadis et al. (2023), Kuehn et al. (2024), Chiou et al. (2025) in Table 1-1. These metrics are derived from measurements of permanent tectonic surface ruptures, typically obtained through field surveys, where displacements are measured across individual brittle rupture traces. Consequently, they do not refer to other components of the coseismic deformation field that may be captured by InSAR or other remote sensing techniques. As illustrated in Figure 1-12, the *sum of principal* is applied when the principal fault at surface is composed of multiple sub-parallel fault segments rather than a single continuous trace, with the total displacement summed across each individual segment within a perpendicular area (greyish in Figure 1-12) along an imaginary X/L reference line. The *aggregate displacement* follows the same principle, representing the summation of all measured displacements from both principal (or sum of principal) and distributed surface ruptures within an area perpendicular to the strike of the main fault.

Slip component is also an essential parameter to address and define, as confusion and discrepancies often arise across models. Three types of slip components are distinguished in the databases: horizontal, vertical and net (Figure 1-13). The net-slip represents the true displacement vector of the hanging wall on the fault plane and is rarely measured on the field for technical reasons. The horizontal component usually refers to the horizontal displacement during strike-slip events (in blue in Figure 1-13), but there is also the fault normal component or 'heave' (in green), relevant for normal and reverse faulting, that is along the horizontal plane. The vertical component, or 'throw', only relevant for normal and reverse faulting, has historically been the most commonly measured and reported component in empirical models and databases (Table 1-1), while the horizontal fault normal component was generally omitted. However, more recent works (e.g. Lavrentiadis et al., 2023 in Table 1-1) increasingly report the net slip, which accounts for the dip angle of the fault plane and provides a more complete representation of the actual fault motion. To clarify and avoid ambiguity, the horizontal

displacement mentioned throughout this work refers exclusively to strike-slip faulting.

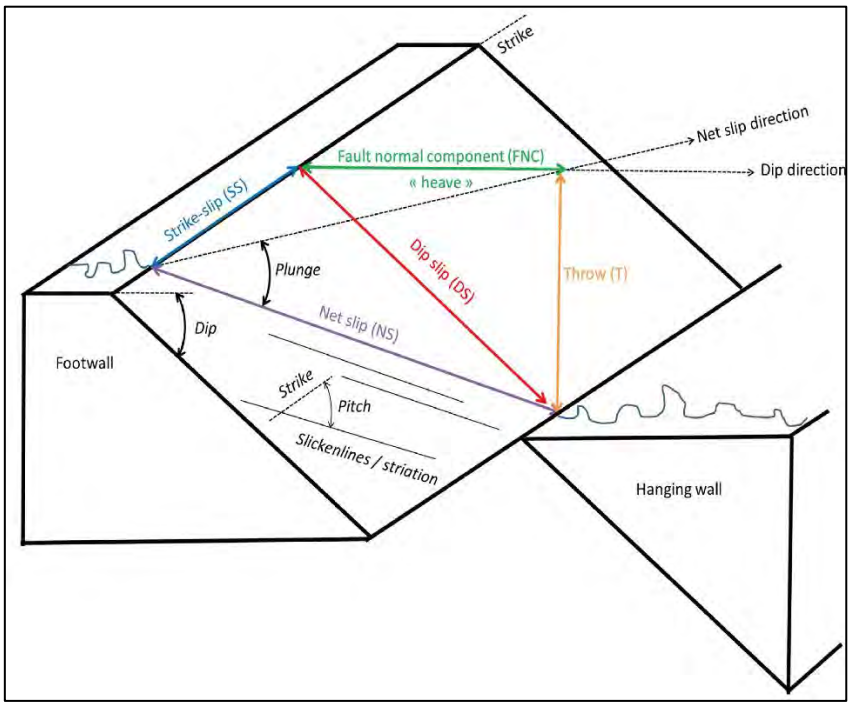



*Figure 1-13: Slip components in FDHA (taken from Nurminen et al., 2022; Figure 2).*

## 1.3. Regulations and published PFDHA application cases

### 1.3.1. Regulatory framework

FDH analyses are essential for specific infrastructures such as nuclear power plants, dams or any other highly sensitive building. However, regulations addressing this hazard vary considerably across countries and infrastructure types, and only a few countries explicitly include fault displacement hazard in their national legislation. The United States of America (Bryant & Hart, 2007; FEMA, 2023) and New Zealand (Kerr et al., 2003; Stahl et al., 2024) are notable examples, with partial consideration also present in Japan (Toda, 2015), China, Chile, and Turkey. In most cases, these guidelines support an avoidance strategy, i.e. avoiding construction near active faults, recognising that no engineering solution can fully mitigate the consequences of direct fault rupture beneath a critical facility.

In Italy, one of the most seismically active countries in the Euro-Mediterranean region, the fault displacement hazard for ordinary buildings is considered only within Level 3 seismic microzonation studies with fault zoning strategies (SM Working Group, 2015; Technical Commission on Seismic Microzonation, 2015). More recently, the Italian national guidelines have made the evaluation of fault displacement hazard mandatory for existing dam sites (DMIT,

2014; Basili et al., 2017).

For nuclear energy-related sites, IAEA guidelines are followed worldwide and represent the most comprehensive regulatory framework available for fault displacement hazard. In the case of a new nuclear installation, regulations and decision-making mainly depend on the presence or absence of a capable fault (IAEA 2019; 2021; 2022). Generally, if a capable fault is found at or near the site, the site is considered unacceptable for hosting the new infrastructure. For existing sites, the situation is generally more complex. The first step is to investigate whether there are faults at or near the site, then to determine whether they are capable and if they represent a potential risk that cannot be mitigated. If the capability of the fault cannot be excluded, FDH analyses must be carried out to determine the probability and potential consequences of surface faulting at the site. These analyses, usually following the *earthquake approach*, must be regularly updated with changes in available geological or seismic data, or if the site is modified (e.g. site extension).

### 1.3.2. Published PFDHA application cases

In the literature, several case studies assessing the FDH at specific sites or for a specific fault have been published. The first was for the Yucca Mountain nuclear waste repository in Nevada, USA, by Stepp et al. (2001) and Youngs et al. (2003). Since then, and led by the nuclear industry (Valentini et al., 2025; IAEA, 2025), FDH analyses have been carried out for multiple other strategic exposed sites, including the Diablo Canyon Power Plant in the USA (Pacific Gas & Electric Company, 2012), the Wushantou dam in Taiwan (Gao and Lee, 2019), the Choman dam in Iran (Moghaddas and Leo, 2019), the Ikata nuclear power plant in Japan (Nishizaka et al., 2021), and the Montedoglio dam in Italy (Testa et al. 2024).

At the fault scale, several studies have focused on characterising displacement hazards associated with individual active faults. Examples include the Anghiari–Città di Castello fault (Testa et al., 2021), the Milun fault (Gao et al., 2022), the Tabriz fault (Hosseini and Rahimi, 2022), and the Willunga fault (Tang and Quigley, 2024). These investigations were mainly motivated either by recent damaging earthquakes on the studied faults (e.g., the Milun fault) and/or by the proximity of strategic infrastructures that could be affected by surface ruptures (e.g. Tang and Quigley, 2024).

Despite methodological advances, most of these studies remain strictly site-specific. Regional-scale fault displacement hazard maps are still lacking due to epistemic uncertainties in active and capable fault characterisation, the considerable variability among published displacement

prediction models, and the absence of free and certified computational frameworks. Such maps would definitely be a valuable tool, offering a broader picture of fault displacement hazard across a region as it is already available for other natural hazards like ground shaking (European Seismic Hazard Model 2020, Danciu et al., 2024). Indeed, they could help guide land-use planning, identify areas requiring more attention and detailed investigation, and ultimately support decisions on where critical infrastructure should or should not be built.

## 1.4. Summary and research gap: main questions

In this introduction, three key parameters controlling fault surface rupture occurrence and characteristics have been identified:

- Earthquake magnitude: the stronger the earthquake, the greater the probability of surface rupture and the larger the displacement at the surface. Surface ruptures are generally generated by earthquakes with a Mw ≥ 5–5.5 (Figure 1-9).

- Hypocentral depth: a lower magnitude earthquake can potentially produce surface rupture if it is sufficiently shallow. The 2019 Le Teil earthquake in France, with a hypocentral depth of only 1.5 km and a moderate magnitude of Mw 4.9, highlights this strong influence of the hypocentral depth on rupture likelihood. Shallow hypocentres, typically within the upper ~15 km of the crust, favour the propagation of rupture to the surface, whereas deeper events are more likely to result in blind ruptures, where the rupture does not reach the surface (Yao and Yang, 2022).

- Style of faulting: Different tectonic contexts produce different surface displacements, which may be vertical, horizontal, or a combination of both. Additionally, strike-slip faulting appears most frequently in the databases (e.g. in FDHI), likely because horizontal displacement is easier to observe in nature than vertical displacement.

However, it is important to note that these three are not the only controlling parameters. Additional factors, such as the complexity of fault geometry both laterally and at depth, the internal architecture of the fault zone, and the mechanical heterogeneity of the surrounding rock mass, also influence rupture propagation. In particular, fault segmentation and geometrical complexity play a key role in controlling rupture propagation, as rupture is often limited by structural complexities such as bends, step-overs or other variations in fault trace geometry (Wesnousky, 2008). The propagation of rupture from the hypocentre (seismogenic source) to

the Earth's surface (represented by active and capable fault) is a complex process that depends on these structural and geological characteristics, which control how deformation is transferred and partitioned within the fault zone, both vertically and laterally. Consequently, they influence the distribution of on-fault and off-fault deformation, as well as the occurrence of principal and distributed surface ruptures. For example, when numerous fault splays are connected to the principal fault, distributed faulting may preferentially be localised along these secondary structures rather than within the surrounding free field. Lithological variations and associated contrasts in mechanical properties may further modulate rupture behaviour by affecting stress concentration and energy dissipation (Faulkner et al., 2010).

In the PFDHA formulations, these factors are not explicitly considered, as the analysis is based only on first-order earthquake-source parameters controlling surface rupture occurrence and characteristics. However, these additional controls remain important in governing rupture propagation but fall outside the scope of this study; they are therefore not investigated further.

Despite these complexities, the growing interest in this topic over recent decades and in recent years has led to significant methodological advances in both the number and quality of available empirical models. However, fault displacement forecast, as many other natural phenomena, is based on empirical models derived from past observations of surface ruptures. PFDHA relies on the basic assumption that fault rupture behaviour exhibits some degree of recurrence, allowing empirical relationships derived from past surface ruptures to be applied to future events. Palaeoseismological trench investigations support this assumption by documenting multiple surface-rupturing earthquakes at a given site along a fault. However, the age of these events is often poorly constrained and only a range can be estimated by diverse dating techniques. Despite these limitations, trenches provide valuable insights into the average slip-per-event, that is the typical displacement associated with individual ruptures, and can also provide a broad estimation of surface rupturing earthquake recurrence, based on the dated sequence of the observed past events. Nevertheless, because surface ruptures are a less frequent phenomenon than the standard ground-motion for example, both the quality and quantity of the available data and detailed observations remain limited.

In contrast, for more recent events where surface ruptures have been directly and accurately documented, multiple ruptures occurring at the same location represent an exceptionally rare situation. Unlike palaeoseismological trenches, which record successive events indirectly and with poorly constrained timing, direct observational data of repeated surface ruptures on the

same fault exist for only a few sites worldwide. Notable examples include the 2016–2017 Central Italy sequence (Civico et al., 2018) and the 2016 Kumamoto earthquake sequence (Sugito et al., 2016), where successive earthquakes of the same sequence reactivated parts of the same fault system. However, because these earthquakes belong to the same rupture sequence and are mechanically related, they do not represent independent occurrences of surface faulting. For evaluating the fundamental assumption of PFDHA, repeated ruptures from distinct earthquake sequences are more relevant, as they represent long-term recurrence rather than successive events within a single seismic sequence. One of the few documented examples is the Longitudinal Valley fault system in Taiwan, which is examined in detail in Chapter 2. These rare cases provide a valuable opportunity to explore how similar successive ruptures on the same fault can be, not to formally test or challenge the initial assumption of PFDHA, but simply because the data exist and permit such an examination.

A parallel limitation exists at a different level: PFDHA studies are usually site-specific (for strategic infrastructures: dam, nuclear power plants, etc.) or fault-specific, but never at a regional scale. In Chapter 3, a new regional-scale approach is presented, using the northern Calabria region in Italy, one of the most seismically active areas in Europe, as the study area. This new approach aims to produce PFDHA maps for different return periods, providing valuable support for risk mitigation strategies, infrastructure planning, lifeline resilience assessment, and territorial risk management.

The two case studies in this thesis show a progression from understanding rupture processes to assessing hazard. Taiwan and northern Calabria are located in different tectonic settings, allowing PFDHA to be examined across contrasting contexts and spatial scales, rather than within a single tectonic environment. Chapter 2 focuses on Taiwan and investigates repeated surface ruptures along the same fault, using well-documented successive events on the Longitudinal Valley Fault system. In contrast, Chapter 3 focuses on future potential ruptures and hazard assessment in northern Calabria, applying PFDHA within a regional-scale framework.

# 2. A particular case of recent repeated fault surface rupture: the Longitudinal Valley in Taiwan

## 2.1. Introduction

Taiwan is an island located at the convergence of the Philippine Sea plate and the Eurasian plate (Angelier et al., 1997; Malavieille et al., 2002). It is one of the most seismically active regions in the world and has produced numerous surface-rupturing earthquakes throughout its historical and instrumental record (Figure 2-1a), such as the 1999 Mw 7.7 Chi-Chi event in Taiwan (Tseng et al., 2026). More specifically, the Longitudinal Valley (LV), on the eastern side of the island, is a narrow, tectonically complex zone where earthquakes of Mw ≥ 5 recur frequently (Figure 2-1a), some of which generate surface fault ruptures. It is located between the Central Range and the Coastal Range (Figure 2-2a), and hosts several long faults (> 100 km) marking the boundaries between the main geologic units: the west-dipping Central Range Fault (CRF) between the Central Range and the LV; the east-dipping Longitudinal Valley Fault system (LVF) delimiting the LV and the Coastal Range. This LVF is composed of several segments (Figure 2-1b) along the valley including the Lichi, Chihshang, Rueisuei, Lingding and Milun segments, from south to north (Chen et al., 2007). This transpressive fault system, characterised by oblique kinematics combining reverse and strike-slip motion, accommodates much of the strong plate convergence (8-9 mm/yr, Yu et al., 1997; Hsu et al., 2016) through both seismic slip, with large earthquakes, and aseismic slip (creeping, Lee et al., 2003; Hsu and Bürgmann, 2006; Thomas et al., 2014), especially in the central section (Chihshang fault). Between the CRF and the LVF, smaller fault segments, such as the Yuli fault (Figure 2-2b), are connected to the main structures and also contribute to accommodating the overall tectonic convergence, although they remain poorly constrained and still debated. Additionally, the Yuli fault differs from the other segments in that it shows no clear evidence of long-term vertical deformation, and is therefore considered as left-lateral (Bonilla et al., 1975; Hsu et al., 1962).

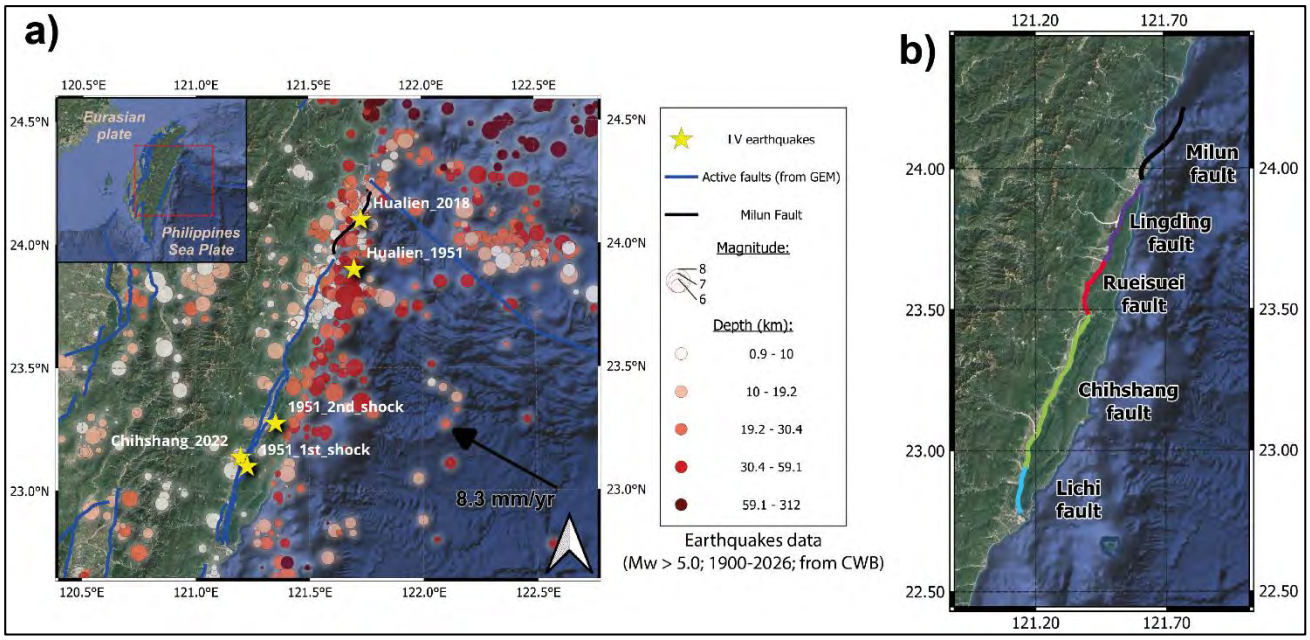



*Figure 2-1: Map of the Longitudinal Valley fault (LVF) system. a) Seismic activity in the Longitudinal Valley in Taiwan during the last century. The active faults are from Styron and Pagani (2020) and Shyu et al. (2020). b) Details of the fault segments forming the LVF.*

PFDHA models are primarily based on empirical datasets compiled with worldwide surface rupture data. The PFDHA approach assumes that two earthquakes of similar magnitude on the same fault would produce similar ruptures, and, therefore, that past ruptures can be used to estimate the future ones. However, very few locations worldwide provide repeated observations of surface ruptures on the same faults during different earthquake sequence, limiting the ability to test this assumption directly. The first one is the LVF, that is studied in this Chapter, and another one is the Weitin fault in Papua New Guinea, where surface ruptures were observed and documented during the 2000 Mw 8.0 earthquake and a second time during the 2019 Mw 7.7 earthquake (Chen et al., 2019).

The LVF presents documented repeated surface ruptures during two distinct surface rupturing sequences in 1951 and between 2018 and 2022 (Figure 2-1) leading to many damages and casualties (85 in total for the 1951 sequence). These newly formed surface ruptures represent the coseismic expression of ongoing tectonic deformation along pre-existing fault structures. The return period of surface rupturing earthquakes there seems to be approximately 67 years (Shyu et al., 2020), which is extremely low compared to most of the other major faults in Taiwan and in the world.

The availability of detailed observations from both earthquake sequences provides a unique opportunity to directly compare the spatial distribution and characteristics of successive surface

ruptures along the same fault, and to test one of the fundamental assumptions of the PFDHA approach. Furthermore, none of the two earthquake sequence events studied in this Chapter are included in the surface rupture databases used to develop the empirical models presented in Chapter 1, with the exception of the 2018 Hualien earthquake, included in the FDHI database. Therefore, these events provide an independent and particularly valuable dataset to check the applicability and robustness of existing empirical models, while their exclusively coseismic nature makes them well suited for evaluating the repeatability of coseismic surface rupture within the PFDHA framework.

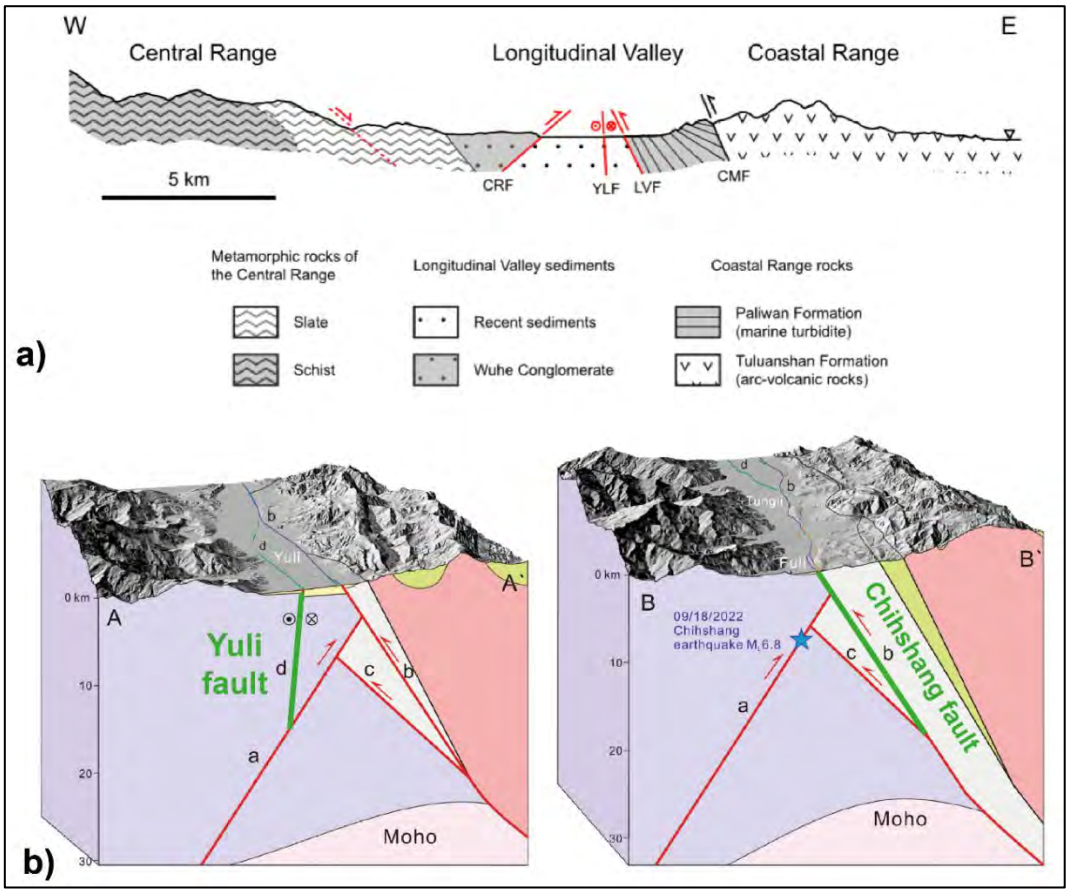



*Figure 2-2: Geometry of the southern part of Longitudinal Valley fault system: a) Schematic geologic cross-section of the LVF (from Shyu et al., 2006; Figure 5). b) Cross-sections illustrating the tectonic setting at two different places along the LVF. The positions of the two cross-sections AA' and BB' are indicated in Figure 2-14 (modified from Chen et al., 2024).*

## 2.2. LVF earthquakes sequences in 1951 and 2018-2022

The 1951 sequence started with the October 22 Mw 7.3 Hualien earthquake in the northern part of the valley (Figure 2-1). This first event occurred on the east-dipping Milun fault and caused many damages and casualties in Hualien city. One month after the Hualien earthquake, on November 24 (with UTC, November 25 with Taiwan time), two consecutives

strong earthquakes (later referred to as Taitung earthquakes) occurred in the southern part of the LVF, with Mw 6.2 and Mw 7.0 (Cheng et al., 1996). However, the magnitude estimates of these two closely spaced events may be associated with some uncertainty, as they occurred only a few minutes apart, potentially complicating the separation and interpretation of their seismic records. Both shocks exhibited a reverse/oblique focal mechanism and caused significant surface ruptures. These two strong shocks nucleated on different faults inside the LV: the first on the Chihshang segment, dipping east and forming part of the LVF, and the second on the west-dipping Yuli segment forming part of the CRF (Figure 2-1).

The second sequence started with the 2018 February 6 Mw 6.4 Hualien earthquake that nucleated on a west-dipping fault segment located to the north of the Milun fault. The rupture was propagated along multiple fault segments, including the Milun fault (Lee et al., 2018). Strictly speaking, the observed rupture along the Milun fault should be considered as distributed, but given the uncertain relationship at depth between the fault segments in the area, a simplified analysis treating it as principal faulting along the Milun fault is performed here.

In 2022, on September 18, an Mw 7.0 earthquake occurred on the CRF approximately 5 km north of the 1951 first shock and 20 km south of the 1951 second shock. The information collected for all the events studied are summarised in Table 2-1.

| Earthquake | Date | Mw | Lon | Lat | Fault segment | Observed rupture length (km) |
|---|---|---|---|---|---|---|
| 1951 Hualien | 22/10/1951 | 7.3 | 121.7 | 23.9 | Milun | 8-36 |
| 1951 Taitung 1st shock (18:47 UTC) | 24/11/1951 | 6.2 | 121.225 | 23.1 | Chihshang | 28 |
| 1951 Taitung 2nd shock (18:50 UTC) | 24/11/1951 | 7.0 | 121.35 | 23.275 | Yuli-Rueisuei | 38 |
| 2018 Hualien | 06/02/2018 | 6.4 | 121.7296 | 24.1006 | Milun | 8-36 |
| 2022 Chihshang | 18/09/2022 | 7.0 | 121.1958 | 23.137 | CRF | 64.6 |

*Table 2-1: Earthquakes data of the 1951 and 2018 sequences in the Longitudinal Valley.*

## 2.3. Methods and surface rupture data collection

Surface ruptures from the 1951 LVF earthquakes were mainly documented using photographs published in 臺灣十大災害地震圖集 *[Atlas of Ten Major Disaster Earthquakes in Taiwan]* (Zheng et al., 1999). These photographs were used to infer the approximate locations of the observed surface ruptures. Additional data were taken from Chen et al. (2007) and Shyu et al. (2007). The collected dataset for both 1951 events consists of 25 surface rupture data points, 7 for the Hualien event and 18 for the Taitung earthquakes (Table 2-2).

| ID | Localisation | Lat | Lon | X/L | Dist. to PF (km) | Horizontal displacement (cm) | Vertical displacement (cm) | Event | Fault segment | Reference | |
|---|---|---|---|---|---|---|---|---|---|---|---|
| 1 | railway near Zhonghua road, Hualien | 23.976196 | 121.610141 | 0.03 | | *250** | | Hualien | Milun | | fig 706 p.181 |
| 2 | Nanbin seawall, SE Hualien | 23.968737 | 121.612303 | 0.00 | 0,2-0,3 | 40 | | Hualien | Milun | | fig 716 p.187 |
| 3 | south of Beipu airport, Hualien | 24.013379 | 121.617897 | 0,14-0,15 | 0-0,5 | | 45 | Hualien | Milun | | fig 719 p.189 |
| 4 | Minyi village, 7km NE of Hualien | 24.001768 | 121.614017 | 0,11-0,12 | 0-0,2 | 200 | | Hualien | Milun | | fig 720 p.190 |
| 5 | Jialiwan roadbed, north of Hualien | | | *0.2** | | 40 | | Hualien | Milun | | fig 721 p.191 |
| 6 | Qixing mountain, Hualien | | | *0.2** | | | 120 | Hualien | Milun | | fig 722 p.191 |
| 7 | building in Qixingtan, Hualien | 24.026673 | 121.630797 | 0.23 | 0-0,1 | | 40 | Hualien | Milun | | fig 723 p.191 |
| 8 | near Dafu, Guangfu, Hualien county | | | | 0 | | 130 | Taitung - 2nd shock | Yuli-Rueisuei | Zheng et al. (1999) | fig 726 p.193 |
| 9 | coastal mountain near Dafu, Guangfu, Hualien county | | | | 0 | | 200 | Taitung - 2nd shock | Yuli-Rueisuei | | fig 727 p.193 |
| 10 | creek east of Dafu farm, Guangfu, Hualien county | 23.602743 | 121.419282 | 0.96 | 0 | | 120 | Taitung - 2nd shock | Yuli-Rueisuei | | fig 729 p.194 |
| 11 | Fuxing village, Ruisui, Hualien county | 23.531136 | 121.389039 | 0.72 | 0 | 161 | 136 | Taitung - 2nd shock | Yuli-Rueisuei | | fig 730 p.195 |
| 12 | East side of Dadu Ya river, Fuxing village, Ruisui, Hualien county | | | | | | 150 | Taitung - 2nd shock | Yuli-Rueisuei | | fig 733 p.197 |
| 13 | Fuxing village, Ruisui, Hualien county | 23.581402 | 121.401447 | 0.88 | 0 | | 100 | Taitung - 2nd shock | Yuli-Rueisuei | | fig 734 p.197 |
| 14 | near the mountain range in SE Fuyuan, Ruisui, Hualien county | | | | | | 120 | Taitung - 2nd shock | Yuli-Rueisuei | | fig 735 p.198 |
| 15 | Xiaozhu bridge on the Malan Diaoxi river, Ruisui, Hualien county | 23.498955 | 121.397955 | 0.63 | 0 | 160 | | Taitung - 2nd shock | Yuli-Rueisuei | | fig 737 p.199 |
| 16 | Yuli elementary school, Yuli, Hualien county | 23.335733 | 121.316848 | 0.08 | 0 | 40 | | Taitung - 2nd shock | Yuli-Rueisuei | | fig 739 p.200 |
| 17 | Songpu village near Guanyin mountain, Yuli, Hualien county | | | | 0 | | 60 | Taitung - 2nd shock | Chihshang | | fig 740 p.201 |
| 18 | fields near Dongli, Fuli, Hualien county | 23.249381 | 121.293253 | 0.66 | 0 | | 200 | Taitung - 1st shock | Chihshang | | fig 742 p.202 |
| 19 | Dafu trenches, Ruisui, Hualien county | 23.591298 | 121.402992 | 0.91 | 0 | | 100 | Taitung - 2nd shock | Yuli-Rueisuei | Chen et al., 2007 | |
| 20 | Anding bridge trenches, Ruisui, Hualien county | 23.569580 | 121.400425 | 0.84 | 0 | | 75 | Taitung - 2nd shock | Yuli-Rueisuei | | |
| 21 | Fushin trenches, Ruisui, Hualien county | 23.573035 | 121.402252 | 0.85 | 0 | | 120 | Taitung - 2nd shock | Yuli-Rueisuei | | |
| 22 | Yuli_Roadway_bridge | 23.313129 | 121.331338 | 0.95 | 0 | 35 | 15 | Taitung - 1st shock | Chihshang | Shyu et al., 2007 | |
| 23 | East_Chihshang | 23.130435 | 121.233177 | 0.12 | 0 | | 50 | Taitung - 1st shock | Chihshang | | |
| 24 | Fuli town | 23.180177 | 121.252048 | 0.33 | 0 | | 20 | Taitung - 1st shock | Chihshang | | |
| 25 | southwest Wanrong | 23.550279 | 121.391399 | 0.78 | 0 | | 155 | Taitung - 2nd shock | Yuli-Rueisuei | | |

*Table 2-2: Compiled surface rupture data for the 1951 Hualien and Taitung earthquakes*

Relocating these data was the most challenging task in this study, as the descriptions of the photographs provided in Zheng et al. (1999) were not always consistent with currently existing places. Considerable effort has been made to relocate them, or at least to narrow down the possible areas where these pictures were taken. Even if the locations are not always precise,

they provide valuable information on the position along the valley and therefore along the fault system. An example of this re-localisation process is shown in Figure 2-3, for the ID n°15 data point of the 1951 Taitung earthquake (in Table 2-2).

The starting point was always the photographs and sketches from Zheng et al. (1999). In Figure 2-3, the image shows the surface rupture inside a riverbed near Rueisuei village, offsetting a wooden bridge by approximately 1.6 metres. This bridge obviously no longer exists, and its location has been lost over time, but Rueisuei village still exists and has the same name. By checking features in the image background, such as the hill, and comparing them with current images from *Google Street View*, a broad potential area where this photograph was taken can be estimated (dashed red line in Figure 2-3).

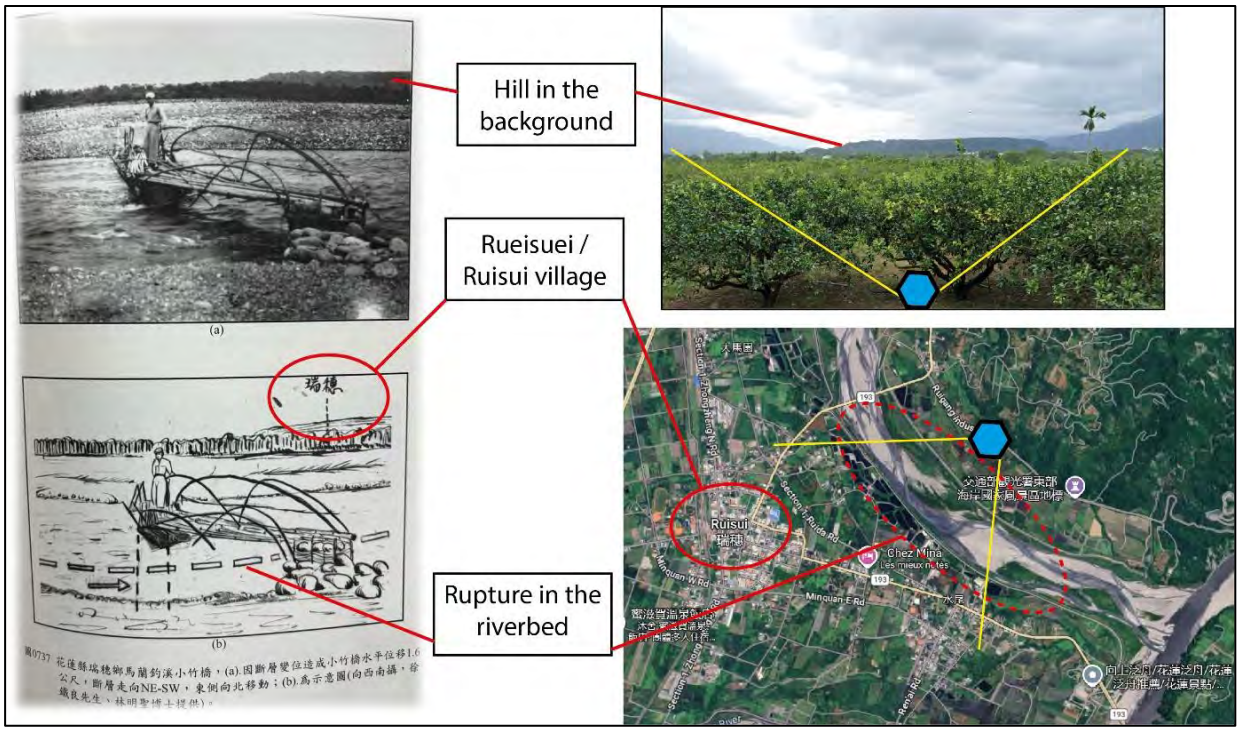



*Figure 2-3: Process followed to relocate one surface rupture photograph from the 1951 Taitung earthquake. The left side shows the original figure from Zheng et al. (1999). The upper right image is from Google Street View, with the blue rhombus representing the same view angle as in the lower right satellite view. The final estimated location of the 1951 photograph is within the dashed red area.*

For the Hualien earthquake, the n°1 in Table 2-2 represents a railway deformation rather than an actual rupture and is therefore discarded. Data points n°5 and n°6 could not be accurately localised but are estimated to be near the Qixingtan village according to the description, on the northern part of the rupture. Therefore, these two points are assumed to be at approximately X/L = 0.2 and potentially at 1 km from the main rupture trace. In total, all the six data points are used for the analyses, although two of them are not reliably localised. . For the Taitung

events, similarly, several surface ruptures photographs could not be reliably localised and are excluded from the analysis (ID n°8, 9, 12, 14 and 17 in Table 2-2), reducing the available data to 13.

After the collection and relocation process, each data point has to be assigned to either *principal* or *distributed* faulting type, following the classic terminology used in Youngs et al. (2003) in order to be consistently compared with the empirical model estimations. This definition process is discussed in the following sections 2.3. and 2.4.

For the two recent earthquakes, in 2018 and 2022, much larger and more accurate datasets are available, provided by comprehensive studies conducted immediately after the earthquakes by national institutes and agencies such as the Central Weather Bureau and the Central Geological Survey (CGS, 2018; 2022). For the 2018 event, the data used in this study are essentially from Hsu et al. (2019), with a filtering based on the type of data as described in (Gao et al., 2022). Type I and II data, representing 'free field displacement' and 'displacement slightly affected by manmade structures' (e.g. roads) respectively, are included while the type III data, i.e. 'displacement of indirect ruptures' (e.g. wall or bridge damages), are excluded, resulting in a final dataset of 137 ruptures (see section 2.3.4.).

For the 2022, a compilation of data from Wang et al. (2024) and the CGS report (2022) is used. The complete dataset for this second event is presented in Table 2-3.

| Latitude | Longitude | Code | Location | Vertical disp. (cm) | Horizontal disp. (cm) | Average H disp. (cm) | Average V disp. (cm) | Average Net disp. (cm) | Fault segment | Reference |
|---|---|---|---|---|---|---|---|---|---|---|
| 23.4472 | 121.38 | KKL_B2 | West of Chunri village | 10-35 | 25-29 | 27 | 22.5 | 37 | Yuli | Wang et al., 2024 |
| 23.4412 | 121.3799 | KKL_31 | West of Chunri village | 13 | 8-9 | 8.5 | 13 | 17 | Yuli | Wang et al., 2024 |
| 23.4432 | 121.3749 | KKL_B1 | West of Chunri village | 8 | 5 | 5 | 8 | 10 | Yuli | Wang et al., 2024 |
| 23.4439 | 121.381 | KKL_B3 | West of Chunri village | 13-80 | 8-9 | 8.5 | 46.5 | 52 | Yuli | Wang et al., 2024 |
| 23.3727 | 121.3362 | 0919_O | Paddle field south of Gaoliao bridge | | 23-38 | 30.5 | | 31 | Yuli | Wang et al., 2024 |
| 23.3493 | 121.322 | 0919_031 | Left bank of Zhou river | | 5 | 5 | | 5 | Yuli | Wang et al., 2024 |
| 23.3481 | 121.3215 | 0919_L | Levee near Yuli Hospital | | 7-9,5 | 8.25 | | 8 | Yuli | Wang et al., 2024 |
| 23.3479 | 121.3216 | 0919_K | Yuli Hospital | | 9 | 9 | | 9 | Yuli | Wang et al., 2024 |
| 23.3479 | 121.3216 | 0919_J | Yuli Hospital | | 20 | 20 | | 20 | Yuli | Wang et al., 2024 |
| 23.3457 | 121.321 | 0919_024 | Campus of Yuli High School | | 5-10 | 7.5 | | 8 | Yuli | Wang et al., 2024 |
| 23.3422 | 121.32 | 0919_010 | Yuli sports field | | 11 | 11 | | 11 | Yuli | Wang et al., 2024 |
| 23.3394 | 121.318 | 1007_005 | Mingkuo rd. sec. 2 | | 13 | 13 | | 13 | Yuli | Wang et al., 2024 |

| | | | | | | | | | | |
|---|---|---|---|---|---|---|---|---|---|---|
| 23.3394 | 121.318 | 0919_003 | Jiankuo fifth st. | | 11 | 11 | | 11 | Yuli | Wang et al., 2024 |
| 23.339 | 121.318 | 0919_002 | Jiankuo fourth st. & Minguo rd. intersection | | 3.9 | 3.9 | | 4 | Yuli | Wang et al., 2024 |
| 23.3385 | 121.318 | 0919_001 | Jiankuo fourth st. & Minguo rd. intersection | 20-27 | | | 23.5 | 26 | Yuli | Wang et al., 2024 |
| 23.3368 | 121.3174 | 0919_H | Old campus of Yuli Elementary School | | 7.3 | 7.3 | | 7 | Yuli | Wang et al., 2024 |
| 23.3359 | 121.3169 | 0919_I | Old campus of Yuli Elementary School | | 10.9 | 10.9 | | 11 | Yuli | Wang et al., 2024 |
| 23.3347 | 121.3166 | 0919_H | Old campus of Yuli Elementary School | | 11.1 | 11.1 | | 11 | Yuli | Wang et al., 2024 |
| 23.3337 | 121.316 | 0919_D | Hsiehtian temple | 5.5 | | | 5.5 | 6 | Yuli | Wang et al., 2024 |
| 23.3334 | 121.3159 | 0919_C | Zhongzheng rd. | | 10-14 | 12 | | 12 | Yuli | Wang et al., 2024 |
| 23.3331 | 121.3159 | 0919_A | Zhongzheng Mingshen intersection | 10-15 | | | 12.5 | 14 | Yuli | Wang et al., 2024 |
| 23.333 | 121.3159 | 0919_B | Zhongzheng Mingshen intersection | 2 | 2.3 | 2.3 | 2 | 3 | Yuli | Wang et al., 2024 |
| 23.3316 | 121.315 | 0920_001 | Yuli roundabout | | 7-7,5 | 7.25 | | 7 | Yuli | Wang et al., 2024 |
| 23.3303 | 121.315 | 0920_003 | Minguo Heping intersection | | 14 | 14 | | 14 | Yuli | Wang et al., 2024 |
| 23.33 | 121.315 | 0920_004 | Minguo rd. sec. 1 | | 10 | 10 | | 10 | Yuli | Wang et al., 2024 |
| 23.3297 | 121.315 | 0920_005 | Minguo rd. sec. 1 | | 3 | 3 | | 3 | Yuli | Wang et al., 2024 |
| 23.3263 | 121.314 | 0920_010 | Chengxi sixth st. | 16 | | | 16 | 18 | Yuli | Wang et al., 2024 |
| 23.3089 | 121.307 | 0920_020 | Renai rd. sec. 1 | | 1,6-12 | 6.8 | | 7 | Yuli | Wang et al., 2024 |
| 23.3045 | 121.306 | 0920_021 | Renai rd. sec. 1 | 16 | | | 16 | 18 | Yuli | Wang et al., 2024 |
| 23.303 | 121.306 | 0920_022 | Left bank of Lele river | 15-18 | 6-9 | 7.5 | 16.5 | 20 | Yuli | Wang et al., 2024 |
| 23.2873 | 121.303 | 0921_014 | Changliang north village | | 75-100 | 87.5 | | 88 | Yuli | Wang et al., 2024 |
| 23.2866 | 121.303 | 0921_013 | Changliang north village | | 85 | 85 | | 85 | Yuli | Wang et al., 2024 |
| 23.286 | 121.303 | 0921_012 | Changliang north village | | 82 | 82 | | 82 | Yuli | Wang et al., 2024 |
| 23.2853 | 121.302 | 0921_011 | Changliang north village | | 82 | 82 | | 82 | Yuli | Wang et al., 2024 |
| 23.2797 | 121.299 | 0921_001 | Changliang north village | | 9 | 9 | | 9 | Yuli | Wang et al., 2024 |
| 23.2795 | 121.3 | 0921_006 | Changliang north village | | 30 | 30 | | 30 | Yuli | Wang et al., 2024 |
| 23.2779 | 121.3 | 0921_003 | Left bank of Hsiukuluan river | 11 | 1 | 1 | 11 | 12 | Yuli | Wang et al., 2024 |
| 23.2641 | 121.3015 | FL29-1 | Campus of Dongli Junior High school | 12 | | | 12 | 13 | Yuli | Wang et al., 2024 |
| 23.2633 | 121.3007 | FL28 | Campus of Dongli Junior High school | | 17 | 17 | | 17 | Yuli | Wang et al., 2024 |
| 23.2256 | 121.2805 | FL04-2 | Fubei Junior High School | 15 | 30 | 30 | 15 | 34 | Yuli | Wang et al., 2024 |
| 23.2059 | 121.2653 | FL34 | Right bank of Luntian river | 40 | | | 40 | 44 | Yuli | Wang et al., 2024 |
| 23.2032 | 121.2639 | FL12 | Right bank of Luntian river | 10 | 7 | 7 | 10 | 13 | Yuli | Wang et al., 2024 |

| | | | | | | | | | | |
|---|---|---|---|---|---|---|---|---|---|---|
| 23.290542 | 121.304374 | 15 | Fig. 2-1-16 | 30-100 | 80-100 | 90 | 65 | 115 | Yuli | CGS report |
| 23.278197 | 121.300104 | 18 | Fig. 2-1-19 | 30-50 | | | 40 | 44 | Yuli | CGS report |
| 23.43639 | 121.377197 | 31 | Fig. 3-1-13 | 100 | | | 100 | 110 | Yuli | CGS report |
| 23.1724 | 121.248 | FL06 | Campus of Fuli Elementary School | | 12 | 12 | | 12 | Chihshang | Wang et al., 2024 |
| 23.14243833 | 121.2366653 | 43 | Fig. 3-3-2 | 10-20 | | | 15 | 16 | Chihshang | CGS report |
| 23.04711944 | 121.1990806 | 55 | Fig. 3-4-4 | | 10 | 10 | | 10 | Chihshang | CGS report |
| 22.97488056 | 121.1706472 | 58 | Fig. 3-4-7 | | 10 | 10 | | 10 | Chihshang | CGS report |

*Table 2-3: Compiled surface rupture dataset for the 2022 Chihshang earthquake.*

## 2.4. Hualien earthquakes

In this section, the surface fault displacements associated with the 1951 and 2018 Hualien earthquakes are compared both with each other and with estimated fault displacement from empirical models. The comparison examines both the spatial distribution and also the amplitude of the observed displacements, to assess how similar these successive ruptures can be. The Milun fault is notable for being located both onshore and offshore. The 1951 and 2018 events ruptured the surface on the onshore section, ~ 8 km, in a quite similar manner (Figure 2-4), but no information is available for the offshore part. Therefore, the total rupture length for both events is unknown and is assumed to be the total full length. The initial Milun fault trace was taken from the Taiwan Earthquake Model (32.6 km long, Shyu et al., 2020) and then slightly updated using the 1951 and 2018 rupture traces, increasing the total length to 36 km.

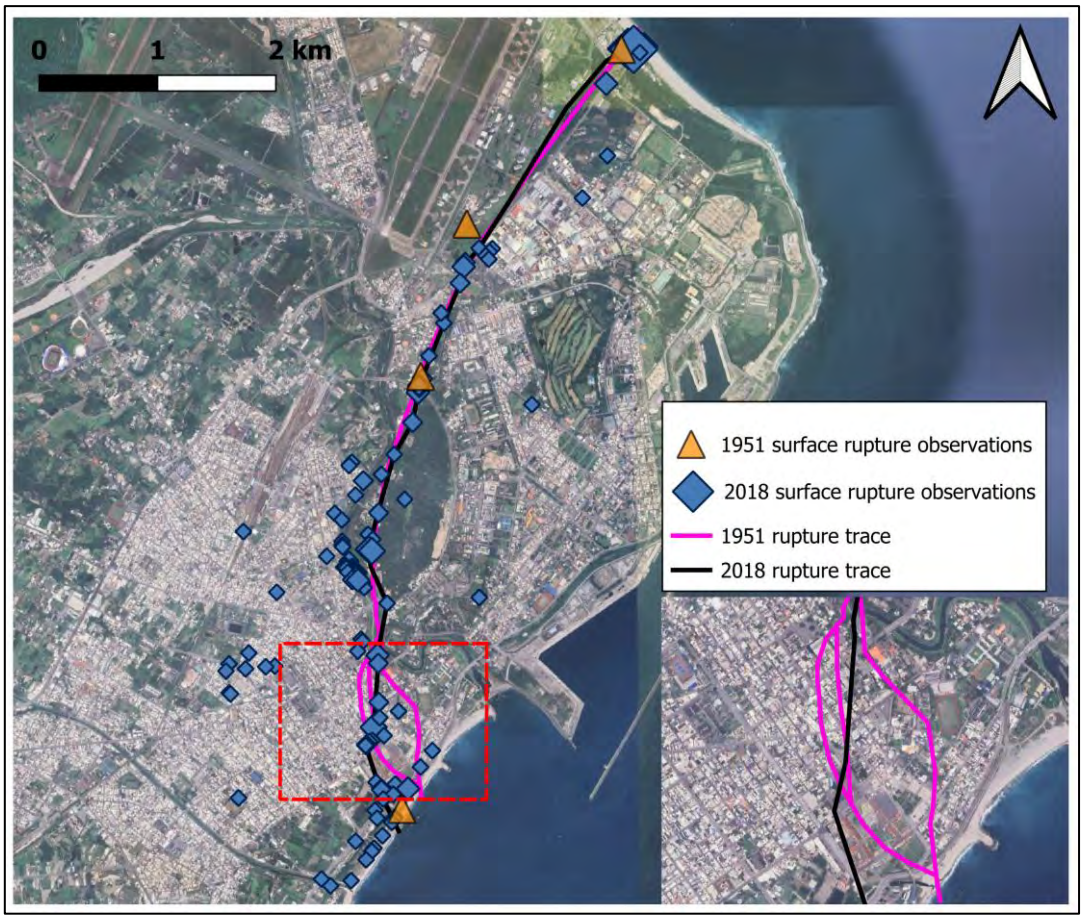



*Figure 2-4: Rupture traces and surface displacement data of the 1951 and 2018 Hualien earthquakes.*

To perform the displacement amplitude analysis, selecting an appropriate empirical model selection here is crucial, as it has to be consistent with the general geological context of the area: an oblique kinematic dominated by compressional regime (reverse faulting) with a non-negligible left-lateral component (Yu et al., 1997; Hsu et al., 2016). Since no available models exclusively account for such context, a separate analysis of both vertical and horizontal observed motion is carried out, using Petersen et al. (2011), for strike-slip motion; and Moss et al. (2022), Moss et al. (2024) and Visini et al. (2025), for reverse faulting (hereafter referred to as PEA11, MEA22, MEA24 and VEA25, respectively).

### 2.4.1. Rupture trace and along-fault displacement comparisons

First, both rupture traces in 1951 and 2018 are similar to each other, with some differences in the southern part of the Milun fault (Figure 2-4). In 1951, the surface rupture is reported to have been divided along three distinct branches, whereas in 2018 it followed a single, more localised trace. However, the 1951 rupture as it is shown in Figure 2-14 (from Lin et al., 2009) may not be fully reliable and could alternatively represent a broader ‘damage zone’

rather than three well-defined traces. If, however, the 1951 rupture did indeed occur along multiple strands, this would suggest a different rupture style compared to 2018, potentially reflecting variations in near-surface fault complexity, stress distribution or changes in surface loading conditions within that segment of the fault system.

Indeed, the Hualien municipality underwent rapid urbanisation after 1951 and is now largely urbanised, with many residential and commercial buildings. Such surface loading is known to induce several phenomena that can modify subsurface physical properties, including changes to the normal stress state through building load, variations in Coulomb failure stress and localised clamping or unclamping effects on underlying fault planes (Kyriakopoulos et al., 2021; Douilly, 2023; Tiwari et al., 2023). All these phenomena may have contributed to directing the rupture preferentially in a single direction in 2018, in contrast to the more distributed pattern observed in 1951. Conversely, in the northern part of the fault, near the military airport, the rupture trace of both events is strikingly similar. This area has remained largely open and undeveloped since 1951, with little change in surface loading conditions. The contrast between the two areas supports the hypothesis that loading related to urbanisation in the southern part of the Milun fault may have been responsible for redirection of the surface rupture trace between 1951 and 2018.

However, this pattern may also reflect the natural variability in fault zone geometry or the influence of other geological processes, such as fault bending. But it is difficult to draw further conclusions regarding the controlling factors based only on the observed rupture locations, and further investigations would be required to determine the real influence of these processes.

In Figure 2-5, the along-fault (i.e. X/L) surface displacements of the two events are compared, by differentiating the horizontal and the vertical component to highlight any potential pattern or similarity. There, since the full rupture length is unknown and only the onshore part of the fault is available, the full fault length, i.e. 36 km is considered as the SRL and for the X/L distribution. Therefore, in Figure 2-5, the maximum X/L is around 0.23.

The main observations of this analysis are that the displacements were larger for the 1951 event than for the 2018 event, for both the vertical and horizontal components. This is consistent with the higher magnitude of the 1951 event compared with the 2018 event (Mw 7.3 vs Mw 6.4). Additionally, in 2018, surface displacement data were observed quite regularly along the fault, highlighting the improvement in surface displacement documentation and measurement over time. Finally, it seems that around X/L ~ 0.2 - 0.25 (northern part of the rupture, near Qixingtan)

there's a peak of vertical displacement for both 1951 and 2018 events.

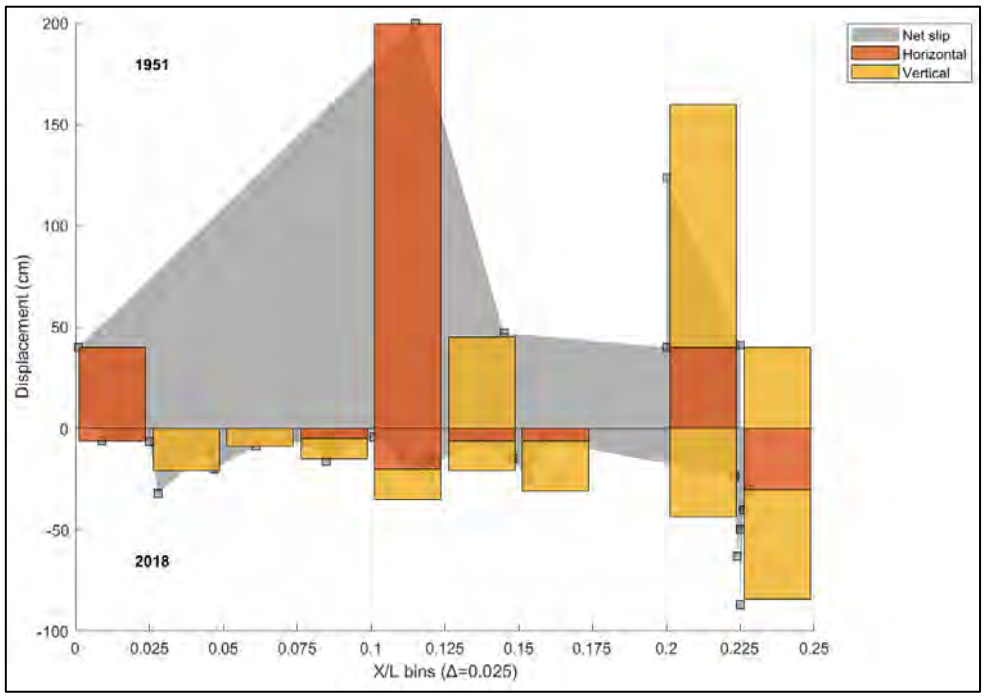



*Figure 2-5: Comparison of the average fault displacement observed along the Milun fault during the 1951 and 2018 Hualien earthquakes.*

## 2.4.2. Surface rupture length comparisons

Before performing any kind of comparison with fault displacement models, it is interesting to check if the total rupture traces reported for both earthquakes in 1951 and 2018 are consistent with the estimated moment magnitude.

| | | | Rupture length (km) | | | | | |
|---|---|---|---|---|---|---|---|---|
| **Event** | **Mw** | **L (km)** | **TEA17 (SS)** | **TEA17 (R)** | **LEO14 (SS)** | **WC94 (All)** | **WC94 (SS)** | **WC94 (R)** |
| 1951 | 7.3 | 36 | 106,73 | 61,55 | 67,55 | 65,61 | 71,12 | 54,83 |
| 2018 | 6,42 | 36 | 26,85 | 17,74 | 20,03 | 16,21 | 15,88 | 15,30 |

*Table 2-4: Hualien earthquakes surface rupture lengths comparison with empirical models (TEA17: Thingbaijam et al., 2017; LEO14: Leonard et al., 2014; WC94: Wells & Coppersmith, 1994; SS: strike-slip faulting; R: reverse faulting).*

The left side of Table 2-4 summarises the Milun fault length and the moment magnitudes reported for both event in 1951 and 2018. The right side shows the theoretical surface rupture length (SRL) for such magnitudes and for different kinematics (strike-slip and reverse). For 1951, all the empirical regressions find a SRL around 55-100 km which is much larger than the

36 km long Milun fault. And conversely, for 2018, the SRL is smaller than the ~36 km Milun fault, which is quite realistic, as not all the fault length would have ruptured during this event. Therefore it's very likely that the moment magnitude of the 1951 event has been significantly overestimated and may actually be lower than 7.3, possibly closer to the value observed in 2018, around Mw 6.5. However, the larger surface displacements observed in 1951 compared with 2018 do not readily support this interpretation An alternative explanation is that the reported magnitude is correct, but part of the rupture occurred on another fault segment, potentially offshore, and therefore was not documented.

### 2.4.3. 1951 Mw 7.3 event displacement amplitude comparison

Given the high uncertainty on the rupture trace position and the data location, all the data points are considered as principal and distributed displacement. For this reason, all data is assigned with both an X/L value, for principal faulting cases, and with an estimated maximum distance from the rupture trace, for distributed faulting cases.

| Horizontal displacement data | | | | |
|---|---|---|---|---|
| **ID** | **X/L** | **Dist. To PF (km)** | **Displacement (cm)** | **Wall** |
| 2 | 0.001 | 0.25 ± 0.1 | 40 | FW |
| 4 | 0.115 | 0.1 ± 0.05 | 200 | FW |
| 5 | *0.2** | *1 ± 0.5** | 40 | FW |
| **Vertical displacement data** | | | | |
| 3 | 0.145 | 0.25 ± 0.1 | 45 | FW |
| 6 | *0.2** | *1 ± 0.5** | 120 | FW |
| 7 | 0.215 | 0.05 ± 0.05 | 40 | FW |

*Table 2-5: Summary of the 1951 Hualien earthquake observed surface rupture data (values marked with an * are estimated as their data point could not be localised).*

**Principal faulting:**

Of the six available surface rupture data, only three provide vertical displacement, while the other three provide only horizontal displacement (Table 2-5). As previously explained, the horizontal and vertical components are analysed separately using PEA11 for the horizontal component, and MEA24 for the vertical component.

PEA11 estimates the horizontal displacement *d* and *ln(d)* following three different regression models: bilinear, quadratic and ellipsoidal, all depending on the magnitude and the X/L ratio. The PEA11 displacement regressions with the 1 sigma envelope are illustrated in Figure 2-6.

MEA24 conversely, estimates the average displacement (AD) and maximum displacement

(MD) from the magnitude using a log-linear relationship. The results are shown in Figure 2-7.

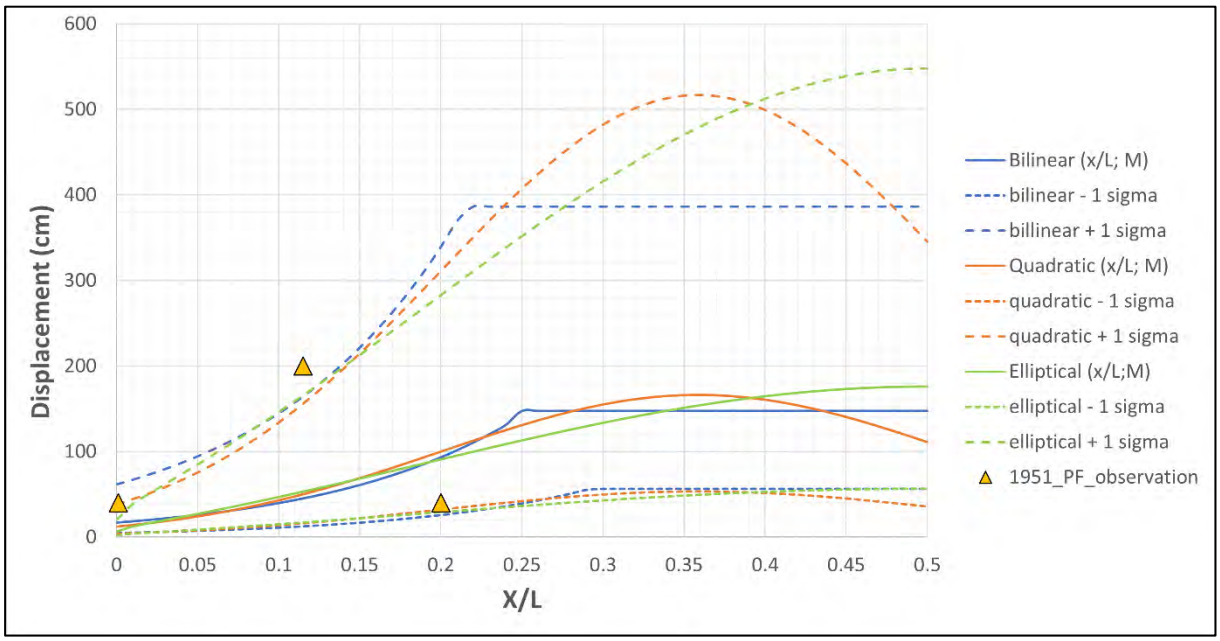



*Figure 2-6: Comparison of the principal horizontal displacement observed along the Milun fault during the 1951 Hualien earthquake with the PEA11 models.*

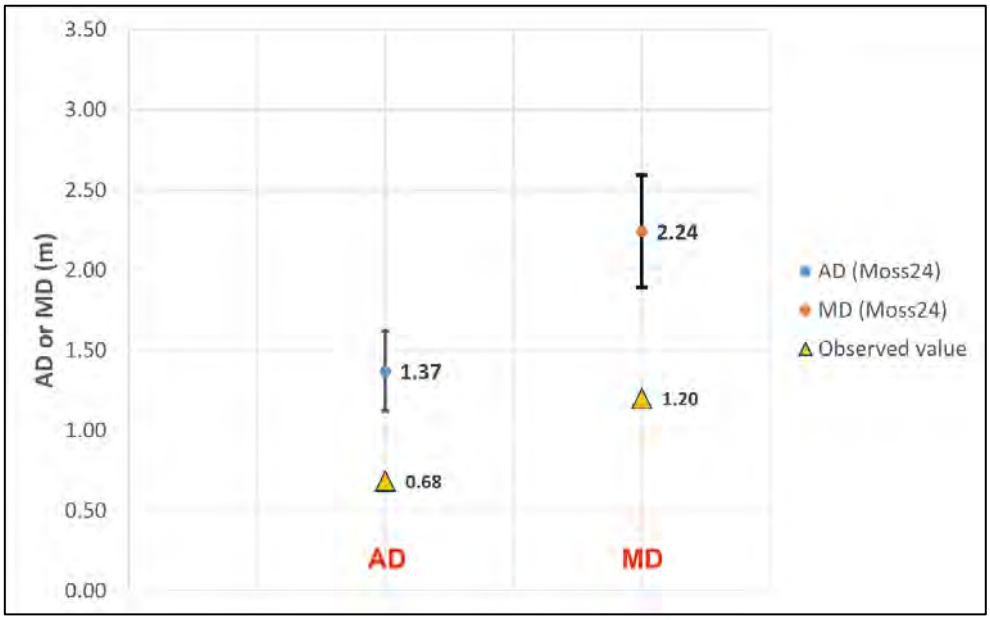



*Figure 2-7: Comparison of the principal vertical displacement observed along the Milun fault during the 1951 Hualien earthquake with AD and MD estimated from MEA24.*

Regarding the horizontal displacement, two of the three observed data points fall within the 1 sigma envelope of the PEA11 model distributions, with the third being very close to it. For the vertical displacement, the observed AD and MD are 0.68 and 1.20 metres, respectively, while the MEA24 estimates are 1.37 ± 0.25 and 2.24 ± 0.35 metres. Thus, given the limited available

data, the horizontal displacement appears to be quite well constrained by PEA11, while MEA24 tends to overestimate the vertical displacement. This overestimation may result from the empirical models being primarily built from pure dip-slip ruptures, whereas the studied events involve oblique kinematics in which Mw reflects the total seismic moment, with only part of the deformation expressed in the vertical component. Consequently, for a given magnitude, the vertical component of an oblique rupture is expected to be smaller than the one of a pure dip-slip rupture, without horizontal component.

**Distributed faulting:**

For distributed faulting, PEA11, MEA22, and VEA25 are used for the comparison, following the same separate analysis by displacement component as for principal faulting.

For the horizontal displacement, PEA11 estimates the normalised displacement ratio D/AD as a function of the distance *r*. The AD obtained from the observations is 0.93 m, and another value, approximately 1.42 m, obtained by averaging various magnitude scaling empirical regressions from MEA24, WC94 (SS) and TEA14 (SS), is also tested. The distributions of the 'de-normalised' displacements with distance from the rupture trace using both observed AD (red) and the AD obtained from the empirical regressions (black), are shown in Figure 2-8.

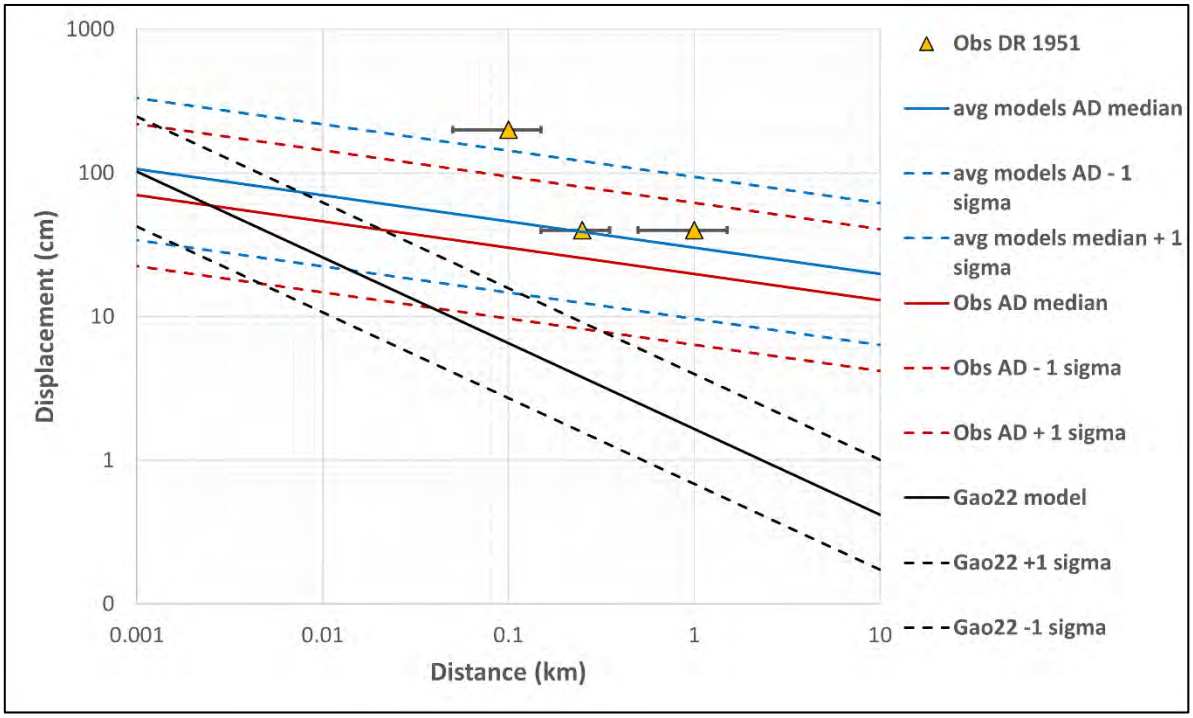



*Figure 2-8: Comparison of the distributed horizontal displacement observed during the 1951 Hualien earthquake with PEA11 model. In red, AD is obtained from the data; in blue using empirical regressions.*

For the vertical displacement, both MEA22 and VEA25 are used. MEA22, in a similar way

than PEA11, estimates the normalised displacement ratio (D/MD here) for various situations: FW, HW, simple or complex faulting, with the footwall and the hanging wall modelled separately based on the FDHI reverse/reverse-oblique earthquake database. In Figure 2-9, the observed distributed vertical displacements are compared with the MEA22 (Moss22). VEA25 model is also used for this part. Their 'Combination A', considering only the Rank 2 of DR (simple DR) relative to a rupture trace of Rank 1 (PF), is considered here, deriving the vertical displacement distribution in function of the distance from the rupture, the magnitude and AD.

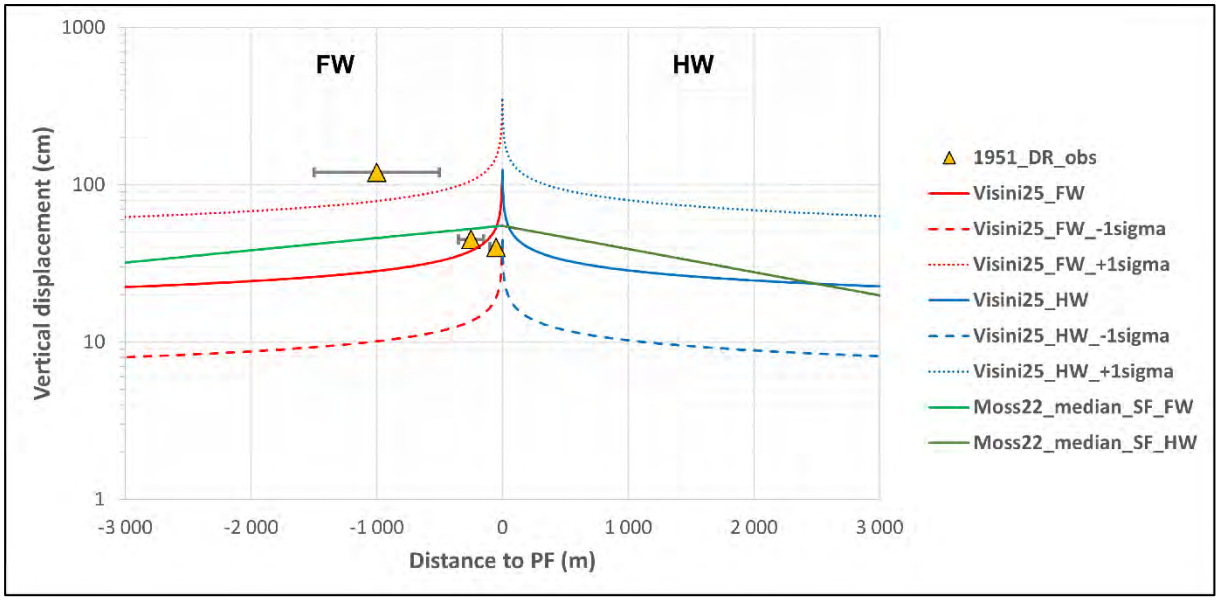



*Figure 2-9: Comparison of the distributed vertical displacement observed during the 1951 Hualien earthquake with empirical regressions from MEA22 (Moss22) and VEA25 (Visini25) (HW: hanging wall, FW: foot wall).*

The main observation is that the models for distributed faulting (PEA11, MEA24 and VEA25) fit quite well with the 1951 distributed rupture observations (Figure 2-8 and Figure 2-9). Indeed, two of the three data points fall within the 1 sigma envelope of PEA11 and VEA25 models and are also very close to the MEA22 median. Additionally, Figure 2-8 includes the model derived by Gao et al. (2022) from distributed ruptures observed during the 2018 Hualien earthquake. It is interesting to see that the 1951 data were actually much higher than this 'reference' model, suggesting that the distributed ruptures were also larger in 1951. However, it is important to note that the high uncertainties in the data position, the overall lack of data, and especially on the hanging wall, make it difficult to draw reliable further conclusions.

### 2.4.4. 2018 Mw 6.42 event displacement amplitude comparison

A similar methodology is applied as for the 1951 event, except that a 50-metres buffer zone around the rupture trace is considered to account for its uncertainty (principal faulting).

All measurements within this zone are considered as principal displacements and the ones outside are considered as distributed. At the end, of the 137 total data, there are 37 PF and 100 DR data, among which 78 are on the hanging wall and 22 are on the footwall (Table 2-6).

| | Number of data | | | | Observed | | MEA24 (R) | | WC94 (SS) | | TEA17 (SS) |
|---|---|---|---|---|---|---|---|---|---|---|---|
| PF zone type | PF | DR | | Total | AD (cm) | MD (cm) | AD (cm) | MD (cm) | AD (cm) | MD (cm) | AD (cm) |
| | | HW | FW | | | | | | | | |
| 20 m | 26 | 84 | 27 | 137 | 26 | 87 | 58 | 95 | 29 | 38 | 36 |
| 50 m | 37 | 78 | 22 | 137 | 21 | 87 | | | | | |

*Table 2-6: Data statistics of the 2018 Hualien earthquake surface rupture.*

The X/L value and the distance to the main rupture is re-calculated for each PF and/or DR data point, to allow comparisons with empirical models. A buffer zone of 20 metres was also tested but the results were not significantly different, therefore only the results for the 50-m zone are presented here.

| Latitude | Longitude | X/L | Vert. disp. (cm) | Horiz. disp. (cm) | wall type | Dist. (km) |
|---|---|---|---|---|---|---|
| 24.02689 | 121.6327 | 0.228 | | 30 | On-fault | |
| 24.02679 | 121.632 | 0.226 | 40 | | On-fault | |
| 24.02678 | 121.6321 | 0.226 | 40 | | On-fault | |
| 24.02671 | 121.6318 | 0.225 | 50 | | On-fault | |
| 24.02671 | 121.6314 | 0.224 | 63 | | On-fault | |
| 24.02669 | 121.6313 | 0.223 | 24 | | On-fault | |
| 24.02666 | 121.6318 | 0.225 | 87 | | On-fault | |
| 24.01154 | 121.6189 | 0.159 | | 6 | On-fault | |
| 24.01012 | 121.6176 | 0.153 | 25 | | On-fault | |
| 24.00888 | 121.6173 | 0.148 | 15 | | On-fault | |
| 24.00582 | 121.616 | 0.137 | | 6 | On-fault | |
| 24.00161 | 121.6142 | 0.122 | 17 | | On-fault | |
| 24.00107 | 121.614 | 0.12 | 16 | | On-fault | |
| 24.00106 | 121.6139 | 0.12 | 24 | | On-fault | |
| 24.00104 | 121.6139 | 0.12 | 15 | | On-fault | |
| 24.00055 | 121.6138 | 0.118 | | 20 | On-fault | |
| 23.99826 | 121.6133 | 0.11 | 15 | | On-fault | |
| 23.99582 | 121.6118 | 0.101 | 4 | | On-fault | |
| 23.99137 | 121.6105 | 0.085 | 16 | | On-fault | |
| 23.98935 | 121.61 | 0.078 | 4 | 5 | On-fault | |
| 23.98446 | 121.6111 | 0.061 | 9 | | On-fault | |
| 23.98049 | 121.6103 | 0.047 | 20 | | On-fault | |
| 23.97988 | 121.6104 | 0.045 | 11 | | On-fault | |
| 23.975 | 121.61 | 0.028 | 32 | | On-fault | |
| 23.97391 | 121.6096 | 0.025 | 6.4 | | On-fault | |
| 23.96952 | 121.6108 | 0.009 | | 6 | On-fault | |
| 24.027 | 121.6324 | 0.227 | 30 | | On-fault | |
| 24.01045 | 121.6178 | 0.154 | | 10 | On-fault | |
| 24.00333 | 121.6147 | 0.128 | 3 | | On-fault | |
| 23.98857 | 121.6096 | 0.075 | | 35 | On-fault | |
| 23.98847 | 121.6095 | 0.075 | 5 | 7 | On-fault | |
| 23.974 | 121.6099 | 0.025 | 6.5 | | On-fault | |
| 23.97081 | 121.6102 | 0.014 | 8 | | On-fault | |
| 23.9703 | 121.6106 | 0.012 | 14 | | On-fault | |

| | | | | | | |
|---|---|---|---|---|---|---|
| 23.97021 | 121.6106 | 0.012 | | 15 | On-fault | |
| 23.96804 | 121.6117 | 0.003 | 4 | | On-fault | |
| 23.96774 | 121.6115 | 0.003 | 3.5 | | On-fault | |

| | | | | | | |
|---|---|---|---|---|---|---|
| 24.0066 | 121.6157 | 0.123 | 4 | | FW | 0.030544797 |
| 23.99524 | 121.6083 | 0.369 | 3.5 | | FW | 0.305123136 |
| 23.99498 | 121.608 | 0.377 | 3.5 | | FW | 0.318790221 |
| 23.9943 | 121.6107 | 0.154 | 1 | | FW | 0.035897298 |
| 23.99382 | 121.6092 | 0.252 | 10.6 | | FW | 0.169173211 |
| 23.99273 | 121.6086 | 0.267 | 3.5 | | FW | 0.19981665 |
| 23.99134 | 121.6068 | 0.364 | 1 | 0.5 | FW | 0.328852274 |
| 23.99084 | 121.6074 | 0.305 | 2 | | FW | 0.258184555 |
| 23.98998 | 121.5992 | 0.922 | 2 | | FW | 1.04697098 |
| 23.98973 | 121.6096 | 0.107 | 3 | 5 | FW | 0.012209442 |
| 23.9892 | 121.6074 | 0.268 | | 2.5 | FW | 0.213224027 |
| 23.98893 | 121.6074 | 0.261 | | 5 | FW | 0.205597584 |
| 23.98883 | 121.6075 | 0.257 | | 5 | FW | 0.201004733 |
| 23.98881 | 121.6075 | 0.256 | | 2 | FW | 0.200759791 |
| 23.98878 | 121.6075 | 0.255 | | 3 | FW | 0.1994242 |
| 23.98858 | 121.6094 | 0.099 | 6 | 5 | FW | 0.000907348 |
| 23.98807 | 121.6062 | 0.344 | 5 | | FW | 0.336044553 |
| 23.98768 | 121.608 | 0.191 | 6 | 10 | FW | 0.153093881 |
| 23.98727 | 121.6082 | 0.167 | 2 | 2 | FW | 0.135386931 |
| 23.98726 | 121.6083 | 0.158 | 4 | 4 | FW | 0.125374224 |
| 23.98723 | 121.6082 | 0.165 | 2 | 2 | FW | 0.187465144 |
| 23.98723 | 121.6077 | 0.205 | 2 | 2 | FW | 0.13481998 |
| 23.98722 | 121.6083 | 0.161 | 6 | 6 | FW | 0.188588919 |
| 23.98722 | 121.6077 | 0.206 | 10 | 10 | FW | 0.130881715 |
| 23.98721 | 121.6083 | 0.162 | 4 | 4 | FW | 0.133017893 |
| 23.98718 | 121.6083 | 0.155 | 3 | 3 | FW | 0.124240316 |
| 23.98716 | 121.6078 | 0.199 | 6 | | FW | 0.182170277 |
| 23.98715 | 121.6083 | 0.159 | 1.5 | 1.5 | FW | 0.129636445 |
| 23.98714 | 121.6077 | 0.204 | 5 | 5 | FW | 0.189479865 |
| 23.98703 | 121.6084 | 0.149 | 2 | 2 | FW | 0.122674367 |
| 23.98703 | 121.6083 | 0.153 | 1.5 | 1.5 | FW | 0.127648699 |
| 23.98702 | 121.6083 | 0.152 | 2 | 2 | FW | 0.126887577 |
| 23.98701 | 121.6084 | 0.147 | 1 | 1 | FW | 0.120200178 |
| 23.987 | 121.6085 | 0.14 | 5 | 5 | FW | 0.111607307 |
| 23.98694 | 121.6085 | 0.139 | 3 | 3 | FW | 0.113305845 |
| 23.98684 | 121.6079 | 0.184 | 4 | | FW | 0.176146184 |
| 23.98682 | 121.6088 | 0.112 | | 1.5 | FW | 0.093140539 |
| 23.98682 | 121.6088 | 0.116 | 3 | 3 | FW | 0.088486233 |
| 23.98681 | 121.6085 | 0.132 | 3 | 3 | FW | 0.114094292 |
| 23.98677 | 121.6086 | 0.131 | 6 | 6 | FW | 0.113063703 |
| 23.98671 | 121.6086 | 0.126 | 7 | 7 | FW | 0.113886153 |
| 23.98668 | 121.6086 | 0.126 | 5 | 5 | FW | 0.113366516 |
| 23.98647 | 121.6087 | 0.111 | 4 | 4 | FW | 0.110659893 |
| 23.98644 | 121.6088 | 0.105 | 5 | 5 | FW | 0.105485929 |
| 23.98642 | 121.6088 | 0.107 | | 3 | FW | 0.109173242 |
| 23.9863 | 121.6089 | 0.097 | | 6 | FW | 0.105232921 |
| 23.98628 | 121.6089 | 0.095 | | 3 | FW | 0.10426591 |
| 23.98627 | 121.6083 | 0.143 | 10.5 | | FW | 0.163357726 |
| 23.98623 | 121.6087 | 0.108 | 21 | | FW | 0.122327421 |
| 23.98613 | 121.609 | 0.084 | | 2 | FW | 0.100736776 |
| 23.986 | 121.6091 | 0.075 | | 1 | FW | 0.098174635 |
| 23.98574 | 121.6092 | 0.062 | | 2 | FW | 0.099566385 |
| 23.98566 | 121.6093 | 0.057 | | 5 | FW | 0.099421764 |
| 23.98534 | 121.602 | 0.617 | 0.5 | | FW | 0.799037141 |
| 23.98172 | 121.609 | 0.025 | 2 | | FW | 0.138276115 |
| 23.98155 | 121.6091 | 0.014 | 5 | | FW | 0.122804927 |
| 23.98081 | 121.6087 | 0.04 | 4 | | FW | 0.147712581 |

| | | | | | | |
|---|---|---|---|---|---|---|
| 23.98071 | 121.5996 | 0.723 | 0.6 | | FW | 1.065397014 |
| 23.97988 | 121.598 | 0.827 | 2 | | FW | 1.233704023 |
| 23.9797 | 121.6018 | 0.555 | | 1 | FW | 0.847159739 |
| 23.97965 | 121.6011 | 0.607 | 2 | | FW | 0.922829499 |
| 23.9795 | 121.5994 | 0.725 | 0.6 | | FW | 1.092006441 |
| 23.97934 | 121.5977 | 0.836 | 1 | | FW | 1.256025678 |
| 23.97767 | 121.598 | 0.791 | 1 | | FW | 1.214410852 |
| 23.97759 | 121.5981 | 0.783 | 1 | | FW | 1.203583378 |
| 23.97365 | 121.6094 | 0.091 | 9.5 | | FW | 0.003350947 |
| 23.97361 | 121.6093 | 0.083 | 5.4 | | FW | 0.008280591 |
| 23.96965 | 121.5987 | 0.554 | 1.5 | | FW | 1.135739673 |
| 23.96866 | 121.6101 | 0.288 | 1 | | FW | 0.082259642 |
| 23.96806 | 121.6102 | 0.348 | 2.25 | | FW | 0.094073334 |
| 23.96672 | 121.6107 | 0.492 | 4 | | FW | 0.116959696 |
| 23.9663 | 121.6085 | 0.27 | 0.5 | | FW | 0.342041396 |
| 23.96577 | 121.61 | 0.476 | 3 | 1 | FW | 0.230744876 |
| 23.96553 | 121.6098 | 0.474 | 3 | 2 | FW | 0.261003518 |
| 23.96489 | 121.6093 | 0.469 | 2 | | FW | 0.343465641 |
| 23.96343 | 121.6056 | 0.237 | 1.5 | 2.5 | FW | 0.744898687 |
| 23.9633 | 121.6081 | 0.467 | 2 | | FW | 0.557177018 |
| 23.96291 | 121.6064 | 0.341 | 2 | | FW | 0.715427074 |
| 24.02641 | 121.6323 | 0.075 | 7 | | HW | 0.018230588 |
| 24.02405 | 121.6295 | 0.033 | 18 | | HW | 0.101486414 |
| 24.01855 | 121.6296 | 0.524 | | 1 | HW | 0.483769101 |
| 24.01533 | 121.6275 | 0.593 | | 3 | HW | 0.489950187 |
| 24.01149 | 121.62 | 0.09 | | 3 | HW | 0.073984117 |
| 24.01126 | 121.6198 | 0.08 | 1 | 2.5 | HW | 0.067428299 |
| 24.01095 | 121.6195 | 0.068 | 2.5 | | HW | 0.062814082 |
| 24.01069 | 121.6197 | 0.109 | 4 | | HW | 0.100010953 |
| 23.99958 | 121.6232 | 0.955 | 1.5 | | HW | 0.920798742 |
| 23.99239 | 121.6126 | 0.081 | 1 | | HW | 0.164143173 |
| 23.98846 | 121.6099 | 0.058 | 15 | 24 | HW | 0.002246625 |
| 23.98487 | 121.6188 | 1.057 | 1 | | HW | 0.757977739 |
| 23.97691 | 121.6104 | 0.189 | 10 | | HW | 0.005508752 |
| 23.97622 | 121.6121 | 0.404 | 0 | 7 | HW | 0.176775689 |
| 23.97573 | 121.6105 | 0.21 | 0 | 6 | HW | 0.022670095 |
| 23.97436 | 121.6108 | 0.27 | 1.5 | | HW | 0.078574473 |
| 23.9732 | 121.6149 | 0.815 | 9 | | HW | 0.499198523 |
| 23.97195 | 121.6139 | 0.709 | 2 | | HW | 0.360509422 |
| 23.97066 | 121.6118 | 0.451 | 1.5 | | HW | 0.11304225 |
| 23.9703 | 121.6128 | 0.608 | 20.8 | 6 | HW | 0.202285403 |
| 23.96988 | 121.6116 | 0.451 | 1 | 3 | HW | 0.069823368 |
| 23.96812 | 121.6117 | 0.546 | 9 | | HW | 0.00021652 |

*Table 2-7: Final surface rupture dataset compiled for the 2018 Hualien earthquake. The first part represents the principal faulting (on-fault) rupture data, while the second part represents the distributed (off-fault) rupture data (FW: foot wall; HW: hanging wall).*

**Principal faulting:**

The dataset includes a total of 37 PF surface rupture data points: 8 with only horizontal displacement, 27 with only vertical and 2 with both. PEA11 models are used to compare with the 10 data points exhibiting horizontal displacement and the results are shown in Figure 2-10.

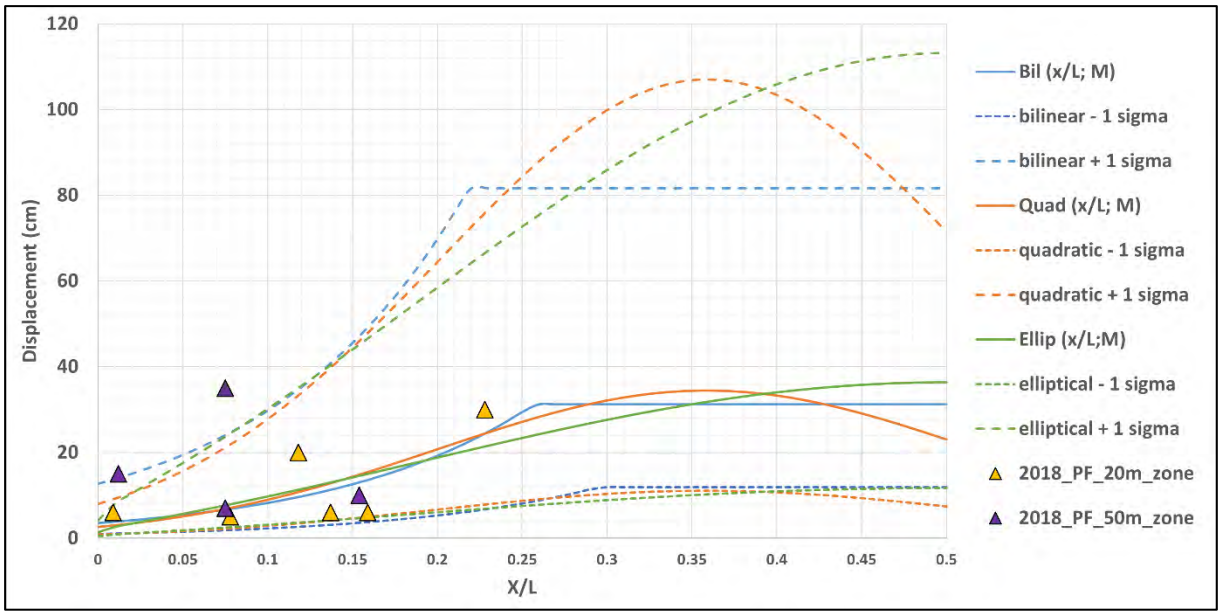



*Figure 2-10: Comparison of the principal horizontal displacement observed along the Milun fault during the 2018 Hualien earthquake with the PEA11 models.*

Most of the principal horizontal displacements observed are within the ± 1 sigma range of the PEA11 regression models (Figure 2-10). Notably, all the data in the smaller 20-m PF zone (yellow in Figure 2-10) better fit to the PEA11 models compared with the few data points added (dark purple) for the 50-m zone, of which two are slightly outside the ± 1 sigma envelope.

For the vertical displacement, the observed AD and MD are 0.21 and 0.87 metres, respectively, while those derived from the MEA24 regressions are 0.58 ± 0.25 and 0.95 ± 0.35 metres (Figure 2-11). The notable difference with the 1951 rupture data is that this time the vertical MD is estimated quite well by MEA24. Conversely, the vertical AD is once again overestimated by MEA24.

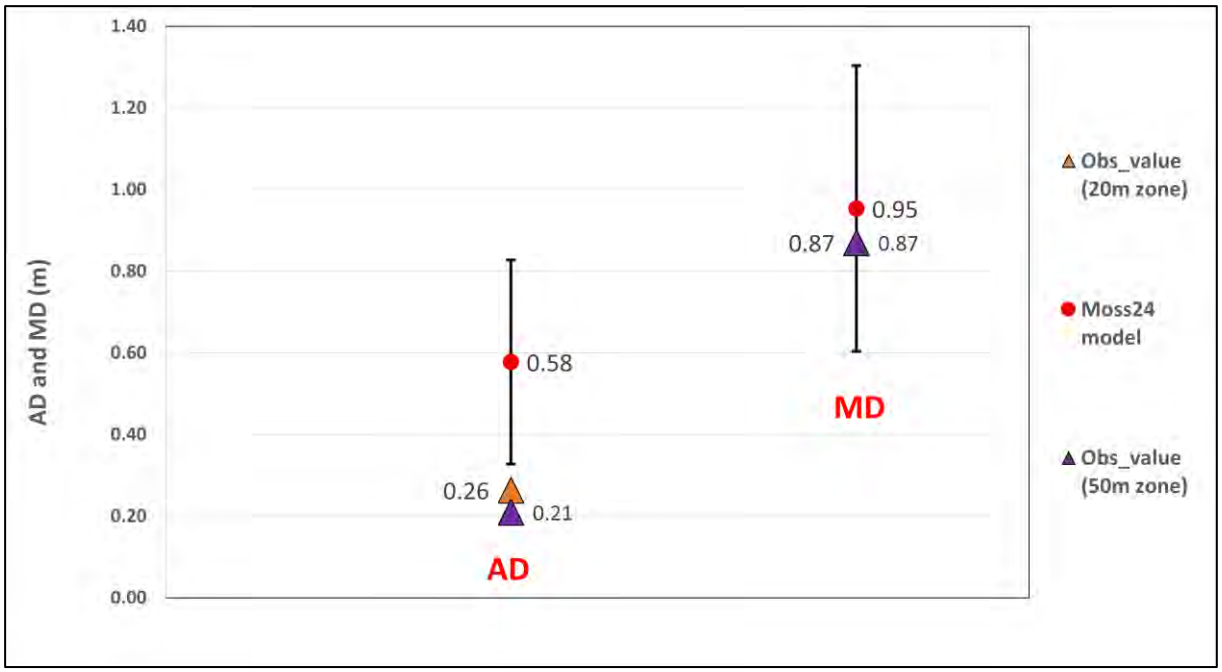



*Figure 2-11: Comparison of the principal vertical displacement observed along the Milun fault during the 2018 Hualien earthquake with AD and MD estimated from MEA24.*

**Distributed faulting:**

For the 2018 Hualien event, 100 distributed rupture data are available, with 78 located on the hanging wall and 22 on the footwall, which is considerably higher than the available data for the 1951 event.

The horizontal displacements, representing the strike-slip motion of the fault system, are compared using PEA11 regressions (Figure 2-12). The D/AD ratio is estimated from the observations using AD derived from the observations (0.21m) and also averaged from multiple empirical relationships (WC94 (SS) and TEA14 (SS) in Table 2-6): 0.32m.

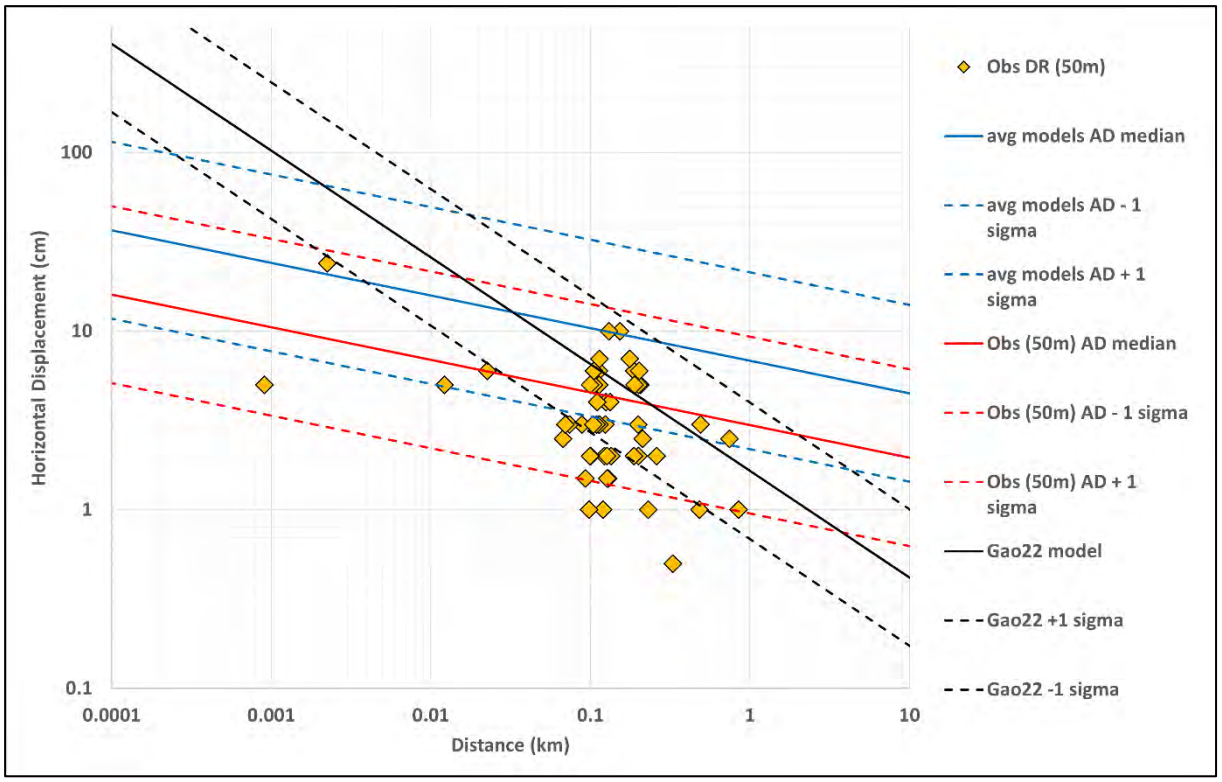



*Figure 2-12: Comparison of the distributed horizontal displacement observed during the 2018 Hualien earthquake with PEA11 model. In red, AD is obtained from the data; in blue using empirical regressions.*

The estimations from the PEA11 with AD calculated from the observed data (in red in Figure 2-12), better fit the DR data compared with the ones derived from the AD averaged from multiple empirical relationships (in blue). Figure 2-12 also shows that the Gao22 model fit quite well with this rupture dataset, which is quite expected since this model is derived from the full rupture dataset of this earthquake, without considering separately the data locations (PF or DR) and the displacement components (vertical and horizontal).

For the vertical displacement, the MEA22 and VEA25 models are used in a similar way than for the 1951 event. For MEA22, the vertical displacement is derived from the D/MD ratio and the MD from MEA24 (0.95m), and for VEA25, it is derived from the AD observed on the PF (0.21m).

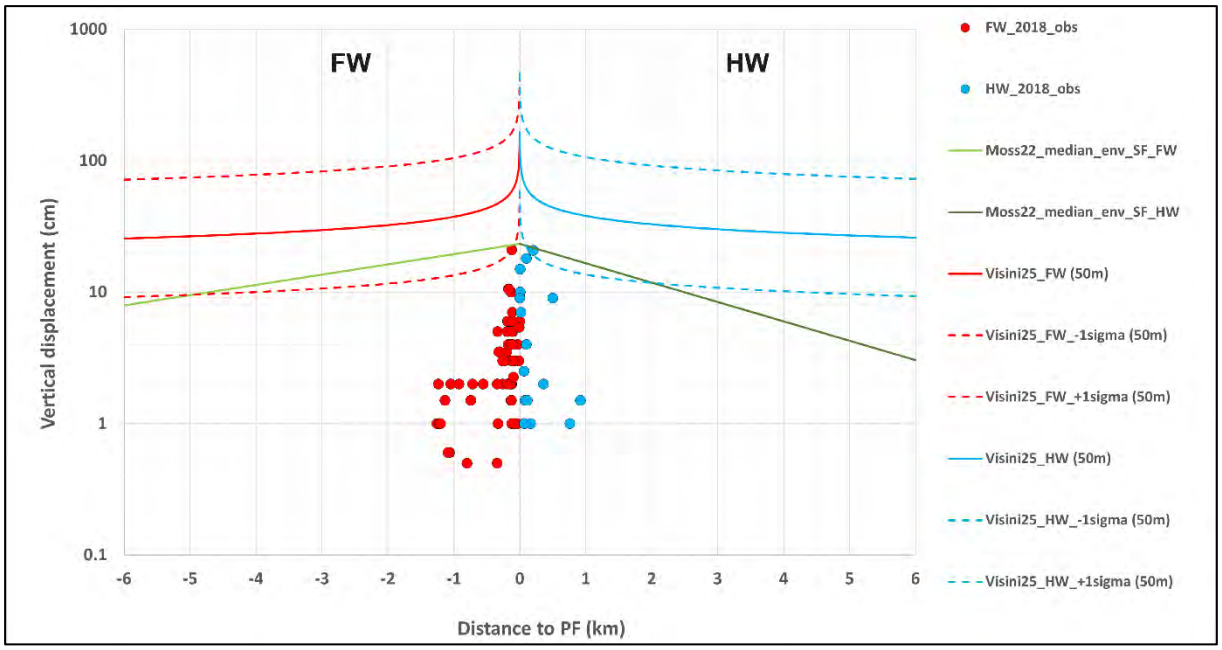



*Figure 2-13: Comparison of the distributed vertical surface displacement observed during the 2018 Hualien earthquake with empirical regressions from MEA22 (Moss22) and VEA25 (Visini25) (HW: hanging wall, FW: foot wall).*

As observed for the principal faulting and for the 1951 event, the modelled displacement with MEA22 and VEA25 are higher than the observed ones (Figure 2-13), meaning that the model overestimates the displacement for such an earthquake. The MEA22 median envelope is quite close to the maximum off-fault displacement observed (30 cm).

### 2.4.5 Brief summary and conclusions of the Hualien successive surface ruptures comparisons

The comparisons between observations of the surface rupture during the 1951 and 2018 Hualien earthquakes reveal some interesting results.

- The 1951 earthquake produced significantly larger surface ruptures than the 2018 event both in terms of spatial distribution and of observed displacement (2 m vs 0.87 m). The higher moment magnitude may be responsible for this difference, although as discussed before, a Mw 7.3 earthquake would be expected to produce a surface rupture exceeding 100 km, which is inconsistent with the one observed at that time, between 8 and 36 km. This suggests that either the Mw 7.3 was overestimated, or that an important part of the rupture may have occurred on a near fault (potentially offshore) and was not reported at that time.

- Horizontal displacements for both events are reasonably well constrained by PEA11, while vertical displacements tend to be overestimated by MEA22, MEA24 and VEA25. This overestimation may reflect the fact that the empirical models relate Mw to a pure dip-slip faulting vertical displacement, whereas the studied events involve oblique kinematics with Mw representing the total seismic moment having only part of the deformation expressed in the vertical component. A similar overestimation would be expected for horizontal displacement if the same bias were present; nevertheless, this is not observed, which may indicate that the rupture is predominantly strike-slip. However, the high uncertainties and the lack of data (< 10), especially for the 1951 event, are a strong limitation and prevent further reliable conclusions.

- Surface rupture traces in 1951 and 2018 on the Milun fault were very similar, with the notable exception of the southern part, where the 1951 rupture followed multiple 'branches' while in 2018 it was confined along a single one. This difference might be linked to the changes in the surface loading associated with the rapid urbanisation of that area over the last decades, but it may also reflect other factors such as variations in fault zone geometry or structural complexity (e.g., fault bending).

## 2.5. Southern LVF Taitung and Chihshang earthquakes

This area is significantly more complex to analyse than the one in the northern part of the LVF, on the Milun fault. Indeed, in 1951, according to Cheng et al. (1996), two consecutive shocks separated by a three-minute interval, ruptured the surface in different fault segments having opposite dipping direction along the LV. The second shock in particular is thought to be associated with the west-dipping Yuli fault, as suggested by its recomputed focal mechanism indicating strike-slip motion. Although the relocation process placed it on the Yuli fault footwall (Figure 2-14), Cheng et al. (1996) acknowledged a wide uncertainty area for their relocation, leaving open the possibility that the second shock was located on the Yuli fault hanging wall.

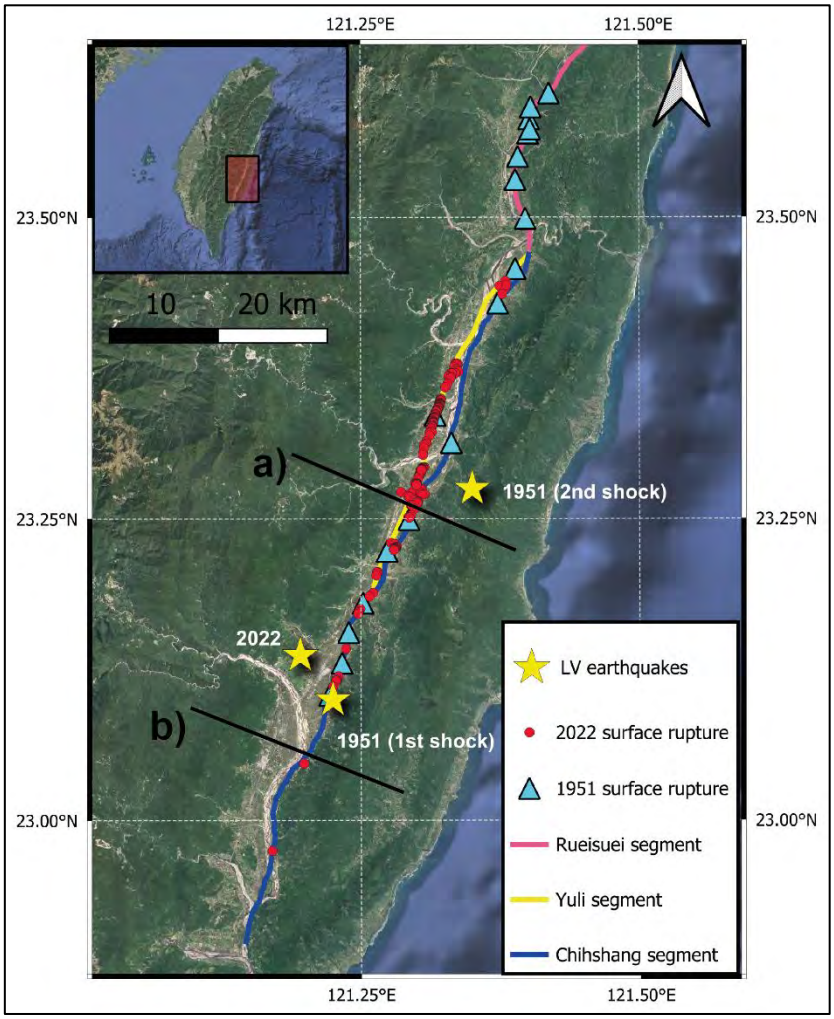



*Figure 2-14: Location of the surface rupture data collected for the 1951 and 2022 earthquakes in the southern part of the LVF. The solid black lines represent the cross-sections of Figure 2-2.*

Surface rupture data for the 1951 events are quite well distributed along the LV. Since two separate shocks are considered, two different rupture traces must also be considered to allow consistent X/L comparison. For that, all the surface rupture data collected, even without

measurements, are considered to create separated ruptures. For the first shock, the rupture trace is essentially running along the Chihshang fault, and its northern tip is close to the southern tip of the Yuli fault. For the second shock, a combined rupture along the Yuli and Rueisuei faults is created, starting from a similar latitude than the northern tip of the first shock rupture and extending north for approximately 38 km (Figure 2-15).

For 2022, the rupture was quite continuous near the Yuli township but north and south of Yuli it was more challenging to follow it. As a single rupture trace is required for the analysis, the rupture is extended to the north up to the Kuokailiang Ridge, where surface rupture was observed but not measured by locals; and to the south, it is extended up to the Chihshang fault, where both faults seem to be connected, and then continue southwards almost until Luye (CGS, 2022). The resulting total rupture trace is approximately 64.6 km long, although it is not continuous along its entire length (Figure 2-15).

### 2.5.1. Rupture location comparisons

As the tectonic context of these sequences is complex, a rupture location comparison is performed using latitude rather than the along-fault (X/L) position to try to observe any kind of surface rupture repartition or distribution along the LV (Figure 2-15 and Figure 2-16). The net displacement presented in this analysis is derived using the fault segment dip angle (Table 2-8).

| ID | H Disp. (cm) | V Disp. (cm) | Net disp. (cm) | X/L | Fault segment | Dip angle | Average dip angle |
|---|---|---|---|---|---|---|---|
| 18 | | 200 | 213 | 0.345 | Chihshang (1st shock) | 42-77E *(Chen and Rau, 2002 - Huang et al., 2025)* 60-75E *(Chen et al., 2024)* | 70°E |
| 22 | 35 | 15 | 38 | 0.052 | | | |
| 23 | | 50 | 53 | 0.12 | | | |
| 24 | | 20 | 21 | 0.334 | | | |
| 10 | | 120 | 170 | 0.037 | Rueisuei (2nd shock) | 40-50E *(CGS, 2022)* | 45°E |
| 11 | 161 | 136 | 251 | 0.276 | | | |
| 13 | | 100 | 141 | 0.123 | | | |
| 15 | 160 | | 160 | 0.374 | | | |
| 19 | | 135 | 191 | 0.092 | | | |
| 20 | | 75 | 106 | 0.158 | | | |
| 21 | | 120 | 170 | 0.147 | | | |
| 25 | | 155 | 219 | 0.219 | | | |
| 16 | 40 | | 40 | 0.082 | Yuli (2nd shock) | 60-72W *(Chen et al., 2024)* | 65°W |

*Table 2-8: Detailed surface rupture data for the 1951 Taitung events.*

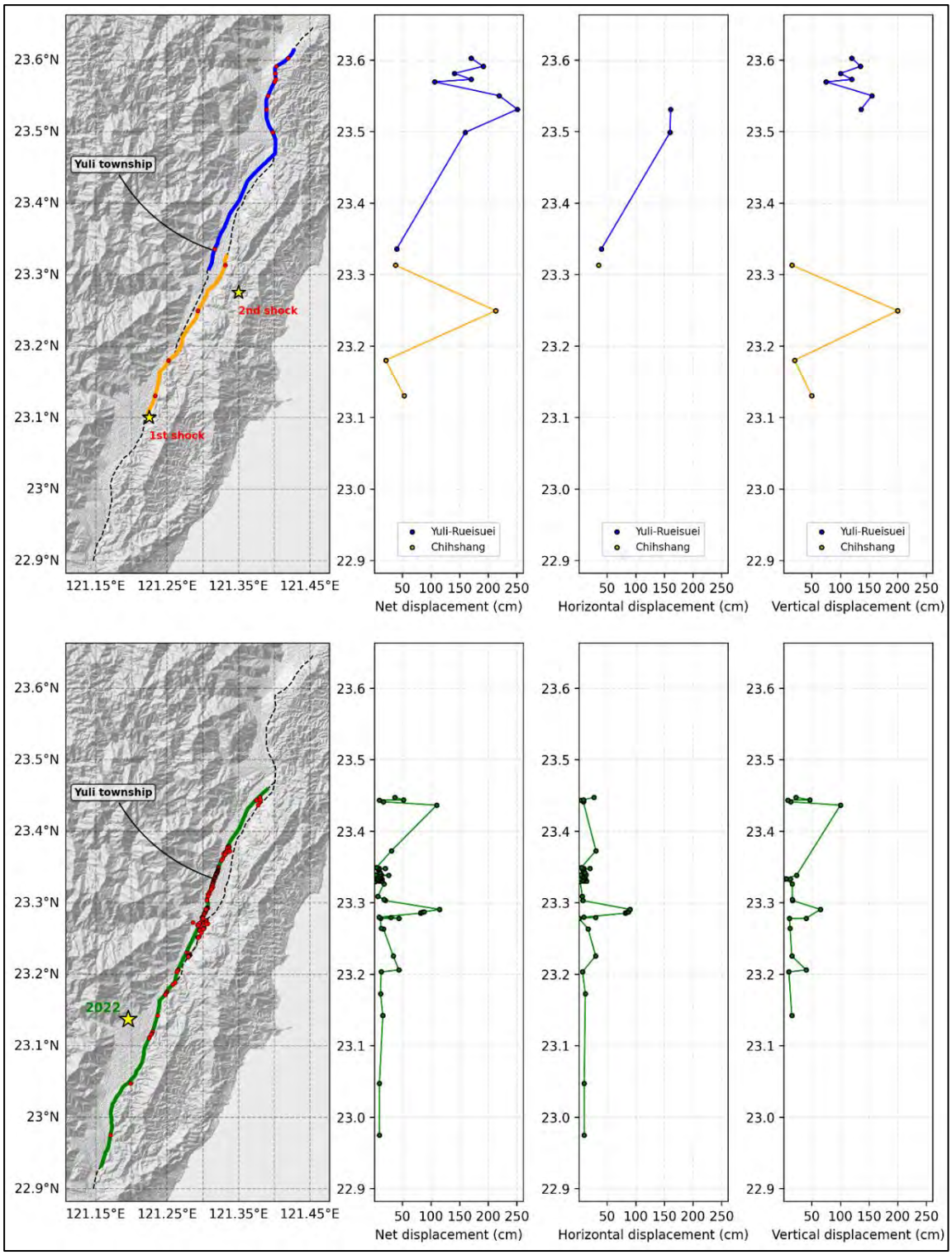



*Figure 2-15: Spatial slip component comparison of the surface ruptures observed during the 1951 and 2022 earthquakes. The upper panels show the 1951 events displacement component comparisons. The lower panels represent the same comparisons for the 2022 earthquake. On the left maps, in blue: Yuli-Rueisuei combined rupture in 1951; in yellow: Chihshang rupture in 1951; in green: Yuli-Chihshang combined rupture in 2022.*

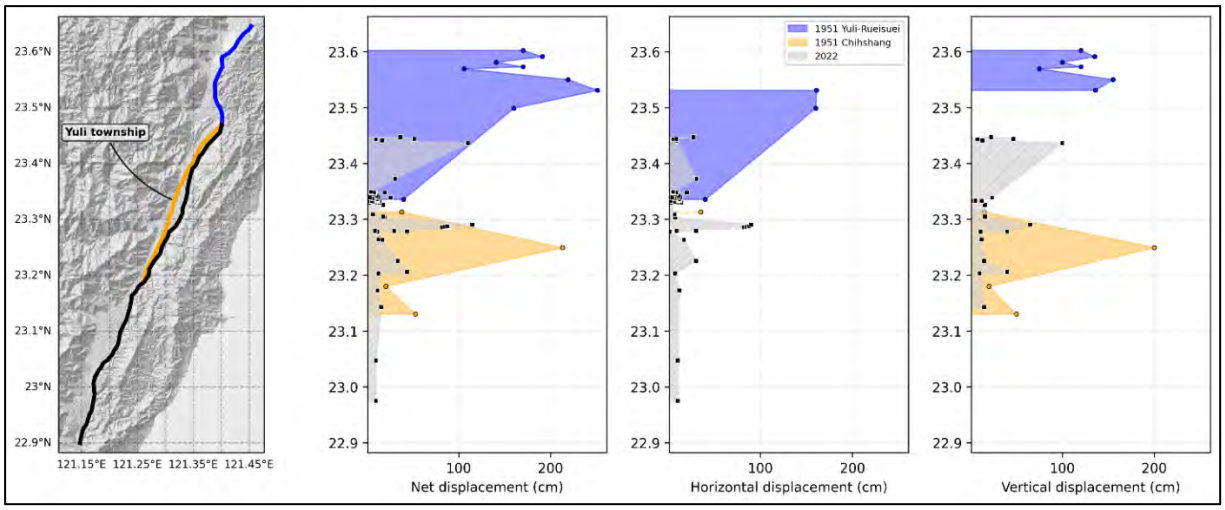



*Figure 2-16: Direct spatial comparison of the observed surface ruptures along the LV during the 1951 and 2022 events. On the map, in black: Chihshang segment; in yellow: Yuli segment; in blue: Rueisuei segment.*

In 1951, the two shocks produced two distinct ruptures (Figure 2-15 and Figure 2-16), on the Chihshang fault and on the combined Yuli and Rueisuei segments. From south to north the displacement distribution vary significantly. On the Chihshang fault, only vertical displacement was observed, indicating a pure reverse motion accommodation. Then, along the Yuli part of the rupture, only horizontal displacement has been observed, explaining the gap on the vertical displacement graph in Figure 2-15 and Figure 2-16, and being consistent with the supposed left-lateral kinematic of this segment. Finally, on the Rueisuei section, both horizontal and vertical displacements were observed, revealing an oblique kinematic.

In 2022, the rupture extended along both the Chihshang and the Yuli faults (Figure 2-15 and Figure 2-16), but this time, not further north, on the Rueisuei fault segment. It is first interesting to remark that despite the earthquake source being located on the CRF, no surface rupture was observed at the epicentral latitude (~ 23.15°N) on any west-dipping faults, but only on the east-dipping Chihshang fault. This may be explained by the fact that the CRF at this location does not reach the surface (Figure 2-2b), but is directly connected with the east-dipping LVF (Chen et al., 2024). The rupture would therefore have propagated along dip and joined the Chihshang fault, and laterally along the CRF, ultimately reaching the surface further north, along the Yuli fault. In terms of displacement component, along the Chihshang segment, where only a few data are available, the horizontal and vertical displacement are comparable (10-30 cm). Along the Yuli fault, similar remarks can be done, with comparable horizontal and vertical displacement distribution and amplitude (5-90 cm for the horizontal and 5-60 for the vertical).

A high vertical displacement peak (0.5-1.0 m) is also observed on the Yuli rupture trace, around

23.45°N. At this location, the surface ruptures were quite continuous but not directly located on the previously mapped main Yuli fault trace. Therefore, even though they are considered as part of the Yuli fault in this analysis, they might actually represent one of the numerous small fault splays linked to either the Yuli or the Chihshang fault. Given the dominant vertical component displacement, a connection to the Chihshang one appears more likely.

Compared with the 1951 displacement, the global displacements recorded in 2022 are smaller, which is consistent with the lower earthquake magnitude (Mw 6.4 vs 7.0).

Finally, the 2022 surface ruptures are compared with the finite fault model proposed by the U.S Geological Survey (USGS, 2022; Figure 2-17). The high displacement values, both horizontal and vertical, correspond well with the shallower high slip values on the fault (indicated by reddish colours). Indeed, the highest slip values (> 3 m) around latitude 23.3°N, which quickly decrease going towards north and south, correctly match the location of the highest observed surface displacements (0.9 m and ~0.6 m for horizontal and vertical displacements, respectively) on the Yuli segment.

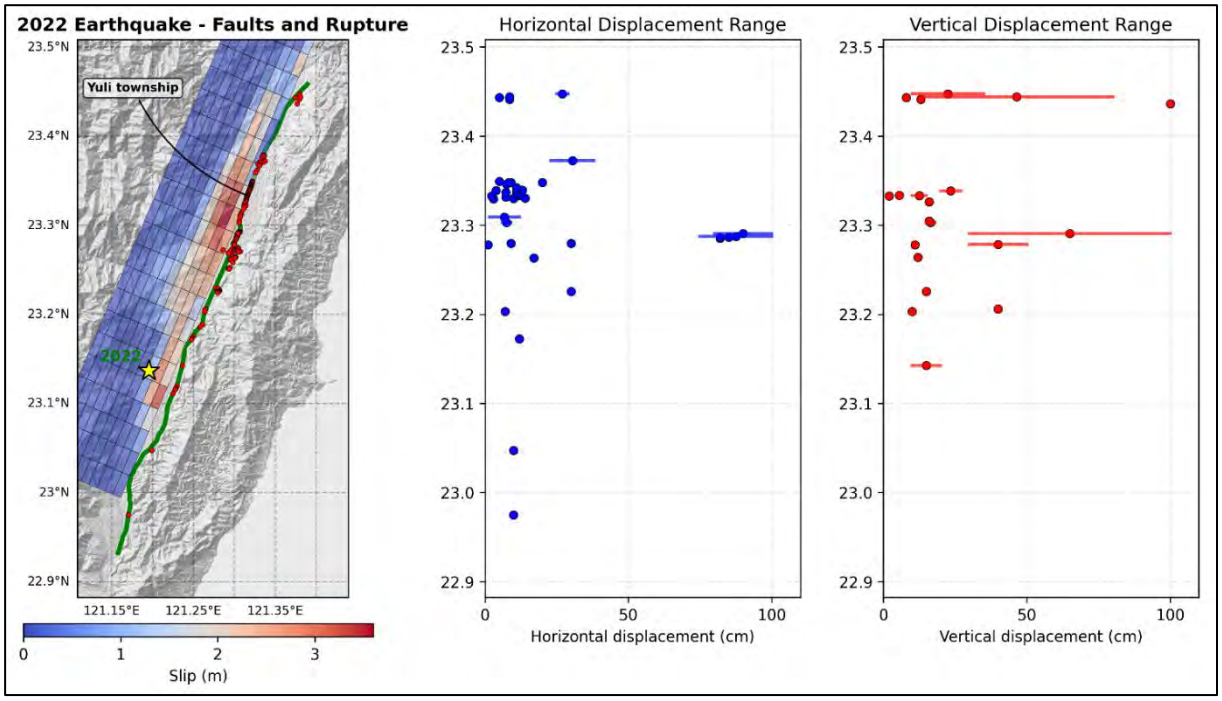



*Figure 2-17: Comparison of the 2022 Chihshang earthquake surface ruptures with a proposed finite fault model (USGS, 2022).*

### 2.5.2. 1951 Mw 6.2 and Mw 7.0 Taitung event displacement amplitude comparison

All surface rupture data collected for the 1951 first and second shocks are actually located on the main rupture trace and are therefore considered as principal rupture data. The X/L values are adjusted here to fit the assumption of symmetry along the fault: X/L = 0.1 or 0.9 is the same, it's symmetric around the theoretical highest displacement at: X/L = 0.5 (Table 2-8).

In the comparison with PEA11 (Figure 2-18), the first shock single rupture data is largely underestimated by the models, while the data for the second shock, on both Yuli and Rueisuei segments, fall within the ± 1 sigma envelope of PEA11.

For the vertical component, observed AD and MD are compared with the one estimated from MEA24 (Figure 2-19). The average displacement AD is quite well estimated by the MEA24 model for both the first and second shock, with respectively 0.71 and 1.15 m against 0.46 ± 0.25 m and 1.02 ± 0.25 m. Conversely, the MD is well constrained for the second shock (1.55 vs 1.67 ± 0.35m), while for the first shock, the maximum observed vertical displacement is much higher than MEA24 estimation, 2.00 ± 0.35 m.

These underestimations may partly reflect uncertainties in the magnitude estimation of the two shocks, given the close temporal occurrence of the two earthquakes and the potential overlap of their seismic records. In addition, the complex rupture characteristics of the event may contribute to differences between the observations and the empirical model predictions.

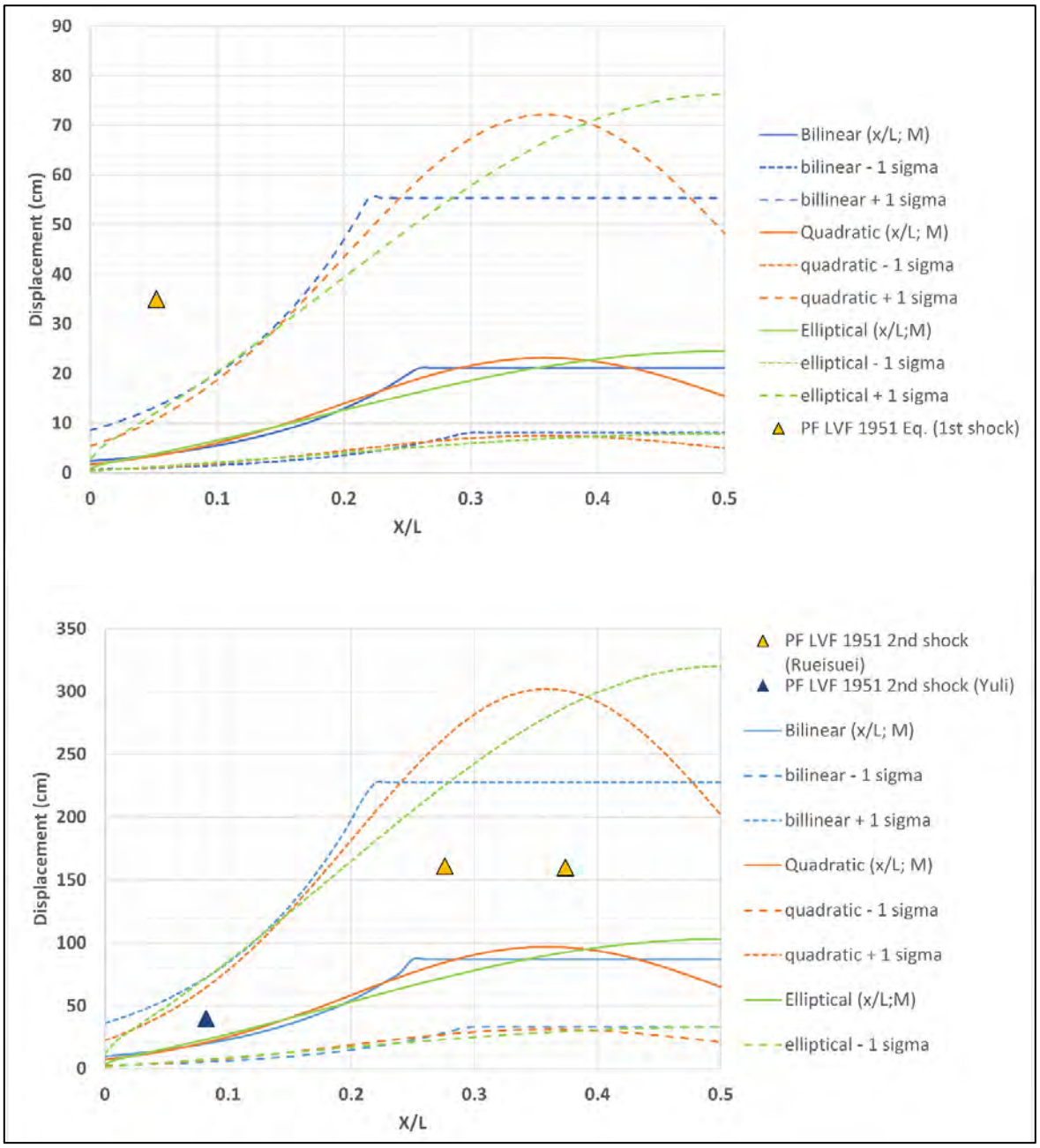



*Figure 2-18: Comparison of the principal horizontal displacement observed along the LV during Taitung 1951 1st shock (top) and 2nd shock (bottom) with the PEA11 models.*

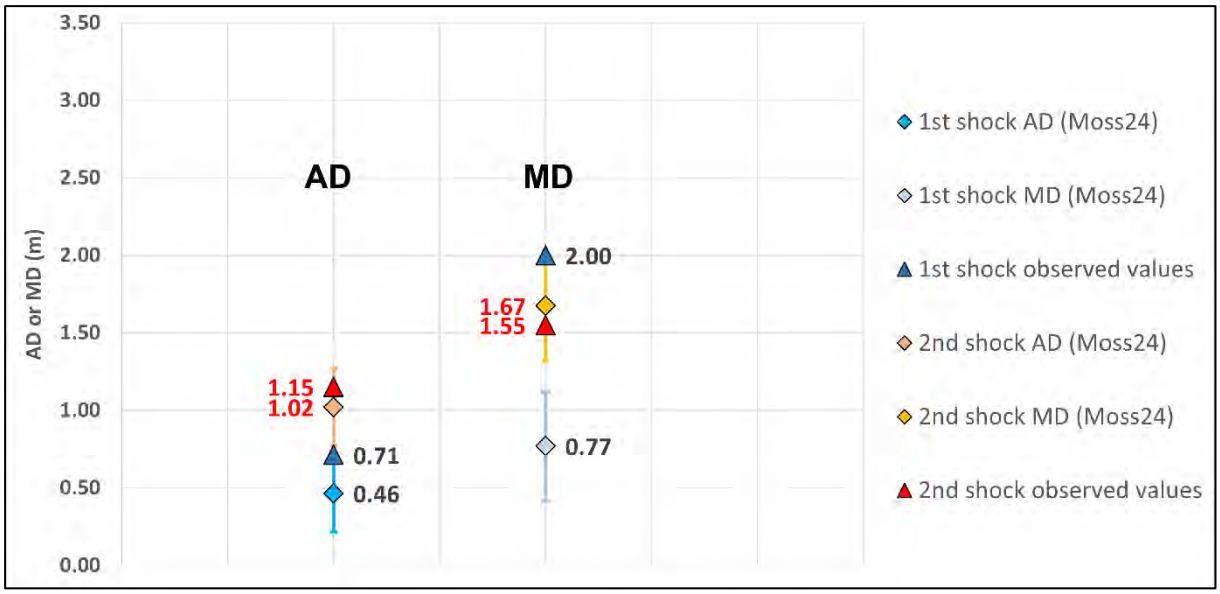



*Figure 2-19: Comparison of the principal vertical displacement observed during the 1951 Taitung earthquakes with the AD and MD estimated with MEA24.*

### 2.5.3. 2022 Mw 7.0 Chihshang event displacement amplitude comparison

In total, 49 surface displacement measurements have been collected by Wang et al. (2024). An important remark, which is not included in this analysis, is that many observations not considered here as not providing proper displacement measurements, such as interviews with local residents, indicated that along the Yuli fault, displacements were predominantly horizontal, while vertical displacements were much more rare and smaller.

The surface rupture data are categorised into PF or DR in a similar way as for the Hualien events (50 m buffer zone) and are assigned with parameters required for the analysis (X/L; distance to the main rupture, foot wall or hanging wall, etc..). In total, the dataset is composed of 38 data (35 on the Yuli fault and 3 on the Chihshang fault) for the PF and 11 for the DR (Table 2-9).

| Latitude | Longitude | Average V disp. (cm) | Average H disp. (cm) | X/L | Fault segment | Dist. To PF (km) | Wall |
|---|---|---|---|---|---|---|---|
| 23.3493 | 121.322 | 0 | 5 | 0.782 | Yuli | | On-fault |
| 23.3481 | 121.3215 | 0 | 8.25 | 0.779 | Yuli | | |
| 23.3479 | 121.3216 | 0 | 9 | 0.779 | Yuli | | |
| 23.3479 | 121.3216 | 0 | 20 | 0.779 | Yuli | | |
| 23.3457 | 121.321 | 0 | 7.5 | 0.775 | Yuli | | |
| 23.3422 | 121.32 | 0 | 11 | 0.769 | Yuli | | |
| 23.3394 | 121.318 | 0 | 13 | 0.762 | Yuli | | |
| 23.3394 | 121.318 | 0 | 11 | 0.762 | Yuli | | |
| 23.339 | 121.318 | 0 | 3.9 | 0.762 | Yuli | | |
| 23.3385 | 121.318 | 23.5 | 0 | 0.761 | Yuli | | |
| 23.3368 | 121.3174 | 0 | 7.3 | 0.758 | Yuli | | |
| 23.3359 | 121.3169 | 0 | 10.9 | 0.756 | Yuli | | |
| 23.3347 | 121.3166 | 0 | 11.1 | 0.754 | Yuli | | |
| 23.3337 | 121.316 | 5.5 | 0 | 0.752 | Yuli | | |
| 23.3334 | 121.3159 | 0 | 12 | 0.751 | Yuli | | |
| 23.3331 | 121.3159 | 12.5 | 0 | 0.751 | Yuli | | |
| 23.333 | 121.3159 | 2 | 2.3 | 0.751 | Yuli | | |
| 23.3316 | 121.315 | 0 | 7.25 | 0.748 | Yuli | | |
| 23.3303 | 121.315 | 0 | 14 | 0.746 | Yuli | | |
| 23.33 | 121.315 | 0 | 10 | 0.745 | Yuli | | |
| 23.3297 | 121.315 | 0 | 3 | 0.745 | Yuli | | |
| 23.3263 | 121.314 | 16 | 0 | 0.738 | Yuli | | |
| 23.3089 | 121.307 | 0 | 6.8 | 0.707 | Yuli | | |
| 23.3045 | 121.306 | 16 | 0 | 0.699 | Yuli | | |
| 23.303 | 121.306 | 16.5 | 7.5 | 0.696 | Yuli | | |
| 23.290542 | 121.304374 | 65 | 90 | 0.673 | Yuli | | |
| 23.2873 | 121.303 | 0 | 87.5 | 0.667 | Yuli | | |
| 23.2866 | 121.303 | 0 | 85 | 0.666 | Yuli | | |
| 23.286 | 121.303 | 0 | 82 | 0.665 | Yuli | | |
| 23.2853 | 121.302 | 0 | 82 | 0.663 | Yuli | | |
| 23.2795 | 121.3 | 0 | 30 | 0.653 | Yuli | | |
| 23.278197 | 121.300104 | 40 | 0 | 0.65 | Yuli | | |
| 23.2779 | 121.3 | 11 | 1 | 0.65 | Yuli | | |
| 23.2059 | 121.2653 | 40 | 0 | 0.515 | Yuli | | |
| 23.2032 | 121.2639 | 10 | 7 | 0.51 | Yuli | | |
| 23.1724 | 121.248 | 0 | 12 | 0.449 | Chihshang | | |
| 23.142438 | 121.2366653 | 15 | 0 | 0.393 | Chihshang | | |
| 22.974881 | 121.1706472 | 0 | 10 | 0.076 | Chihshang | | |
| 23.4472 | 121.38 | 22.5 | 27 | | Yuli | 0.121 | FW |
| 23.4412 | 121.3799 | 13 | 8.5 | | Yuli | 0.569 | FW |
| 23.4432 | 121.3749 | 8 | 5 | | Yuli | 0.045 | FW |
| 23.4439 | 121.381 | 46.5 | 8.5 | | Yuli | 0.446 | FW |
| 23.3727 | 121.3362 | 0 | 30.5 | | Yuli | 0.258 | FW |

| | | | | | | | |
|---|---|---|---|---|---|---|---|
| 23.2797 | 121.299 | 0 | 9 | | Yuli | 0.080 | HW |
| 23.2641 | 121.3015 | 12 | 0 | | Yuli | 0.745 | on-fault (rank 1.5) |
| 23.2633 | 121.3007 | 0 | 17 | | Yuli | 0.706 | on-fault (rank 1.5) |
| 23.2256 | 121.2805 | 15 | 30 | | Yuli | 0.517 | on-fault (rank 1.5) |
| 23.43639 | 121.377197 | 100 | 0 | | Yuli | 0.724 | FW |
| 23.047119 | 121.1990806 | 0 | 10 | | Chihshang | 0.259 | HW (Chihshang) / FW (Yuli) |

*Table 2-9: Compiled dataset of surface rupture measurements of the 2022 Chihshang earthquake. The green cells represent the principal faulting data while the blue ones the distributed faulting ones.*

**Principal faulting:**

Figure 2-20 shows the comparisons with PEA11 models for the observed horizontal displacement. Most of the horizontal rupture data are significantly lower and outside the ± 1 sigma envelope (Figure 2-20), suggesting that PEA11 overestimated the displacement for such earthquake magnitude.

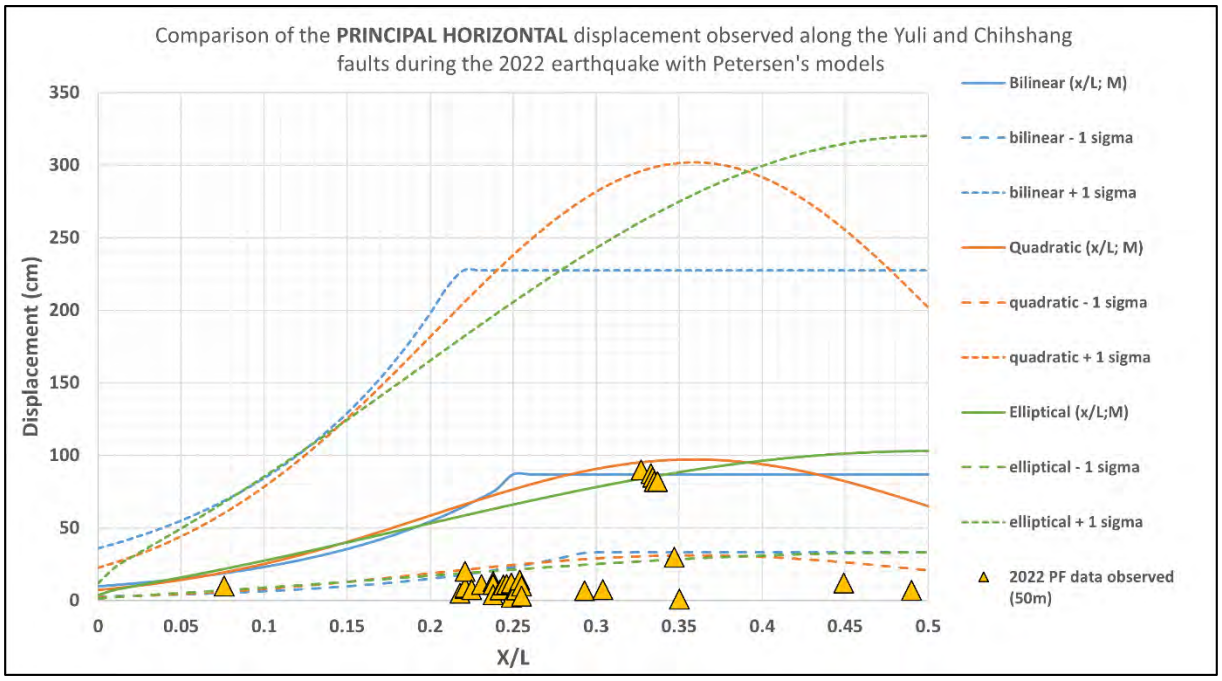



*Figure 2-20: Comparison of the principal horizontal displacement observed along the Yuli and Chihshang faults during the 2022 earthquake with the PEA11 models.*

For the vertical component, the AD and MD obtained with MEA24 for a Mw = 7.0 are, respectively, 1.02 and 1.67 m. These values are substantially larger than the observed AD and MD of 0.21 m and 0.65 m, respectively (Figure 2-21).

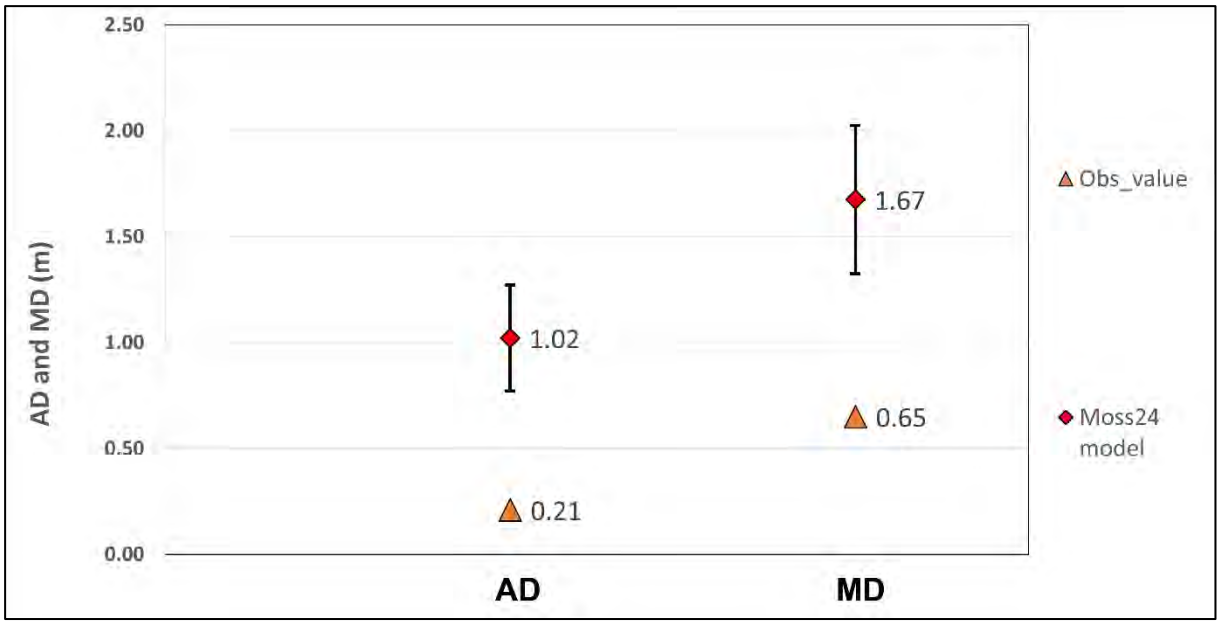



*Figure 2-21: Comparison of the principal vertical displacement observed along the Yuli and Chihshang faults during the 2022 earthquake with the AD and MD estimated with MEA24.*

**Distributed faulting:**

Regarding the distributed faulting during the 2022 Chihshang earthquake, it is also more complex here. Indeed, there are many different types of off-fault SR observations. First, there are some classic DR near the PF but also displacement on the Chihshang fault, in parallel with the Yuli fault (same latitude) (rank 1.5 following the definition of Nurminen et al., 2020). Additionally, since the Yuli and Chihshang faults are not dipping in the same direction, determining the relative position between footwall and hanging wall is quite tricky. Therefore, the Yuli fault is considered as the PF (HW on west and FW on east) until the junction with the Chihshang fault, after which the Chihshang fault is considered as the PF (HW on east and FW on west). At the end, 7 simple DR on the Yuli segment (6 FW and 1 HW), 1 simple DR on the HW of the Chihshang segment and, finally, 3 ‘rank 1.5’ DR on the Chihshang fault but on the Yuli FW, constitute the final dataset (Table 2-9).

The observed distributed horizontal displacement is compared with the one derived from the D/AD ratio estimated using PEA11. The D/AD is ‘de-normalised’ by multiplying with an average AD value obtained from several regressions, and the AD calculated from observations. The averaged AD from models is 0.85 m and the observed one is 0.22 m (different from the one used in the MEA24 model comparison since only the horizontal displacement is relevant here).

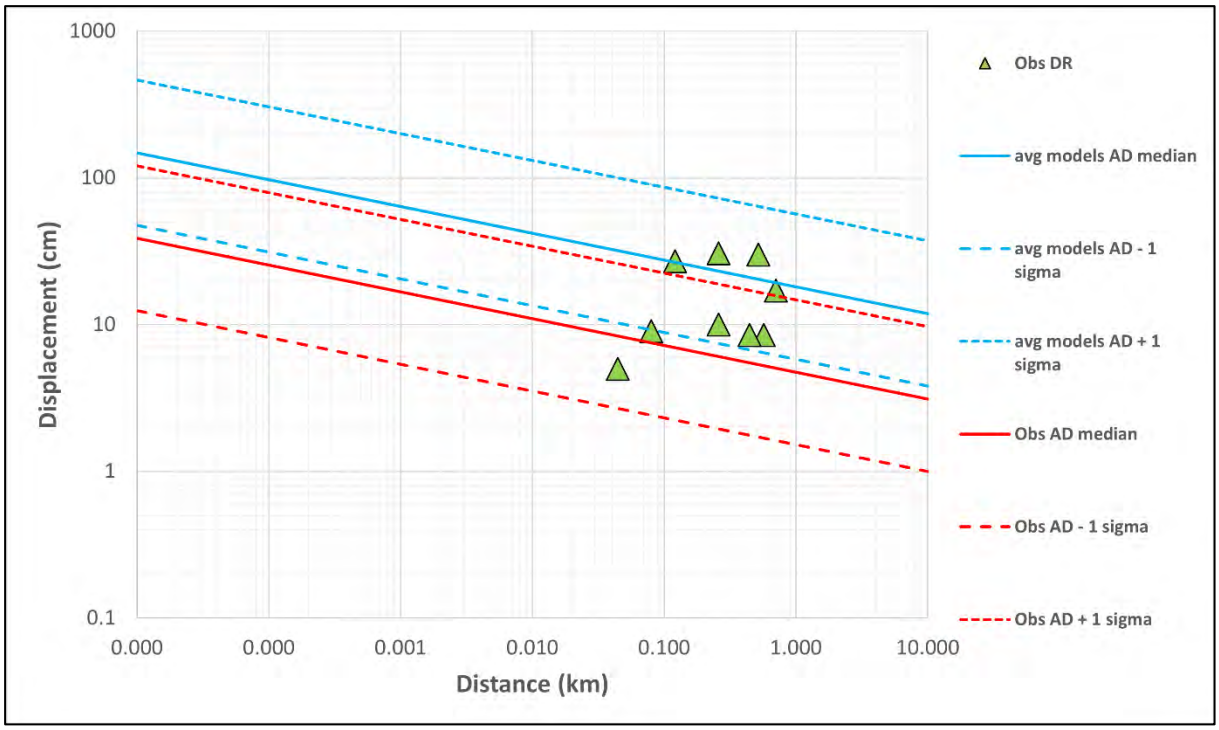



*Figure 2-22: Comparison of the distributed horizontal displacement observed during the 2022 Chihshang earthquake with PEA11 model. In red, AD is obtained from the data; in blue using empirical regressions.*

In Figure 2-22, the data fit better with the model derived AD (blue lines) than with the observed one (red lines). Indeed, 7 out of 9 points are within the ± 1 sigma envelope of the model derived AD, while only 5 out of 9 are within the ± 1 sigma envelope for the observation.

For the distributed vertical displacements, the same kind of comparisons are performed using MEA22 and VEA25 models. The MEA22 model estimates the D/MD ratio, which is then 'de-normalised' using MD value from MEA24 (1.67 m). For the VEA25 model, the simplest 'Combination A', accounting for simple DR relative to PF (rank 2 relative to rank 1) is chosen for 5 of the data points. The 'Combination C', accounting for DR on a pre-existing fault (rank 1.5) relative to the rank 1 main rupture, is considered for the 2 data points on the Chihshang fault (ranked 1.5) in parallel of the PF on Yuli. This specific dataset is presented in Table 2-10 and the analysis results in Figure 2-23.

| Latitude | Longitude | Avg. vert. disp. (cm) | Rank 1 Fault | Dist. to PF (km) | Wall | Rank | VEA25 Combination |
|---|---|---|---|---|---|---|---|
| 23,4472 | 121,38 | 22,5 | Yuli | 0.121 | FW | 2 | A |
| 23,4412 | 121,3799 | 13 | Yuli | 0.5569 | FW | 2 | A |
| 23,4432 | 121,3749 | 8 | Yuli | 0.045 | FW | 2 | A |
| 23,4439 | 121,381 | 46,5 | Yuli | 0.446 | FW | 2 | A |
| 23,2641 | 121,3015 | 12 | Yuli | 0.745 | on-fault (rank 1.5) | 1,5 | C |
| 23,2256 | 121,2805 | 15 | Yuli | 0.517 | on-fault (rank 1.5) | 1,5 | C |
| 23,43639 | 121,377197 | 100 | Yuli | 0.724 | FW | 2 | A |

*Table 2-10: Vertical distributed surface rupture data of the 2022 Chihshang earthquake and their ranking following the new classification from Nurminen et al. (2020).*

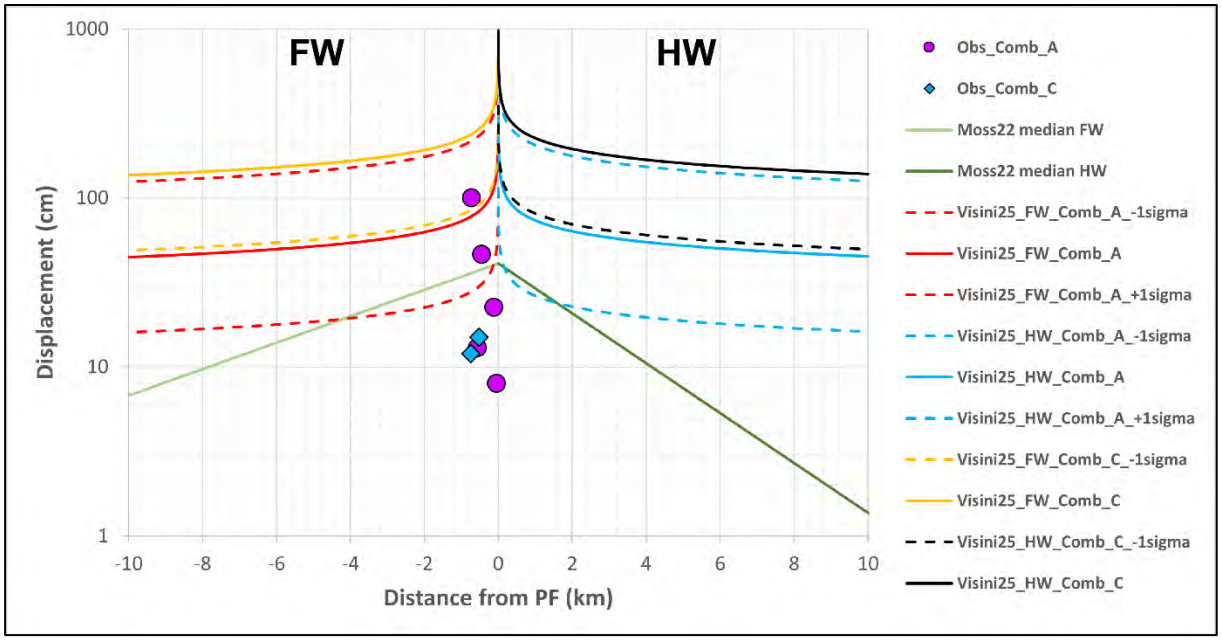



*Figure 2-23: Comparison of the distributed vertical displacement observed during the 2022 Chihshang earthquake with empirical regressions from MEA22 (Moss22) and VEA25 (Visini25) (HW: hanging wall, FW: foot wall).*

Comparisons are showing that the MEA22 model fit quite well the data. Conversely, VEA25 model is overestimating the vertical displacement for Combination C data types. For Combination A, two of the five observed data fall within the ± 1 sigma envelope indicating a decent estimation.

### 2.5.4. Brief summary and conclusions of the south LV successive rupture analysis

- The surface ruptures did not occur exactly at the same locations in both episodes. In 1951, it was distributed along the Chihshang, Yuli and Rueisuei segments, for a total length of ~70 km, whereas in 2022 the SR was observed only on the Yuli and Chihshang fault segments, for a comparable total length of ~ 65 km. This difference is explained by the varying epicentral location of the 1951 and the 2022 events along the LV, which largely control which fault segment slipped and where the surface ruptured.

- Considering only the measured displacement data: the Chihshang, Yuli and Rueisuei segments seem to all accommodate both vertical and horizontal displacements on the LV. However, considering also the non-measurements observations (interviews with locals from Wang et al., 2024) the horizontal displacement on the Yuli fault was dominant, supporting the idea that Yuli fault is mostly accommodating the strike-slip motion in the LV area.

- Comparisons with empirical models show a large variability in prediction accuracy for these specific surface rupturing earthquakes. The 1951 events are quite well constrained by the model tested ( PEA11 and MEA24), although the uncertainty associated with the magnitude estimates of the consecutive shocks represents an important limitation. Conversely, for the 2022 event, the on-fault displacements are largely overestimated while the off-fault are reasonably well estimated.

## 2.6. Conclusions

This Chapter examined two rare cases of documented recurrent surface ruptures on the same fault system, providing a unique opportunity to assess the repeatability of surface rupturing earthquakes and to test the predictive capacity of existing PFDHA empirical models.

On the Milun fault, the two rupturing episodes of 1951 and 2018 display broadly similar behaviour, with comparable surface rupture traces and displacements of the same order of magnitude. However, notable differences are present, particularly where the rupture geometry in the southern part of Hualien city changed from a multi-branch pattern in 1951 to a single trace in 2018, potentially reflecting the influence of urbanisation-related surface loading or other factors such as variations in fault zone geometry or structural complexity (e.g., fault

bending) on rupture surface expression.

On the southern part of the LVF, the 1951 and 2022 events activated several fault segments, which are organised and connected in a complex manner. The ruptures, whose extent was primarily controlled by the epicentral location, propagated along segments dipping in opposite directions (Yuli-Rueisuei in 1951 and Chihshang-Yuli in 2022). Displacement data suggest that these segments of the LVF accommodate both vertical and horizontal motion, with a dominant vertical component on the Chihshang and Rueisuei segments, and a dominant left-lateral component on the Yuli fault.

Most of the differences observed between the two rupturing episodes in 1951 and 2018-2022 can likely be explained either by the natural variability of the phenomenon (epicentral location, magnitude) or by independent changes in the environment (urbanisation-related surface loading, structural complexity of the fault system architecture in Hualien).

Comparisons with empirical models, performed at the displacement component level, showed contrasting results and may reflect the limitations of globally derived models when applied to specific tectonic contexts. Overall, the PEA11 model estimated well the lateral motion observed in the LV while the other models for the reverse faulting motion (MEA22, MEA24 and VEA25) tend to overestimate this vertical displacement component. This overestimation highlights the limitation of comparing displacement components independently in oblique-slip events, where the total rupture displacement is partitioned between vertical and horizontal components.

However, the large uncertainties on the data location, especially for the 1951 earthquakes, the faults relationships, combined with the complex fault relationships ,and their implications for data classification (PF vs. DR, HW vs. FW), significantly affect the robustness of these results. This case study highlights the limitations of current PFDHA models when applied to complex fault systems involving oblique kinematics and potential multi-fault ruptures. For future PFDHA applications in this area, a better understanding of the tectonic context and fault interactions will be essential to define reliable input parameters and improve the robustness of fault displacement hazard assessments.

# 3. PFDHA application to the northern Calabria region, Italy

This chapter is a more detailed version of the paper '*Probabilistic Fault Displacement Hazard in northern Calabria (Italy): Exploring Epistemic Uncertainty and Model Components in PFDHA Mapping'* currently submitted to the journal Bulletin of Earthquake Engineering.

## 3.1. Introduction

The Calabrian Arc forms part of a complex orogenic system resulting from long-term convergence between the African–Adria and Eurasian plates (Malinverno & Ryan, 1986; Gueguen et al., 1998; Faccenna et al., 2001). It lies between the NW-SE-trending Apennines to the north and the E-W-trending Sicilian–Maghrebian chain to the south-west and is influenced by the subduction of the Ionian lithosphere beneath the Tyrrhenian Basin at a rate of approximately 5 mm/yr (Devoti et al., 2008; Carafa et al., 2015; Prada et al., 2020). Slab retreat and rollback of the Ionian plate drive the south-eastward migration of the Calabrian Arc, opening the Tyrrhenian back-arc basin and producing a complex tectonic regime of extension and transtension (Cifelli et al., 2007; Handy et al., 2010).

The crustal architecture of the area is characterised by a crystalline basement overlain by Mesozoic–Cenozoic sedimentary deposits and by Neogene–Quaternary basins developed syn- and post-orogenesis, such as the Crati and Crotone basins. Ongoing deformation is mainly localised along NW–SE and NNW–SSE-trending fault systems with normal to oblique-normal kinematics, which play a key role in the development of these intramontane basins (Tansi et al., 2007; Brozzetti et al., 2017b). Although this tectonic framework is generally accepted, the relative roles of extensional and strike-slip components remain contentious (Ferranti et al., 2009).

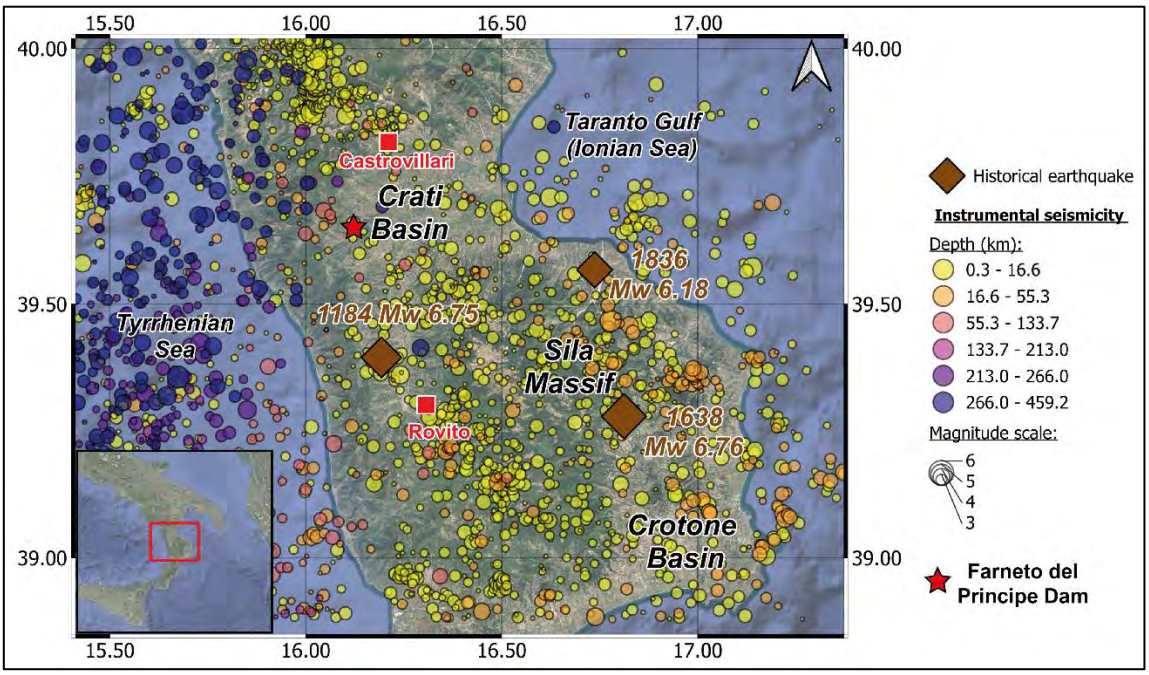



*Figure 3-1: Seismicity map of the study area, in Calabria region, Italy (inset map). The instrumental earthquakes (coloured circles) are taken from the ISIDe Working Group (2007), (M ≥ 2.5; 1980-2025); the main historical events (brown rhombs) taken from CPTI15 (Rovida et al., 2020) are labelled by date and magnitude. By red squares two specific locations we investigated.*

The Crati Basin (also referred to as the Crati Valley), the main feature of northern Calabria, is bounded by the Pollino range to the north, the Catena Costiera to the west, and the Sila Massif to the southeast, and represents a key example of basin formation within this deformational regime. In terms of seismic activity, this area has recorded some of the strongest events in Italian history (Figure 3-1), such as the 1184 Mw 6.75 Crati Valley earthquake, the 1638 Mw 6.76 earthquake, and the 1836 Mw 6.18 earthquake (Rovida et al., 2025). Seismicity is characterised by generally low long-term rates punctuated by episodic activity, such as the 2010–2014 Pollino swarm and its main shock of Mw 5.1 (Totaro et al., 2015; Cheloni et al., 2017; Pastori et al., 2021), highlighting the presence of active faults capable of generating significant deformation. Additionally, the Italian Seismic Hazard Map indicates very high seismic hazard levels for the area, with PGA values of 0.200–0.275 g (10% exceedance probability in 50 years), placing it among the most hazardous regions in Italy (Stucchi et al., 2011).

This Chapter presents a comprehensive PFDHA study for northern Calabria, including and detailing all the steps required to obtain the final hazard curves and hazard maps. The methodology follows the same workflow as the classic PSHA (Cornell, 1968) as shown earlier. This study is initially part of a private project for the Farneto del Principe dam near the

Roggiano-Gravina municipality, in northern Calabria. The Firmo Fault, located just beneath the dam footprint, is reported in the Italian database of capable faults (ITHACA) and may therefore represent a potential hazard for the structure. This ~16 km-long fault is characterised by normal kinematics, although its existence and activity remain debated. The aim of the original project was to investigate this fault through fieldwork (trenching, geophysical surveys, etc.) and to perform a PFDHA analysis for the dam site. However, in this work, the study area has been enlarged to allow a regional-scale fault displacement analysis, and the results presented here are therefore representative of this broader scale. Nevertheless, the methodology still requires starting from the dam vicinity, in particular to assess whether a fault is present beneath or close to the site. However, in this work the study area has been enlarged in order to perform a regional-scale fault displacement analysis and the results presented here are therefore representative of this broader scale. Nevertheless, the methodology applied implies to start by exploring the vicinity of the dam, more particularly by confirming or not the existence of the Firmo fault beneath or close to the dam, and to identify the other faults present in the surrounding area.

## 3.2. Local earthquake relocation

Before performing a PFDH analysis, it is necessary to examine the regional seismicity in order to have a first order understanding of the seismic source distribution in the area and to identify any potential seismic activity related to the Firmo fault. Starting from the ISIDe catalogue (ISIDe Working group, 2007), the area exhibits mainly two types of earthquakes: (i) shallow, small-to-moderate earthquakes affecting the crustal domain of the entire region; and (ii) deeper earthquakes, associated with the subduction of the Ionian slab beneath the Calabrian Arc, particularly in the western sector of the area of interest (Figure 3-1).

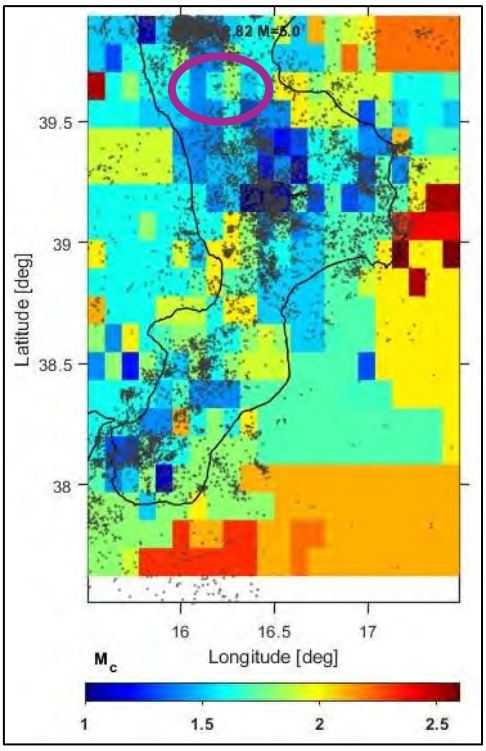



*Figure 3-2: Magnitude of completeness of the ISIDe catalogue. The area of interest is represented by the purple ellipse.*

The magnitude of completeness (Mc) of the ISIDe catalogue (Figure 3-2) in the study area is relatively high (Mc ~ 2) compared to other regions in Italy and northern Calabria, which may reflect either data limitation or a natural seismic gap. The quite sparse seismic network in the area (Figure 3-3), consisting of only a few stations from the INGV network, likely contributed to this high Mc. Moreover, most of these stations have been deployed recently, after 2019 (Figure 3-3), suggesting that older events, particularly of low magnitude, may have not always been recorded.

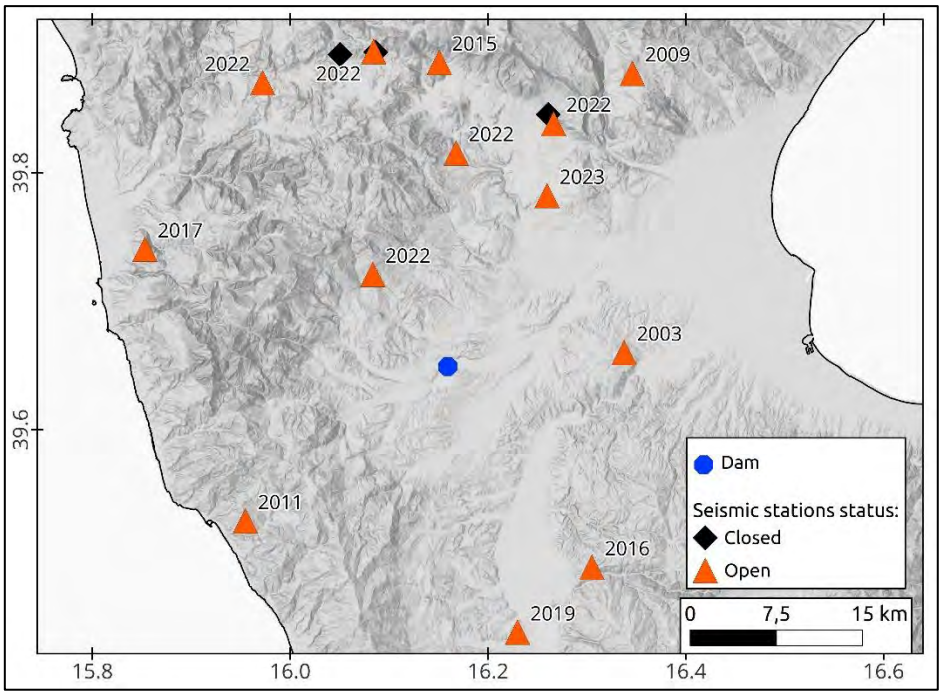



*Figure 3-3: Seismic network around the Farneto dam in 2023, in northern Calabria.*

The first step of the analysis consisted of compiling a comprehensive seismic dataset for the study area, using multiple catalogues: the INGV ISIDe catalogue, and the University of Calabria (UniCAL). The initial area of interest was defined as a 20 km radius circular area around the Farneto dam (Figure 3-4) and the hypocentral depth was limited to the upper 15 km in order to exclude deep events related to the subduction zone, in the Tyrrhenian sea. In total, more than 500 events were collected (Figure 3-4a) using the ISIDe and UniCAL catalogues, with some events being present in both but having different location and magnitude. Given the variations in the seismic information across catalogues and the local scale of the study, a harmonisation procedure was required to obtain the most accurate location as possible for each event and to discard events having a poorly constrained location. Waveform data for all selected events were therefore retrieved using the FDSN web service of the European Integrated Data Archive (EIDA), a distributed infrastructure operated within ORFEUS (Observatories and Research Facilities for European Seismology). The dataset includes seismic records provided by the Istituto Nazionale di Geofisica e Vulcanologia (INGV), primarily from the Italian IV seismic network (INGV; 2005). Data retrieval and preprocessing were carried out using the ObsPy Python framework (Beyreuther et al., 2010). Additional waveform data were provided by the University of Calabria through its regional seismic network.

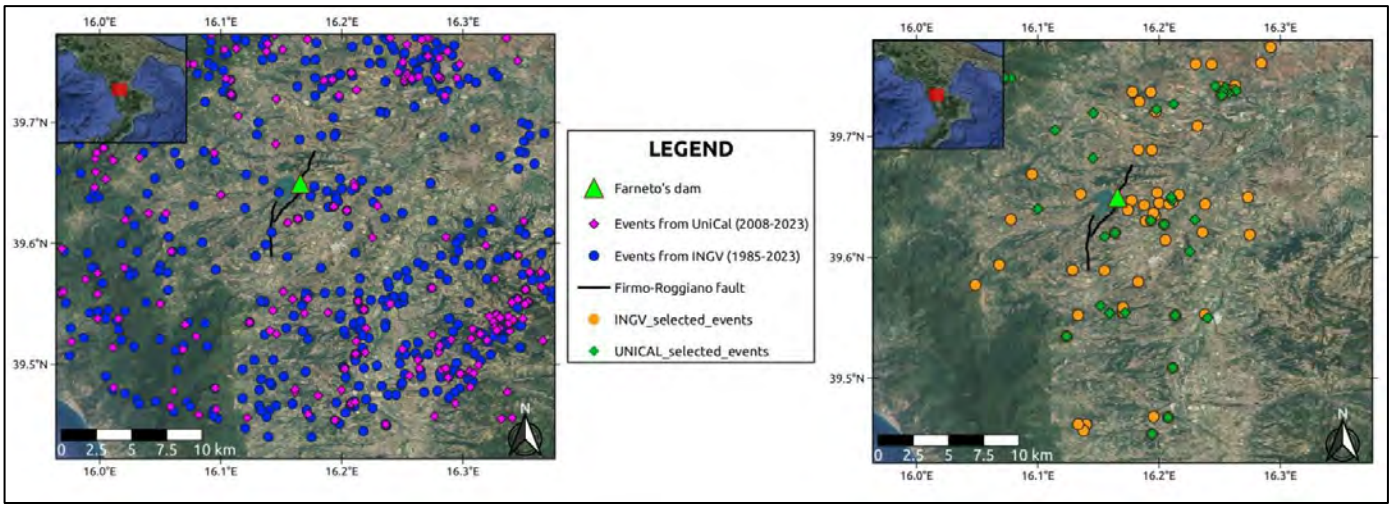



*Figure 3-4: Earthquake data collection around the Farneto dam. a) All events in the 20 km study area. b) All events for which waveforms could be found.*

In total, waveforms were successfully collected for 62 events occurring between January 2008 to December 2023 (Figure 3-4b). In details, 28 events were exclusively recorded by INGV while 34 were recorded either by both networks or by UniCAL but then automatically incorporated inside the ISIDe catalogue (so having the same information). Differences in event locations between the INGV and UniCAL catalogues are clearly visible in Figure 3-4b, as not all orange (INGV) and green (UniCAL) symbols overlap.

All waveforms, for each event and seismic station, were reanalysed using the SEISGRAM2K software (Lomax, 2004). The P- and S- phases, along with their polarity, were picked, when possible, in order to perform a uniform relocation and obtain a more homogeneous final dataset. The solutions were then relocated using the Hypo71 program (Lee and Lahr, 1972). A total of nine earthquakes were relocated outside the initial area of interest and were therefore excluded from the final dataset. On the cross-sections AB and A'B' in Figure 3-5, an additional depth cut was applied at 15 km to be consistent with the initial earthquake selection, reducing the dataset to 42 events. These cross-sections do not reveal any clear spatial earthquake organisation or clustering of earthquakes that could be potentially associated with or aligned along the Firmo fault plane.

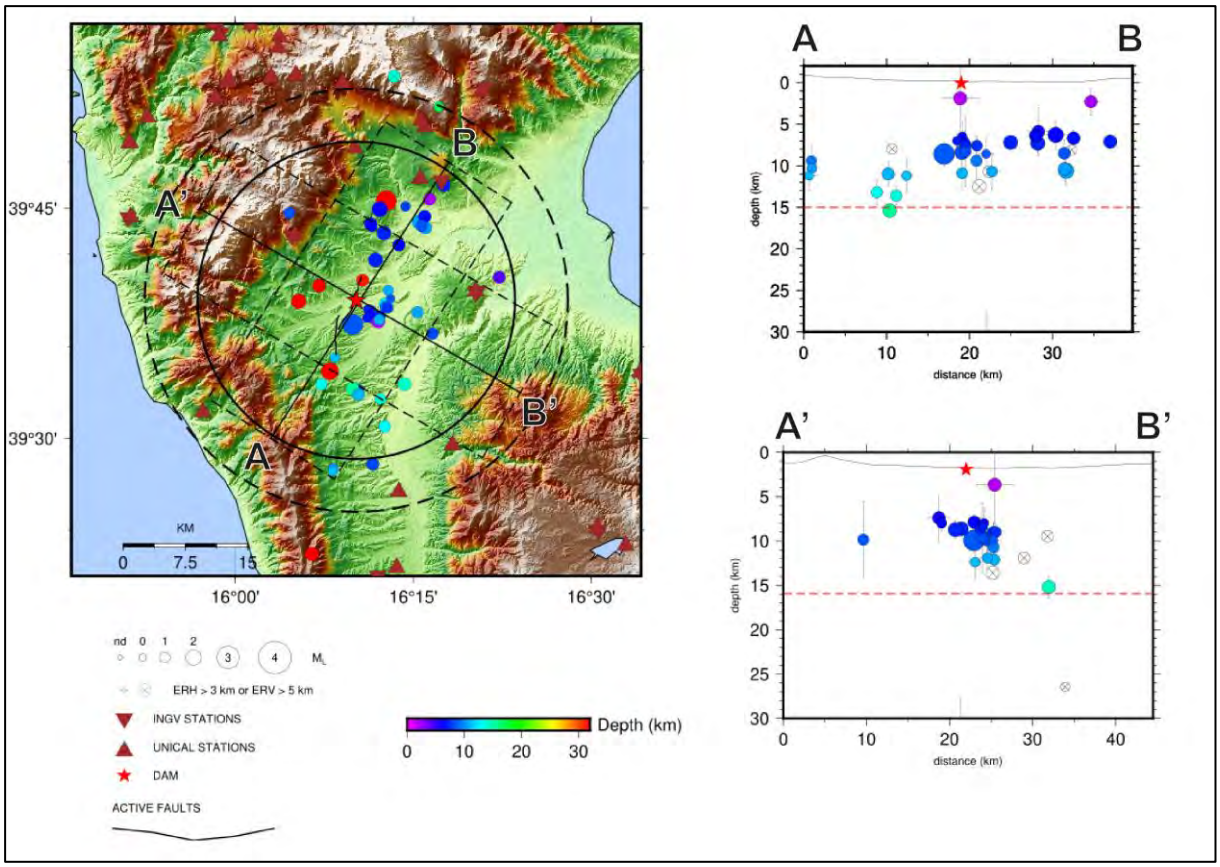



*Figure 3-5: Relocated dataset using Hypo71 software.*

Finally, the Gutenberg–Richter law was evaluated using the ZMAP MATLAB-based software package (Wiemer et al., 2001; version ZMAP7), with this final constrained dataset of 42 events (Figure 3-6). The magnitude of completeness is estimated at Mc = 1.2, while the resulting b-value is approximately $1.39 \pm 0.20$, which is significantly higher than the classic reference value (~1.0). This elevated b-value likely reflects limitations in the seismic dataset rather than tectonic variability, including the incomplete recording of lower-magnitude events. This interpretation is supported by two factors previously mentioned: the relatively high magnitude of completeness of the ISIDe catalogue and the limited seismic station coverage in the area, both of which contribute to reduced detection capability and catalogue incompleteness.

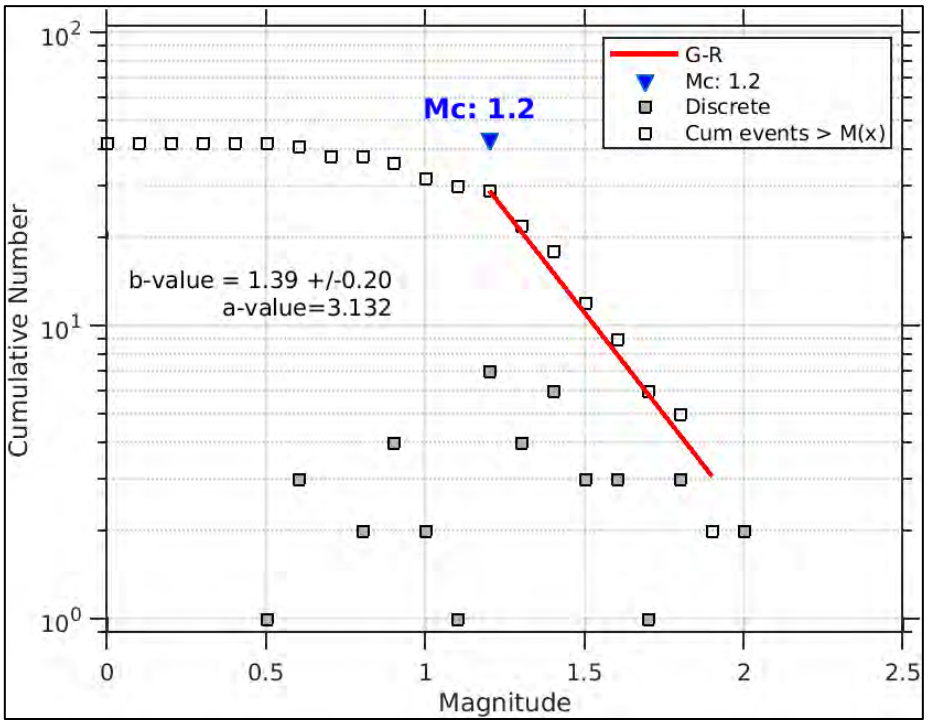



*Figure 3-6: Gutenberg-Richter law computed from the 42 events of the relocated events dataset.*

The seismic analysis alone does not provide clear evidence regarding the presence or activity of the Firmo fault beneath the Farneto dam. However, multidisciplinary investigations conducted in the vicinity of the dam, such as electrical resistivity tomography (ERT) and palaeoseismological trenching, have confirmed the existence of this fault (further details are provided in the following section). With the presence of the fault now confirmed, which is a key factor for surface fault displacement hazard assessment, it is now possible to proceed with the PFDH analysis.

## 3.3. Refining the seismotectonic model in northern Calabria

As mentioned in section 1.2.1.1., defining the seismotectonic model for the area of interest is the first step in PSHA and PFDHA approaches. Having a thorough understanding of the presence of active and capable faults in the area is essential for reliably assessing the hazard.

In northern Calabria, numerous faults associated with the geological structures of the Pollino Range, the Crati Valley, and the Sila Massif have been investigated to varying degrees in the literature. However, interpretations of these structures differ among authors, and several sources remain debated. In the following section, the main interpretations and working hypotheses proposed in previous studies are summarised, in order to develop a new synthetic tectonic model, starting with a critical review of the Italian database of active and/or capable faults.

All active and capable faults, as well as sources potentially able to generate moderate to strong earthquakes (M > 5.5) within a broad area of northern Calabria (approximately a 50 km radius), are described. For each structure, a compilation and homogenisation of the available geological, geomorphological, geophysical, and paleoseismological information is done to constrain key seismotectonic parameters, including fault geometry, dip angle, kinematics and slip rate.

### 3.3.1. Seismogenic sources review

The DISS database (Database of Individual Seismogenic Sources, Basili et al., 2008, 2025) provides valuable information on seismogenic sources at the national scale. In northern Calabria, five sources are potentially capable of generating earthquakes with a magnitude greater than 5.5. From north to south, these are the Rimendiello-Mormanno (ITCS038; Figure 3-7a; n° 1), the Pollino (ITCS033; Figure 3-7a; n° 2), the Amendolara (ITCS041; Figure 3-7a; n° 3), the Crati Valley (ITCS015; Figure 3-7a; n° 4), and the Cecita source (ITCS176; Figure 3-7a; n° 5). These are composite sources, modelled mainly using regional literature data; with the exception of the Amendolara source, they include several individual sources (ISS, shown in yellow in Figure 3-7a) identified from historical events or recognised through palaeoseismology. There are also other sources, indicated as debated sources (DSS, shown in purple in Figure 3-7a), which are found in the literature but are considered insufficiently reliable to be included in the other categories.

The ITHACA database (ITaly HAzard from CApable faults, ITHACA Working Group, 2019), created and managed by ISPRA (*Istituto Superiore per la Protezione e la Ricerca Ambientale*), is the database of active and capable, or potentially capable, faults in Italy. Many of these capable faults are found in northern Calabria and the Crati Valley (Figure 3-7b), which represent a significant concern and a potential risk to several strategic sites and cities in the area. There are some similarities with the DISS catalogue, as some sources are present in the same areas: Pollino and Castrovillari, San Sosti, Crati Valley faults, Rossano area, and Sila Massif. However, there are still many discrepancies and many more individual sources than in the DISS catalogue.

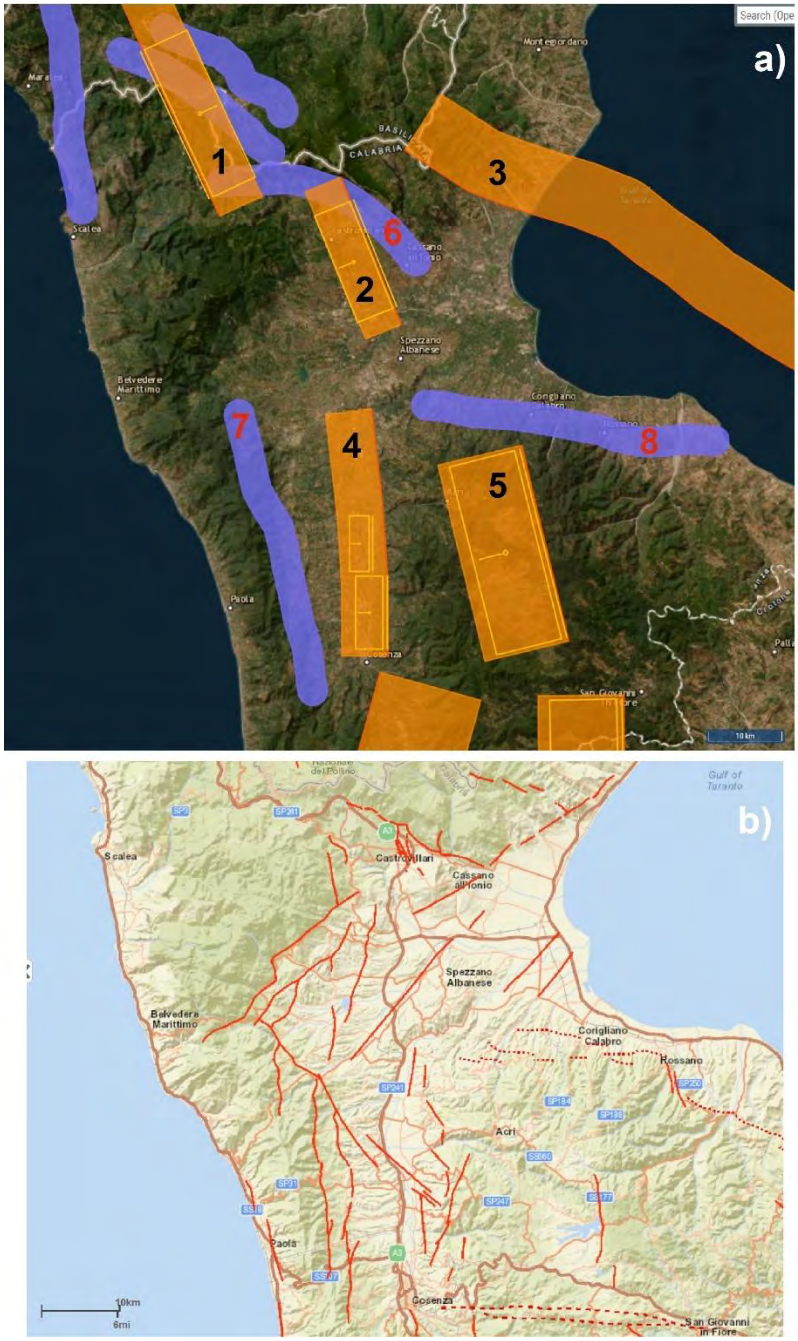



*Figure 3-7: Seismogenic sources and capable faults in northern Calabria. a) Seismogenic sources from the DISS database (Basili et al., 2008; DISS Working Group, 2025), with: 1- Rimendiello-Mormanno (ITCS038); 2- Pollino (ITCS033); 3- Amendolara (ITCS041); 4- Crati Valley (ITCS015); 5- Cecita lake (ITCS176). In purple, the debated sources, with: 6- Pollino (ITDS009); 7- Catena Costiera (ITDS030); 8- Rossano (ITDS028). b) Capable faults from ITHACA (ITHACA Working Group, 2019).*

This situation, in which divergent seismogenic sources are identified, is quite common in Italy and highlights the importance of critically considering all sources, studies conducted, and data available online and in the published literature to better understand and assess the seismic hazard of an area. In the following section, the available data in the literature for each fault system are described, from north to south.

### *Pollino - Castrovillari*

The Pollino chain is located north of the Sibari plains and has been very active recently (2010–2014 seismic swarm (Totaro et al., 2015; Cirillo et al., 2022; De Gori et al., 2022). This area contains faults with opposing dips, towards the east and west such as the Rimendiello-Mormanno fault (DISS n°1; Figure 3-7a), while the Pollino fault dips to the south (DISS n°6 on Figure 3-7a; Figure 3-8). Within this tectonically complex framework, the Pollino Fault Zone (PFZ) represents the main WNW–ESE-trending structure separating the Pollino massif to the north from the Castrovillari basin to the south. It has sometimes been considered a single structure (Papanikolaou and Roberts, 2007), but most authors regard it as segmented. For example, Ferranti et al. (2019) consider it to comprise two main segments (western and eastern Pollino faults). The QUIN 2.0 database (Lavecchia et al., 2024) also provides structural data for this system, identifying three distinct segments: Eastern Pollino, Western Pollino, and Cozzo Vardo–Cozzo Nisco (CVN), from east to west. The total length of the fault zone is approximately 30 km (10 km + 13 km + 10 km for the three segments), with an overall dip angle of 50–65° SSW and a direction varying from N120 in the east to N80 in the west. Brozzetti et al. (2017a) present similar data for these faults, although they do not distinguish between the eastern and western Pollino segments. In their study, the CVN is characterised by a variable direction (80–120°N depending on the site) and an inclination of around 50–70°, dipping southwards. Additionally, Ferranti et al. (2019) provides slip rate data calculated from speleoseismic evidence, around 0.4-0.6 mm/yr.

It is generally accepted that this fault zone was active as a strike-slip fault during the Pliocene–Pleistocene, but its recent activity is debated in the literature. Some authors (Cinti et al., 2002) believe that the Pollino fault is no longer active and that deformation is now accommodated by the Castrovillari/Frascineto faults (see below). Others (Michetti et al., 1997) consider the Pollino fault to remain active, with nearby faults regarded as minor faults whose activity is still linked to that of the Pollino fault.

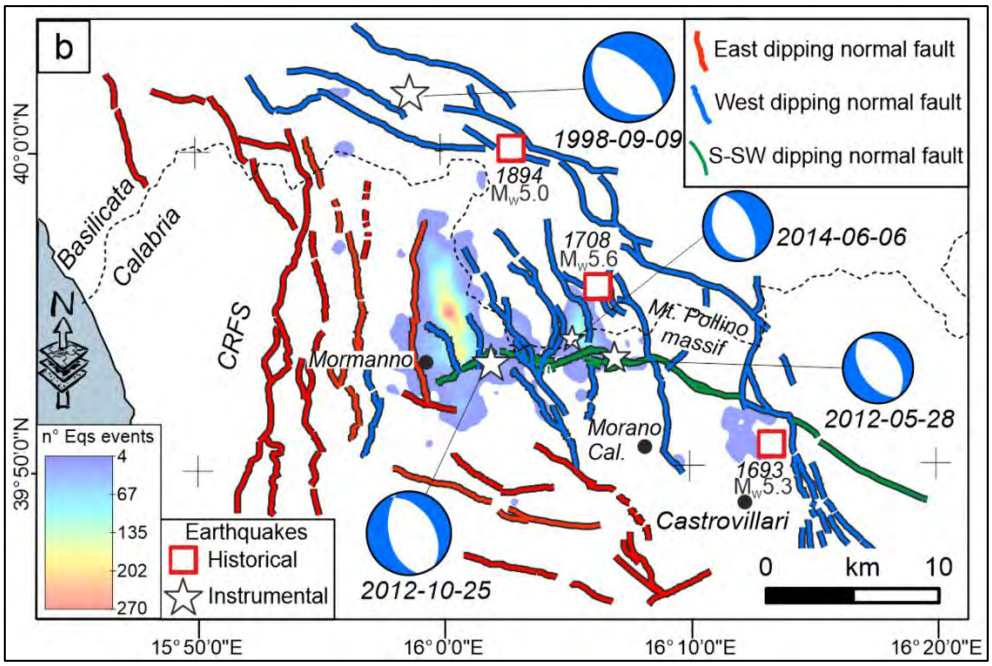



*Figure 3-8: Faults in the Pollino chain (from Cirillo et al., 2022; Figure 1b). The PFZ is shown in green.*

South of the Pollino range, the Castrovillari normal fault system trends NW–SE and is structurally connected to the Pollino Fault Zone. This system broadly corresponds to the Castrovillari individual source (DISS n°2 in Figure 3-7a) and is included within the composite source ITCS033, named "Pollino", highlighting the complexity and ongoing debate surrounding fault geometries in this area. It consists of several NW–SE–striking normal faults with a mean orientation of about 150° (Figure 3-9) and a cumulative length of 13–20 km (Cinti et al., 2002). Detailed investigations of fault scarps south of this system, at the Rocchino site, were carried out by Cinti et al. (2015) using GPR, ERT, and trenching. At this locality, the scarps dip toward the southwest at angles of 70–80°. Trench analyses indicate a slip per event of approximately 0.6 m and a slip rate of approximately 0.6 mm/yr. These values are consistent with those reported by Cinti et al. (2002), who estimated slip per event between 0.5 and 1.6 m and a vertical slip rate of about 0.2–0.5 mm/yr (with a maximum of 1 mm/yr). Cinti et al. (2002) also conducted radiocarbon dating on samples collected from paleoseismological trenches. The most recent earthquake occurred between 530 AD and 1100 AD, but there is no record of this event in the Italian catalogue of historical earthquakes (Rovida et al., 2025).

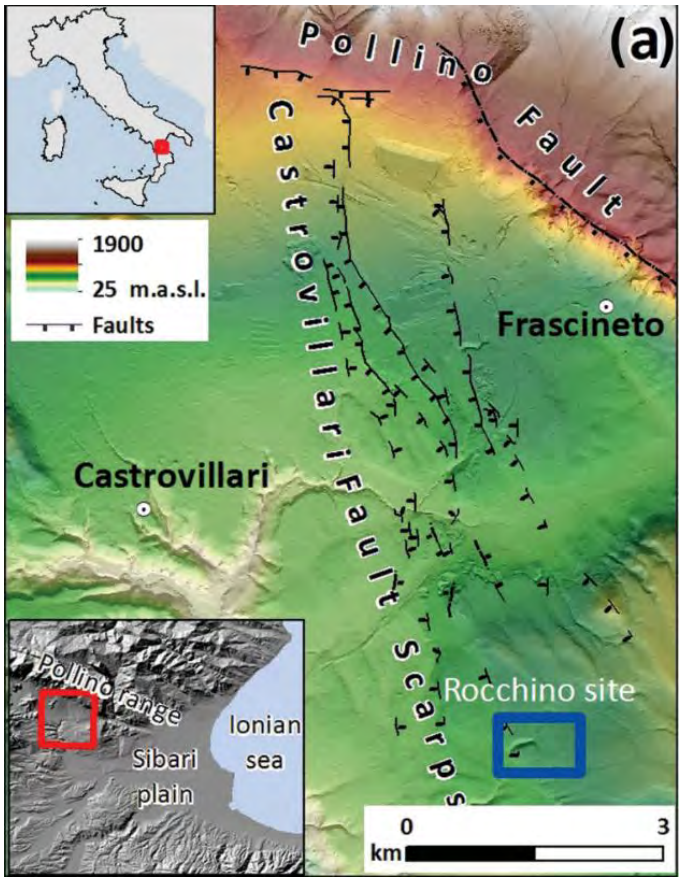



*Figure 3-9: Castrovillari fault system (from Cinti et al., 2015; Figure 1a)*

## *Sibari*

The Sibari Fault Zone (SFZ) is located within the Sibari Plain (Figure 3-10) and intersects the archaeological site of Sybaris. This fault system was recently identified and characterised by Cinti et al. (2024). It extends from the Ionian Sea to Terranova da Sibari over a length of approximately 18 km, strikes roughly NE–SW, and displays normal to right-oblique kinematics (Cinti et al., 2024). Fault activity is indicated by morphological evidence and anomalies in the drainage network. The archaeological site of Sibari is also affected, with some structures showing damage. The only precise information on the fault comes from this archaeological site, where the fault strikes approximately 45–60°N. No clear data are available for the dip angle, but ERT sections and some field observations suggest a sub-vertical or vertical fault. Based on the age and measured movements of the marine terraces in the area, estimated slip rates are 0.05–0.18 mm/year for the vertical component and 0.41–0.72 mm/year for the right-lateral component. According to Cinti et al., 2024, the last earthquake on this fault occurred around 1300–1100 years B.P., with an average recurrence time of approximately 700–1000 years. Indicators and parameters for this fault zone are summarised in Figure 3-10.

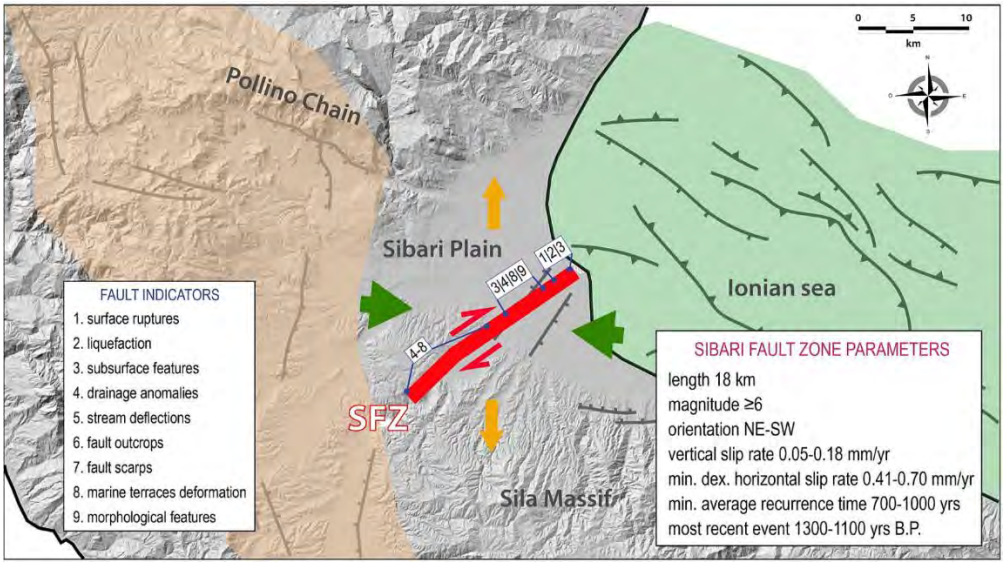



*Figure 3-10: Sibari Fault Zone (from Cinti et al., 2024; Figure 18)*

## *Amendolara*

According to Ferranti et al. (2014), the Amendolara fault system located offshore from Sibari, near the Calabrian coast of the Gulf of Taranto, likely represents the eastern continuation of the PFZ. It is divided into three main segments, from north-west to south-east, named the Valsinni, Amendolara, and Cariati segments, respectively VS, AS and CS in Figure 3-11. These segments are 11.3, 17.5, and 18 km long, respectively (values used in their numerical modelling, based on bathymetry and stratigraphy), and have been defined using offshore seismic methods. Fault geometry was reconstructed through modelling, which indicates a consistent NW–SE strike (~120°N). Amendolara and Cariati segments have a dip angle of approximately 45°NE and 45°SW for the Valsinni segment. Ferranti et al. (2014) interpreted these structures as oblique-reverse faults associated with the collision between the Apennine chain and the Calabrian arc. Using a simplified approach based on sediment-layer growth and associated age constraints, they estimated slip rates of approximately 0.5 mm/yr for the Amendolara and Cariati segments.

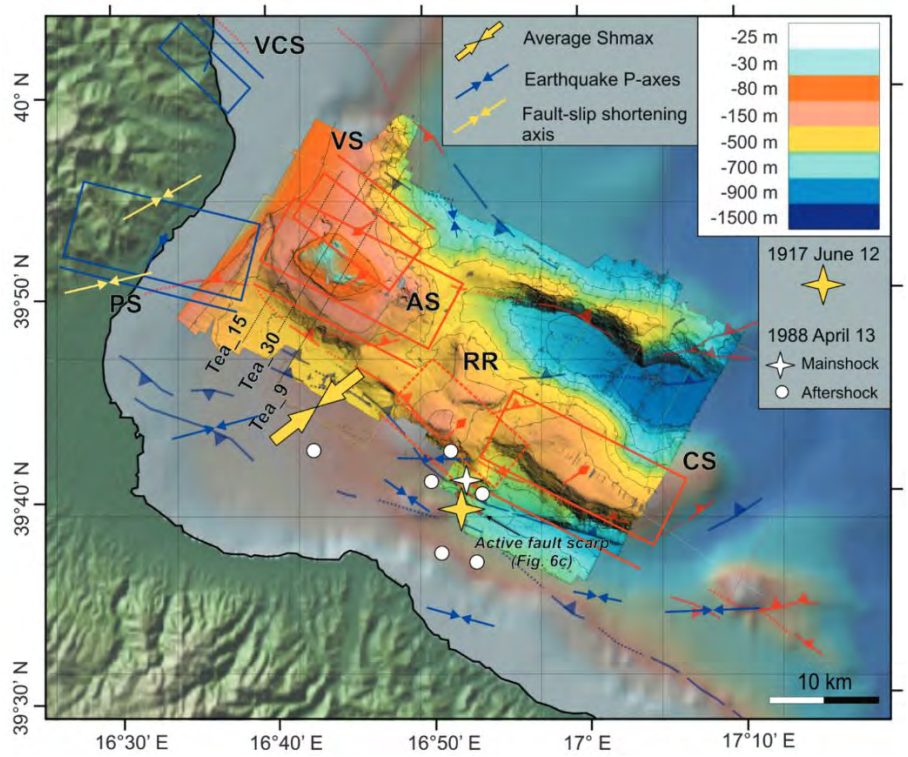



*Figure 3-11: Tectonic map of the Amendolara ridge, in the Gulf of Taranto. Amendolara fault system proposed by Ferranti et al., 2014; with AS: Amendolara segment; VS: Valsinni segment; CS: Cariati segment.*

## *San Sosti - Altomonte*

As shown in the ITHACA database (Figure 3-7b), southwest of the Pollino chain, several parallel normal fault segments with an NNE–SSW orientation and SE dip separate the Crati Basin from the Coastal Chain (Figure 3-12). In the DISS database, no seismogenic source is present in this area. These segments can be considered two different fault systems. The first, the westernmost, consists of the two fault segments San Sosti (SSF) and Acquaformosa–Saracena (ASF), and is approximately 25 km long. The second system, located east of the first, extends from Mottafollone to Centrale Tallarito for approximately 22 km and consists of three segments: Mottafollone (MoF), Altomonte (AlF), and Centrale Tallarito (TaF). Brozzetti et al. (2017) conducted a structural survey in this area, sampled several sites along these segments, and found a global dip angle of 45–60° SE.

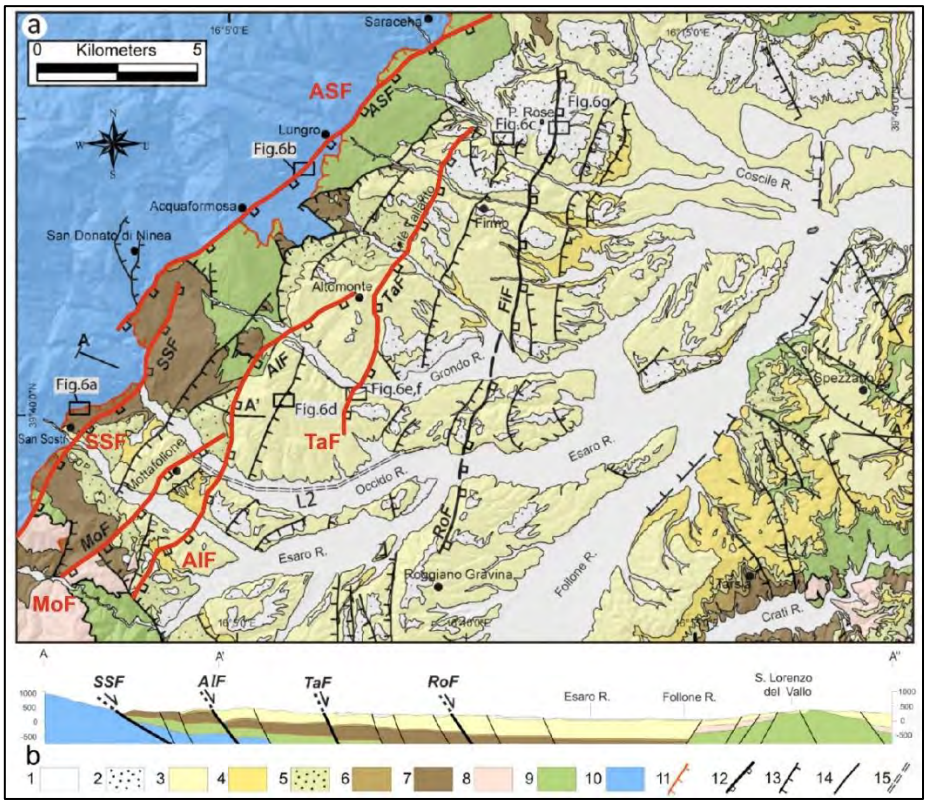



*Figure 3-12: Fault segments located in the northern part of the Crati Valley (modified from Brozzetti et al., 2017a)*

In this area, the available structural data are largely consistent across databases and among different authors; however, their tectonic interpretations remain partly divergent or uncertain. Brozzetti et al. (2017a) interpreted the San Sosti fault and the Crati Graben Detachment Fault (CGDF; see section below) as expressions of the same structure cropping out at different locations, while the MoF and AlF were considered synthetic faults to this main system; forming, all together, a larger fault system (Figure 3-13).

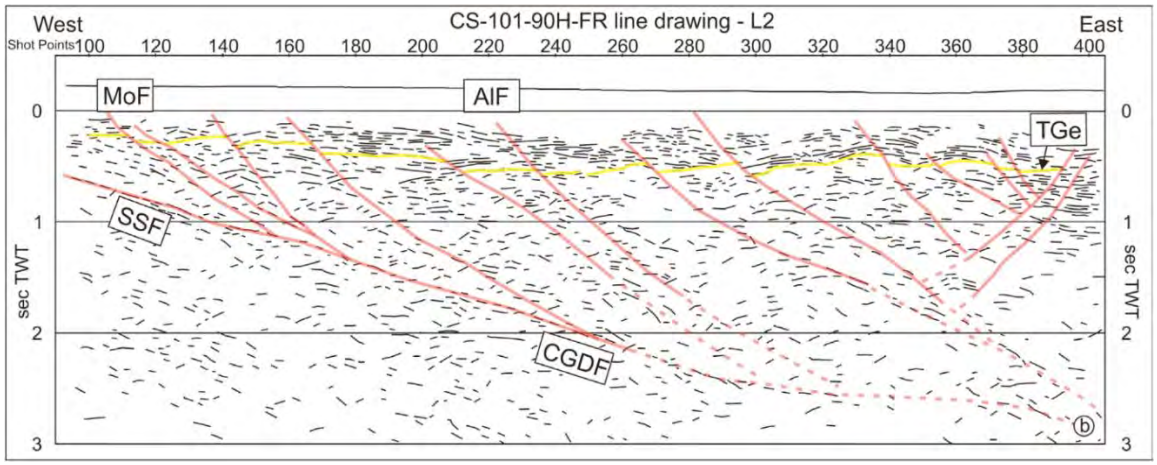



*Figure 3-13: Interpretation of a seismic line in the northern part of the Crati valley (Line L2 in Figure 3-12; from Brozzetti et al., 2017a)*

### *Farneto*

The trace of the Farneto and Roggiano Gravina faults derive from an original study performed by the University of Chieti - Pescara and the National Institute of Oceanography and Applied Geophysics (OGS) along the former ITHACA faults named 'Firmo' and 'Roggiano Gravina'. The former Firmo fault has been renamed Farneto fault and is considered here part of the Farneto - Roggiano Gravina system (Boncio et al., 2022, 2023, 2025).

The Farneto fault is a high-angle normal fault dipping WNW, with an estimated length ranging from a minimum of 7 to a maximum ~9.8 km. The Roggiano Gravina fault is also a high-angle normal fault, W-dipping, with a length of ~5.6 km. These two faults form a system with a total length of ~13.7 km (Farneto – Roggiano Gravina system). No clearly displaced deposits younger than 40 ka have been identified along either fault. This age threshold is adopted as a chronological benchmark for defining active and capable faults according to the Italian guidelines (Technical Commission on Seismic Microzonation, 2015). However, both faults exhibit evidence of activity during and after the late Middle Pleistocene, including (Boncio et al., 2025): (i) displacement of a paleosurface overlain by a paleosol dated to the Marine Isotope Stage 7 (~215 ka); (ii) displacement of colluvial deposits dated ~160 ka along the Farneto fault; (iii) possible displacement (inferred from high-resolution seismic reflection data) of the base of Upper Pleistocene alluvial deposits of the Esaro River; and (iv) multiple lines of evidence suggesting that the Farneto fault has generated surface faulting in the past, rather than representing a purely exhumed inactive structure. Assuming fault activity from the late Middle Pleistocene to the present, estimated average slip rates range between 0.04 and 0.11 mm/yr, with a mean value of ~0.09 mm/yr for the entire Farneto – Roggiano Gravina fault system.

### *Crati Valley faults*

The Crati Valley (hereinafter CV) is a north-south basin commonly considered a graben, bounded by normal faults on both the eastern and western sides, dipping towards the centre of the graben. There are two interpretations of the area: Spina et al. (2011), propose that the faults in the eastern sector, which dip to the west, form the main seismogenic system, while the western sector, dipping to the east, are interpreted as antithetic faults. This interpretation has been adopted by the compilers of the DISS, with the Crati Valley ITCS015 source (Figure 3-7a). In contrast, Brozzetti et al. (2017b), propose the opposite, identifying the western faults as the main seismogenic system and the west-dipping faults as antithetic. This hypothesis, considered debated (Debated Seismogenic Source, DSS) in DISS, has been adopted in the alternative

seismogenic model developed in recent years (Mucciarelli et al., 2013).

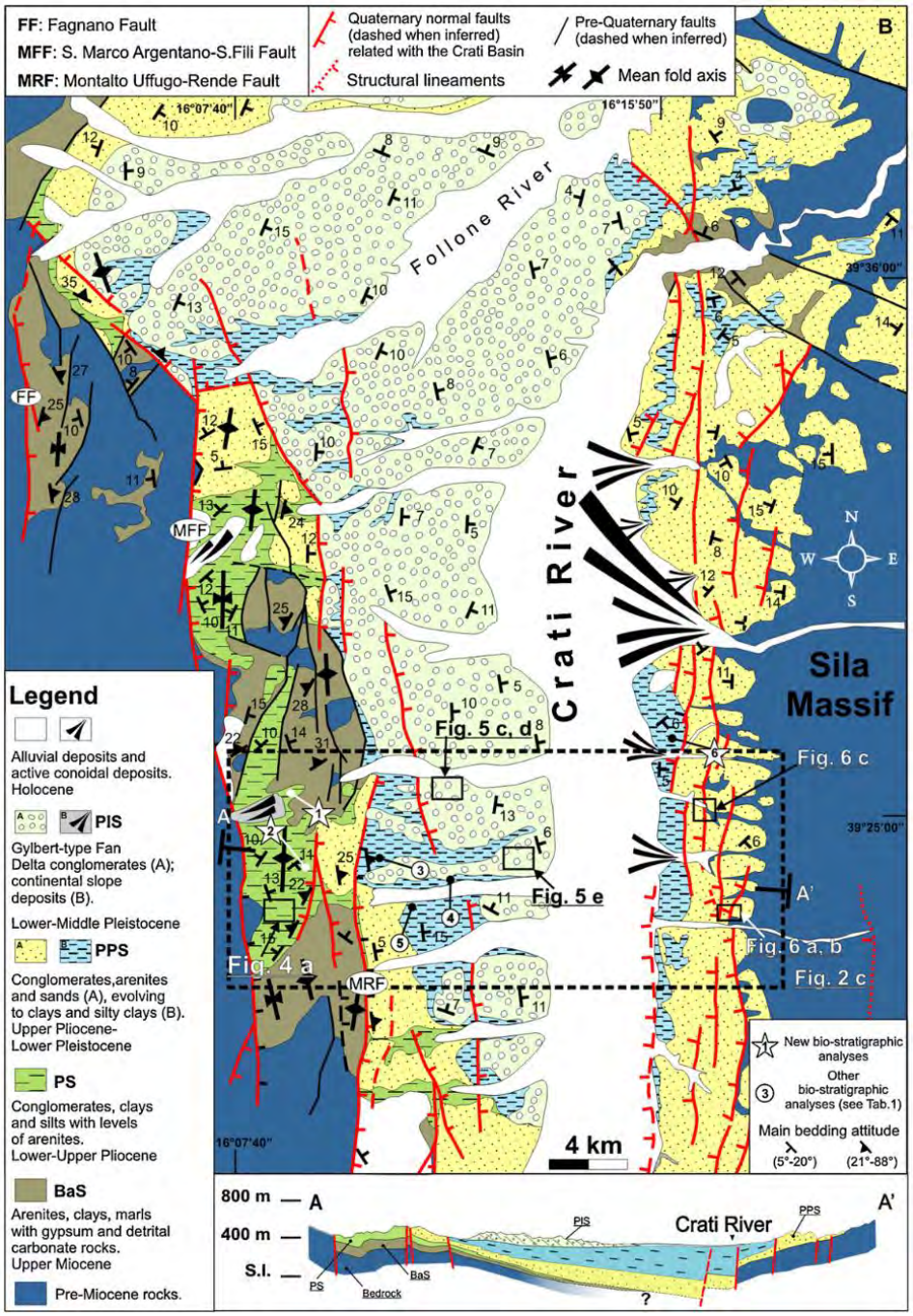



*Figure 3-14: Geological map of the Crati Valley (from Spina et al., 2011; Figure 3b)*

Furthermore, according to Spina et al. (2011), the western part of the CV is characterised by three main east-dipping faults with normal kinematics, running from west to east (Figure 3-14): the Fagnano fault (FF: 8 km), the San Marco Argentano-San Fili fault (MFF: 15 km), and the Montalto Uffugo-Rende fault (MRF: 25 km). Their structural investigation at various sites in both the eastern and western fault systems show that, in the southern and central parts of the CV, the faults have a dip angle of around 50–70° and an average direction of 11°N, while in the

north the average direction is 348°N. Unfortunately, detailed structural data are not available for both sides of the CV. The only studied normal fault located in the eastern part has a direction of approximately N20° and a high angle (70–80°W). In this article, the authors also interpreted an E–W seismic line crossing the central part of the CV (Figure 3-15a) and consider the submerged fault to the west as the main fault. A slip rate of 0.9 mm/year is obtained based on the cumulative displacement since the Middle Pleistocene (600 m in 700 ka, at the centre of the seismic profile).

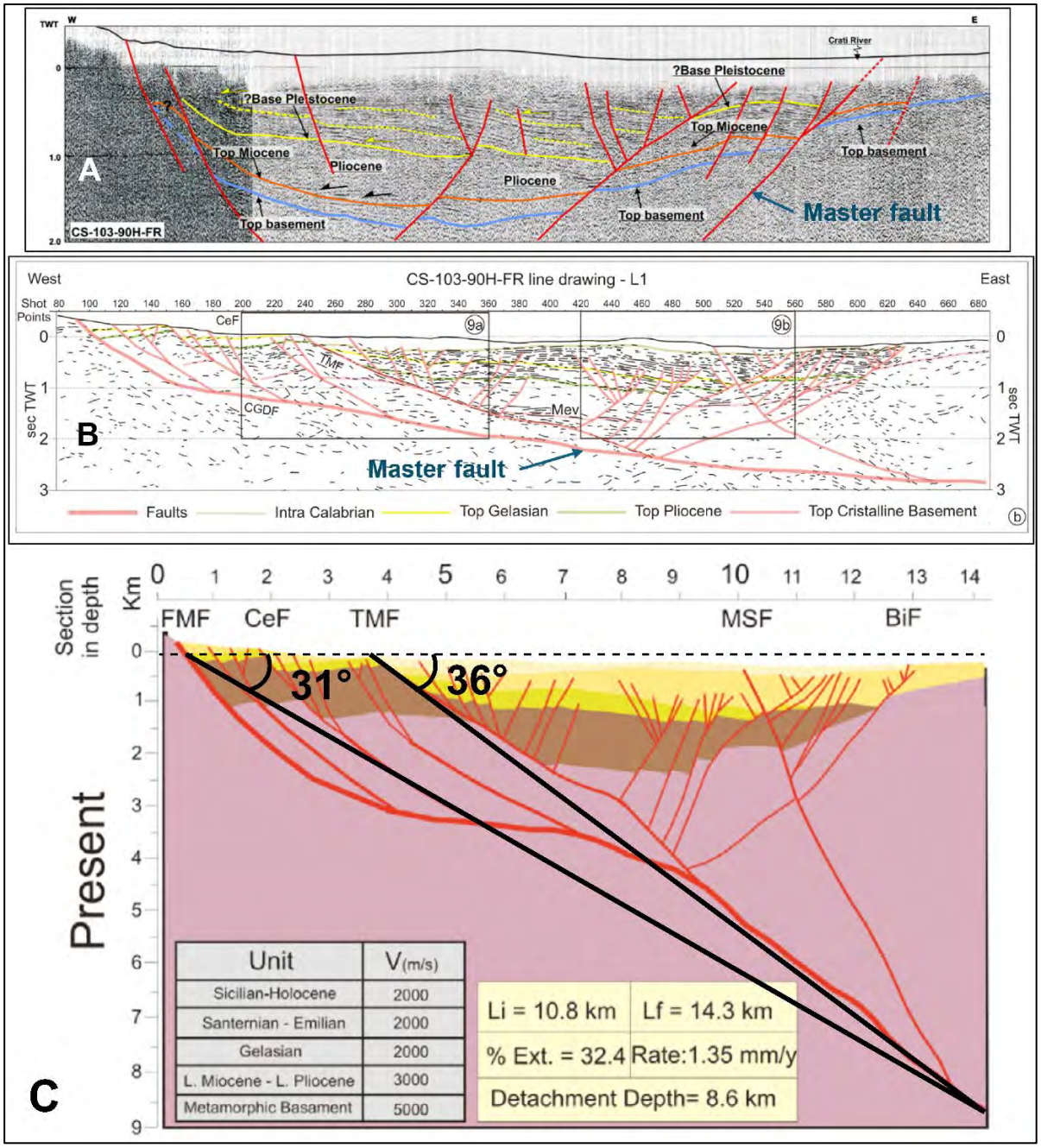



*Figure 3-15: Interpretation of a seismic line across the central part of the Crati Valley. (modified from: A) Spina et al., 2011; B) Brozzetti et al., 2017b. C) Seismic section transformed in depth (modified from Brozzetti et al., 2017b)*

Brozzetti et al. (2017b) also conducted a structural survey and analysed the same seismic line, reaching a different interpretation. The survey focused on the northern and central parts of the CV system, and the structural data are similar to those reported by Spina et al. (2011) and QUIN 2.0. According to Brozzetti et al. (2017b), the main fault is the western fault of the CV (Figure 3-15), defined as the Crati Graben Detachment Fault (CGDF), which extends for about 60 km and dips eastward. The CGDF is the same structure identified as the San Marco Argentano-San Fili fault (MFF) by Spina et al. (2011). According to Brozzetti et al. (2017b) the dip angle at the surface is 30–45°. When measured on their seismic section converted to depth, the average dip is approximately 31°, while when calculated with respect to the Torano-Martorano structure (extended version of the MRF in Spina et al., 2011), the average dip is approximately 36° (Figure 3-15).

The QUIN 2.0 database provides additional structural data for the western sector of the CV. For the Fagnano fault (referred to as the Fagnano Castello fault in QUIN but FF in Spina et al., 2011), the direction is approximately N350°, with a dip angle between 36° and 78° NE. According to the fault trace reported in this database, the length is 10 km. The San Marco Argentano–San Fili (MFF) fault is divided into two distinct segments in QUIN. The northern segment is called Santa Catarina–Albanese (approximately 15 km), while the southern segment is called Cervicati–San Fili (15 km). These segments have roughly the same direction (N350°) as the Fagnano Castello fault but have a slightly greater dip than the values proposed in Spina et al. (2011): from 40° to 80° E (average approximately 65°) for Santa Catarina–Albanese and from 40° to 80° E (average approximately 55°) for Cervicati–San Fili.

The central part of the western east-dipping alignment, known as Montalto Uffugo-Rende, is again different in the QUIN database. It is divided into two or three segments, considering the Savuto fault, which connects the alignment to the left-lateral Falconara-Carpanzano fault further south. The northern segment, called Torano Castello, is about 6.5–7 km long and dips eastward at an angle of 79°. The Montalto-Uffugo segment is about 15 km long and has a variable dip of 15–75° (averaging around 55°E). These two faults have a similar orientation (almost N–S) and are fairly parallel to the more westerly faults. The 10 km long Savuto fault, located to the south, has a slightly different orientation (~N10) and an inclination of 50–85° (~70°). The total length of this alignment is therefore 35 km if all three segments are included, and only 25 km if only the Torano Castello and Montalto-Uffugo faults are considered.

### *Rossano*

This fault is located southeast of the Sibari Plain, north of the Sila Massif, and south of the Gulf of Taranto (Figure 3-16). It strikes WNW–ESE, dips northward at a steep angle (approximately 80°), and has an estimated length of 10–20 km. Although its geometry is relatively well defined, the structure remains poorly constrained in terms of recent kinematics and contrasting interpretations have been proposed.

On the basis of structural evidence such as slickenlines, Galli et al. (2010) interpreted the fault as a pure dip-slip structure with dominant normal kinematics. They subdivided it into three main segments, from west to east: Corigliano, Rossano, and Crosia (Figure 3-16b). The fault may extend further eastward along the Crosia segment; however, in this study, evidence is limited to the western sector and a possible continuation toward Mirto cannot be confirmed. The Rossano segment was interpreted as the source of the historical earthquake of 1836 (Mw 6.2) and of a paleo-event dated to around 950 AD (Bartholomaeus Rossanensis, 11th century). From these data, Galli et al. (2010) estimated a recurrence interval of approximately 0.9 ka and a slip rate ranging between 0.5 and 0.7 mm/yr.

Alternatively, this fault system has been interpreted within a broader regional transpressional (Figure 3-16a) framework linking the southern Apennines to the Calabrian Arc (Gori et al., 2016).

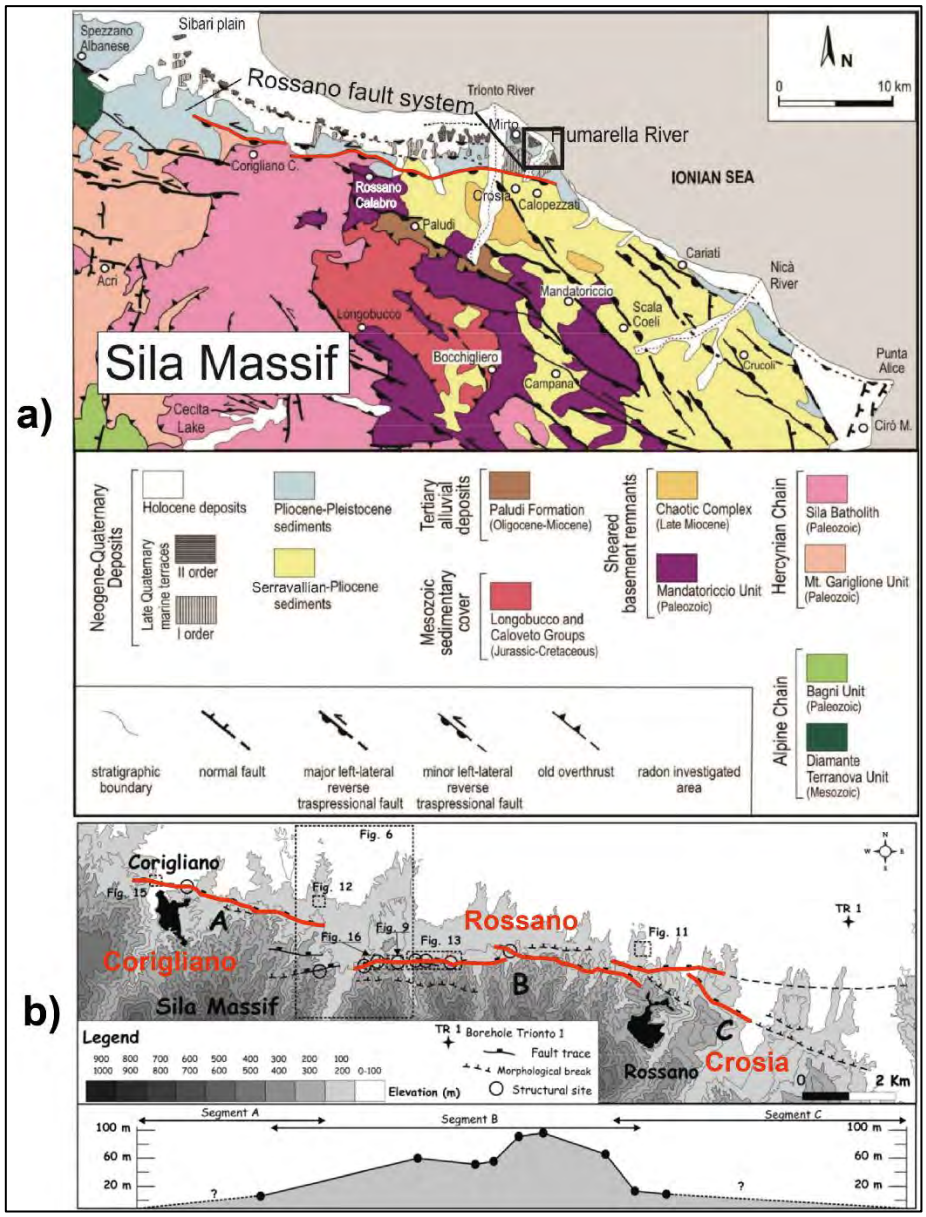



*Figure 3-16: Rossano fault system. a) Geo-structural map of the northern part of the Sila Massif (modified from Gori et al., 2016); b) Rossano fault segmentation with Corigliano, Rossano and Crosia segments (modified from Galli et al., 2010)*

## *Laghi - Cecita*

The Laghi and Cecita faults are located in the central sector of the Sila Massif, east of the Crati Valley (Figure 3-17). This area is associated with major historical earthquakes, including those of 6 August 1638 (Mw 6.8), 21 March 1744 (Mw 5.7), and 8 March 1832 (Mw 6.6), with magnitudes derived from macroseismic data in the CPTI15 catalogue (Rovida et al., 2020; 2022). Palaeoseismological investigations carried out along the Laghi fault by Galli and Bosi (2003) and Galli et al. (2007) provided key constraints on fault geometry and activity. The fault strikes NW–SE (~N140°) and dips toward the southwest at high angles (approximately 50–

60°). Trenching revealed a sequence of surface-rupturing earthquakes, including both historically documented events and older events not reported in the Italian seismic catalogue. One of these events is correlated with the Mw 6.8 earthquake of 1638, whereas the penultimate event is dated to the 6th–7th century AD and the third and fourth most recent events to the 1st and 2nd millennia BC. Based on these data, the authors proposed a recurrence interval of approximately 0.8–1.0 ka and a slip rate of about 1.2 mm/yr. Galli and Bosi (2003) further suggested that the Laghi fault may connect northward with the Cecita fault, a ~15 km long structure. Although no historical earthquakes have been associated with the Cecita fault (Rovida et al., 2020; 2022), its behaviour appears comparable to that of other faults in the region, with inferred recurrence intervals of about 1–2 ka, implying the potential for strong future earthquakes.

The kinematics of the Laghi and Cecita faults remain debated. Based on trench data, Galli and Bosi (2003) and Galli et al. (2007) described an oblique motion dominated by a normal component with a significant left-lateral contribution. In contrast, Civile et al. (2022) interpreted these structures as part of the Petilia–Sosti regional shear zone, characterised by prevailing left-lateral motion. More recently, Palano et al. (2023), based on a geodetic strain model, also supports a predominantly normal-faulting kinematic regime.

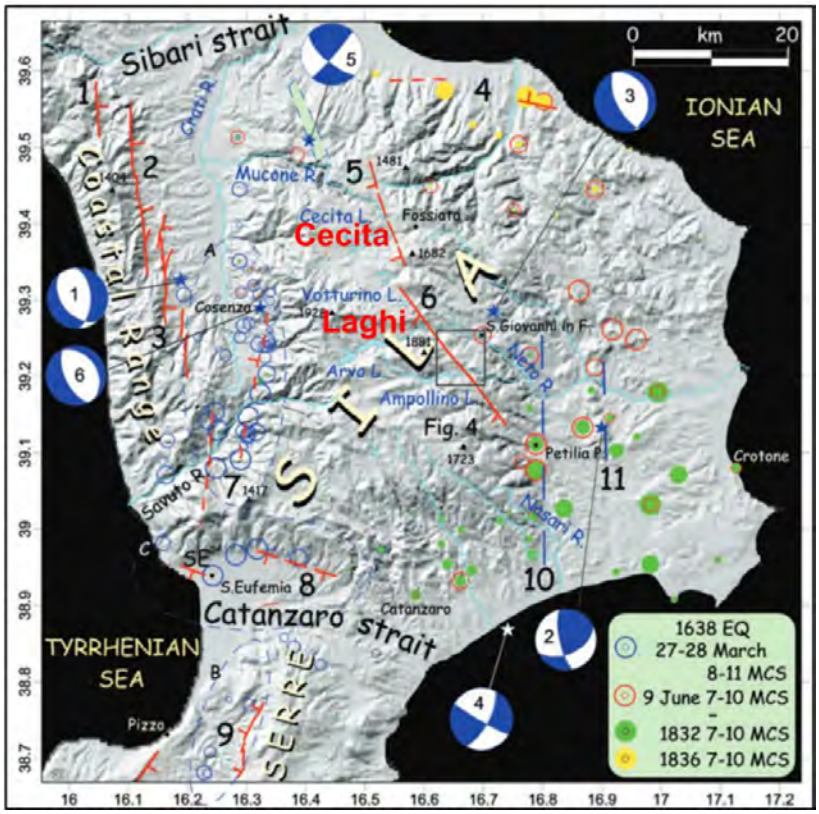



*Figure 3-17: Potential active faults in the Sila Massif (modified from Galli and Bosi, 2003)*

### 3.3.2. Seismogenic sources parametrisation

Based on the compiled geological, geomorphological, and seismotectonic information, a final source model is built. Small fault segments and regional lineaments, such as those reported in the ITHACA database, were excluded as they are not expected to generate earthquakes of sufficient magnitude (Mw > 5.5) to produce surface rupture.

For each selected source, a brief description is provided below to justify the choices made in constructing the fault source model from the available geological and tectonic information. The following descriptions focus on the definition of the surface expression adopted for each fault source, whereas the corresponding subsurface parameters are discussed at the end of this section. Particular attention is given to the slip rate, which is a key parameter in PFDHA. To account for epistemic uncertainty, this parameter is expressed as a range of values rather than as a single estimate. The resulting simplified seismotectonic model is summarised in Table 3-1 and Figure 3-18.

| | | | | | Geologic slip-rate | | Geodetic slip-rate | | | |
|---|---|---|---|---|---|---|---|---|---|---|
| Source ID | Source name | L (km) | Dip | Seismogenic depth (min-max) (km) | min SR (mm/yr) | max SR (mm/yr) | min SR (mm/yr) | max SR (mm/yr) | Associated historical earthquake | Kin |
| 1 | Pollino (***) | 30 (**) | 50 (*) | 0-19 | 0.4 (5) | 0.6 (5) | | | | N (5,6) |
| 2 | Castrovillari | 13 (2,3) | | 0-10 | 0.6 (2,3) | 1.0 (2,3) | | | | N (2,3) |
| 3 | Amendolara | 17.5 (10) | 45 (*) | 2-8.7 | 0.4 (10) | 0.6 (10) | | | Mw 5.5 in 1917 (10) | R/SSRL (10) |
| 4 | SS-AQSA (***) | 26 (**) | 50 (*) | 0-19 | | | 0.37 (15) | 0.57 (15) | | N (7) |
| 5 | Alt-Tall (***) | 19 (**) | | 0-14.6 | | | 0.37 (15) | 0.57 (15) | | N (7) |
| 6 | Farneto-Roggiano | 13.7 (**) | | 0-10.5 | 0.05 (****) | 0.12 (****) | | | | N |
| 7 | Sibari | 18.5 (1) | 90 (*) | 0-18.5 | 0.41 (1) | 0.72 (1) | | | | SSRL (1) |
| 8 | West Crati | 36 (**) | 36 (7) | 0-19 | 0.8 (14) | 1.0 (14) | 0.7 (8) | 0.9 (8) | | N (7,9) |
| 9 | East Crati | 41.5 (**) | 50 (16) | 0-19 | 0.8 (14) | 1.0 (14) | 0.7 (8) | 0.9 (8) | | N (7,9) |
| 10 | Rossano | 15 (11) | | 0-11.5 | 0.5 (11) | 0.7 (11) | | | Mw 6.2 in 1836 (11) | N (11) |
| 11 | Laghi | 25 (**) | | 0-19 | 1.0 (12, 13) | 1.4 (12, 13) | | | Mw 6.7 in 1638 (12, 13) | N (12, 13) |
| 12 | Cecita | 15.7 (**) | | 0-12 | 1.0 (12, 13) | 1.4 (12, 13) | | | | N (12, 13) |

*Table 3-1: Detailed source parameters used to build the final seismotectonic model in northern Calabria. (1) Cinti et al., 2024; (2) Cinti et al., 2015; (3) Cinti et al., 2002; (4) Brozzetti et al., 2017a; (5) Ferranti et al., 2019; (6) DISS WG, 2025; (7) Brozzetti et al., 2017b; (8) Meschis et al., 2022; (9) QUIN 2.0 (Lavecchia et al., 2024); (10) Ferranti et al., 2014; (11) Galli et al., 2010; (12) Galli and Bosi, 2003; (13) Galli et al., 2007; (14) Spina et al., 2011; (15) extrapolated from GNSS data, global slip-rate value has to be partitioned between the different faults considered; (16) calculated from the focal mechanism nodal planes, at a regional scale (check Supplementary materials); (*) hypothesised values; (**) measured from the surface fault traces; (***) combined from different sources; (****) obtained from the work on the Farneto del Principe dam (Boncio et al., 2025).*

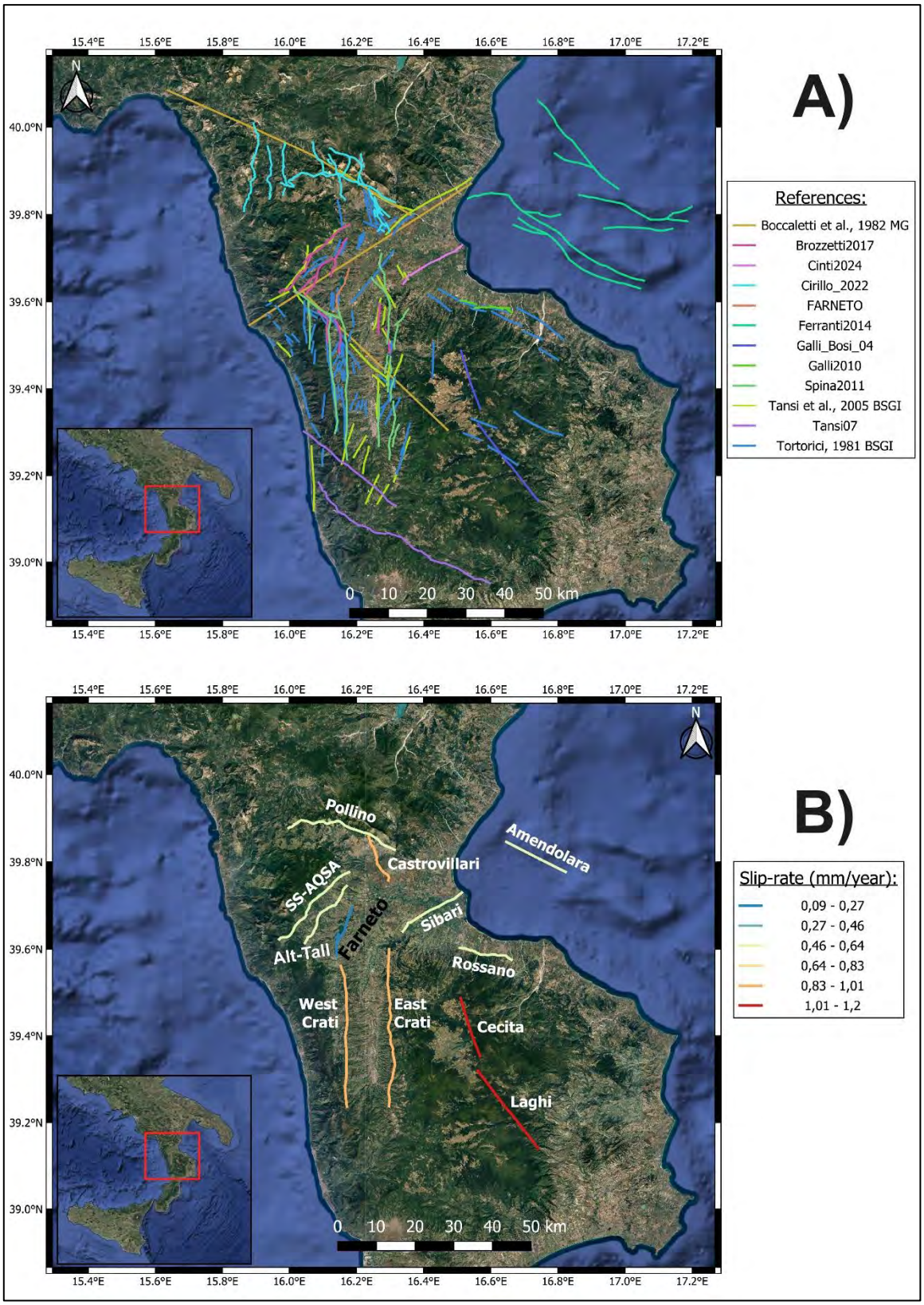



*Figure 3-18: Refined active and capable faults in Northern Calabria. A) Traces of active faults collected in the literature; B) Surface expression of the final simplified seismotectonic model (SS-AQSA: San Sosti – Acquaformosa system; Alt-Tall: Altomonte-Tallarito system).*

### *Pollino - Castrovillari*

As discussed above, the Pollino and Castrovillari faults are sometimes interpreted as a single fault system. However, as no widely accepted interpretation exists, both structures are treated here as independent. Following the surface traces proposed by Cirillo et al. (2022), the Pollino source is constructed by combining the two normal-fault segments: Pollino and CVN segments (21 km and 10 km long, respectively). The resulting source has a total length of approximately 30 km and exhibits normal kinematics. Slip-rate values are taken from Ferranti et al. (2019), who derived rates from speleoseismic evidence, and range between 0.4 and 0.6 mm/yr.

For Castrovillari, interpretations and datasets are relatively consistent among authors; therefore, the most recent constraints from Cinti et al. (2015) are adopted. The source, which exhibits normal kinematics, is built by merging the mapped fault segments shown in Figure 3-9, resulting in a total length of about 13 km. A slip-rate range of 0.6–1.0 mm/yr is assigned based on the better-constrained estimates of Cinti et al. (2015) compared to those of Cinti et al. (2002).

### *Sibari*

For the Sibari fault, the only available reference is Cinti et al. (2024). The fault is approximately 18.5 km long and is considered predominantly strike-slip, as the horizontal slip rate (0.41–0.70 mm/yr) greatly exceeds the vertical component (0.05–0.18 mm/yr). The vertical component is thus neglected, and the fault is assumed to be pure strike-slip and vertical (dip angle = 90°). The resulting minimum and maximum slip rates are 0.41 and 0.70 mm/yr, respectively.

### *Amendolara*

Ferranti et al. (2014) already defined a seismogenic source associated with the offshore faults investigated in their study; these sources are adopted here, as no alternative relevant references are available for this structure. For the present model, only the Amendolara segment is considered, as the Valsinni and Cariati segments lie slightly outside the study area. The Amendolara source is 17.5 km long and dips 45° to the northeast, with a reverse kinematics. The seismogenic depth range extends from 2 to 8.7 km. Slip rate values reported by Ferranti et al. (2014) range from 0.4 to 0.6 mm/yr. This source is interpreted by the same authors as responsible for the Mw 5.5 earthquake of 1917.

### *San Sosti – Altomonte*

In this area, several fault segments are present, leading to various possible interpretations or combinations. Fault segments can be treated as independent sources or combined into larger systems through joint rupture. In any case, all available structural and geometric data are taken from Brozzetti et al. (2017b), and all faults in this area are assumed to have normal kinematics.

To simplify the model, the individual segments are grouped into two parallel fault systems. The western system, named San Sosti–Acquaformosa (SS-AQSA), is composed of the San Sosti (13 km) and Acquaformosa–Saracena (15.5 km) segments, both dipping to the southeast. Their joint rupture defines a composite source 26 km long, with geometric parameters identical to those of the individual segments. The eastern system, renamed here Altomonte-Tallarito (Alt-Tall), consists of the Altomonte (12.5 km), and Centrale Tallarito (10 km) segments, which together form a composite source about 19 km long, also characterised by similar geometric parameters than the individual segments.

Because seismic-line interpretations (Figure 3-15c) suggest that the two systems are connected at depth and form a complex structure, they should not be considered simultaneously as independent sources. Accordingly, different scenarios can be explored with (1) only the western SS-AQSA system as active; (2) only the eastern Alt-Tall system as active; or (3) both systems are active, sharing the local geodetic deformation and the derived slip rate. To make it simpler here, only the exclusive scenarios (1) and (2), with individual systems, are explored (see section 3.2.3.). Regarding the slip rate, since no direct measurements are available for this area; it is estimated from regional strain-rate data and is approximately 0.47 mm/yr (see section below). This slip rate value is therefore exclusively assigned to the fault system considered in each scenario, and not divided between the two systems.

### *Farneto-Roggiano*

For this source, data from the Farneto dam project are used (Boncio et al., 2025). This fault is built by merging the Firmo and the Roggiano Gravina faults, for a total length of 13.7 km, and is now named Farneto-Roggiano. In addition, a Mw 2.8 earthquake occurred on 28 November 2023, which is interpreted as being associated with this fault source. One of the two nodal planes of its focal mechanism, computed using the FOCMEC algorithm (Snoke et al., 1984), indicates a normal fault plane oriented approximately NE-SW (Figure 3-19), which could be consistent with the Farneto-Roggiano fault as it was defined previously.

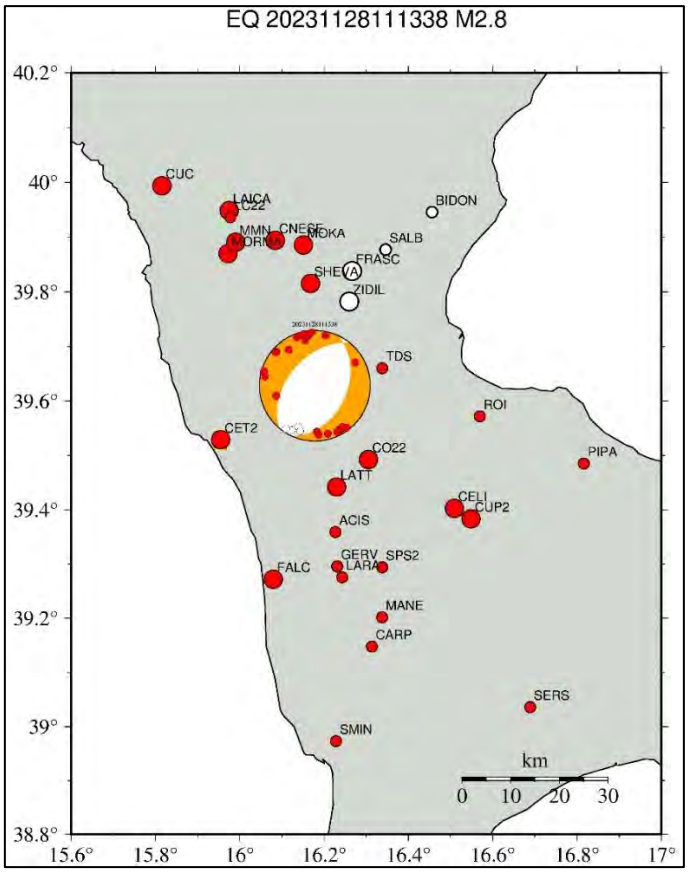



*Figure 3-19: Focal mechanism of the Mw 2.8 November 2023 earthquake in the central Crati Valley area. In red, are shown the stations used to compute the focal mechanism.*

## *Crati Valley faults*

As seen in the previous section, this area is complex and still debated among authors. While structural data are generally consistent, interpretations vary considerably. For the purposes of the model, two alternative sources are defined: the East Crati and West Crati faults. These two sources represent separate scenarios and should not be considered simultaneously (see rupture scenarios, Figure 3-24).

For the **West Crati fault**, Brozzetti et al. (2017b) is adopted as the main reference, as it identifies this structure as the master fault in the valley. However, the fault traces provided by Brozzetti et al. (2017b) only cover the northern part of the Crati Valley. To obtain a more complete representation of the structure, the trace proposed by Spina et al. (2011) which extends over almost the entire valley, is therefore used as the geometric basis. A key issue concerns the selection of the fault segment used to define the seismogenic source, given the presence of several parallel structures. Defining a single source that includes all parallel faults in the western Crati Valley is not appropriate, because most of these structures are interpreted as synthetic

faults. Therefore, among the three main candidates (MRF, MFF, and FMF), the MRF is selected because it represents the largest segment and thus provides a more conservative estimate of seismic hazard. The northern tip of the source is shifted 5 km southward to the intersection between the MRF and an E–W-trending fault segment (circle in Figure 3-20a). At the southern end, the trace of Spina et al. (2011) is truncated before the actual termination of the fault. The source is therefore extended 4 km farther south following the trace proposed by Tansi et al. (2007) (circle in Figure 3-20b). The resulting West Crati source is 36 km long and dips eastward. Regarding the slip rate, Spina et al. (2011) derived from cumulative displacement since the Middle Pleistocene (600 m in 700 ka) a value of 0.9 mm/yr for the area. Finally, a dip angle at depth of 36° (Figure 3-15c) is adopted based on Brozzetti et al. (2017b).

For the **East Crati fault**, Spina et al. (2011) is adopted as the preferred reference, as it identifies the East Crati fault as the master structure in the Crati Valley and provides a more continuous trace than those proposed by Brozzetti et al. (2017b) and ITHACA, which appear excessively segmented. The source geometry is therefore based on Spina et al. (2011), connecting the parallel fault segments from north to south. The northern end of the source is limited at the Crati River, as no field data are available for the segments located farther north (QUIN 2.0; Brozzetti et al., 2017b), despite their representation on published maps. The southern tip is once again truncated in their map and was therefore extended using the trace proposed by Tansi et al. (2007) (Figure 3-20c). The resulting East Crati source is 41.5 km long, dips westward, and is assigned the same slip rate of 0.9 mm/yr as the West Crati source.

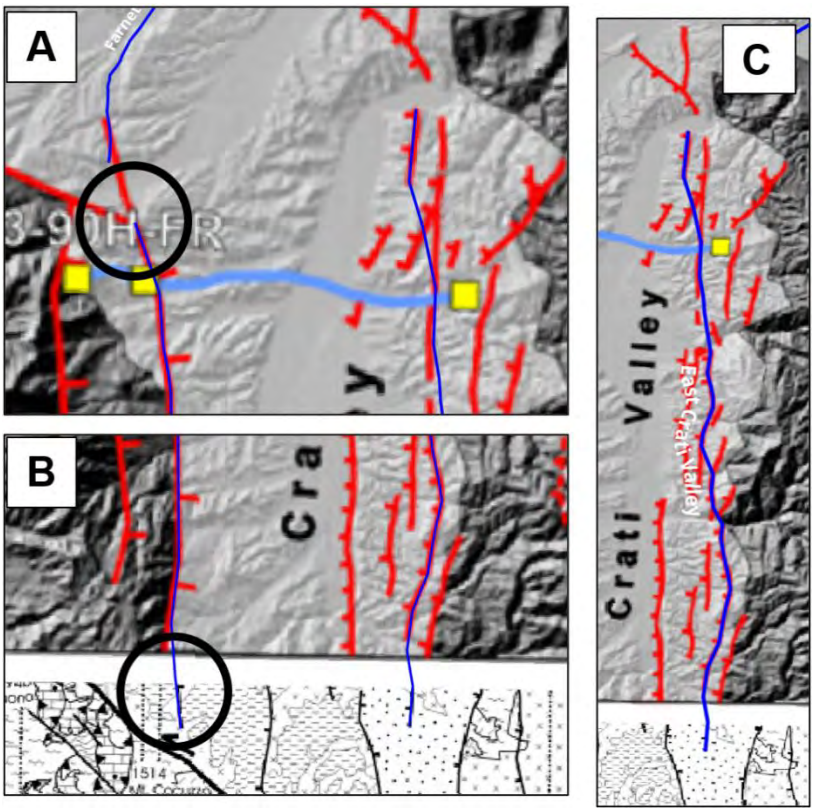



*Figure 3-20: Details regarding the construction of the final fault sources in the Crati Valley: in blue, the proposed simplification with respect to the segments mapped on the surface. A: northern sector of the western system, taken from Spina et al., 2011; B: western Crati, southern part, from Spina et al., 2011 and Tansi et al., 2007 for the termination; C: eastern Crati source, from north to south.*

Both the East and West Crati faults are treated as alternative individual sources, similar to the approach previously applied to the San Sosti – Acquaformosa (SS-AQSA) and Altomonte-Tallarito (Alt-Tall) sources. This simplification allows the model to account for the main regional seismogenic structures while avoiding the inclusion of minor or synthetic faults that do not significantly affect the hazard assessment.

### *Rossano*

For the Rossano fault, the interpretation by Galli et al. (2010) is adopted, as it is the only reference based on direct field observations (slickenlines) and data collected on the fault itself. Therefore, normal faulting behaviour is used in the model. The source is built from the 3 segments: Corigliano, Rossano and Crosia. It is 15 km long, dips 80° northward, and has slip rate values ranging from 0.5 to 0.7 mm/yr. It is also associated with the Mw 6.2 historical earthquake of 1836.

## *Laghi - Cecita*

Similarly, for the Laghi fault, and by extension the Cecita fault, priority is given to available field data. Therefore, the interpretation by Galli and Bosi (2003) is considered. According to their proposed surface trace, the Laghi fault is approximately 25 km long, dips at an angle of 60°W, and exhibits predominantly normal behaviour. Again, to simplify the model, the strike-slip component is neglected. A broader slip-rate range of 1–1.4 mm/yr is used, rather than the 1.2 mm/yr suggested by Galli and Bosi (2003). Finally, the 1638 Mw 6.7 historical earthquake is associated with the Laghi fault.

Although the Cecita fault is poorly constrained, it is also included in the model because of its potential seismic significance. Galli and Bosi (2003) are again used as the reference. The fault exhibits the same behaviour as the Laghi fault, with normal-fault kinematics and a length of 15.7 km.

## *Other parameters*

Despite this exhaustive literature review, several key source parameters remain poorly constrained for some faults. In particular, subsurface information such as the seismogenic thickness or the dip angle at depth are still lacking, along with some slip rates in the western Crati Valley area. The following section briefly describes the approach adopted to estimate these parameters.

### *Seismogenic thickness*

Seismogenic thickness is a very important input in the calculation of surface faulting hazard because it provides valuable information on the depth of hypocentres, and the downdip (W) extent of possible ruptures on the fault, which are not available in the literature data. Our strategy here was to use the hypocentral depth of earthquakes located by the CLASS catalogue (Latorre et al., 2022), on a regional scale, and to consider this as the seismogenic thickness. Given the small size of the investigated structures, and the predominantly dip-slip character of the surface earthquakes in the study area, we have imposed a limit value for the aspect ratio, i.e., the L/W ratio <= 1. This prevents, for example, a 5 km long fault from extending to a depth of 50 km (aspect ratio L/W = 5/50 = 0.1).

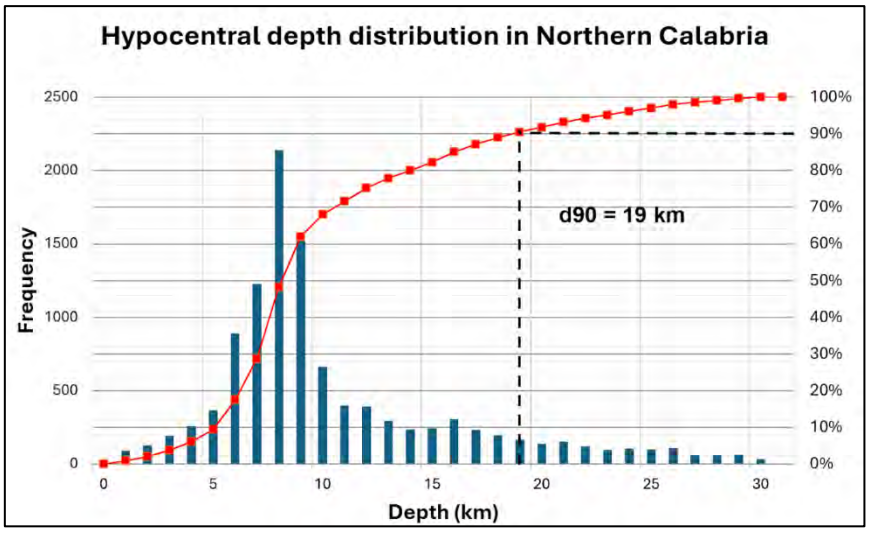



*Figure 3-21: Hypocentral depth distribution in northern Calabria, using the CLASS catalogue (Latorre et al., 2022). The blue bars represent the frequency distribution of hypocentral depths, the red line is the cumulative distribution function, and the black dashed line represents the d90 depth threshold, below which 90% of earthquakes occur.*

Only the shallow earthquakes are in our interest in Calabria, as the deep events on the western part are likely related to the subduction zone and are not able to cause surface dislocation. Only events with a good quality (A, B or C) located in the first 30 km of the crust are selected (subduction-related hypocentres were not considered). Their hypocentral depth distribution is represented on Figure 3-21, which shows that most of them are located between 5 and 10 km depths. For the seismogenic depth, the 90th percentile, for which 90% of the events are shallower is considered: d90 = 19 km. This thickness corresponds to a maximum fault width of: $W_{max} = \frac{T}{sin(\alpha)}$ ; with α being the average dip-angle at depth (50° for most of the sources with a normal kinematic, as explained in the next section). For all the faults having a length $L$ smaller than this $W_{max}$ , the seismogenic depth is constrained to fit an aspect ratio of 1, with: $T = sin(\alpha) \cdot L$ .

***Source geometry at depth***

Having an idea of the dip-angle of the seismogenic source at depth is usually not an easy task. Three different methods are commonly used: with surface data (geomorphic data), with subsurface data (seismic lines), or using the focal mechanisms' nodal planes. Here, for the faults for which only surface data are available, all the focal mechanisms available online and in the literature are collected. Since only the shallow events are in our interest, the selection is limited to the first 25 km in depth. Data are taken from RCMT (Pondrelli, 2002; Pondrelli et al., 2006), TDMT (Scognamiglio et al., 2006) databases for most of the earthquakes. In the literature, first-

motion polarity method (FP) data are used from Chiappetta and La Rocca., 2023 and Ciaccio et al. (2021). The computed focal mechanism of the 28 November 2023 earthquake next to the dam is also used (see section 3.2.2., part Farneto-Roggiano).

In total 10, 41 and 14 focal mechanisms for RCMT, TDMT and first-motion polarity methods, respectively, are collected, of which 65 solutions lie inland. For some earthquakes, solutions with different methods are available: in these cases, priority was given to RCMT, FP and finally TDMT solutions respectively. The selected mechanisms are shown in Figure 3-22, the solutions in Table 3-2.

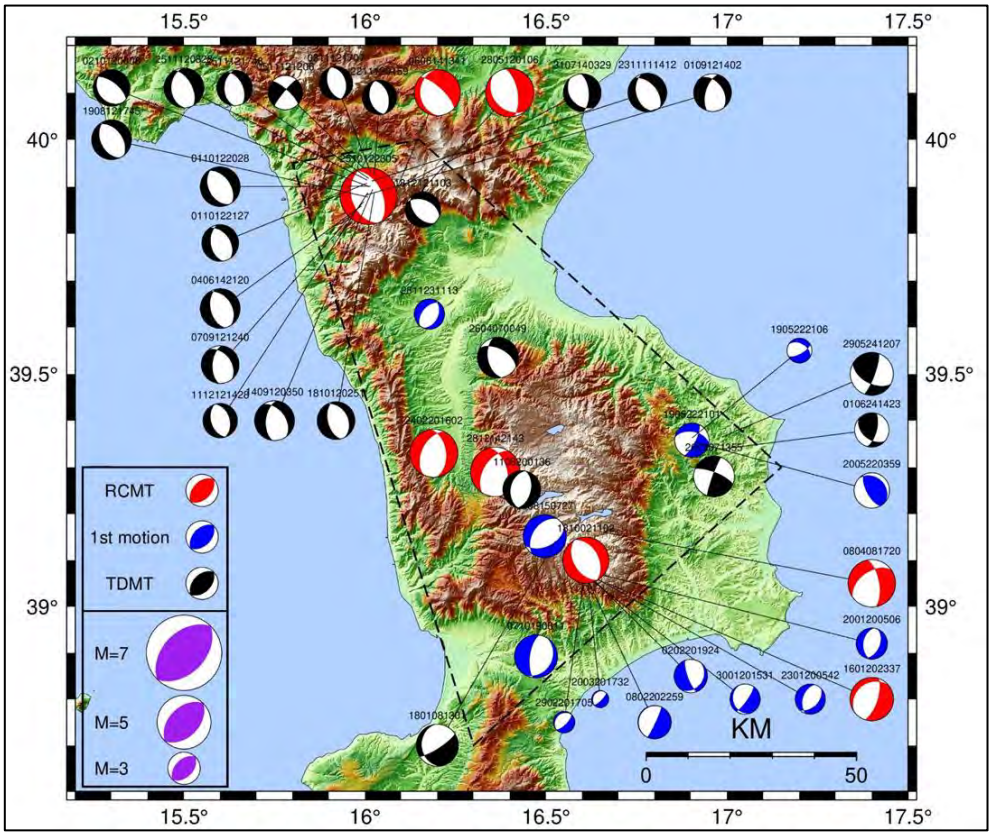



*Figure 3-22: Map of the focal mechanisms collected in northern Calabria (red: RCMT database; black: TDMT database; blue: 1st motion polarity data from Chiappetta and La Rocca, (2023) and Ciaccio et al. (2021)).*

As is well known, the focal mechanism represents a double-pair rupture model in which it is not possible to determine a priori which plane actually generated the earthquake. The selection of which nodal plane for each mechanism is most likely to be the fault plane that generated the earthquake is generally based on locally available geological information. Thus, the selected nodal planes are indicated in Table 3-2, they are differentiated by colours, with yellow for 'reliable', and orange for 'uncertain' or if further information is needed to confirm the selection. The average dip angle is calculated for these two categories, yielding values of 48°, 58°, and

51° for the yellow, orange, and combined ("yellow + orange") groups, respectively. At the end, as the difference is not so large, an average value of 50°, that is closer to the yellow category, is considered in our model.

| | | | | nodal plane 1 | | | nodal plane 2 | | | | |
|---|---|---|---|---|---|---|---|---|---|---|---|
| ID | Lon | Lat | Depth | Strike | Dip | Rake | Strike2 | Dip2 | Rake2 | Date | Source |
| 1 | 16,61 | 39,10 | 10 | 332 | 44 | -88 | 149 | 46 | -92 | 18/10/2002 11:02 | RCMT |
| 2 | 16,96 | 39,28 | 23 | 200 | 84 | 163 | 292 | 73 | 6 | 26/03/2007 13:55 | TDMT |
| 3 | 16,37 | 39,54 | 10 | 298 | 54 | -126 | 168 | 49 | -51 | 26/04/2007 00:49 | TDMT |
| 4 | 16,53 | 39,14 | 9 | 57 | 78 | -67 | 173 | 26 | -152 | 18/01/2008 13:01 | TDMT |
| 5 | 16,66 | 39,16 | 10 | 235 | 49 | -35 | 350 | 64 | -134 | 08/04/2008 17:20 | RCMT |
| 6 | 16,02 | 39,91 | 8 | 319 | 51 | -106 | 163 | 41 | -72 | 23/11/2011 14:12 | TDMT |
| 7 | 16,12 | 39,86 | 3 | 137 | 31 | -119 | 350 | 63 | -74 | 28/05/2012 01:06 | RCMT |
| 8 | 16,01 | 39,88 | 8 | 322 | 47 | -99 | 156 | 44 | -80 | 19/08/2012 17:45 | TDMT |
| 9 | 16,00 | 39,88 | 8 | 197 | 60 | -57 | 324 | 43 | -134 | 01/09/2012 14:02 | TDMT |
| 10 | 16,00 | 39,87 | 6 | 184 | 56 | -64 | 323 | 42 | -123 | 07/09/2012 12:40 | TDMT |
| 11 | 16,02 | 39,89 | 6 | 186 | 54 | -62 | 325 | 45 | -122 | 14/09/2012 03:50 | TDMT |
| 12 | 16,02 | 39,90 | 9 | 324 | 49 | -96 | 153 | 41 | -83 | 01/10/2012 20:28 | TDMT |
| 13 | 16,01 | 39,91 | 9 | 171 | 47 | -72 | 326 | 46 | -108 | 01/10/2012 21:27 | TDMT |
| 14 | 16,01 | 39,90 | 7 | 308 | 65 | -96 | 142 | 26 | -78 | 02/10/2012 00:08 | TDMT |
| 15 | 16,03 | 39,89 | 9 | 166 | 54 | -82 | 332 | 37 | -101 | 18/10/2012 02:51 | TDMT |
| 16 | 16,01 | 39,88 | 15 | 162 | 40 | -84 | 335 | 44 | -96 | 25/10/2012 23:05 | RCMT |
| 17 | 16,02 | 39,93 | 9 | 161 | 49 | -92 | 344 | 41 | -88 | 03/11/2012 17:07 | TDMT |
| 18 | 16,00 | 39,94 | 10 | 220 | 83 | -15 | 312 | 75 | -172 | 05/11/2012 12:06 | TDMT |
| 19 | 16,03 | 39,92 | 8 | 344 | 47 | -91 | 166 | 43 | -89 | 22/11/2012 01:59 | TDMT |
| 20 | 16,01 | 39,91 | 9 | 332 | 57 | -105 | 178 | 36 | -68 | 25/11/2012 08:28 | TDMT |
| 21 | 16,01 | 39,92 | 9 | 335 | 52 | -107 | 181 | 41 | -69 | 25/11/2012 17:48 | TDMT |
| 22 | 16,01 | 39,89 | 9 | 162 | 46 | -91 | 344 | 44 | -88 | 11/12/2012 14:28 | TDMT |
| 23 | 16,16 | 39,85 | 8 | 139 | 49 | -72 | 293 | 44 | -109 | 18/12/2012 11:03 | TDMT |
| 24 | 15,99 | 39,86 | 8 | 166 | 50 | -78 | 328 | 42 | -104 | 04/06/2014 21:20 | TDMT |
| 25 | 16,09 | 39,90 | 10 | 178 | 26 | -48 | 313 | 71 | -108 | 06/06/2014 13:41 | RCMT |
| 26 | 16,10 | 39,90 | 8 | 356 | 61 | -71 | 140 | 34 | -121 | 31/07/2014 03:29 | TDMT |
| 27 | 16,36 | 39,29 | 11 | 346 | 50 | -124 | 212 | 50 | -57 | 28/12/2014 21:43 | RCMT |
| 28 | 16,50 | 39,15 | 18,2 | 65 | 50 | -70 | 215 | 44 | -112 | 03/08/2015 07:27 | FP |
| 29 | 16,47 | 38,89 | 21,4 | 30 | 25 | -70 | 188 | 67 | -99 | 07/10/2019 06:11 | FP |
| 30 | 16,67 | 39,05 | 10 | 233 | 26 | -58 | 18 | 69 | -104 | 16/01/2020 23:37 | RCMT |
| 31 | 16,61 | 39,08 | 9,3 | 22 | 47 | -80 | 188 | 44 | -101 | 20/01/2020 05:06 | FP |
| 32 | 16,61 | 39,07 | 7,9 | 45 | 45 | -70 | 198 | 48 | -109 | 23/01/2020 05:42 | FP |
| 33 | 16,62 | 39,06 | 9,7 | 35 | 78 | -73 | 162 | 21 | -144 | 30/01/2020 15:31 | FP |
| 34 | 16,63 | 39,06 | 12 | 35 | 26 | -38 | 160 | 74 | -111 | 02/02/2020 19:24 | FP |
| 35 | 16,61 | 39,07 | 7 | 25 | 85 | -90 | 205 | 5 | -90 | 08/02/2020 22:59 | FP |
| 36 | 16,19 | 39,33 | 10 | 353 | 47 | -114 | 206 | 48 | -66 | 24/02/2020 16:02 | RCMT |
| 37 | 16,61 | 39,08 | 6,9 | 45 | 70 | -90 | 225 | 20 | -90 | 29/02/2020 17:05 | FP |
| 38 | 16,61 | 39,08 | 6,9 | 45 | 75 | -85 | 206 | 16 | -108 | 20/03/2020 17:32 | FP |
| 39 | 16,43 | 39,25 | 15 | 13 | 50 | -88 | 190 | 40 | -92 | 11/08/2020 01:36 | TDMT |
| 40 | 16,90 | 39,36 | 26 | 280 | 49 | -24 | 26 | 72 | -136 | 19/05/2022 21:01 | FP |
| 41 | 16,90 | 39,36 | 23,8 | 302 | 41 | -36 | 61 | 67 | -125 | 19/05/2022 21:06 | FP |
| 42 | 16,91 | 39,35 | 25,3 | 312 | 25 | 72 | 152 | 66 | 98 | 20/05/2022 03:59 | FP |
| 43 | 16,18 | 39,63 | 10,8 | 220 | 50 | -80 | 25 | 41 | -102 | 28/11/2023 11:13 | FP |
| 44 | 16,99 | 39,37 | 25 | 20 | 79 | 143 | 118 | 54 | 13 | 29/05/2024 12:07 | TDMT |
| 45 | 16,99 | 39,34 | 19 | 15 | 67 | 130 | 130 | 45 | 34 | 01/06/2024 14:23 | TDMT |

*Table 3-2: Collection of the focal mechanism solutions in northern Calabria, plotted on Figure S2. The highlighted cells represent the nodal plane that more likely created the associated event (yellow: strong reliability; orange: weak reliability)*

### *Geodetic slip rate*

As mentioned before, geologic slip rate data are not available for every source present in northern Calabria. In this case, geodetic data can provide an insight for the slip rate. Meschis et al. (2022) used GNSS data to determine the regional strain rate in Calabria. Then, knowing the dip-angle of the faults, the net slip rate on the fault can be approximated.

The San Sosti – Acquaformosa and Altomonte – Centrale Tallarito systems are two sub-parallel potential sources for which no geologic slip rate was found in the literature. The strain rate around the Acquaformosa GNSS station was estimated using a methodology similar to that of Meschis et al. (2022). The analysis, performed with the GridStrain MATLAB tool developed by Teza et al. (2008), yielded a strain rate of $1.55 \times 10^{-8}$ $yr^{-1}$ (minimum $1.2 \times 10^{-8}$ $yr^{-1}$ and maximum $1.9 \times 10^{-8}$ $yr^{-1}$, this maximum value is shown in Figure 3-23). The distance between the AQSA and SLDV stations is around 20 km. By multiplying those two values, a horizontal slip rate in this area of 0.3 mm/yr is obtained. Given the dip-angle at depth previously determined (50°), the net slip rate is easily calculated with: $\frac{0.3}{cos(50°)} = 0.47\ mm/yr$. This slip rate value represents the total slip rate in this area but as two potential sources are present inside, this value is exclusively assigned to each individual source (San Sosti and Altomonte-Tallarito) considered in alternative scenarios.

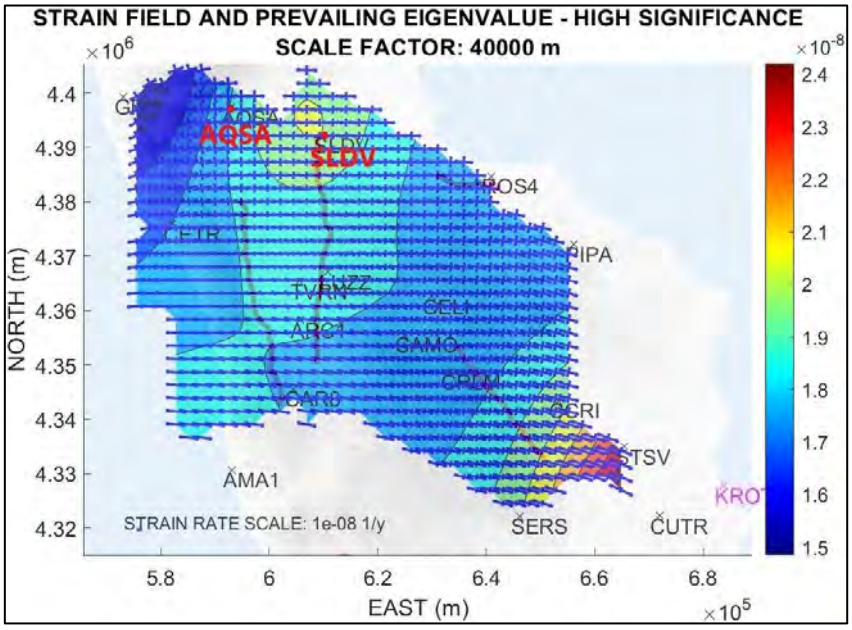



*Figure 3-23: Maximum strain field obtained from GNSS data in northern Calabria. The Acquaformosa (AQSA) and San Lorenzo del Vallo (SLDV) stations are represented on the map. The strain field between those two stations is around 1.9 E-8 yr-1.*

### 3.3.3. Rupture scenarios

As mentioned in the previous section, the activity of some potential sources remains debated. Therefore, four scenarios representing alternative source configurations that account for source-specific activity uncertainty are considered in northern Calabria. Each scenario assumes mutually exclusive activation of either the East Crati or West Crati source, and either the San Sosti-Acquaformosa or Altomonte-Tallarito source (Figure 3-24). This approach is

adopted to avoid double-counting seismic hazard, as faults considered connected at depth cannot be treated as independent sources. Regarding the VEA25 combination selection, combinations B and C include the additional distributed rupture (DR) ranks 1.5, 2.2, 2.3, and 3. Among these, ranks 1.5 and 3 could be interesting for us: rank 1.5 accounts for faults that are connected at depth (Figure 1-12b), while rank 3 represents ruptures that may be triggered on faults during an earthquake on an adjacent primary fault source (Figure 1-12b). However, to maintain consistency with our scenario-based framework and to limit computational complexity, we adopt the simpler combination A, considering only rank 2 DR associated with rank 1 primary faults (PF). In our approach, alternative faults are treated as mutually exclusive and are therefore not allowed to coexist within the same scenario. This assumption is incompatible with rank 1.5, which implies geometrical connectivity between faults. Including such cases would lead to inconsistencies between the YEA03 scenarios (where alternative faults are excluded) and the VEA25 implementation (where they would be implicitly included), ultimately resulting not only to biased averaging but also to spatial inconsistencies in the resulting hazard maps, due to the uneven inclusion or exclusion of fault sources across scenarios. In addition, the Amendolara source is excluded from the calculations because of its offshore location. It lies more than 10 km from the coastline, which is the classic threshold beyond which the probability of distributed of surface rupture is considered negligible. Nevertheless, this source could probably lead to tsunami hazard, but this is beyond the scope of this research.

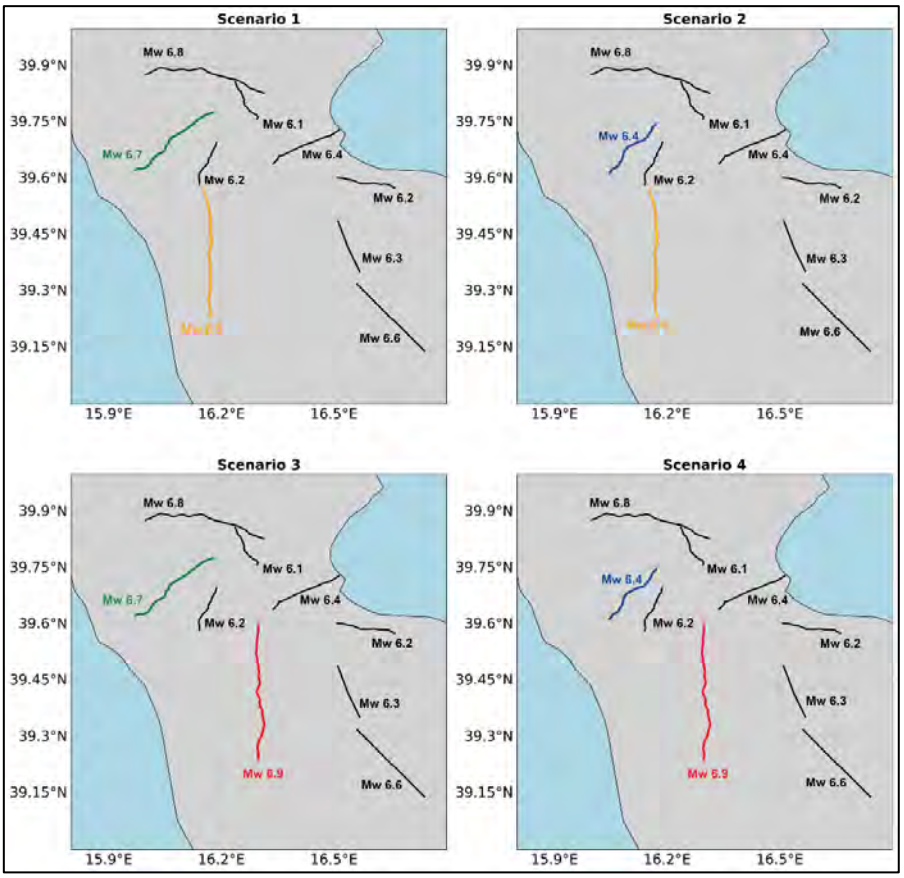



*Figure 3-24: Geometric sketch of the four scenarios used in our study (alternative fault pairs are shown in red and yellow for the East Crati and West Crati faults, and in green and blue for the San Sosti and Altomonte-Tallarito faults, respectively).*

## 3.4. MFD characterisation

After defining and parametrising the source model, the second step is to characterise, for each source, the earthquake frequency or activity rate $\alpha$ and the maximum magnitude expected $M_{max}$. To estimate these two parameters for each source, the open-source code FiSH (Pace et al., 2016) is used. Given the geometrical and kinematic parameters of the source, and various formulations of empirical relationships, it derives probability density functions of the complete rupture of the fault (Maximum magnitude), budgeting the total amount of seismic moment derived from the geometry and slip rate, as it computes activity rates given a pre-defined Magnitude-Frequency Distribution (MFD) model. Given the substantial lack of medium-to-small events in the historical and instrumental earthquake catalogue that could be associated with the sources, to model a more traditional log-linear MFD (Gutenberg-Richter type), a Characteristic Gaussian model is preferred here. In addition, although some sources, such as Rossano, Amendolara or Laghi, are associated with historical earthquakes and could potentially be modelled using a time-dependent approach (e.g., Brownian Passage Time), a

time-independent Poissonian model is adopted instead to ensure consistency across all the sources. This type of MFD allocates the total seismic moment budget on a Gaussian distribution, centred on $M_{max}$ , within a magnitude range of one sigma. $M_{max}$ are calculated using various empirical relationships from Wells and Coppersmith (1994) for normal, strike-slip and reverse faulting and then averaged (Figure 3-25).

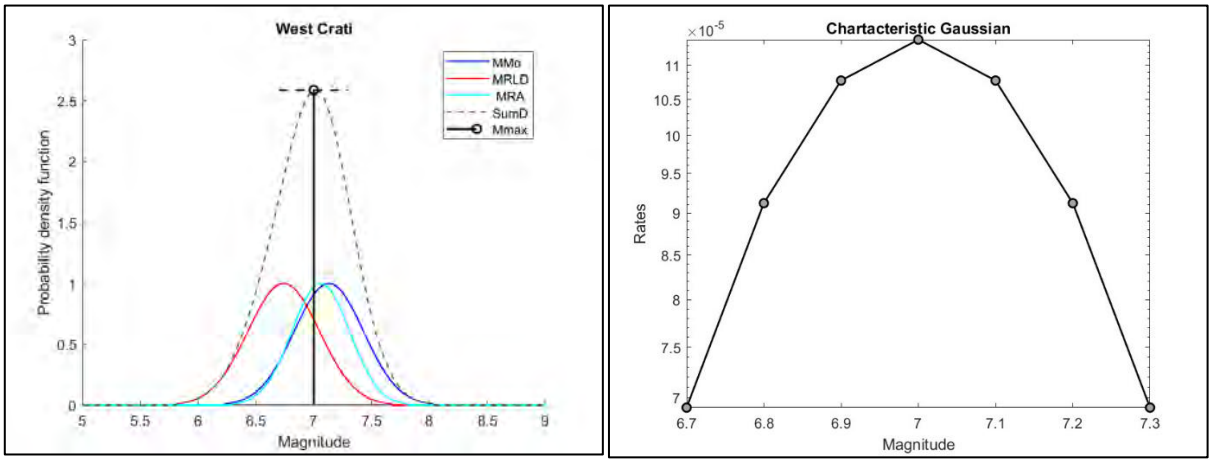



*Figure 3-25: MFD characterisation for the West Crati source. On the left: Magnitude estimations using various scaling relationships from Wells and Coppersmith, (1994). MMo: Moment magnitude; MRLD: Magnitude from rupture length at depth; MRA: Magnitude from rupture area; SumD: sum of the magnitude distributions; Mmax: Averaged maximum magnitude expected. On the right: activity rate distribution.*

The maximum displacement (MD) and average displacement (AD) are two other crucial parameters used in PFDHA, as they modulate the ratio D/AD or D/MD in the $P(D>d)_{princ.}$ term in Eq. (5) and Eq. (6). No reliable observations are available for the analysed sources, and thus they are computed from magnitude scaling relationships of Wells and Coppersmith (1994), with the suitable style of faulting for each source (normal, strike-slip or reverse faulting).

The computed $M_{max}$, the activity rates and other source parameters are reported in Table 3-3, which lists the final set of seismic sources parametrised in this study. By using a characteristic earthquake MFD, a kind of *worst-case scenario* approach is adopted, assuming that each fault source ruptures completely. However these *worst-case scenarios* are framed in a probabilistic approach, as the probability of occurrence of such full-rupture earthquakes is considered through the activity rate $\alpha$.

| Source ID | Source name | Length (km) | AD (m) | MD (m) | Mmax | Activity rate | | | | | | |
|---|---|---|---|---|---|---|---|---|---|---|---|---|
| | | | | | | Mmax - 0,3 | Mmax - 0,2 | Mmax - 0,1 | Mmax | Mmax + 0,1 | Mmax + 0,2 | Mmax + 0,3 |
| 1 | Pollino | 30.0 | 0.59 | 1.16 | 6.7 ± 0.3 | 6.91E-05 | 9.13E-05 | 1.08E-04 | 1.14E-04 | 1.08E-04 | 9.13E-05 | 6.91E-05 |
| 2 | Castrovillari | 13.0 | 0.25 | 0.34 | 6.1 ± 0.3 | 2.00E-04 | 2.64E-04 | 3.12E-04 | 3.30E-04 | 3.12E-04 | 2.64E-04 | 2.00E-04 |
| 3 | Amendolara | 17.5 | 0.59 | 1.04 | 6.4 ± 0.3 | 5.64E-05 | 7.45E-05 | 8.80E-05 | 9.30E-05 | 8.80E-05 | 7.45E-05 | 5.64E-05 |
| 4 | San Sosti-Acquaformosa | 26.0 | 0.59 | 1.16 | 6.7 ± 0.3 | 5.64E-05 | 7.44E-05 | 8.79E-05 | 9.29E-05 | 8.79E-05 | 7.44E-05 | 5.64E-05 |
| 5 | Altomonte-Tallarito | 19.0 | 0.38 | 0.63 | 6.4 ± 0.3 | 8.91E-05 | 1.18E-04 | 1.39E-04 | 1.47E-04 | 1.39E-04 | 1.18E-04 | 8.91E-05 |
| 6 | Farneto-Roggiano | 13.7 | 0.29 | 0.41 | 6.2 ± 0.3 | 1.67E-05 | 2.20E-05 | 2.60E-05 | 2.75E-05 | 2.60E-05 | 2.20E-05 | 1.67E-05 |
| 7 | Sibari | 18.5 | 0.28 | 0.36 | 6.4 ± 0.3 | 1.01E-04 | 1.34E-04 | 1.58E-04 | 1.67E-04 | 1.58E-04 | 1.34E-04 | 1.01E-04 |
| 8 | West Crati | 36.0 | 0.79 | 1.74 | 6.9 ± 0.3 | 9.76E-05 | 1.29E-04 | 1.52E-04 | 1.61E-04 | 1.52E-04 | 1.29E-04 | 9.76E-05 |
| 9 | East Crati | 41.5 | 0.79 | 1.74 | 6.9 ± 0.3 | 7.09E-05 | 9.36E-05 | 1.11E-04 | 1.17E-04 | 1.11E-04 | 9.36E-05 | 7.09E-05 |
| 10 | Rossano | 15.0 | 0.29 | 0.41 | 6.2 ± 0.3 | 1.41E-04 | 1.86E-04 | 2.20E-04 | 2.33E-04 | 2.20E-04 | 1.86E-04 | 1.41E-04 |
| 11 | Laghi | 25.0 | 0.51 | 0.94 | 6.6 ± 0.3 | 1.95E-04 | 2.58E-04 | 3.05E-04 | 3.22E-04 | 3.05E-04 | 2.58E-04 | 1.95E-04 |
| 12 | Cecita | 15.7 | 0.33 | 0.51 | 6.3 ± 0.3 | 2.18E-04 | 2.88E-04 | 3.40E-04 | 3.60E-04 | 3.40E-04 | 2.88E-04 | 2.18E-04 |

*Table 3-3: Final parametrised source model for northern Calabria.*

## 3.5. PSHA calculations in northern Calabria

A way to assess whether our new parameterised model is reliable and reasonable in terms of source geometry is to compute the ground-motion hazard map for northern Calabria and to compare it with the Italian national hazard map (MPS04; Meletti et al., 2006, Stucchi et al., 2011, Figure 3-26). The goal is not to reproduce the reference model exactly, but to obtain comparable results within the same range, thereby verifying that our model provides a realistic representation of seismic source size and contribution in the study area. The MPS04 map is based on the seismic zonation (ZS9 model, Meletti et al., 2008), in which Italy is divided into seismogenic zones defined from geological, tectonic, and historical seismicity data. Within each zone, earthquake occurrence is computed using a Poisson process and a Gutenberg–Richter frequency–magnitude relationship, with parameters derived from the national earthquake catalogue CPTI04 (Catalogo Parametrico dei Terremoti Italiani; Gasperini et al., 2004). Ground motion is estimated through a set of attenuation relationships (Ground Motion Prediction Equations, GMPE) combined within a logic-tree framework to account for epistemic uncertainties, ultimately producing probabilistic seismic hazard maps in terms of PGA for specified exceedance probabilities (e.g., 10% in 50 years). In northern Calabria, MPS04 predicts maximum PGA values of about 0.25–0.275 g for a 10% probability of exceedance in 50 years, among the highest in Italy.

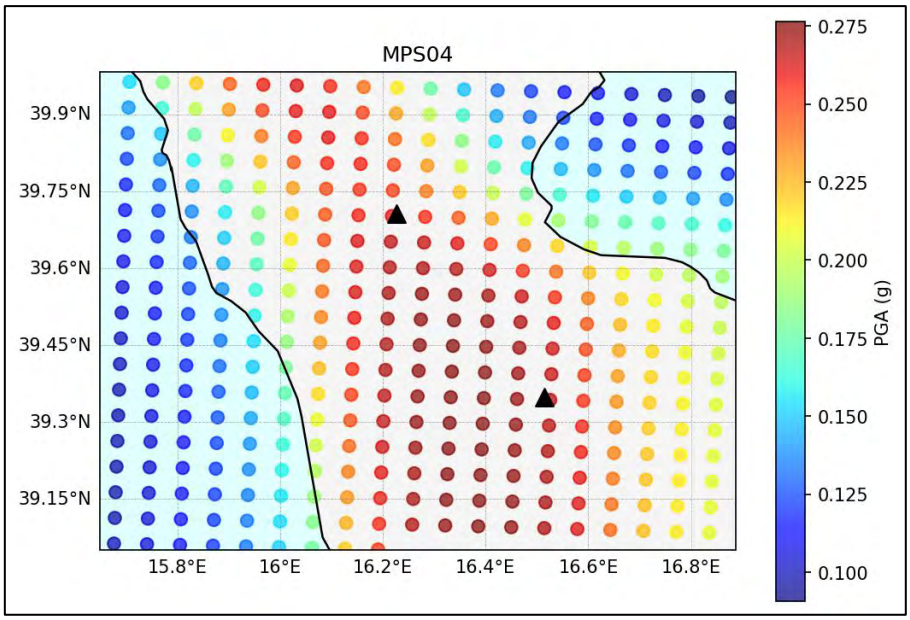



*Figure 3-26: Northern Calabria hazard map representing the PGA having 10% chance to be exceeded in the next 50 years. The triangles represent the two sites chosen for hazard curves comparison. Data from MPS04 (Meletti et al., 2006).*

For the four scenarios explored in northern Calabria, the ground motion hazard maps are computed using the OpenQuake Engine software (Pagani et al., 2014) and are shown in Figure 3-27. The four maps are very similar across scenarios and show a similar spatial pattern of high hazard: concentrated in the Sila Massif and the Crati Basin, with maximum values around 0.25 g. They slightly differ by the PGA values particularly within the Crati Basin, where the alternative fault configurations have a visible impact: PGA increases from ~0.20 g in scenarios 1-3 to ~0.24 g in scenarios 2-4). For each scenario, the differences with the MPS04 map are also represented in Figure 3-27. Overall, our new fault model tends to underestimate the hazard, with an average ΔPGA of about -0.05 g. However, two main areas exhibit higher discrepancies. The first corresponds to the northern and southern map boundaries, where PGA is underestimated (up to ~0.18 g), likely due to the absence of contribution from sources located outside the modelled area. The second is the Crati Valley, where the hazard is also underestimated by our model (ΔPGA ~0.10 g).

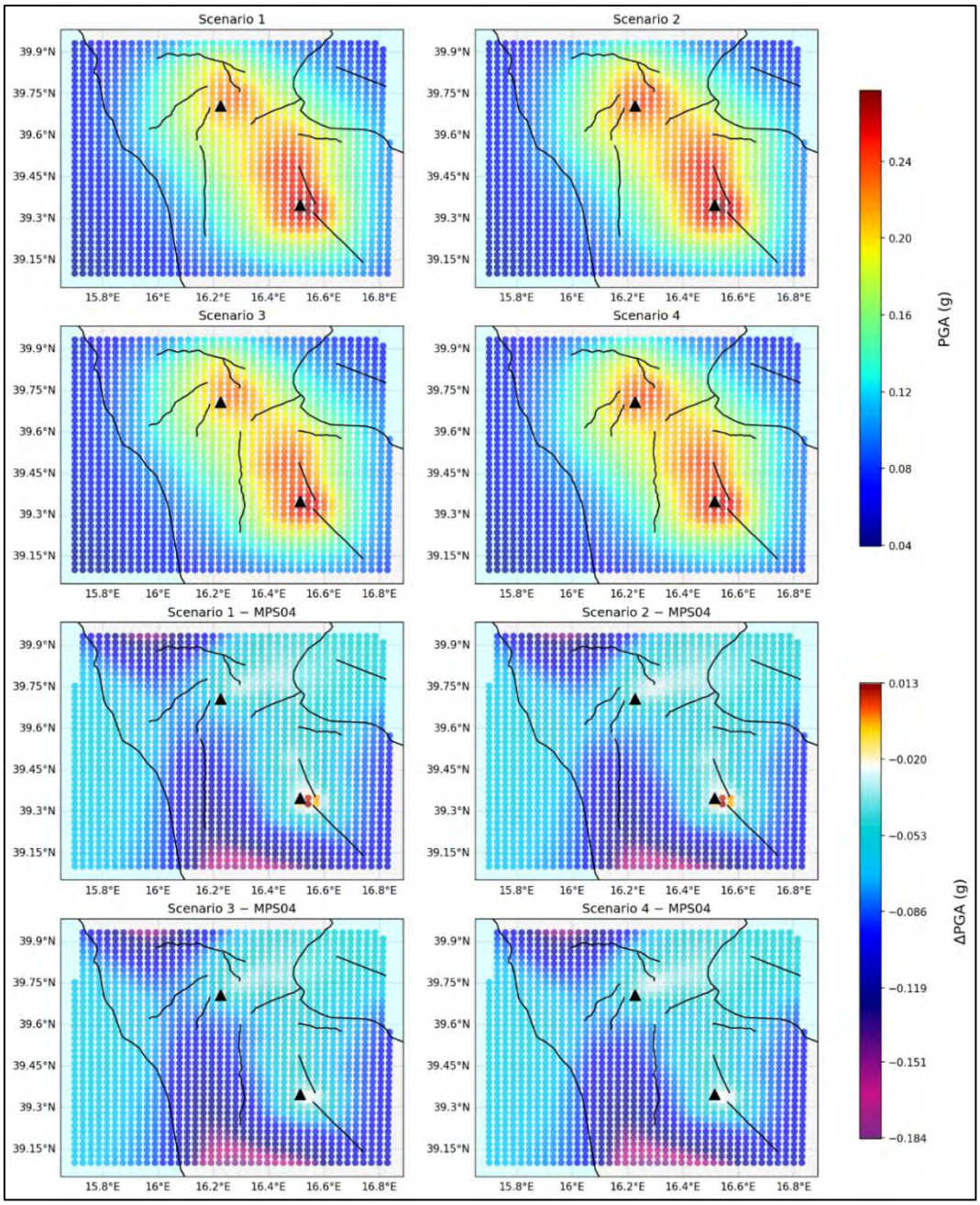



*Figure 3-27: Seismic hazard maps derived from our fault model for northern Calabria. The top four panels show the four fault-configuration scenarios (PGA, 10% probability of exceedance in 50 years), while the bottom four illustrate the differences relative to the MPS04 dataset (Meletti et al., 2006).*

Additionally, two specific sites, one located in the central part of the Crati Basin and the other in the Sila Massif, are selected to compare site-by-site the hazard. The hazard curves corresponding to a 10% probability of exceedance in 50 years (POE) are shown in Figure 3-28. For both sites, the alternative scenarios yield very similar results, as the hazard curves are nearly perfectly overlapping, which is consistent with the observations done from the map. The MPS04 curve and those obtained with our new fault model exhibit different behaviours; however, they fall within the same range and order of magnitude, which supports the overall

consistency and reliability of the proposed parametrised model.

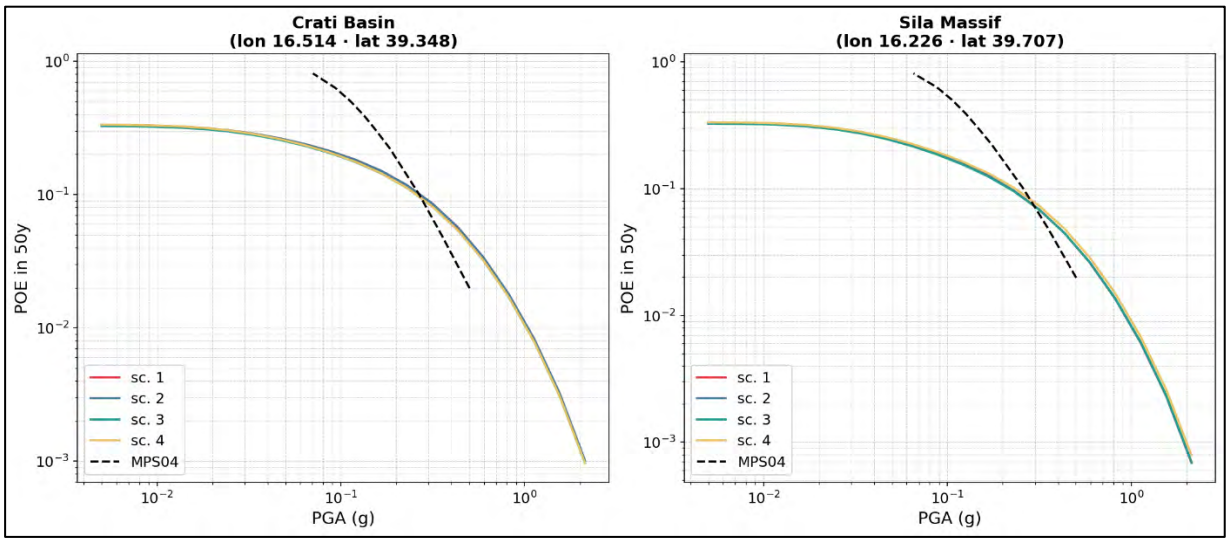



*Figure 3-28: Probability of exceedance in 50 years comparison for two sites in northern Calabria (Crati Basin on the left and Sila Massif on the right side).*

## 3.6. PFDHA calculations in northern Calabria

In this section, we perform hazard map calculations at a regional scale in northern Calabria but also focus on specific sites for directly comparing the models' variability through hazard curves.

### 3.6.1. Model selection and parametrisation

Regional-scale mapping and single site-specific analyses are both controlled by the choice of models, and displacement metrics, but in different manners. In a spatial representation of hazard, where both on-fault and off-fault have to be used, results of different models can be compared to evaluate the impact of model choices or can be weighted using a logic-tree approach, only if the displacement metrics of all the models are coherent and compatible together. For example, aggregate displacement from LEA23 cannot be used in a logic-tree along with a classic on-fault/off-fault (such as YEA03) since they do not represent the same things. Similarly, consistency among displacement components across the different models must also be evaluated. In northern Calabria, both normal and strike-slip faults are present, producing vertical and horizontal displacements, respectively. Representing these components on the same map without distinction would be meaningless and potentially misleading. Although net slip could in principle be derived from the fault dip angle and slip vectors for all faulting styles, this approach is not appropriate here because of the associated uncertainties. Therefore, we display normal and strike-slip faulting on the same maps using different colour scales, which does not

introduce ambiguity, as the two faulting styles affect different areas (see section 3.5.2.).

The models and the logic-tree approach used for the hazard map calculations are described in Table 3-4 and Figure 3-29. For normal faults, YEA03 is used for both principal and distributed faulting and VEA25 only for DR. In the case of VEA25, only combination A (e.g. rank 2 DR relative to rank 1 PF) is tested as it is the most relevant. Combinations B and C are not suitable since, based on our fault model, no rank 1.5 ruptures are possible here (see section 3.2.3.). For strike-slip, only PEA11 is based on the classic on-fault/off-fault rupture definitions.

| Model | Faulting style | Displacement metrics | Slip component | Displacement type |
|---|---|---|---|---|
| **YEA03** *(Youngs et al., 2003)* | N | D/AD, D/MD | vertical | Single principal and single distributed |
| **PEA11** *(Petersen et al., 2011)* | SS | D, D/AD | horizontal | |
| **KEA24** *(Kuehn et al., 2024)* | N<br>SS<br>R | D | net | Aggregate displacement |
| **LEA23** *(Lavrentiadis et al., 2023)* | N<br>SS<br>R | D, AD, MD | net | Sum of principal<br>&<br>Aggregate displacement |
| **VEA25** *(Visini et al., 2025)* | N<br>R | D, PF throw | vertical | New definition of distributed faulting (rank 1 / 1.5 / 2 / 3) |

*Table 3-4: Summary of the fault displacement hazard models used in our calculations.*

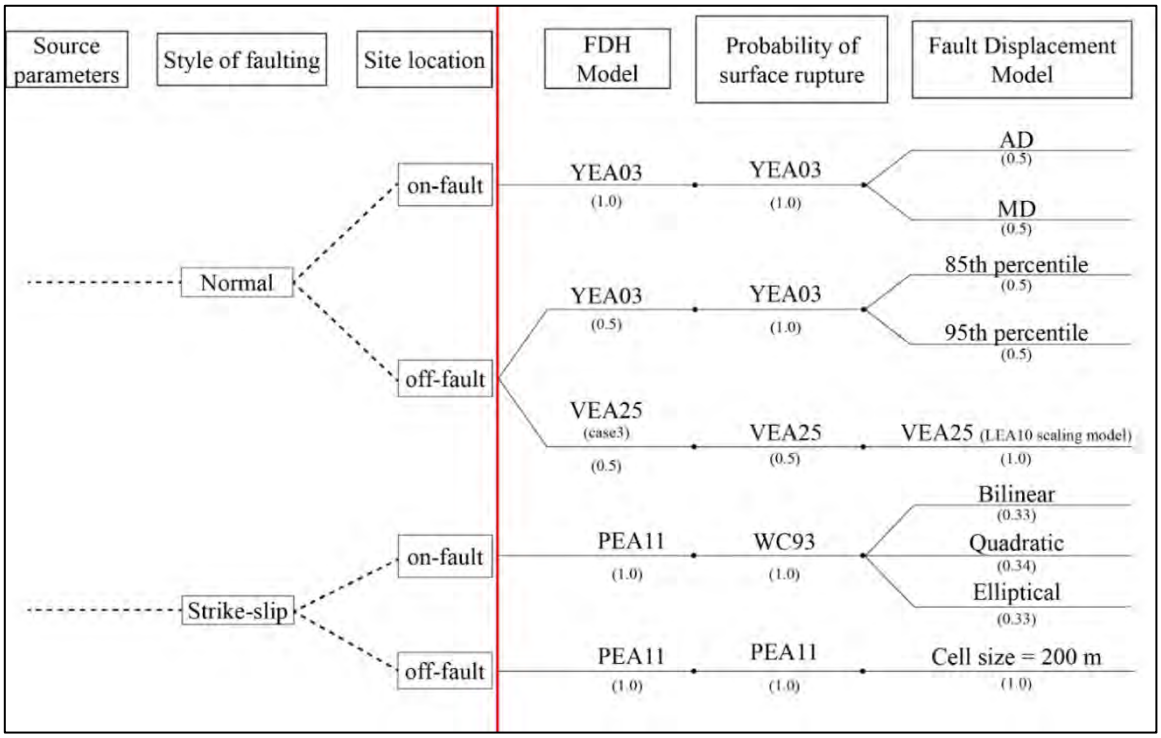



*Figure 3-29: Logic flow used for fault displacement hazard map calculations. On the left of the red line, alternative choices are site-dependent; on the right, different branches of the logic-tree approach are modelled for all the sites. WC93 stays for Wells and Coppersmith, 1993; LEA10 for Leonard et al., 2010 (both applied for*

*calculating the throw (AD) on the principal fault). Other acronyms are previously defined in the text.*

After addressing these parametric variabilities, further methodological settings must be established to generate the hazard maps. For principal faulting, fault traces are resampled and sites are defined every 200 m, whereas for distributed faulting a grid with a spacing of 0.05° is adopted. Hazard curves are computed for all fault-trace sites and for all grid sites located within 10 km of the nearest fault, beyond which the hazard is considered negligible. To construct the hazard maps, the displacement value corresponding to the target annual rate of exceedance is extracted from each hazard curve and plotted. The target annual rate is defined as the inverse of the selected return period (1/RP), with RP equal to 10 ka or 100 ka. Additionally, since the cell size for off-fault displacement is set at 500 m in YEA03, we use the same size with VEA25, where 50 m and 500 m are available. Similarly, in PEA11, a 500 m cell size is not available, so we use the largest available, 200 m.

Finally, it has to be remembered that YEA03 and VEA25 use entirely different approaches to model distributed rupture probability. YEA03 uses a gridding approach: the study area is divided into square cells (500×500 m), and the probability of distributed rupture within each cell is computed as the ratio of cells containing distributed ruptures to total cells. VEA25 uses the slicing approach: the probability is decomposed into P_slice (across-strike, based on distance r) and P_along (along-strike, via Monte Carlo simulation of the F ratio). So, there are across-strike site and along-strike site dimensions, handled separately. "Matching" the same spatial grid resolution has a remarkable impact on results, as it is shown in the site-specific cases (section 3.5.2.2.), but an in-depth discussion on this topic goes beyond the scope of this paper, and should be addressed in future works.

For site-specific analyses (section 3.5.2.2.), we directly compare the older model (YEA03) with the newer ones: LEA23, KEA24, and VEA25, that use various displacement metrics which are, in this case, not a limitation anymore.

All calculations presented in this study, both site-specific and regional-scale, were performed using a prototypal PFDHA module (Chen et al., 2025) built upon the open-source OpenQuake Engine (Pagani et al., 2014). This module provides a standardised computational pipeline for surface rupture hazards, integrating both principal and distributed faulting models. Individual model implementations have been verified against published reference implementations (Sarmiento et al., 2025) and against original source codes provided by model developers.

### 3.6.2. Regional-scale mapping

In our opinion, the main interest of a regional-scale mapping of the displacement hazard is the comparison of alternative scenarios, as they represent irreducible epistemic uncertainties, and the visualization of the weight and potential interference of various sources, for prioritization of further investigation, or for regulation/planning purposes. Figure 3-30, for example, shows the hazard maps for scenario 3 with a return period of 100 ka, using the two models, YEA03 and VEA25, that have compatible displacements metrics. Coloured areas represent the portion of the territory where an appreciable surface displacement is expected (d>1 cm). VEA25 model displays a larger coloured area around each source than YEA03 (i.e., larger area affected by significant distributed faulting). This is especially evident in the area between the San Sosti and Farneto faults.

It is particularly important to understand how these maps are constructed. As explained in section 3.5.1, hazard curves are computed for each site; however, only those sites where the hazard curve reaches the target rate are shown on the map. Consequently, locations with zero displacement on the maps do not indicate the absence of hazard but rather reflect the applied thresholding of the hazard curves. Similarly, when different models are combined according to the simplified logic-tree scheme of Figure 3-29, it is done by averaging the hazard curves (i.e., the annual rates) at each site before constructing the map. So, a site showing a zero displacement in Figure 3-30 (e.g. YEA03) can actually contribute to the averaged hazard curve, explaining why the number of the non-zero displacement sites of the average is different from the models it is calculated from. For example in Figure 3-31b, the resulting averaged displacement map for scenario 3, built from the two maps shown on Figure 3-30, shows an intermediate spatial extent, with 7119 grid sites exceeding the target rate, compared to 6150 sites in YEA03 and 7672 sites in VEA25.

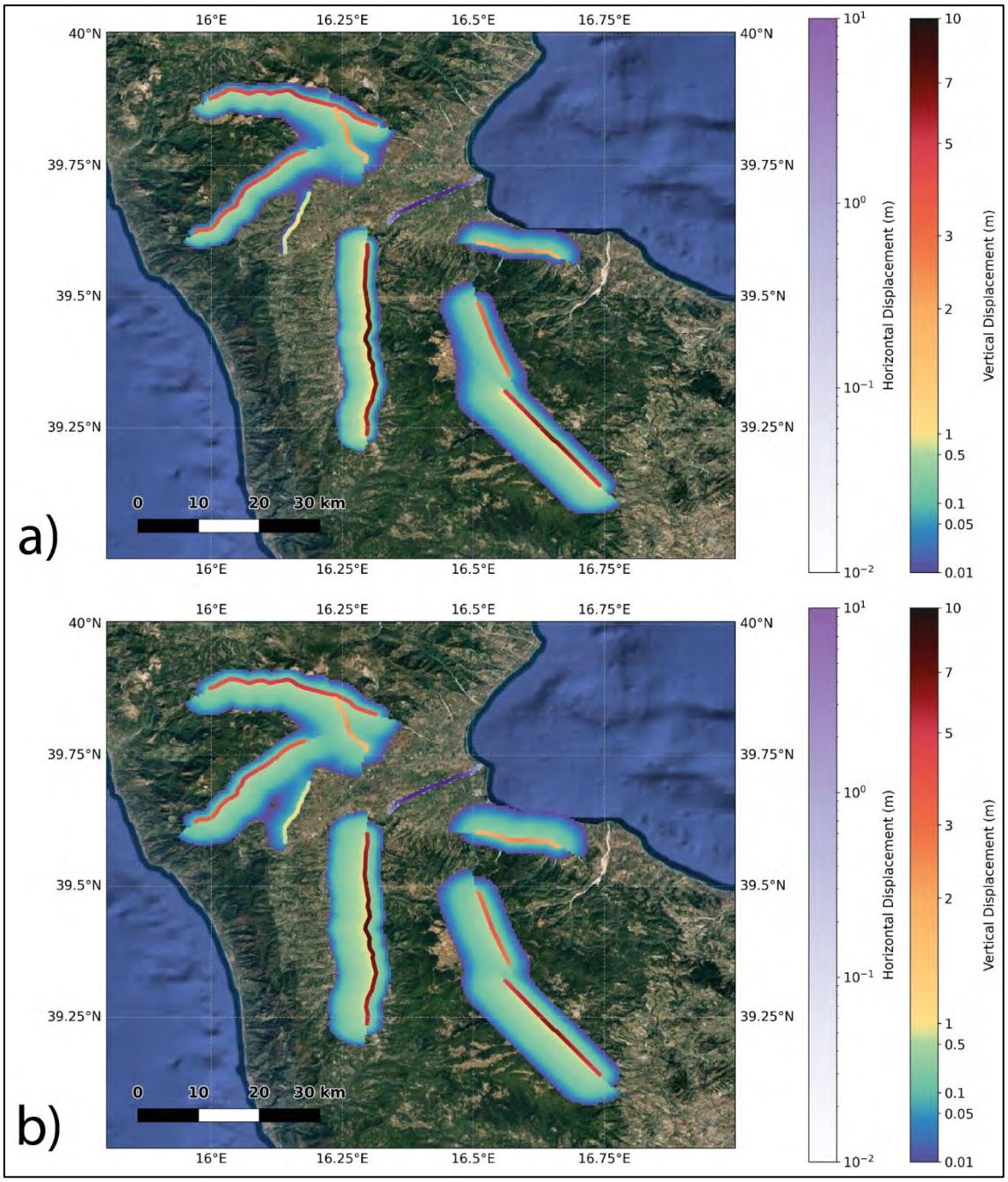



*Figure 3-30: Fault Displacement Hazard maps comparison between YEA03 (frame a) ) and VEA25 (frame b) ) for scenario 3 and a return period of 100 ka. The colour scale bars are different for horizontal and vertical displacements, representing respectively strike-slip and normal faults.*

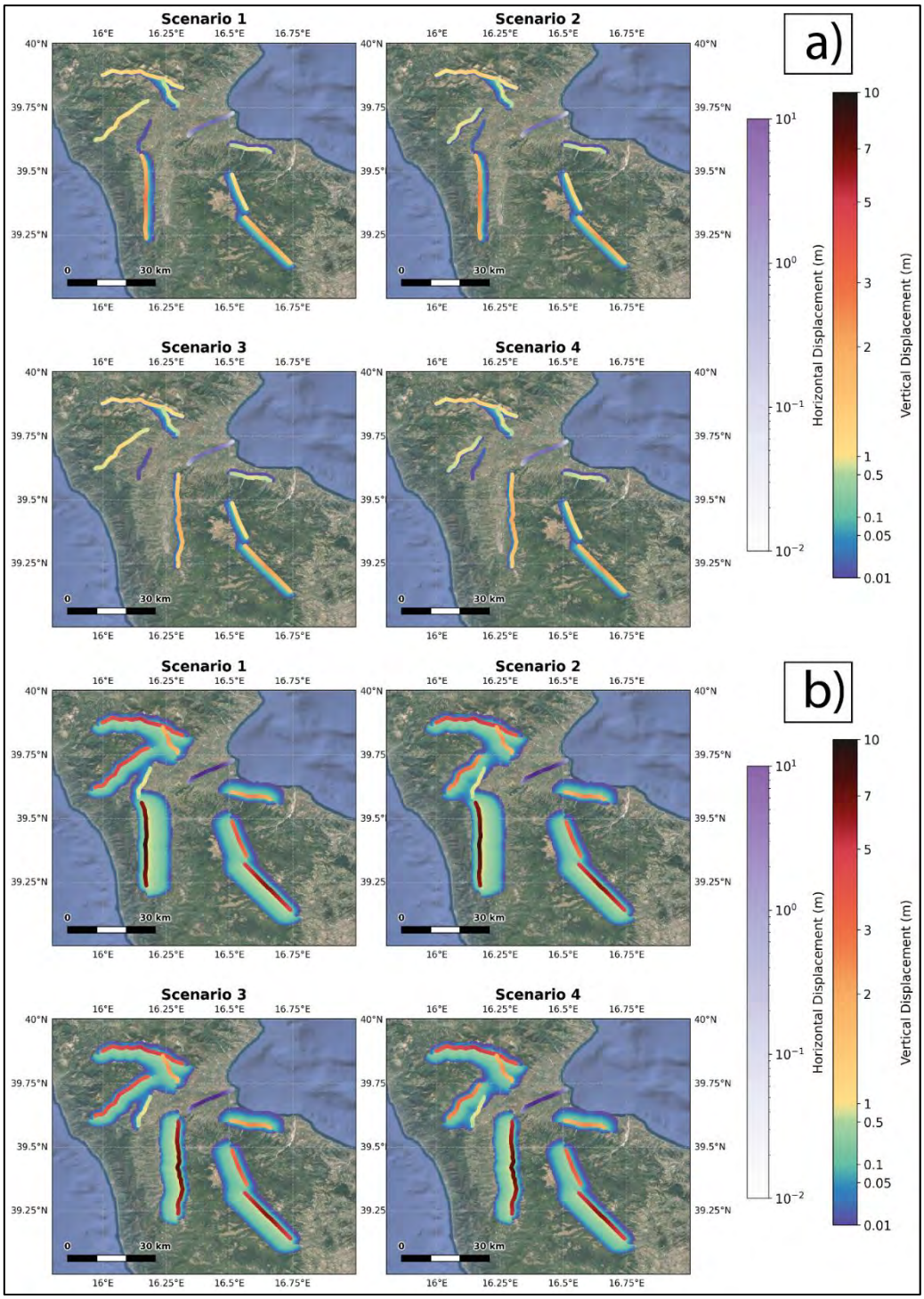



*Figure 3-31: 4 scenario fault displacement hazard maps using YEA03 and VEA25 models equally weighted, a) for a return period of 10 ka, and b) for 100 ka. Colour scale bars as in the previous figure.*

## 3.6.3. Results and discussions

### *3.6.3.1 Regional PFDHA study*

The hazard maps for the four fault sources scenarios explored are shown in Figure 3-31. Each map represents the displacement expected in the given return period (10 ka and 100 ka). These two long periods are chosen following the first PFDHA study in the Yucca mountain (Stepp et al., 2001), which adopted 10 ka and 100 ka (or $10^{-4}$ and $10^{-5}$ $yr^{-1}$ for the annual rates of exceedance) based on the 'Frequency Category 1' and 'Frequency category 2' of the U.S Department of Energy at that time. These return periods also fall within the $10^{4}$–$10^{5}$ years (NEA, 2021) adopted in modern regulation of nuclear power plants, representing the conditions for safe shut down without release of radioactive material (Shutdown Earthquake - SSE, also called Design Basis Earthquake -DBE).

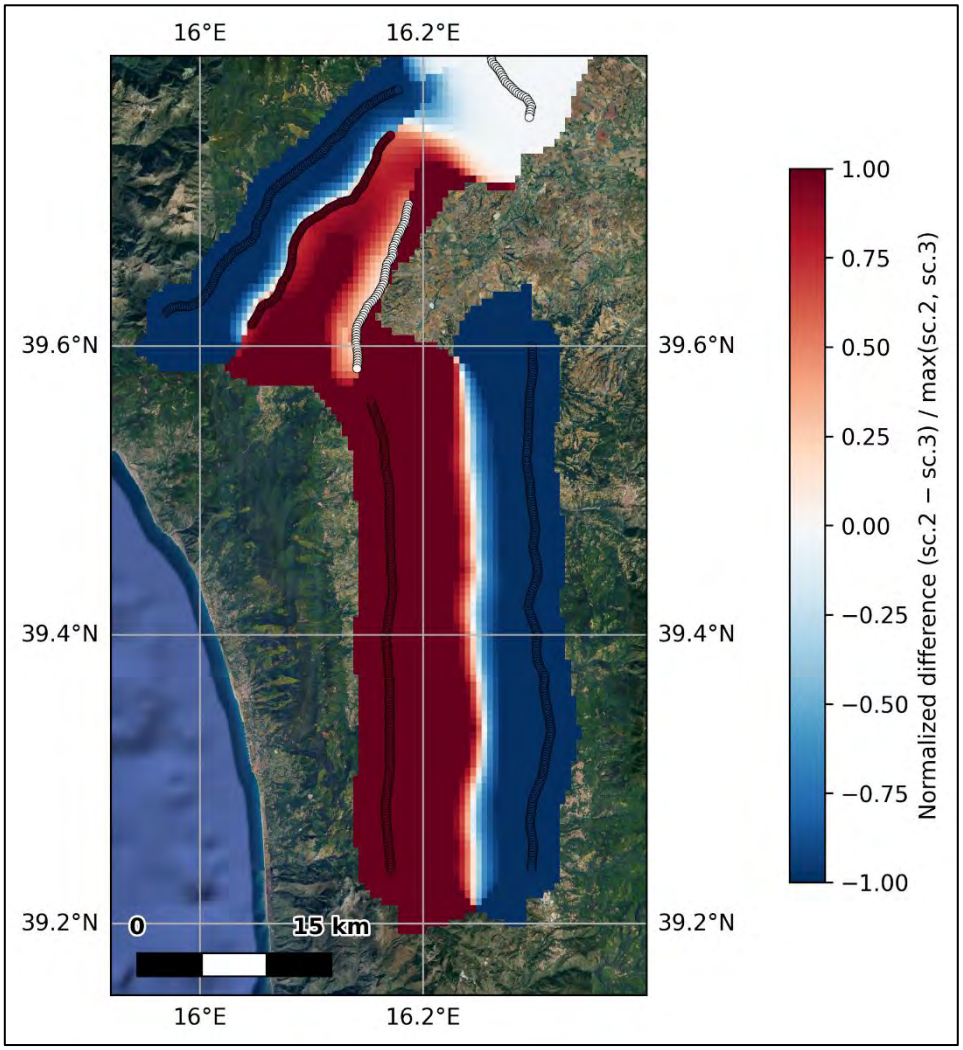



*Figure 3-32: Differences map between scenario 2 and scenario 3. Circles represent the sampled sites along the fault traces.*

Note that for a return period of 10 ka, the expected surface displacement is concentrated on the surface fault traces and within a few hundred metres around them; for 100 ka, a wide coloured stripe is present up to the maximum distance from the fault traces imposed in the calculation (10 km). However, the expected displacement decays rapidly to a few centimetres (blueish colour) in about 5 km distance from the main fault, and it is not symmetrical for normal faults; this is due to the different decays expected in hanging wall and footwall conditions.

Figure 3-32 represents an example of the maximum differences among scenarios in a selected sub-area including the fault sources San Sosti-Acquaformosa (ID n°4 in Table 3-3), Altomonte-Tallarito (n°5), Farneto-Roggiano (n°6), and West and East Crati valley faults (n° 8-9) (frame reference given in Figure 3-1). Scenario 2 is considered as the 'worst' case for reciprocal interferences, since the two closest, alternative faults (n°5 and n°8) are considered active. Conversely, a 'less dangerous' interference is modelled by scenario 3, as faults n°4 and n°9 are further away. For each site, the normalised difference of displacement at 100 ka return period is calculated as follows: (sc. 2 - sc. 3) / max (sc. 2; sc. 3) in order to avoid the division by 0 when only one scenario is influencing the site.

Areas in dark colours are controlled by a single scenario, respectively red for scenario 2 (in the colour scale normalised values > 0.75), and blue for scenario 3 (< -0.75). White areas and circles, such as in the northeastern corner and along n°6 source, represent sites not affected by the alternative scenarios. Conversely, it is interesting to note some thin stripes of whitish, or light red and blue, as they delineate sites that are less affected by the choice done by the sources models: this is the case for example along the N-S white axis of the Crati valley, where the expected displacement due to DR is invariant to the activation of the East or West Crati fault. Similarly, at the hanging wall of the Altomonte-Tallarito source, a thin white stripe delineates the sites equally affected by the DR due to the activation of the nearby source (n°5), or by the DR due to the westernmost, more distant and dangerous source n°4. These considerations may help quantifying the impact of epistemic uncertainties related to the fault source model. For end users, such comparisons provide an indication of the areas where hazard estimates are most sensitive to the assumed fault scenarios and where alternative interpretations of the seismotectonic framework may lead to significantly different displacement predictions. These zones can therefore be considered critical areas for preliminary planning purposes, potentially requiring avoidance. However, these regional-scale results should be regarded as a first-level evaluation, and site-specific studies remain necessary for detailed hazard assessment and engineering decisions.

### *3.6.3.2 Hazard curves for specific sites*

In this section, we focus on two specific sites in northern Calabria to highlight model variability in the two components of a PFDH analysis, i.e. the principal and distributed faulting. The two sites where hazard curves have been calculated are: Rovito (Cosenza province), a small municipality (about 3,000 inhabitants) intercepting the East Crati fault, is taken to illustrate the modelling variability related to principal faulting (red squares on Figure 3-1); and Castrovillari (Cosenza province, about 20,500 inhabitants) is retained for presenting the contribution of distributed faulting.

***Principal faulting case - Rovito***

Analysing a specific site instead of mapping an extended area prevents some inconsistencies coming from the different displacement metrics used by the various models. Here, we take Rovito town as a first study-case. The site coordinates we selected lie precisely on the surface trace of the East Crati fault, one of the most important (but still debated) fault sources in our regional model. The hazard in the selected site is dominated by principal faulting components, and we test the variability of different scenarios, and various models to calculate the total hazard curves. YEA03 model is compared with two more recent models, both applicable to principal faulting in a normal regime: KEA24 and LEA23. Regarding the parameter selection here, for YEA03 we test the same branches as in Figure 3-30, with both AD and MD, and 85th and 95th percentile, explored for principal and distributed faulting, respectively. These four branches are then combined with an equal weight and referred to as YEA03 (avg). The hazard curves of the two significantly different scenarios, 1 and 3, which consider whether or not the East Crati Fault is active, are shown in Figure 3-33a.

Scenarios 2 and 4 are discarded as their results in Rovito are nearly identical to those of scenario 1 and 3 respectively. Indeed the main difference in the hazard curves comes from the assumption that the East Crati Fault is the active one or not.

In both scenarios, the different models' curves are overlapping for small displacement values (up to about 10 cm, vertical black dotted line). YEA03 (solid line) decays slightly faster in scenario 3, up to about $10^{-5}$ yr, while in scenario 1 the LEA23 model (dash and dotted line) always gives slightly smaller displacements. Differences among the models are anyway very limited. At the AFOE value of $1\times10^{-4}$ yr, displacements of 1.52, 1.87, and 2.64 m are expected for YEA03, LEA3, and KEA24 models respectively, in scenario 3, while scenario 1 curves never intercept this $1\times10^{-4}$ yr rate. If we want to express the results in terms of probabilities of

exceeding a given displacement of 10 cm in 50 years, the POE (50y) are 2.21%; 2.42% and 2.58% for YEA03, LEA3 and KEA24, respectively for scenario 3.

As demonstrated before by Figure 3-32, the study site lies on a fault trace governed by principal faulting, and the alternative scenarios 1-2 (in which the West Crati Fault is active instead of the East Crati Fault) result in negligible displacement hazard at the Rovito site.

***Distributed faulting case - Castrovillari***

Castrovillari is the second municipality presented in this analysis: the selected site is located near, but not on top of, the Castrovillari and Pollino sources (Figure 3-1). Here, we examine the variability in the case of distributed faulting models, comparing the available estimates by YEA03 (using a 500 m grid size), and VEA25, using both 50 m and 500 m grid sizes, as our models. The different scenarios do not impact in this location and therefore only scenario 3 is given.

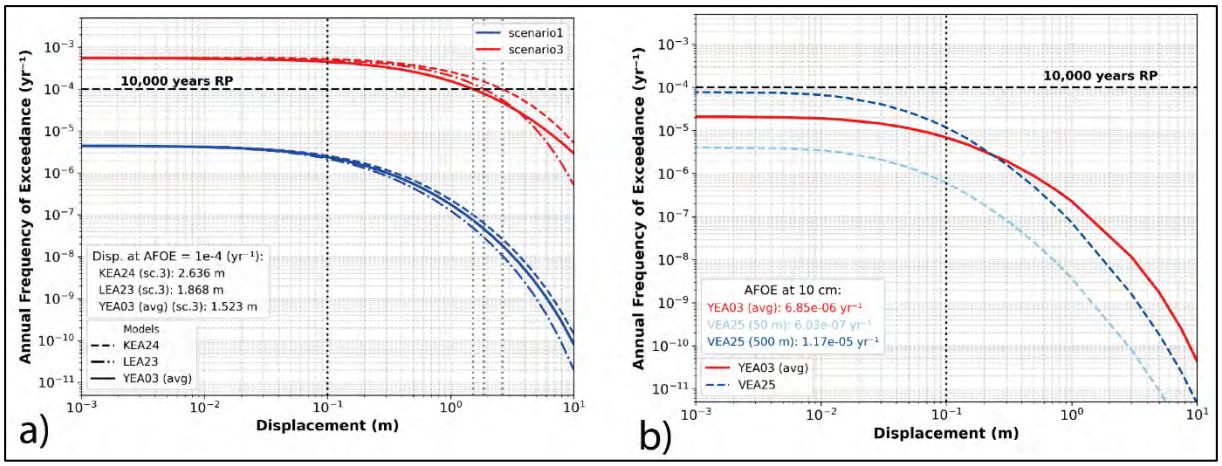



*Figure 3-33: Fault displacement hazard models variability a) for principal faulting on the East Crati fault (Rovito town); b) for distributed faulting in Castrovillari.*

In Figure 3-33b, we see that when using a grid size of 500 m, these two models intersect each other, with VEA25 giving a higher AFOE than YEA03 for small displacements ($10^{-4}$ to $10^{-1}$ m), and the contrary above about 20-30 cm of displacement. Using a smaller grid size in VEA25 (pale blue dashed line) the hazard curve shape is more similar to YEA03, but always significantly below it (one order of magnitude below).

The grid size selection, when available, is crucial for the type of site under investigation. Proper model and grid size selection are necessary for a specific site. For a large site, a larger grid size (i.e. 500 m) is acceptable, but for a point site, such as here, the smallest size is preferable, providing a more precise indication of the fault displacement hazard.

Apart from this observation, it is clear that the AFOE is lower than the 10E-4 value of interest for significant surface displacement values. For 10 cm, they are $6.85\times10^{-5}$, $6.03\times10^{-7}$, and $1.17\times10^{-5}$ for YEA03, VEA25 (50 m), and VEA25 (500 m), respectively. These values correspond to POE in 50 years for 10 cm of 0.342%, 0.003% and 0.059% for YEA03, VEA25 (50 m), and VEA25 (500 m), respectively, which are extremely low.

These results, obtained for both Rovito and Castrovillari, are consistent with the benchmarking exercise conducted by the IAEA (Figure 21 and 22 in: IAEA, 2025). For the on-fault case, the three models (YEA03, KEA24, and LEA23) provide comparable hazard estimates, with differences becoming more pronounced only for larger displacement values, as also observed in the benchmark. For the off-fault case, the results show a similar behaviour to the benchmark, with YEA03 predicting hazard levels approximately one order of magnitude higher than VEA25 when using comparable combinations (only rank 2 as DR) and spatial resolutions (500 m and 100 m in the benchmark, compared with 500 m and 50 m here for YEA03 and VEA25, respectively).

### *3.6.3.3 Some considerations on sigma truncation*

A preliminary sensitivity analysis on sigma truncation has been finally performed on Rovito results obtained with the most widely used model proposed by Youngs et al., 2003. This test was motivated by the large values of displacements obtained in the right tail of the hazard curve (about 10 m of displacement with AFOE ~ $10^{-6}$), as they are scarcely plausible even for a Mw ~ 6.9 rupture on East Crati Fault, see Table 3-3). In PFDHA, sigma truncation refers to limiting the range of variability (uncertainty) in the predicted quantity (fault displacement, or ground motion in PSHA), modelled empirically by a log-normal distribution with given standard deviation σ (sigma). The cutoff imposed by sigma truncation (typically at ± 2σ or ± 3σ, in the prototype tool used here set at ± 6σ) excludes extremely large values that have non-zero probability, and avoids giving weight to implausibly extreme displacement values that could otherwise dominate hazard estimates at very low probabilities (long return periods).

Figure 3-34 shows the impact of sigma truncation on the principal faulting displacement curve: note the different bending of the curves corresponding to 3-sigma truncation (standard values adopted in PSHA analyses) and 1-sigma, and the further decrease of values obtained with trial truncation at 0.5 sigma, or 0 sigma (thus using only the mean values of the empirical model).

We believe this test can help understand how rare-event hazard curves may be driven by extreme, poorly constrained displacement predictions, driving the hazard results towards more

physically reasonable and stable values, especially for engineering design application at low exceedance probabilities. It is beyond the scope of this paper to further comment on these results.

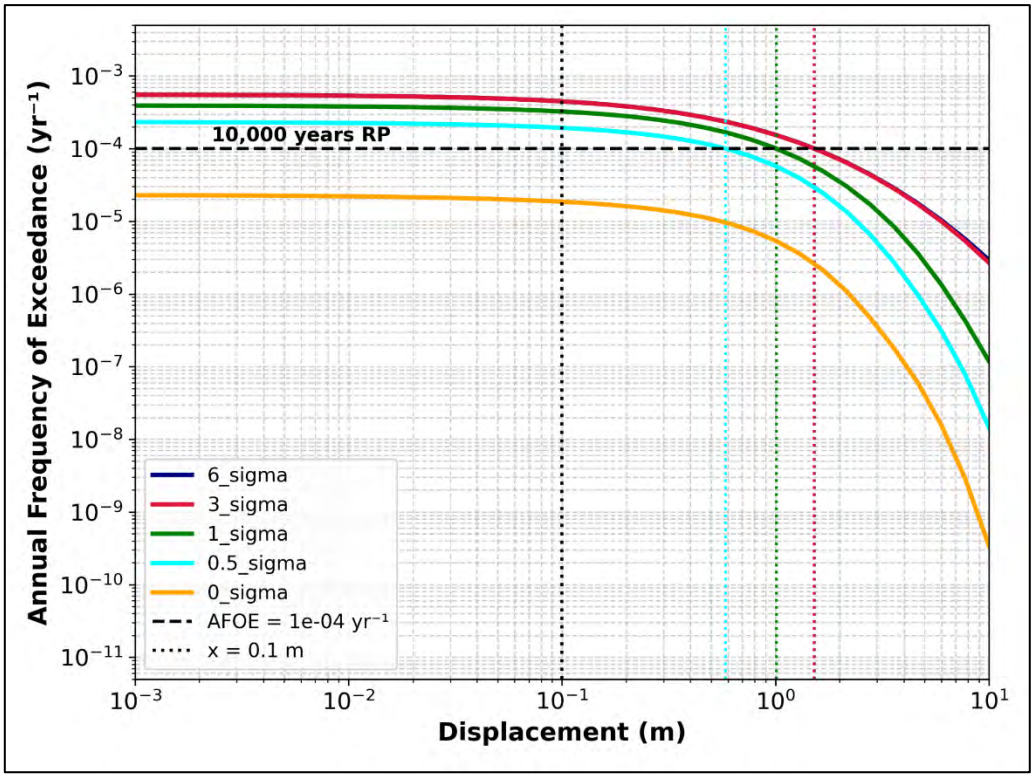



*Figure 3-34: Sigma truncation exploration at the Rovito site (using YEA03 only). The 6 sigma curve (the standard value set for our calculations) coincides with the 3 sigma truncation curve.*

## 3.7. Conclusions

- In northern Calabria, several seismic sources are capable of generating earthquakes with magnitudes greater than Mw 6.5, potentially producing surface rupture. However, the return periods associated with surface displacements significant for safety concerns (≥ 10 cm) are extremely long, generally exceeding 10 ka and, in some cases, 100 ka.
- The different scenarios highlight the importance of accurately defining the seismotectonic framework and the precise geometry and location of active and capable faults. The hazard is primarily controlled by the main fault systems and, consequently, by the surface expression of the fault traces.
- Conventional PSHA return periods (corresponding to annual probabilities of exceedance on the order of $10^{-3}$) are generally too short for PFDHA applications, as such thresholds are rarely reached for surface faulting events. Surface-rupturing earthquakes are significantly rarer than ground-motion exceedances. Therefore,

considering return periods on the order of 10 ka (corresponding to annual probabilities of exceedance of $10^{-4}$), or even longer, may be more appropriate for assessing the potential impact of earthquake surface rupture, especially for long-lived infrastructure that may be highly vulnerable to coseismic ground displacement.

- Sensitivity analyses on sigma truncation indicate that the large aleatory uncertainties inherent in PFDHA models strongly influence the results, leading to estimates of fault displacement at long return periods that may exceed physically plausible values based on fault dimensions. Therefore, the tails of the hazard curves should be truncated to maintain physically realistic displacement estimates.
- Epistemic uncertainties, particularly those related to fault-source characterization, have a major impact on the results and should therefore be carefully investigated and, where possible, reduced through detailed local-scale studies.
- PFDHA maps developed for different return periods can provide valuable support for risk mitigation strategies, infrastructure planning, lifeline resilience assessment, and territorial risk management.

# 4. General conclusions and perspectives

Fault surface rupture is a natural phenomenon whose occurrence and magnitude are primarily governed by three parameters:

- Earthquake magnitude: the stronger the earthquake, the greater the probability of surface rupture and the larger the displacement at the surface. Surface ruptures are generally generated by earthquakes with a Mw of 5–5.5.
- Hypocentral depth: a lower magnitude earthquake can potentially produce surface rupture if it is shallow.
- Style of faulting: Different tectonic contexts produce different surface displacements, which may be vertical, horizontal, or a combination of both.

In addition to these first-order controls, rupture occurrence and surface expression are also influenced by more complex factors, including fault geometry and segmentation, fault-zone architecture, and mechanical and lithological heterogeneities, which modulate rupture propagation and the distribution of deformation.

Surface fault displacement can have significant consequences on human society and must be considered and integrated in national and international building codes and civil engineering guidelines. Even though some engineering solutions can partly mitigate the consequences of such surface ruptures (e.g. Denali earthquake), the avoidance strategy of such hazard, i.e. capable fault, seems to be the safest approach.

PFDHA is currently the main approach to estimate this hazard, and such analyses are now required for both new and already existing nuclear infrastructures. The IAEA, as the leading regulatory body for the nuclear industry, has been crucial in driving research and providing guidance on this topic. PFDHA has been defined only recently, by Youngs et al. (2003) and has raised a lot of interest in the scientific community in the last decades. Considerable efforts all over the world have been made to collect both historical rupture data through paleoseismological trenches, and more recent data, through dedicated data collection campaigns conducted immediately after strong earthquakes. The SURE (Baize et al., 2019; Nurminen et al., 2020; Nurminen et al., 2022) and FDHI (Sarmiento et al., 2021) databases now provide a valuable range of observed data in the world, forming the foundations for the development of many empirical models.

The rare case of recurrent surface ruptures in the Longitudinal Valley Fault system in Taiwan, the Milun fault (1951 and 2018) and the southern LVF (1951 and 2022), provides a unique opportunity to investigate one of the fundamental assumptions underlying PFDHA: that future surface ruptures can be inferred from observations from past ruptures. Comparisons between successive surface rupturing earthquakes in the LVF showed that they produce broadly similar patterns of surface displacements, while the observed differences can mostly be explained by natural variability in earthquake characteristics (e.g. epicentral location and earthquake magnitude) or by independent environmental changes such as potential urbanisation-related surface loading. These repeated ruptures therefore provide valuable empirical evidence on both the spatial persistence and the natural variability of surface deformation, supporting the use of past rupture observations to characterise future fault displacement hazard assessments.

Even though PFDHA is now applicable in most standard tectonic contexts, with models accounting for different faulting styles, displacement metrics, and displacement components, comparisons with empirical models performed in the specific context of the Longitudinal Valley Fault system showed contrasting results. The strike-slip motion was reasonably well estimated by Petersen et al. (2011) model, while vertical displacement was almost systematically overestimated by reverse faulting models, highlighting the limitations of globally derived empirical models when applied to a poorly covered tectonic context (oblique kinematics) or to specific regional with few data present in existing datasets.

The regional PFDHA application in northern Calabria demonstrated that the region is exposed to fault displacement hazard, especially in the vicinity of the main fault systems. However, the return periods associated with surface displacements significant for safety concerns (≥ 10 cm) are extremely long, generally exceeding 10 ka and, in some cases, 100 ka. The scenario approach highlighted the importance of accurately defining the seismotectonic framework and the precise geometry and location of active and capable faults as the hazard is primarily controlled by the main fault systems and their surface expression. Careful consideration of aleatory uncertainties is also essential to ensure physically realistic displacement estimates, as at long return periods, the tails of the hazard curves can reach unrealistically high displacement values and should therefore be truncated. Finally, the northern Calabria study case also illustrated that PFDH studies can be conducted at a regional scale, enabling a new spatial visualisation of the hazard, and the exploration of various fault source configurations, representing a promising step towards integrating fault displacement hazard into land-use planning frameworks.

**Perspectives:**

The results presented in this thesis highlight several specific challenges that should be addressed in future PFDHA developments. The Taiwan case study demonstrated that current empirical models may have difficulties reproducing surface displacement patterns associated with complex fault systems, oblique kinematics, and multi-fault ruptures. Future developments should therefore aim to better incorporate these complexities. The northern Calabria case study further highlighted the strong influence of uncertainties related to the seismotectonic model and the selection of empirical PFDHA models, which can significantly affect the resulting hazard estimates. Improving the characterisation of fault sources and better quantifying and propagating epistemic and aleatory uncertainties will therefore be essential to increase the reliability and robustness of future PFDHA assessments. More generally, despite the significant progress made in recent years, much still remains to be defined, refined, and improved in the fault displacement hazard assessment and several key aspects should be further addressed in future developments of PFDHA:

- Clearer implementation of the hazard assessment in the national and international building codes and guidelines is needed. PFDHA has been defined based on the standard PSHA, but ground shaking and surface faulting are two different phenomena, with a significant difference in occurrence probability and physical implication. The definition of clear hazard thresholds and categories comparable to those used in ground-motion hazard would represent a significant step forward. Regional fault displacement hazard maps could naturally serve as a first layer of decision-making for land-use planning, in the same way seismic or flood hazard maps already do.

- Regarding the surface rupture data, new technologies and collection approaches offer promising opportunities. Systematic installation of CCTV cameras along major fault traces worldwide could provide real-time recordings of future surface rupture events, significantly expanding the observational database. More generally, an increased number of data, and in particular a broader regional coverage encompassing a wider range of tectonic contexts, are always beneficial in strengthening empirical models and improving the reliability of hazard forecasts.

- Numerical models (Mammarella et al., 2024) or physics-based (Gómez-Novell et al., 2026) instead of classic empirical approaches, may provide valuable and promising alternatives, especially in complex tectonic context, or in regions with few surface

rupture data present in the worldwide datasets.

# References


Angelier, J., Chu, H.-T., and Lee, J.-C.: Shear concentration in a collision zone: kinematics of the Chihshang Fault as revealed by outcrop-scale quantification of active faulting, Longitudinal Valley, eastern Taiwan, Tectonophysics, 274, 117–143, https://doi.org/10.1016/S0040-1951(96)00301-0, 1997.

Baize, S., Nurminen, F., Sarmiento, A., Dawson, T., Takao, M., Scotti, O., Azuma, T., Boncio, P., Champenois, J., Cinti, F. R., Civico, R., Costa, C., Guerrieri, L., Marti, E., McCalpin, J., Okumura, K., and Villamor, P.: A Worldwide and Unified Database of Surface Ruptures (SURE) for Fault Displacement Hazard Analyses, Seismological Research Letters, 91, 499–520, https://doi.org/10.1785/0220190144, 2019.

Bartholomaeus Rossanensis: Του οσίου πατρός ήμῶν Νείλου τοῦ νέου, in: Codice greco criptense B. B. 2. di S. Bartolomeo, edited by: Giovanelli, G., Badia di Grottaferrata, Roma, Italy, 1972.

Basili, R., Valensise, G., Vannoli, P., Burrato, P., Fracassi, U., Mariano, S., Tiberti, M. M., and Boschi, E.: The Database of Individual Seismogenic Sources (DISS), version 3: Summarizing 20 years of research on Italy's earthquake geology, Tectonophysics, 453, 20–43, https://doi.org/10.1016/j.tecto.2007.04.014, 2008.

Basili, R., D'Amico, V., Meletti, C., and Valensise, G.: Linee guida per la redazione e le istruttorie degli studi sismotettonici relativi alle grandi dighe, technical report prepared for ENEL, Istituto Nazionale di Geofisica e Vulcanologia, Rome, https://www.dighe.eu/normativa/allegati/2017_Linee_guida_studi_sismottettonici.pdf, 2017.

Beyreuther, M., Barsch, R., Krischer, L., Megies, T., Behr, Y., and Wassermann, J.: ObsPy: A Python Toolbox for Seismology, Seismological Research Letters, 81, 530–533, https://doi.org/10.1785/gssrl.81.3.530, 2010.

Boncio, P., Peruzza, L., Civile, D., Mirabella, F., Pace, B., Testa, A., Zecchin, M., Affatato, A., Barbagallo, A., Palermo, A., Falleti, G., and Schibuola, A.: Valutazione della pericolosità sismica da fagliazione superficiale della Diga Farneto del Principe in Comune di Roggiano Gravina (CS) – Relazione della Fase 1, Rapporto interno Convenzione CUP B47I18075860006, OGS-2022/117_CRS-21, Chieti–Trieste, Italy, 152 pp., 3 Tav., 1 All., 2022.

Boncio, P., Peruzza, L., Testa, A., Mirabella, F., Civile, D., Zecchin, M., Caffau, M., Accaino, F., and Affatato, A.: Valutazione della pericolosità sismica da fagliazione superficiale della Diga Farneto del Principe in Comune di Roggiano Gravina (CS) – Relazione dell'Atto Aggiuntivo alla Fase 1, Convenzione CUP B47I18075860006, Rapporto interno OGS-2023/105, Chieti–Trieste, Italy, 53 pp., 3 Tav., 2023.

Boncio, P., Peruzza, L., Testa, A., Mirabella, F., Civile, D., Zecchin, M., Accaino, F., Affatato, A., Baradello, L., Fernandez, H., and Forlin, E.: Valutazione della pericolosità sismica da fagliazione superficiale della Diga Farneto del Principe in Comune di Roggiano Gravina (CS) – Relazione della Fase 2, Convenzione CUP B47I18075860006, Rapporto interno

OGS-INGEO, Chieti–Trieste, Italy, 77 pp., 3 Tav., 7 All., 2025.

Bonilla, M. G.: A review of recently active faults in Taiwan, USGS Report, 50pp, available at: https://nehrpsearch.nist.gov/static/files/USGS/PB2006108298.pdf, 1975.

Boschi, E., Giardini, D., Pantosti, D., Valensise, G., Arrowsmith, R., Basham, P., Bürgmann, R., Crone, A. J., Hull, A., and McGuire, R. K.: New trends in active faulting studies for seismic hazard assessment, Annali di Geofisica, 39, 1301–1307, 1996.

Brozzetti, F., Cirillo, D., de Nardis, R., Cardinali, M., Lavecchia, G., Orecchio, B., Presti, D., and Totaro, C.: Newly identified active faults in the Pollino seismic gap, southern Italy, and their seismotectonic significance, Journal of Structural Geology, 94, 13–31, https://doi.org/10.1016/j.jsg.2016.10.005, 2017a.

Brozzetti, F., Cirillo, D., Liberi, F., Piluso, E., Faraca, E., De Nardis, R., and Lavecchia, G.: Structural style of Quaternary extension in the Crati Valley (Calabrian Arc): evidence in support of an east-dipping detachment fault, IJG, 136, 434–453, https://doi.org/10.3301/IJG.2017.11, 2017b.

Bryant, William A. and Hart, Earl W.: Fault-rupture hazard zones in California: Alquist-Priolo earthquake fault zoning act with index to earthquake fault zones maps, California Geological Survey, Special Publication 42, 42 pp., https://www.dtsc-ssfl.com/files/lib_ceqa/ref_draft_peir/Chap4_5-Geology/68321_Bryant,_WA_and_EW_Hart_2007.pdf, 2007.

Carafa, M. M. C., Barba, S., and Bird, P.: Neotectonics and long-term seismicity in Europe and the Mediterranean region, Journal of Geophysical Research: Solid Earth, 120, 5311–5342, https://doi.org/10.1002/2014JB011751, 2015.

Central Geological Survey (CGS): 20180206 花蓮地震地質調查報告 [Geological Survey Report of the 06/02/2018 Hualien Earthquake], Ministry of Economic Affairs, Taiwan, available at: https://faultnew.moeacgs.gov.tw/Reports/More/1dbcb959c822446a8044275e171b71a3, 2018.

Central Geological Survey (CGS): 20220917 關山地震、0918 池上地震地質調查報告 [Geological Survey Report of the 17/09/2022 Guanshan Earthquake and 18/09 Chihshang Earthquake], Ministry of Economic Affairs, Taiwan, available at: https://fault.gsmma.gov.tw/Reports/More/63cc5a4b2020403d9f79d3c33a7aba0c, 2022.

Cheloni, D., D'Agostino, N., Selvaggi, G., Avallone, A., Fornaro, G., Giuliani, R., Reale, D., Sansosti, E., and Tizzani, P.: Aseismic transient during the 2010–2014 seismic swarm: evidence or longer recurrence of M ≥ 6.5 earthquakes in the Pollino gap (Southern Italy)?, Sci Rep, 7, 576, https://doi.org/10.1038/s41598-017-00649-z, 2017.

Chen, H. and Rau, R.: Earthquake Locations and Style of Faulting in an Active Arc-Continent Plate Boundary: the Chihshang Fault of Eastern Taiwan, AGU Fall Meeting Abstracts, ADS Bibcode: 2002AGUFM.T61B1277C, T61B-1277, 2002.

Chen, W.-S., Yen, I.-C., Fengler, K. P., Rubin, C. M., Yang, C.-C., Yang, H.-C., Chang, H.-C., Lin, C.-W., Lin, W.-H., Liu, Y.-C., and Lin, Y.-H.: Late Holocene paleoearthquake activity in

the middle part of the Longitudinal Valley fault, eastern Taiwan, Earth and Planetary Science Letters, 264, 420–437, https://doi.org/10.1016/j.epsl.2007.09.043, 2007.

Chen, K., Milliner, C., and Avouac, J.-P.: The Weitin Fault, Papua New Guinea, Ruptured Twice by Mw 8.0 and Mw 7.7 Earthquakes in 2000 and 2019, Geophysical Research Letters, 46, 12833–12840, https://doi.org/10.1029/2019GL084645, 2019.

Chen, W. S., Wu, Y. M., Yeh, P. Y., Lai, Y. X., Ke, S. S., Ke, M. C., and Yang, C. Y.: Insights into the seismogenic structures of the arc-continent convergent plate boundary in eastern Taiwan, Terr Atmos Ocean Sci, 35, 1–21, https://doi.org/10.1007/s44195-024-00065-7, 2024.

Chen, Y.-S., Moratto, L., Pagani, M., Fernandez, H., and Peruzza, L.: Towards a unified probabilistic fault displacement hazard assessment: combining physics-based simulations and OpenQuake engine implementation, Miscellanea INGV, 102, 137–144, 2025.

Cheng, S.-N., Yeh, Y.-T., and Yu, M.-S.: The 1951 Taitung earthquake in Taiwan, JOURNAL-GEOLOGICAL SOCIETY OF CHINA-TAIWAN-, 39, 267–286, 1996.

Chiappetta, G. D. and La Rocca, M.: Low-magnitude seismic swarms in the Calabrian Arc (Italy), J Seismol, 27, 847–862, https://doi.org/10.1007/s10950-023-10171-7, 2023.

Chiou, B., Chen, R., Thomas, K., Milliner, C., Dawson, T., and Petersen, M.: Fault displacement model for surface principal rupture of strike-slip faults, Earthquake Spectra, 41, 2746–2782, https://doi.org/10.1177/87552930251337703, 2025.

Ciaccio, M. G., Di Stefano, R., Improta, L., Mariucci, M. T., and BSI Working Group: First-Motion Focal Mechanism Solutions for 2015–2019 M ≥ 4.0 Italian Earthquakes, Front. Earth Sci., 9, 630116, https://doi.org/10.3389/feart.2021.630116, 2021.

Cifelli, F., Mattei, M., and Rossetti, F.: Tectonic evolution of arcuate mountain belts on top of a retreating subduction slab: The example of the Calabrian Arc, Journal of Geophysical Research: Solid Earth, 112, https://doi.org/10.1029/2006JB004848, 2007.

Cinti, F. R., Moro, M., Pantosti, D., Cucci, L., and D'Addezio, G.: New constraints on the seismic history of the Castrovillari fault in the Pollino gap (Calabria, southern Italy), Journal of Seismology, 6, 199–217, https://doi.org/10.1023/A:1015693127008, 2002.

Cinti, F. R., Pauselli, C., Livio, F., Ercoli, M., Brunori, C. A., Ferrario, M. F., Volpe, R., Civico, R., Pantosti, D., Pinzi, S., De Martini, P. M., Ventura, G., Alfonsi, L., Gambillara, R., and Michetti, A. M.: Integrating multidisciplinary, multiscale geological and geophysical data to image the Castrovillari fault (Northern Calabria, Italy), Geophys. J. Int., 203, 1847–1863, https://doi.org/10.1093/gji/ggv404, 2015.

Cinti, F. R., Alfonsi, L., Cucci, L., Pantosti, D., Pauselli, C., Ercoli, M., Brunori, C. A., Cianflone, G., and Dominici, R.: The NE-SW Sibari fault zone: A seismic hazard source in Ionian Northern Calabria (Italy), Tectonophysics, 873, 230214, https://doi.org/10.1016/j.tecto.2024.230214, 2024.

Cirillo, D., Totaro, C., Lavecchia, G., Orecchio, B., de Nardis, R., Presti, D., Ferrarini, F., Bello, S., and Brozzetti, F.: Structural complexities and tectonic barriers controlling recent seismic activity in the Pollino area (Calabria–Lucania, southern Italy) – constraints from stress

inversion and 3D fault model building, Solid Earth, 13, 205–228, https://doi.org/10.5194/se-13-205-2022, 2022.

Civico, R., Pucci, S., Villani, F., Pizzimenti, L., De Martini, P. M., and Nappi, R.: Surface ruptures following the 30 October 2016 Mw 6.5 Norcia earthquake, central Italy, Journal of Maps, 14, 151–160, https://doi.org/10.1080/17445647.2018.1441756, 2018.

Civile, D., Zecchin, M., Tosi, L., Da Lio, C., Muto, F., Sandron, D., Affatato, A., Accettella, D., and Mangano, G.: The Petilia-Sosti Shear Zone (Calabrian Arc, southern Italy): An onshore-offshore regional active structure, Marine and Petroleum Geology, 141, 105693, https://doi.org/10.1016/j.marpetgeo.2022.105693, 2022.

Cornell, C. A.: Engineering seismic risk analysis, Bulletin of the Seismological Society of America, 58, 1583–1606, https://doi.org/10.1785/BSSA0580051583, 1968.

Danciu, L., Giardini, D., Weatherill, G., Basili, R., Nandan, S., Rovida, A., Beauval, C., Bard, P.-Y., Pagani, M., Reyes, C. G., Sesetyan, K., Vilanova, S., Cotton, F., and Wiemer, S.: The 2020 European Seismic Hazard Model: overview and results, Natural Hazards and Earth System Sciences, 24, 3049–3073, https://doi.org/10.5194/nhess-24-3049-2024, 2024.

De Gori, P., Lucente, F. P., Govoni, A., Margheriti, L., and Chiarabba, C.: Seismic swarms in the Pollino seismic gap: Positive fault inversion within a popup structure, Front. Earth Sci., 10, 968187, https://doi.org/10.3389/feart.2022.968187, 2022.

De Polo, C. M.: The maximum background earthquake for the Basin and Range Province, western North America, International Journal of Rock Mechanics and Mining Sciences & Geomechanics Abstracts, 31, 271, https://doi.org/10.1016/0148-9062(94)90084-1, 1994.

Devoti, R., Riguzzi, F., Cuffaro, M., and Doglioni, C.: New GPS constraints on the kinematics of the Apennines subduction, Earth and Planetary Science Letters, 273, 163–174, https://doi.org/10.1016/j.epsl.2008.06.031, 2008.

DISS Working Group: Database of Individual Seismogenic Sources (DISS), Version 3.3.1: A compilation of potential sources for earthquakes larger than M 5.5 in Italy and surrounding areas, Istituto Nazionale di Geofisica e Vulcanologia (INGV) [data set], https://doi.org/10.13127/diss3.3.1, 2025.

DMIT: Norme tecniche per la progettazione e la costruzione degli sbarramenti di ritenuta (dighe e traverse), Ministero delle Infrastrutture e dei Trasporti, Decreto 26 giugno 2014, Gazzetta Ufficiale della Repubblica Italiana, n. 156, 2014.

Douilly, R.: Effect of Asymmetric Topography on Rupture Propagation Along Fault Stepovers, Journal of Geophysical Research: Solid Earth, 128, e2023JB026484, https://doi.org/10.1029/2023JB026484, 2023.

Faccenna, C., Becker, T. W., Lucente, F. P., Jolivet, L., and Rossetti, F.: History of subduction and back arc extension in the Central Mediterranean, Geophys J Int, 145, 809–820, https://doi.org/10.1046/j.0956-540x.2001.01435.x, 2001.

Faulkner, D. R., Mitchell, T. M., Jensen, E., and Cembrano, J.: Scaling of fault damage zones with displacement and the implications for fault growth processes, Journal of Geophysical Research: Solid Earth, 116, https://doi.org/10.1029/2010JB007788, 2011.

FEMA: Federal guidelines for dam safety – Earthquake analyses and design of dams, Federal Emergency Management Agency, Washington, DC, USA, 76 pp., https://www.fema.gov/sites/default/files/documents/fema_rm-federal-guidelines-for-dam-safety.pdf, 2023.

Ferranti, L., Santoro, E., Mazzella, M. E., Monaco, C., and Morelli, D.: Active transpression in the northern Calabria Apennines, southern Italy, Tectonophysics, 476, 226–251, https://doi.org/10.1016/j.tecto.2008.11.010, 2009.

Ferranti, L., Burrato, P., Pepe, F., Santoro, E., Mazzella, M. E., Morelli, D., Passaro, S., and Vannucci, G.: An active oblique-contractional belt at the transition between the Southern Apennines and Calabrian Arc: The Amendolara Ridge, Ionian Sea, Italy, Tectonics, 33, 2169–2194, https://doi.org/10.1002/2014TC003624, 2014.

Ferranti, L., Pace, B., Valentini, A., Montagna, P., Pons-Branchu, E., Tisnérat-Laborde, N., and Maschio, L.: Speleoseismological Constraints on Ground Shaking Threshold and Seismogenic Sources in the Pollino Range (Calabria, Southern Italy), Journal of Geophysical Research: Solid Earth, 124, 5192–5216, https://doi.org/10.1029/2018JB017000, 2019.

Ferrario, M. F. and Livio, F.: Conditional probability of distributed surface rupturing during normal-faulting earthquakes, Solid Earth, 12, 1197–1209, https://doi.org/10.5194/se-12-1197-2021, 2021.

Galli, P. and Bosi, V.: Catastrophic 1638 earthquakes in Calabria (southern Italy): New insights from paleoseismological investigation, Journal of Geophysical Research: Solid Earth, 108, ETG 1-1-ETG 1-20, https://doi.org/10.1029/2001JB001713, 2003.

Galli, P., V, S., and Spina, V.: New paleoseismic data from the Lakes and Serre faults: Seismotectonic implications for Calabria (Southern Italy), Bollettino- Societa Geologica Italiana, 126, 2007.

Galli, P., Spina, V., Ilardo, I., and Naso, G.: Evidence of active tectonics in southern Italy: the Rossano Fault (Calabria), in: Recent progress on earthquake geology, edited by: Galli, P., Nova Science Publishers, New York, 49–78 pp., 2010.

Gao, J.-C. and Lee, C.-T.: Probabilistic Fault Displacement Hazard Analysis: An Example from a Safety Evaluation Project of the Wushantou Reservoir, EGUGA, Vienna, Austria, https://meetingorganizer.copernicus.org/EGU2019/EGU2019-6514.pdf, 2019.

Gao, J., Chan, C., Ma, K., and Lee, C.: Probabilistic Fault Displacement Hazards along the Milun Fault, Bulletin of the Seismological Society of America, 112, 2745–2757, https://doi.org/10.1785/0120210312, 2022.

Gasperini, P., Camassi, R., Mirto, C, and Stucchi, M.: Catalogo Parametrico dei Terremoti Italiani (CPTI04) (Version 1.0) [data set], Istituto Nazionale di Geofisica e Vulcanologia (INGV), https://doi.org/10.6092/INGV.IT-CPTI04, 2004.

Gómez-Novell, O., Visini, F., Álvarez-Gómez, J. A., Pace, B., and García-Mayordomo, J.: Coseismic surface rupture probabilities from earthquake cycle simulations: influence of fault geometry, Natural Hazards and Earth System Sciences, 26, 651–673, https://doi.org/10.5194/nhess-26-651-2026, 2026.

Gori, S., Falcucci, E., Fubelli, G., Muto, F., and Dramis, F.: Active transpressive surface faulting in north-eastern Calabria, Southern Italy: Early results of geomorphological, stratigraphic and paleoseismological analyses, 2016.

Gueguen, E., Doglioni, C., and Fernandez, M.: On the post-25 Ma geodynamic evolution of the western Mediterranean, Tectonophysics, 298, 259–269, https://doi.org/10.1016/S0040-1951(98)00189-9, 1998.

Handy, M. R., M. Schmid, S., Bousquet, R., Kissling, E., and Bernoulli, D.: Reconciling plate-tectonic reconstructions of Alpine Tethys with the geological–geophysical record of spreading and subduction in the Alps, Earth-Science Reviews, 102, 121–158, https://doi.org/10.1016/j.earscirev.2010.06.002, 2010.

Honegger, D. G., Nyman, D. J., Johnson, E. R., Cluff, L. S., and Sorensen, S. P.: Trans-Alaska Pipeline System Performance in the 2002 Denali Fault, Alaska, Earthquake, Earthquake Spectra, 20, 707–738, https://doi.org/10.1193/1.1779239, 2004.

Hosseini, M. and Rahimi, H.: Probabilistic fault displacement hazard analysis for the north Tabriz fault, Natural Hazards and Earth System Sciences, 22, 3571–3583, https://doi.org/10.5194/nhess-22-3571-2022, 2022.

Hsu, T.-L.: Recent faulting in the Longitudinal Valley of eastern Taiwan, Mem. Geol. Soc. China, 1, 95–102, 1962.

Hsu, L. and Bürgmann, R.: Surface creep along the Longitudinal Valley fault, Taiwan from InSAR measurements, Geophysical Research Letters, 33, https://doi.org/10.1029/2005GL024624, 2006.

Hsu, Y.-J., Yu, S.-B., Loveless, J. P., Bacolcol, T., Solidum, R., Luis Jr, A., Pelicano, A., and Woessner, J.: Interseismic deformation and moment deficit along the Manila subduction zone and the Philippine Fault system, Journal of Geophysical Research: Solid Earth, 121, 7639–7665, https://doi.org/10.1002/2016JB013082, 2016.

Hsu, Y.-C., Chang, C.-P., Yen, J.-Y., Kuo-Chen, H., and Wang, C.-C.: Investigating the structure of the Milun Fault from surface ruptures of the 2018 Hualien Earthquake, Terr. Atmos. Ocean. Sci., 30, 337–350, https://doi.org/10.3319/TAO.2018.09.28.01, 2019.

Huang, W. J., Fitrianto, M. T., Chen, C. C., Chang, P. Y., Yen, I. C., Le Béon, M., and Lu, S. T.: Complexity of near-surface deformation and subsurface structure of the Chihshang creeping fault-line scarp, eastern Taiwan: insights from integration of geological and geophysical data, Earth Planets Space, 77, 10, https://doi.org/10.1186/s40623-025-02135-7, 2025.

IAEA: Seismic hazards in site evaluation for nuclear installations, IAEA Safety Standards Series No. SSG-9, International Atomic Energy Agency, Vienna, https://www-pub.iaea.org/mtcd/publications/pdf/pub1448_web.pdf, 2010.

IAEA: Site evaluation for nuclear installations, IAEA Safety Standards Series No. SSR-1, International Atomic Energy Agency, Vienna, https://www-pub.iaea.org/MTCD/Publications/PDF/P1837_web.pdf, 2019.

IAEA: An Introduction to Probabilistic Fault Displacement Hazard Analysis in Site Evaluation for

Existing Nuclear Installations, TECDOC series 1987, International Atomic Energy Agency, https://www-pub.iaea.org/MTCD/Publications/PDF/TE-1987web.pdf, 2021.

IAEA: Seismic hazards in site evaluation for nuclear installations, Specific Safety Guides SSG-9 (Rev. 1), International Atomic Energy Agency, Vienna, https://www-pub.iaea.org/MTCD/Publications/PDF/PUB1950_web.pdf, 2022.

IAEA: Benchmarking Current Practices in Probabilistic Fault Displacement Hazard Analysis for Nuclear Installations, IAEA-TECDOC-2092, International Atomic Energy Agency, Vienna, https://www-pub.iaea.org/MTCD/publications/PDF/TE-2092web.pdf, 2025.

ISIDe Working Group: Italian Seismological Instrumental and Parametric Database (ISIDe), Istituto Nazionale di Geofisica e Vulcanologia (INGV) [data set], https://doi.org/10.13127/ISIDE, 2007.

INGV: Rete Sismica Nazionale (RSN) [data set], Istituto Nazionale di Geofisica e Vulcanologia (INGV), https://doi.org/10.13127/SD/X0FXNH7QFY, 2005.

ITHACA Working Group: ITHACA (ITaly HAzard from CApable faulting): A database of active capable faults of the Italian territory, Version December 2019, ISPRA Geological Survey of Italy [data set], http://sgi2.isprambiente.it/ithacaweb/Mappatura.aspx, 2019.

Kerr, J., Nathan, S., Van Dissen, R., Webb, P., Brunsdon, D., and King, A.: Planning for the development of land on or close to active faults: A guideline to assist resource management planners in New Zealand, Ministry for the Environment, Wellington, New Zealand, https://environment.govt.nz/assets/Publications/Files/planning-development-faults-graphics-dec04-1.pdf, 2003.

Kuehn, N. M., Kottke, A. R., Sarmiento, A. C., Madugo, C. M., and Bozorgnia, Y.: A Fault Displacement Model Based on the FDHI Database, Earthquake Spectra, 87552930241291077, https://doi.org/10.1177/87552930241291077, 2024.

Kyriakopoulos, C., Wu, B., and Oglesby, D. D.: Asymmetric Topography Causes Normal Stress Perturbations at the Rupture Front: The Case of the Cajon Pass, Geophysical Research Letters, 48, e2021GL095397, https://doi.org/10.1029/2021GL095397, 2021.

Latorre, D., Di Stefano, R., Castello, B., Michele, M., and Chiaraluce, L.: Catalogo delle Localizzazioni ASSolute (CLASS) (Version 1.0) [Data set]. Istituto Nazionale di Geofisica e Vulcanologia (INGV)., https://doi.org/10.13127/class.1.0, 2022.

Latour, S., Lebihain, M., Bhat, H. S., Twardzik, C., Bletery, Q., Hudnut, K. W., and Passelègue, F.: Direct estimation of earthquake source properties from a single CCTV camera, Science, 390, 463–467, https://doi.org/10.1126/science.adz1705, 2025.

Lavecchia, G., Bello, S., Andrenacci, C., Cirillo, D., Pietrolungo, F., Talone, D., Ferrarini, F., de Nardis, R., Galli, P., Faure Walker, J., Sgambato, C., Menichetti, M., Monaco, C., Gambino, S., De Guidi, G., Barreca, G., Carnemolla, F., Brighenti, F., Giuffrida, S., Pirrotta, C., Carboni, F., Ferranti, L., Valoroso, L., Toscani, G., Barchi, M. R., Roberts, G., and Brozzetti, F.: QUIN 2.0 - new release of the QUaternary fault strain INdicators database from the Southern Apennines of Italy, Sci Data, 11, 189, https://doi.org/10.1038/s41597-024-03008-6, 2024.

Lavrentiadis, G. and Abrahamson, N.: Fault-displacement models for aggregate and principal displacements, Earthquake Spectra, 87552930231201531, https://doi.org/10.1177/87552930231201531, 2023.

Lee, W. and Lahr, J. C.: *HYPO71: A computer program for determining hypocenter, magnitude, and first motion pattern of local earthquakes*, U.S. Geological Survey Open-File Report 72-224, 100 pp., https://doi.org/10.3133/ofr72224, 1972.

Lee, J.-C., Angelier, J., Chu, H.-T., Hu, J.-C., Jeng, F.-S., and Rau, R.-J.: Active fault creep variations at Chihshang, Taiwan, revealed by creep meter monitoring, 1998–2001, Journal of Geophysical Research: Solid Earth, 108, https://doi.org/10.1029/2003JB002394, 2003.

Lee, S., Lin, T., Liu, T., and Wong, T.: Fault-to-Fault Jumping Rupture of the 2018 Mw 6.4 Hualien Earthquake in Eastern Taiwan, Seismological Research Letters, 90, 30–39, https://doi.org/10.1785/0220180182, 2018.

Leonard, M.: Earthquake Fault Scaling: Self-Consistent Relating of Rupture Length, Width, Average Displacement, and Moment Release, Bulletin of the Seismological Society of America, 100, 1971–1988, https://doi.org/10.1785/0120090189, 2010.

Leonard, M.: Self-Consistent Earthquake Fault-Scaling Relations: Update and Extension to Stable Continental Strike-Slip Faults, Bulletin of the Seismological Society of America, 104, 2953–2965, https://doi.org/10.1785/0120140087, 2014.

Lin, C.-W., Chen, W.-S., Liu, Y.-C., and Chen, P.-T.: Milun fault, in: Active faults of eastern and southern Taiwan: explanatory text of the 1:25 000 active fault strip maps, Special Publication of the Central Geological Survey, MOEA, 23, 11–20, 2009.

Lomax, A.: SeisGram2K: Seismogram visualization tool. Available at: http://alomax.free.fr/seisgram/SeisGram2K.html, 2004.

Machette, M. N.: Active, capable, and potentially active faults — a paleoseismic perspective, Journal of Geodynamics, 29, 387–392, https://doi.org/10.1016/S0264-3707(99)00060-5, 2000.

Malavieille, J., Lallemand, S. E., Dominguez, S., Deschamps, A., Lu, C.-Y., Liu, C.-S., Schnuerle, P., Angelier, J., Collot, J. Y., Deffontaines, B., Fournier, M., Hsu, S. K., Le Formal, J. P., Liu, S. Y., Sibuet, J. C., Thareau, N., and Wang, F.: Arc-continent collision in Taiwan: New marine observations and tectonic evolution, in: Geology and geophysics of an arc-continent collision, Taiwan, Geological Society of America, https://doi.org/10.1130/0-8137-2358-2.187, 2002.

Malinverno, A. and Ryan, W. B. F.: Extension in the Tyrrhenian Sea and shortening in the Apennines as result of arc migration driven by sinking of the lithosphere, Tectonics, 5, 227–245, https://doi.org/10.1029/TC005i002p00227, 1986.

Mammarella, L., Visini, F., Boncio, P., Baize, S., Scotti, O., Beauval, C., Pace, B., and Thompson, S.: Conditional probability of surface rupture: A numerical approach for principal faulting, Earthquake Spectra, 87552930241293570, https://doi.org/10.1177/87552930241293570, 2024.

McCalpin, J. P. and Slemmons, D. B.: Statistics of paleoseismic data, unpublished final technical

report submitted to the U.S. Geological Survey, GEO-HAZ Consulting, Inc., 62 pp., https://www.researchgate.net/publication/259443806_STATISTICS_OF_PALEOSEISMIC_DATA, 1998.

Meletti, C., Montaldo, V., Stucchi, M., and Martinelli, F.: Database della pericolosità sismica MPS04, Istituto Nazionale di Geofisica e Vulcanologia (INGV) [data set], https://doi.org/10.13127/SH/MPS04/DB, 2006.

Meletti, C., Galadini, F., Valensise, G., Stucchi, M., Basili, R., Barba, S., Vannucci, G., and Boschi, E.: A seismic source zone model for the seismic hazard assessment of the Italian territory, Tectonophysics, 450, 85–108, https://doi.org/10.1016/j.tecto.2008.01.003, 2008.

Meschis, M., Teza, G., Serpelloni, E., Elia, L., Lattanzi, G., Di Donato, M., and Castellaro, S.: Refining Rates of Active Crustal Deformation in the Upper Plate of Subduction Zones, Implied by Geological and Geodetic Data: The E-Dipping West Crati Fault, Southern Italy, Remote Sensing, 14, 5303, https://doi.org/10.3390/rs14215303, 2022.

Michetti, A. M., Ferreli, L., Serva, L., and Vittori, E.: Geological evidence for strong historical earthquakes in an "aseismic" region: The Pollino case (Southern Italy), Journal of Geodynamics, 24, 67–86, https://doi.org/10.1016/S0264-3707(97)00018-5, 1997.

Moghaddas, N. H. and Leo, C.: Probabilistic Fault Displacement Hazard Analysis of Choman Dam Site, West of Iran., Journal of Seismology & Earthquake Engineering, 21, 25, 2019.

Moss, R. E. S. and Ross, Z. E.: Probabilistic Fault Displacement Hazard Analysis for Reverse Faults, Bulletin of the Seismological Society of America, 101, 1542–1553, https://doi.org/10.1785/0120100248, 2011.

Moss, R. E. S., Stanton, K. V., and Buelna, M. I.: The Impact of Material Stiffness on the Likelihood of Fault Rupture Propagating to the Ground Surface, Seismological Research Letters, 84, 485–488, https://doi.org/10.1785/0220110109, 2013.

Moss, R., Thompson, S., Kuo, C.-H., Younesi, K., and Baumont, D.: Reverse Fault PFDHA, Report GIRS-2022-05, Natural Hazards Risk and Resiliency Research Center, B. John Garrick Institute for the Risk Sciences, University of California, Los Angeles, https://doi.org/10.34948/N3F595, 2022.

Moss, R. E. S., Thompson, S. C., Kuo, C.-H., Younesi, K., and Baumont, D.: New probabilistic fault displacement hazard models for reverse faulting, Earthquake Spectra, 87552930241288560, https://doi.org/10.1177/87552930241288560, 2024.

Mucciarelli, M., Peruzza, L., and Caroli, P.: Tuning of Seismic Hazard Estimates by Means of Observed Site Intensities, Journal of Earthquake Engineering, 4, 141–159, https://doi.org/10.1080/13632460009350366, 2000.

NEA: Assessment of the Safe Shutdown Earthquake Robustness Against On-site Observations, OECD Publishing, Paris, France, 2021.

Nishizaka, N., Onishi, K., Ishikawa, Y., Ono, M., Miyakoshi, J., Ikeda, M., Tsuji, T., Kumamoto, T., and Okumura, K.: Probabilistic Fault Displacement Hazard Analysis Using Model of Seismic Source Characteristics at the Ikata Site Based on Guidelines for Sshac Level 3, Journal of Japan Association for Earthquake Engineering, 24, 2_57-2_78,

https://doi.org/10.5610/jaee.24.2_57, 2024.

NRC (U.S. Nuclear Regulatory Commission): Regulatory Guide 1.165: Identification and Characterization of Seismic Sources and Determination of Safe-Shutdown Earthquake Ground Motion, Office of Nuclear Regulatory Research, U.S. Nuclear Regulatory Commission, Washington, DC, USA, available at: https://www.nrc.gov/docs/ml0037/ML003740084.pdf, 1997.

Nurminen, F., Boncio, P., Visini, F., Pace, B., Valentini, A., Baize, S., and Scotti, O.: Probability of Occurrence and Displacement Regression of Distributed Surface Rupturing for Reverse Earthquakes, Front. Earth Sci., 8, https://doi.org/10.3389/feart.2020.581605, 2020.

Nurminen, F., Baize, S., Boncio, P., Blumetti, A. M., Cinti, F. R., Civico, R., and Guerrieri, L.: SURE 2.0 – New release of the worldwide database of surface ruptures for fault displacement hazard analyses, Sci Data, 9, 729, https://doi.org/10.1038/s41597-022-01835-z, 2022.

Pace, B., Visini, F., and Peruzza, L.: FiSH : MATLAB Tools to Turn Fault Data into Seismic-Hazard Models, Seismological Research Letters, 87, 374–386, https://doi.org/10.1785/0220150189, 2016.

Pacific Gas & Electric Company: Confirmatory analysis of seismic hazard at the Diablo Canyon Power Plant from the Shoreline Fault Zone, Research Information Letter 12-01, ADAMS Accession No. ML121230035, https://www.nrc.gov/docs/ml1212/ml121230035.pdf, 2012.

Pagani, M., Monelli, D., Weatherill, G., Danciu, L., Crowley, H., Silva, V., Henshaw, P., Butler, L., Nastasi, M., Panzeri, L., Simionato, M., and Vigano, D.: OpenQuake Engine: An open hazard (and risk) software for the Global Earthquake Model, Seismol. Res. Lett., 85, 692–702, https://doi.org/10.1785/0220130087, 2014.

Palano, M., Billi, A., Conti, A., Cuffaro, M., Orecchio, B., Presti, D., Scolaro, S., Sparacino, F., and Totaro, C.: The intra-orogenic normal Lakes Fault (Sila, Calabria, southern Italy): new insights from geodetic and seismological data, IJG, 142 (2023) f.3, https://doi.org/10.3301/IJG.2023.18, 2023.

Papanikolaou, I. D. and Roberts, G. P.: Geometry, kinematics and deformation rates along the active normal fault system in the southern Apennines: Implications for fault growth, Journal of Structural Geology, 29, 166–188, https://doi.org/10.1016/j.jsg.2006.07.009, 2007.

Pastori, M., Margheriti, L., De Gori, P., Govoni, A., Lucente, F. P., Moretti, M., Marchetti, A., Di Giovambattista, R., Anselmi, M., De Luca, P., Nardi, A., Agostinetti, N. P., Latorre, D., Piccinini, D., Passarelli, L., and Chiarabba, C.: The 2011–2014 Pollino Seismic Swarm: Complex Fault Systems Imaged by 1D Refined Location and Shear Wave Splitting Analysis at the Apennines–Calabrian Arc Boundary, Front. Earth Sci., 9, https://doi.org/10.3389/feart.2021.618293, 2021.

Petersen, M. D., Dawson, T. E., Chen, R., Cao, T., Wills, C. J., Schwartz, D. P., and Frankel, A. D.: Fault Displacement Hazard for Strike-Slip Faults, Bulletin of the Seismological Society of America, 101, 805–825, https://doi.org/10.1785/0120100035, 2011.

Pezzopane, Stephen K. and Dawson, Timothy E.: Fault displacement hazard: a summary of issues and information, in: Seismotectonic Framework and Characterization of Faulting at Yucca

Mountain, Nevada, U.S. Geological Survey Administrative Report prepared for the U.S. Department of Energy, Chap. 9, 160, 1996.

Pizza, M., Ferrario, M. F., Thomas, F., Tringali, G., and Livio, F.: Likelihood of Primary Surface Faulting: Updating of Empirical Regressions, Bulletin of the Seismological Society of America, 113, 2106–2118, https://doi.org/10.1785/0120230019, 2023.

Pondrelli, S.: European-Mediterranean Regional Centroid-Moment Tensors Catalog (RCMT), Istituto Nazionale di Geofisica e Vulcanologia (INGV), https://doi.org/10.13127/RCMT/EUROMED, 2002.

Pondrelli, S., Salimbeni, S., Ekström, G., Morelli, A., Gasperini, P., and Vannucci, G.: The Italian CMT dataset from 1977 to the present, Physics of the Earth and Planetary Interiors, 159, 286–303, https://doi.org/10.1016/j.pepi.2006.07.008, 2006.

Prada, M., Ranero, C. R., Sallares, V., Grevemeyer, I., de Franco, R., Gervasi, A., and Zitellini, N.: The structure of Mediterranean arcs: New insights from the Calabrian Arc subduction system, Earth and Planetary Science Letters, 548, 116480, https://doi.org/10.1016/j.epsl.2020.116480, 2020.

Rodriguez Padilla, A. M. and Oskin, M. E.: Displacement Hazard from Distributed Ruptures in Strike-Slip Earthquakes, Bulletin of the Seismological Society of America, 113, 2730–2745, https://doi.org/10.1785/0120230044, 2023.

Rovida, A., Locati, M., Camassi, R., Lolli, B., and Gasperini, P.: The Italian earthquake catalogue CPTI15, Bull Earthquake Eng, 18, 2953–2984, https://doi.org/10.1007/s10518-020-00818-y, 2020.

Rovida, A., Locati, M., Camassi, R., Lolli, B., Gasperini, P., and Antonucci, A.: Italian Parametric Earthquake Catalogue (CPTI15), version 4.0 [data set], Istituto Nazionale di Geofisica e Vulcanologia (INGV), https://doi.org/10.13127/cpti/cpti15.4 , 2022.

Rovida, A., Locati, M., Antonucci, A., and Camassi, R.: The Italian Archive of Historical Earthquake Data, ASMI, Earth Syst. Sci. Data, 17, 3109–3124, https://doi.org/10.5194/essd-17-3109-2025, 2025.

Sarmiento, A., Madugo, D., Bozorgnia, Y., Shen, A., Mazzoni, S., Lavrentiadis, G., Dawson, T., Madugo, C., Kottke, A., Thompson, S., Baize, S., Milliner, C., Nurminen, F., Boncio, P., and Visini, F.: *Fault Displacement Hazard Initiative Database*, Report GIRS-2021-08, https://doi.org/10.34948/N36P48, 2021.

Sarmiento, A., Lavrentiadis, G., Bozorgnia, Y., Chen, R., Chiou, B., Dawson, T., Kottke, A., Kuehn, N., Madugo, C., Moss, R., Thompson, S., and Zandieh, A.: Comparisons of FDHI fault displacement models for principal and aggregate displacement, Earthquake Spectra, 87552930251327894, https://doi.org/10.1177/87552930251327894, 2025.

Scognamiglio, L., Tinti, E., and Quintiliani, M.: Time Domain Moment Tensor (TDMT), Istituto Nazionale di Geofisica e Vulcanologia (INGV) – Osservatorio Nazionale Terremoti [data set], https://doi.org/10.13127/TDMT, 2006.

Shyu, J. B. H., Sieh, K., Avouac, J.-P., Chen, W.-S., and Chen, Y.-G.: Millennial slip rate of the Longitudinal Valley fault from river terraces: Implications for convergence across the

active suture of eastern Taiwan, Journal of Geophysical Research: Solid Earth, 111, https://doi.org/10.1029/2005JB003971, 2006.

Shyu, J. B. H., Chung, L.-H., Chen, Y.-G., Lee, J.-C., and Sieh, K.: Re-evaluation of the surface ruptures of the November 1951 earthquake series in eastern Taiwan, and its neotectonic implications, Journal of Asian Earth Sciences, 31, 317–331, https://doi.org/10.1016/j.jseaes.2006.07.018, 2007.

Shyu, J. B. H., Yin, Y.-H., Chen, C.-H., Chuang, Y.-R., and Liu, S.-C.: Updates to the on-land seismogenic structure source database by the Taiwan Earthquake Model (TEM) project for seismic hazard analysis of Taiwan, Terr. Atmos. Ocean. Sci., 31, 469–478, https://doi.org/10.3319/TAO.2020.06.08.01, 2020.

Slemmons, D. B. and McKinney, R.: Definition of "active Fault": Final Report, Department of Defense, Department of the Army, Corps of Engineers, Waterways Experiment Station, Soils and Pavements Laboratory, 32 pp., 1977.

SM Working Group: Guidelines for Seismic Microzonation (English edition), Dipartimento della Protezione Civile and Conference of Regions and Autonomous Provinces of Italy, https://www.centromicrozonazionesismica.it/documents/18/GuidelinesForSeismicMicrozonation.pdf, 2015.

Snoke, J. A., Munsey, J. W., Teague, A. G., and Bollinger, G. A.: A program for focal mechanism determination by combined use of polarity and SV-P amplitude ratio data, *Earthquake Notes*, 55, 15–20, 1984.

Spina, V., Tondi, E., and Mazzoli, S.: Complex basin development in a wrench-dominated back-arc area: Tectonic evolution of the Crati Basin, Calabria, Italy, Journal of Geodynamics, 51, 90–109, https://doi.org/10.1016/j.jog.2010.05.003, 2011.

Stahl, T., Underwood, A., Litchfield, N., Wotherspoon, L., Moss, R., and Fraser, J.: Resilience to Fault Displacement Hazards, https://www.naturalhazards.govt.nz/assets/Publications-Resources/QuakeCoRE-FDHA.pdf, 2024.

Stepp, J., Wong, I., Whitney, J., Quittmeyer, R., Toro, G., Youngs, R., Coppersmith, K., Savy, J., Sullivan, T., and Members, Y.: Probabilistic Seismic Hazard Analyses for Ground Motions and Fault Displacement at Yucca Mountain, Nevada, Earthquake Spectra, 17, 113–151, https://doi.org/10.1193/1.1586169, 2001.

Stucchi, M., Meletti, C., Montaldo, V., Crowley, H., Calvi, G. M., and Boschi, E.: Seismic Hazard Assessment (2003–2009) for the Italian Building Code, Bulletin of the Seismological Society of America, 101, 1885–1911, https://doi.org/10.1785/0120100130, 2011.

Styron, R. and Pagani, M.: The GEM Global Active Faults Database, Earthquake Spectra, 36, 160–180, https://doi.org/10.1177/8755293020944182, 2020.

Sugito, N., Goto, H., Kumahara, Y., Tsutsumi, H., Nakata, T., Kagohara, K., Matsuta, N., and Yoshida, H.: Surface fault ruptures associated with the 14 April foreshock (Mj 6.5) of the 2016 Kumamoto earthquake sequence, southwest Japan, Earth Planets Space, 68, 170, https://doi.org/10.1186/s40623-016-0547-5, 2016.

Takao, M., Tsuchiyama, J., Annaka, T., and Kurita, T.: Application of Probabilistic Fault

Displacement Hazard Analysis in Japan, Journal of JAEE, 13, 17–36, https://doi.org/10.5610/jaee.13.17, 2013.

Takao, M., Ueta, K., Annaka, T., Kurita, T., Nakase, H., Kyoya, T., and Kato, J.: Reliability Improvement of Probabilistic Fault Displacement Hazard Analysis, Journal of Japan Association for Earthquake Engineering, 14, 2_16-2_36, https://doi.org/10.5610/jaee.14.2_16, 2014.

Takao, M., Tani, T., Oshima, T., Annaka, T., and Kurita, T.: Maximum Likelihood Estimation of the Parameters regarding Displacement Evaluation of Distributed Fault in PFDHA, Journal of Japan Association for Earthquake Engineering, 16, 2_96-2_101, https://doi.org/10.5610/jaee.16.2_96, 2016.

Tang, Y. and Quigley, M.: Probabilistic fault displacement hazard analysis for primary and distributed surface ruptures in Australia, Australian Earthquake Engineering Society National Conference, Melbourne, Victoria, Australia, 20–22 November 2025, https://aees.org.au/wp-content/uploads/2025/11/10.-Gideon-Tang.pdf, 2025.

Tansi, C., Muto, F., Critelli, S., and Iovine, G.: Neogene-Quaternary strike-slip tectonics in the central Calabrian Arc (southern Italy), Journal of Geodynamics, 43, 393–414, https://doi.org/10.1016/j.jog.2006.10.006, 2007.

Technical Commission on Seismic Microzonation: Land use guidelines for areas with active and capable faults (ACF), Conference of the Italian regions and autonomous provinces–Civil protection department, Rome, 2015.

Testa, A., Valentini, A., Boncio, P., Pace, B., Visini, F., Mirabella, F., and Pauselli, C.: Probabilistic fault displacement hazard analysis of the Anghiari - Città di Castello normal fault (Italy), IJG, 140 (2021) f.3, https://doi.org/10.3301/IJG.2021.07, 2021.

Testa, A., Boncio, P., Pace, B., Mirabella, F., Pauselli, C., Ercoli, M., Auciello, E., Visini, F., and Baize, S.: Probabilistic fault displacement Hazard analysis in an extensional setting: Application to a strategic Dam and methodological implications, Engineering Geology, 343, 107817, https://doi.org/10.1016/j.enggeo.2024.107817, 2024.

Teza, G., Pesci, A., and Galgaro, A.: Grid_strain and grid_strain3: Software packages for strain field computation in 2D and 3D environments, Computers & Geosciences, 34, 1142–1153, https://doi.org/10.1016/j.cageo.2007.07.006, 2008.

Thingbaijam, K. K. S., Martin Mai, P., and Goda, K.: New Empirical Earthquake Source-Scaling Laws, Bulletin of the Seismological Society of America, 107, 2225–2246, https://doi.org/10.1785/0120170017, 2017.

Thomas, M. Y., Avouac, J.-P., Champenois, J., Lee, J.-C., and Kuo, L.-C.: Spatiotemporal evolution of seismic and aseismic slip on the Longitudinal Valley Fault, Taiwan, Journal of Geophysical Research: Solid Earth, 119, 5114–5139, https://doi.org/10.1002/2013JB010603, 2014.

Thompson, S.: Fault Displacement Metrics and Definitions, in: Bozorgnia, Y., and Sarmiento, A.: Fault Displacement Hazard Initiative: FDHI overview. YouTube, https://youtu.be/iuRulb7BmWE?si=WVDkjsbySH0-RLaA&t=3661, 2024.

Tiwari, D. K., Hari, M., Kundu, B., Jha, B., Tyagi, B., and Malik, K.: Delhi urbanization footprint and its effect on the earth's subsurface state-of-stress through decadal seismicity modulation, Sci Rep, 13, 11750, https://doi.org/10.1038/s41598-023-38348-7, 2023.

Toda, S.: Seismic and displacement hazard assessments on active faults in Japan, 10th Asian Regional Conference of IAEG, https://www.jseg.or.jp/2015ARC/data/PaperofKeynote/Shinji_Toda.pdf, 2015.

Totaro, C., Seeber, L., Waldhauser, F., Steckler, M., Gervasi, A., Guerra, I., Orecchio, B., and Presti, D.: An Intense Earthquake Swarm in the Southernmost Apennines: Fault Architecture from High-Resolution Hypocenters and Focal Mechanisms, Bulletin of the Seismological Society of America, 105, 3121–3128, https://doi.org/10.1785/0120150074, 2015.

Tseng, T., Ma, K., Yen, J., Asimaki, D., Klinger, Y., and Mai, P. M.: Introduction to the Special Section on Earthquake Hazards 25 Years After Chi-Chi: Learning from the Past to Prepare for the Future, Bulletin of the Seismological Society of America, 116, 1–4, https://doi.org/10.1785/0120250259, 2025.

USGS: Finite-Fault Model for the September 18, 2022 Mw 6.9 Chihshang, Taiwan Earthquake, U.S. Geological Survey National Earthquake Information Center, available at: https://earthquake.usgs.gov/earthquakes/eventpage/us7000i90q/finite-fault, 2022.

Valentini, A., Fukushima, Y., Contri, P., Ono, M., Sakai, T., Thompson, S. C., Viallet, E., Annaka, T., Chen, R., Moss, R. E. S., Petersen, M. D., Visini, F., and Youngs, R. R.: Probabilistic Fault Displacement Hazard Assessment (PFDHA) for Nuclear Installations According to IAEA Safety Standards, Bulletin of the Seismological Society of America, 111, 2661–2672, https://doi.org/10.1785/0120210083, 2021.

Valentini, A., Visini, F., Boncio, P., Scotti, O., and Baize, S.: Twenty-Five Years of Probabilistic Fault Displacement Hazard Assessment, Reviews of Geophysics, 63, e2024RG000875, https://doi.org/10.1029/2024RG000875, 2025.

Visini, F., Boncio, P., Valentini, A., Scotti, O., Nurminen, F., Baize, S., and Pace, B.: Empirical regressions for distributed faulting of dip-slip earthquakes, Earthquake Spectra, 87552930241308860, https://doi.org/10.1177/87552930241308860, 2025.

Wang, Y., Wu, S.-H., Chou, H. L. B., Li, Y.-Y., Cheng, W. S., Ho, A., Chen, J.-M., Liu, S.-C., Hsieh, C.-Y., Duan, S., Saw Myat Min, Ei Mhone Nathar Myo, Tsai, Y.-L., Liang, N.-W., Liao, J.-H., Lam, T. Y. A., Chang, E.-W., and Shyu, J. B. H.: Surface ruptures of the 2022 Guanshan-Chihshang earthquakes in central Longitudinal Valley area, eastern Taiwan, Terr Atmos Ocean Sci, 35, 16, https://doi.org/10.1007/s44195-024-00077-3, 2024.

Wells, D. and Coppersmith, K.: Likelihood of surface rupture as a function of magnitude, Seismol. Res, Lett, 64, 974–1002, 1993.

Wells, D. L. and Coppersmith, K. J.: New empirical relationships among magnitude, rupture length, rupture width, rupture area, and surface displacement, Bulletin of the Seismological Society of America, 84, 974–1002, https://doi.org/10.1785/BSSA0840040974, 1994.

Wesnousky, S. G.: Displacement and Geometrical Characteristics of Earthquake Surface Ruptures: Issues and Implications for Seismic-Hazard Analysis and the Process of Earthquake Rupture, Bulletin of the Seismological Society of America, 98, 1609–1632,

https://doi.org/10.1785/0120070111, 2008.

Wiemer, S.: A Software Package to Analyze Seismicity: ZMAP, Seismological Research Letters, 72, 373–382, https://doi.org/10.1785/gssrl.72.3.373, 2001.

Wilkinson, M. W., McCaffrey, K. J. W., Jones, R. R., Roberts, G. P., Holdsworth, R. E., Gregory, L. C., Walters, R. J., Wedmore, L., Goodall, H., and Iezzi, F.: Near-field fault slip of the 2016 Vettore Mw 6.6 earthquake (Central Italy) measured using low-cost GNSS, Sci Rep, 7, 4612, https://doi.org/10.1038/s41598-017-04917-w, 2017.

WSSPC: Active fault definition for the Basin and Range Province, Western States Seismic Policy Council (WSSPC), San Francisco, CA, USA, 1997.

Xu, X., Kang, W., Wang, T., Zhang, X., Liu, Y., Zhang, Y., Zhao, J., Li, K., Wang, Q., Cheng, J., and Ren, J.: The Mw7.7 Myanmar earthquake: a continental longest surface-rupturing supershear cascading event, npj Nat. Hazards, 2, 73, https://doi.org/10.1038/s44304-025-00125-z, 2025.

Yang, H., Quigley, M., and King, T.: Surface slip distributions and geometric complexity of intraplate reverse-faulting earthquakes, GSA Bulletin, 133, 1909–1929, https://doi.org/10.1130/B35809.1, 2021.

Yao, S. and Yang, H.: Hypocentral dependent shallow slip distribution and rupture extents along a strike-slip fault, Earth and Planetary Science Letters, 578, 117296, https://doi.org/10.1016/j.epsl.2021.117296, 2022.

Yoshimi, M. and Maruyama, T.: 第九報 2024年能登半島地震の緊急調査報告（陸域に出現した地表変状の現地調査）[9th Report: Emergency Survey of the 2024 Noto Peninsula Earthquake – Field Investigation of Surface Deformation on Land], Geological Survey of Japan, AIST, available at: https://www.gsj.jp/hazards/earthquake/noto2024/noto2024-09.html, 2024.

Youngs, R. R., Arabasz, W. J., Anderson, R. E., Ramelli, A. R., Ake, J. P., Slemmons, D. B., McCalpin, J. P., Doser, D. I., Fridrich, C. J., Swan, F. H., Rogers, A. M., Yount, J. C., Anderson, L. W., Smith, K. D., Bruhn, R. L., Knuepfer, P. L. K., Smith, R. B., dePolo, C. M., O'Leary, D. W., Coppersmith, K. J., Pezzopane, S. K., Schwartz, D. P., Whitney, J. W., Olig, S. S., and Toro, G. R.: A Methodology for Probabilistic Fault Displacement Hazard Analysis (PFDHA), Earthquake Spectra, 19, 191–219, https://doi.org/10.1193/1.1542891, 2003.

Yu, S.-B., Chen, H.-Y., and Kuo, L.-C.: Velocity field of GPS stations in the Taiwan area, Tectonophysics, 274, 41–59, https://doi.org/10.1016/S0040-1951(96)00297-1, 1997.

Yu, J., REN, Z., ZHANG, H., LI, C., WANG, S., GONG, Z., ZHOU, X., XU, Y., LIANG, P., MA, Z., and LI, J.: SURFACE RUPTURE OF THE FEBRUARY 6, 2023 MW7.5 ELBISTAN EARTHQUAKE IN TURKEY, SEISMOLOGY AND GEOLOGY, 46, 1263, https://doi.org/10.3969/j.issn.0253-4967.2024.06.003, 2025.

Zheng, S., Ye, Y., Xu, M., and Xin, Z.: 臺灣十大災害地震圖集 [Atlas of Ten Major Disaster Earthquakes in Taiwan], Central Weather Bureau and Institute of Earth Sciences, Academia Sinica, Taiwan, 1999.